Doctoral Thesis – María del Carmen Castell Capitán

Alternative photosynthetic redox proteins in the diatom *Phaeodactylum tricornutum*

Instituto de Bioquímica Vegetal y Fotosíntesis, Universidad de Sevilla – CSIC

Departamento de Bioquímica Vegetal y Biología Molecular, Universidad de Sevilla

Sevilla, 2021

Cover. Electron microscopy image of a *Phaeodactylum tricornutum* cell. The image was obtained, in collaboration with Dr. Purificación Calvo, in the microscopy service of the CITIUS (University of Seville).

Instituto de Bioquímica Vegetal y Fotosíntesis

Departamento de Bioquímica Vegetal y Biología Molecular

Universidad de Sevilla y Consejo Superior de Investigaciones Científicas

TESIS DOCTORAL

Alternative photosynthetic redox proteins in the diatom *Phaeodactylum tricornutum*

Trabajo presentado por María del Carmen Castell Capitán para optar al grado de Doctora

María del Carmen Castell Capitán

Sevilla, 2021

Directores:

HERVAS MORON MANUEL - 29741409V

Firmado digitalmente por HERVAS MORON MANUEL - 29741409V
Fecha: 2021.06.09 23:28:48 +02'00'

Dr. Manuel Hervás Morón
Catedrático de Bioquímica y Biología Molecular

NAVARRO CARRUESCO JOSE ANTONIO - 28571375Q

Firmado digitalmente por NAVARRO CARRUESCO JOSE ANTONIO - 28571375Q
Nombre de reconocimiento (DN): c=ES, serialNumber=IDCES-28571375Q, givenName=JOSE ANTONIO, sn=NAVARRO CARRUESCO, cn=NAVARRO CARRUESCO JOSE ANTONIO - 28571375Q
Fecha: 2021.06.09 23:23:18 +02'00'

Dr. José Antonio Navarro Carruesco
Investigador Científico del CSIC

Agradecimientos/Acknowledgements

Este trabajo ha sido realizado en el Instituto de Bioquímica Vegetal y Fotosíntesis (Universidad de Sevilla – CSIC), en el Centro de Investigaciones Científicas Isla de la Cartuja, gracias a un contrato predoctoral de Formación de Profesorado Universitario (FPU) del Ministerio de Educación, Cultura y Deporte (FPU16/04040). El trabajo ha sido financiado a través de ayudas del Ministerio de Economía, Industria y Competitividad (BIO2015-64165-P) y de la Junta de Andalucía (PAIDI BIO-022).

En primer lugar, quiero agradecer a mis directores de tesis, Manuel Hervás y José Antonio Navarro, por su paciencia, su dedicación y la confianza que depositaron en mí desde el principio. Vosotros, que me habéis enseñado tanto durante estos años, sois los mejores jefes que jamás hubiera soñado. Gracias por vuestro apoyo, por vuestra ayuda y por mostrarme lo bonito que es hacer ciencia cuando hay ganas y compañerismo.

A Pilar B., por enseñarme todo lo que sé, por la paciencia que has tenido conmigo todos estos años y por seguir ahí. Da gusto aprender de personas como tú. Más que una compañera de laboratorio, me llevo a una amiga para toda la vida. A Mercedes Roncel y José María Ortega, por compartir vuestros conocimientos conmigo y vuestro apoyo en todo lo que he necesitado.

Gracias a Conso, Fernando y Vicente por vuestra ayuda siempre que la he necesitado. Agradezco también a los técnicos del IBVF, Alicia, José Enrique, Rocío y Carlos, su ayuda durante la realización de determinados experimentos. A Nacho Algarín, del Centro Público Integrado de Formación Profesional Marítimo Zaporito (San Fernando, Cádiz), por habernos suministrado algunas de las estirpes de algas usadas en este trabajo. Gracias al grupo de Biotencología de semillas (IRNAS, Sevilla) por el uso de su sistema de biolistica.

I would like to thank Dr. Angela Falciatore and Dr. Benjamin Bailleul for allowing me to stay for three months in their laboratory in Paris and for teaching me so much.

A Juan Fernández Recio, por permitirme visitar su laboratorio en Logroño durante unas semanas y descubrir un mundo nuevo para mí, la bioinformática. Gracias a Luis y Mireia, por enseñarme tanto y por la paciencia que tuvisteis conmigo.

Gracias a mis compañeros, ¿qué digo compañeros?, amigos: Manuel, Ana, Laura y Diego. Gracias por ayudarme, por apoyarme, por las cervezas, por los descansitos de media mañana, por los desayunos en la Manuela, por todo. A Pilar A., que pasó rápido de ser compañera de laboratorio a una gran amiga. A Macarena, gracias por nuestras charlas y por tu alegría. Y a

muchos otros compañeros del IBVF, por ayudarme cuando lo he necesitado y por hacer más ameno el día a día en el trabajo.

Gracias a mi familia, mi gran familia. Mamá, papá, Sandra, gracias por vuestro apoyo absoluto, por confiar ciegamente en mí y por aguantarme durante esta etapa. Sin vosotros no podría haberlo conseguido. Gracias a todos mis tíos, a mis primos, a mis abuelos, y a aquellos que ya no están entre nosotros, pero que sé que estarían orgullosos de mí. A Juanma, por ser siempre el primero en querer leerse todos mis artículos. Agradezco también a todos mis amigos por su cariño y por estar ahí siempre.

And, last but not least, I would like to thank my love, Jonathan. Thanks for your patience during these four years, for your unconditional support, for believing in me and for making our apartment a lovely home for both of us.

Index

Index

Figures

Tables

Abbreviations

Å	Angstrom
ADP	Adenosine diphosphate
Ap	Ampicillin
APS	Ammonium Persulfate
ASW	Artificial Seawater
ATP	Adenosine triphosphate
ATPC	ATPase gamma subunit
BD	Brownian Dynamics
BLAST-N	Standard Nucleotide Basic Local Alignment Search Tool
BLAST-P	Standard Protein Basic Local Alignment Search Tool
BSA	Bovine Serum Albumin
Cb_6	Cytochrome b_6
Cb_6f	Cytochrome b_6f
Cc_{550}	Cytochrome c_{550}
Cc_6	Cytochrome c_6
cDNA	Complementary DNA
Cf	Cytochrome *f*
Chl	Chlorophyll
Cm	Chloramphenicol
C. caldarium	*Cyanidium caldarium*
C. gracilis	*Chaetoceros gracilis*
C. merolae	*Cyanidioschyzon merolae*
C. muellerii	*Chaetoceros muellerii*
C. reinhardtii	*Chlamydomonas reinhardtii*
CTAB	Cetyl-trimethyl-ammonium bromide
C-terminus	Carboxyl terminus
Da	Dalton
DCBQ	2,5-Dichloro-1,4-benzoquinone
DCMU	3-(3,4-dichlorophenyl)-1,1-dimethylurea
DEAE	Diethylaminoethyl
DIC	Differential interference contrast

DNA	Deoxyribonucleic acid
DNase	Deoxyribonuclease
dNTP	Deoxyribonucleotide triphosphate
DOPE	Discrete Optimized Protein Energy
DTT	Dithiothreitol
E. coli	*Escherichia coli*
EDTA	Ethylenediaminetetraacetic acid
E. huxleyi	*Emiliana huxleyi*
ET	Electron Transfer
F_0	Minimal fluorescence yield of dark-adapted samples
FCP	Fucoxanthin Chl *a*/*c* binding protein
F. cylindrus	*Fragilaripsis cylindrus*
Fd	Ferredoxin
FL3-H	Fluorescence parameter measured by flow cytometry
Fld	Flavodoxin
F_m	Maximal fluorescence yield of dark-adapted samples
FMN	Flavin mononucleotide
FNR	Ferredoxin-$NADP^+$ reductase
FPLC	Fast Protein Liquid Chromatography
FSC-H	Forward scatter parameter measured by flow cytometry
F_v	Difference between F_0 and F_m
F_v/F_m	Maximum quantum yield of PSII
Fx	Fucoxanthin
gDNA	Genomic DNA
H_2O_{MQ}	High purity water
HTL	High temperature thermoluminescence
I. galbana	*Isochrysis galbana*
IPTG	Isopropyl-β-D-1-thiogalactopyranoside
K_A	Association rate constant
K. brevis	*Karenia brevis*
K_D	Dissociation rate constant
k_{ET}	First-order electron transfer rate constant

kDa	kiloDalton
Km	Kanamycin
LB	Luria-Bertani
LHC	Light-harvesting pigment-protein complex
MALDI-TOF	Matrix-assisted laser desorption/ionization time-of-flight
MES	2-(*N*-morpholino)ethanesulfonic acid
MS	Mass spectroscopy
MW	Molecular weight
$NADP^+$	Oxidized nicotinamide adenine dinucleotide phosphate
NADPH	Reduced nicotinamide adenine dinucleotide phosphate
NCBI	National Center for Biotechnology Information
N. gaditana	*Nannochloropsis gaditana*
NIP	Normalized Interface Propensity
NPQ	Non-photochemical quenching
nt	Nucleotide
N-terminus	Amino terminus
OD	Optical density
OPO	Optical Parametric Oscillator-based spectrophotometer
PAGE	Polyacrylamide gel electrophoresis
PAM	Pulse-amplitude modulation fluorometer
PAR_{max}	Maximum photosynthetically active radiation intensity
PBS	Phycobilisome
Pc	Plastocyanin
PCR	Polymerase Chain Reaction
PDB	Protein Data Bank
P_m	Level of maximal P_{700}^+ signal observed upon P_{700} full oxidation
PMSF	Phenylmethylsulfonyl fluoride
PQ	Plastoquinone
PSI	Photosystem I
PSII	Photosystem II
P. tricornutum	*Phaeodactylum tricornutum*
qPCR	Quantitative real time PCR

rETR	Relative linear electron transport rates
RC	Reaction centre
Redox	Reduction-oxidation reaction
RNA	Ribonucleic acid
RNase	Ribonuclease
rpm	Revolutions per minute
RT	Room temperature
RT-PCR	Reverse Transcription followed by a PCR
RubisCO	Ribulose-1,5-biphoshate-carboylase/-oxygenase
SD	Standard deviation
SDS	Sodium dodecyl sulfate
Sm	Streptomycin
Sp	Spectinomycin
SSC-H	Side scatter parameter measured by flow cytometry
STL	Standard thermoluminescence
$t_{1/2}$	Half-life time
TBE	Tris – Borate – EDTA
TBS	Tris Buffered Saline
TEMED	N,N,N',N'-tetramethylethylenediamine
T. elongatus	*Thermosynechococcus elongatus*
TL	Thermoluminescence
T. oceanica	*Thalassiosira oceanica*
Tris	Tris(hydroxymethyl)aminomethane
UV-Vis	Ultraviolet – visible spectroscopy
v/v	Volume/volume relation
WT	Wild type
w/v	Weight/volume ratio
x*g*	Times gravity force
X-gal	5 -bromo-4-cloro-3-indolil-s-D-galactopiranosido
Y(NA)	Acceptor side limitations
Y(ND)	Donor side limitations
Y(I)	Quantum yields of PSI photochemistry

Y(II)	Quantum yields of PSII photochemistry
YFP	Yellow Fluorescent Protein

1. Introduction

1.Introduction

1.1. The oxygenic photosynthesis

Oxygenic photosynthesis consists in the conversion of solar energy into chemical energy, captured as organic matter, using water as an electron donor to reduce CO_2 and generating oxygen as a by-product (Blankenship, 2014; Flori, 2016; Johnson, 2016). This type of photosynthesis had its appearance in ancestral cyanobacteria more than 2.4 billion years ago, triggering drastic changes in Earth's geochemistry and biosphere, among them the increase in the levels of molecular oxygen in the atmosphere, globally known as the Great Oxidation Event (GOE) (Lyons et al., 2014; Blaustein, 2016). By allowing an improved energy production through respiration, oxygen provided the basis for the development of more complex aerobic life forms and almost all biomass on Earth (Hall, 1976; Johnson, 2016).

Oxygenic photosynthesis is a crucial process in the acquisition and storage of solar energy in the biosphere (Benoiston et al., 2017). Globally, it is estimated that photosynthesis captures approximately 3 x 10^{21} J per year and is responsible of the annual assimilation of about 100 Gt of carbon (Hall, 1976; Johnson, 2016). Photosynthesis is accomplished both on the land, which is dominated by plants, and in the oceans, which are mostly colonized by the phytoplankton, including diatom algae (Benoiston et al., 2017; Flori et al., 2017). Thus, photosynthetic productivity is roughly equally shared between terrestrial and oceanic systems, which makes photosynthesis a global process extended by the totality of the Earth's surface (Field et al., 1998; Woodward, 2007). However, primary producers in the oceans represent less than 1% of the photosynthetic biomass on Earth (Field et al., 1998; Falkowski et al., 2004; Bowler et al., 2010).

Oxygenic photosynthesis involves two types of reactions: the "light" reactions, where water is split using light into oxygen, protons and electrons, and the "dark" reactions, where the chemical energy stored in the protons and electrons obtained from the "light" reactions is used to reduce CO_2 to carbohydrates (Johnson, 2016). The "light" reactions involve the electron transfer (ET) from water to $NADP^+$ to form NADPH, but are also coupled to proton transfers that lead to the phosphorylation of ADP into ATP. In the "dark" reactions, the Calvin-Benson cycle uses ATP and NADPH to convert CO_2 into carbohydrates, regenerating ADP and $NADP^+$ (Johnson, 2016).

The productivity of photosynthetic organisms is related to the efficiency of their photosynthetic ET chain. The main features of the sophisticated machinery that performs oxygenic photosynthesis are maintained from cyanobacteria to plants. Thus, in the

photosynthetic chain coexists three large membrane complexes: photosystem II (PSII), cytochrome *b*$_6$*f* (Cb$_6$f) and photosystem I (PSI), that are connected by mobile electron transporters (Hervás et al., 2003; Blankenship, 2014).

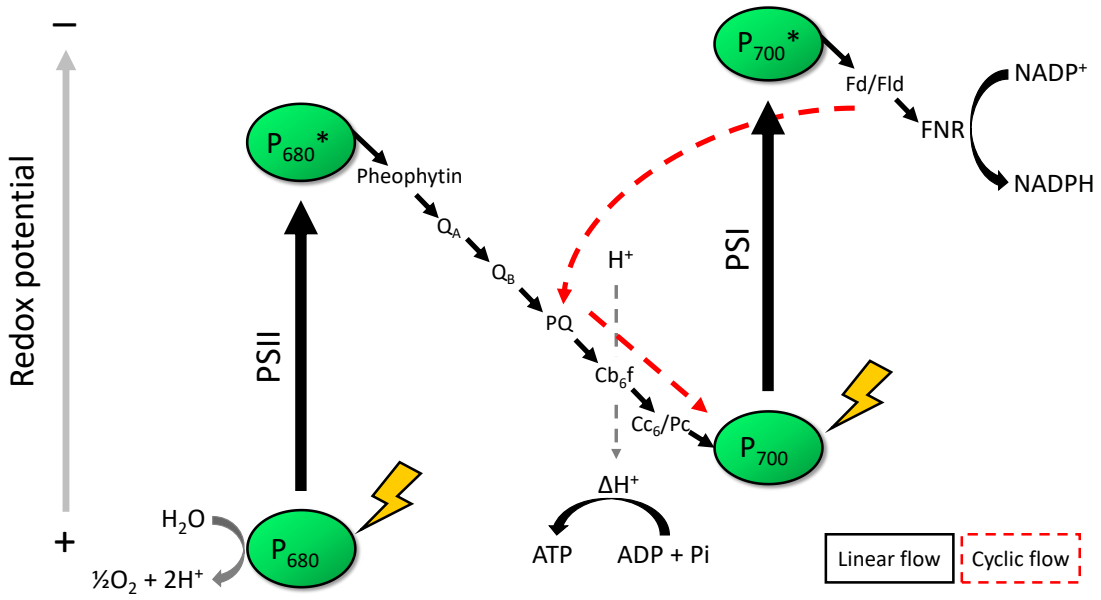

Figure 1.1. The "Z-Scheme" of the photosynthetic electron transfer chain.

The conversion of solar energy into energy-rich compounds (and a proton motive force) involves two light reactions, one for oxidizing water in PSII, and the other for reducing the proteins ferredoxin (Fd) or flavodoxin (Fld) by PSI (Figure 1.1). The light-driven ET reactions of photosynthesis first implies the splitting of water by PSII (Johnson, 2016). The ET from PSII to Cb$_6$f is carried out by plastoquinone (PQ), which moves freely within the membrane, whereas the transport of electrons from Cb$_6$f to PSI is mediated inside the thylakoid lumen by two soluble metalloproteins: the heme-protein cytochrome *c*$_6$ (Cc$_6$) or the copper-protein plastocyanin (Pc). The electron flow through Cb$_6$f involves the movement of protons from outside to inside the thylakoidal membrane into the lumen, which, added to the protons generated by the water oxidation and those taken by the reduction of NADP$^+$ in the stroma, contributes to the generation of a proton gradient used for the synthesis of ATP, according to the chemiosmotic hypothesis of Mitchell (Mitchell, 1961; Allen, 2002). The so-called linear electron flow consists in the ET from PSII to PSI through Cb$_6$f, to generate reduced Fd or Fld, introducing low redox potential electrons into cell metabolism, which can be used for the synthesis of NADPH catalysed by the enzyme ferredoxin-NADP$^+$ reductase (FNR) (Figure 1.1) (Hervás et al., 2003; Pierella

Karlusich et al., 2014). Alternatively, in the so-called cyclic electron flow, Fd or Fld can donate electrons back to PSI via Cb_6f or the quinone pool (Shikanai, 2014; Nawrocki et al., 2019). Therefore, whereas the linear flow is used to generate both redox energy and ATP, the aim of the cyclic flow is the transduction of light energy into ATP. The balance between the cyclic and linear electron flow regulates the ratio ATP/NADPH (Shikanai, 2014).

1.2. The main lineages in the evolution of oxygenic photosynthesis

Oxygenic photosynthesis seems to have evolved solely once with the emergence of cyanobacteria, but it subsequently spread via endosymbiosis to a vast variety of eukaryotic clades. The primary symbiotic eukaryote carrying out oxygenic photosynthesis is believed to have evolved from the engulfment of an ancestral cyanobacterium by a eukaryotic host cell that already contained a mitochondrion. The engulfed cyanobacterium would then become the precursor of the eukaryotic chloroplast. Three major primary groups evolved from this ancestral symbiont: green algae, red algae and the Glaucophytes (Figure 1.2). Green and red algae, by its turn, gave origin to the two main lineages of eukaryotic photosynthetic organisms, the green and red lineages (Falkowski et al., 2004).

In the green lineage, land plants have evolved from green algae (Chlorophyta), whereas secondary endosymbiotic events gave place to other secondary groups having green-type chloroplasts: Euglenophytes, Chlorarachniophytes and “green” Dinoflagellates. The Chlorophyta along with the land plants form the vast majority of the green lineage. About 90% of all known species of Chlorophyta live in freshwater, but there are also many marine representatives (Not et al., 2012). In marine habitats, Chlorophyta are especially important within the smallest size classes such as picoplankton and nanoplankton (Not et al., 2012).

In the same way, in the red lineage secondary endosymbiotic processes from the primary red algae gave origin to a great diversity of algae containing red-type chloroplasts, as Cryptophytes, Haptophytes, Stramenopiles (or Heterokonts, including diatoms) and "red" Dinoflagellates (Figure 1.2) (Falkowski et al., 2004). The red lineage is widely varied, and its components are widespread and often very abundant in diverse marine areas, but they can also be found in freshwater habitats (Not et al., 2012). Cryptophytes and Stramenopiles are present both in marine and freshwater areas, but Haptophytes and Dinoflagellates are mainly found in marine ecosystems (Not et al., 2012). In the contemporary oceans, most eukaryotic phytoplankton is constituted by secondary red symbionts (Falkowski et al., 2004).

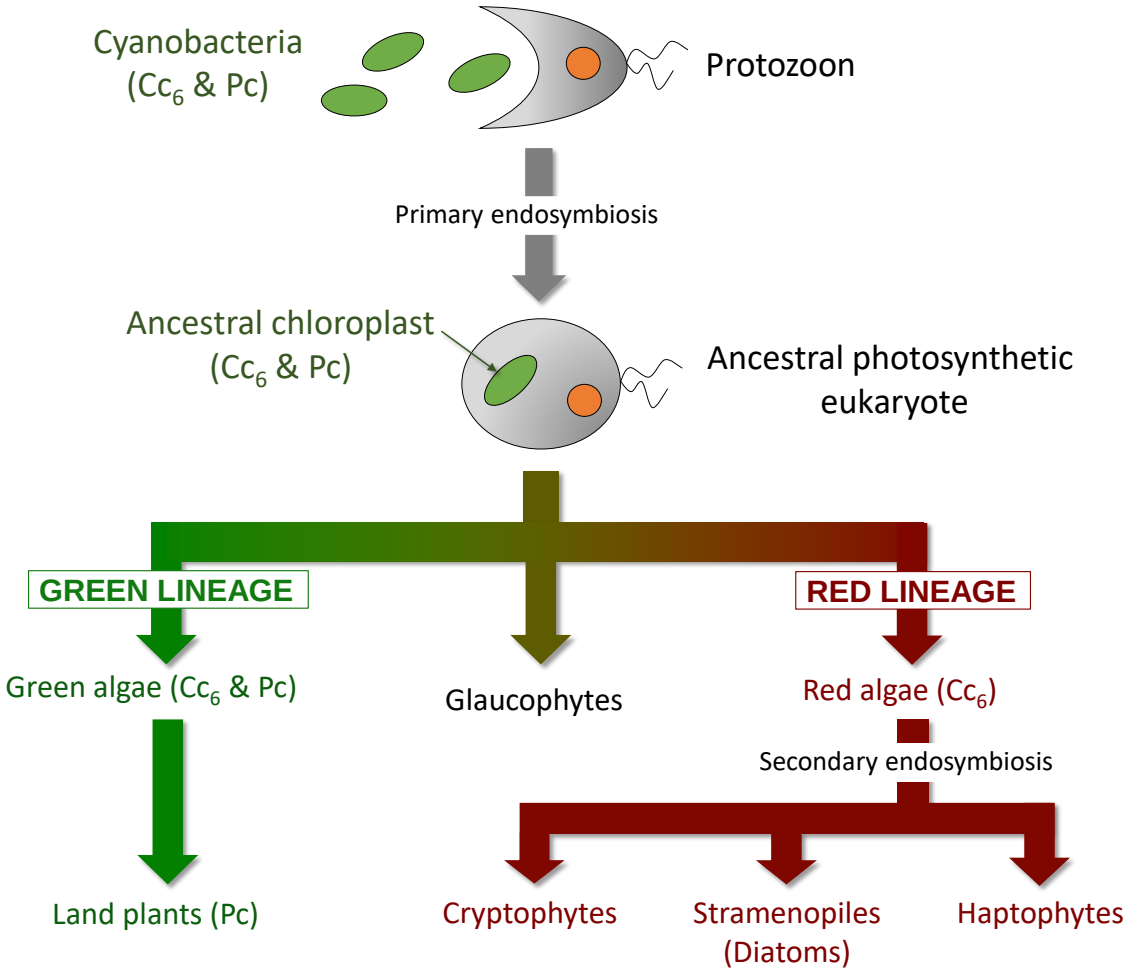

Figure 1.2. Endosymbiosis and the evolution of the chloroplast and the soluble carriers, plastocyanin and cytochrome *c*$_6$, in the main eukaryotic photosynthetic lineages.

1.3. The iron hypothesis

Photosynthetic productivity is restricted by environmental limitations, among them light and temperature stress or the lack of key elements and nutrients, as iron or nitrogen, with the final result of a compromised cell growth and a reduction in the sequestration of CO_2. In particular, iron is essential in crucial cellular processes as photosynthesis, respiration or nitrogen fixation (Crichton, 2016). Iron was readily available at the anaerobic environments predominating in the origin of life, but its bioavailability was drastically reduced in the course of the oxygenation of the planet promoted by the rise of oxygenic photosynthesis, shifting from the ferrous iron form (Fe^{2+}) to the ferric oxidized species (Fe^{3+}) (Shaked & Lis, 2012). Thus, in the context of a photosynthesis that requires iron-based cofactors (see below), it is well established that iron is a limiting nutrient, and photosynthetic organisms have developed specific mechanisms to cope with iron deficiency, including the achievement of efficient iron acquisition

mechanisms to fulfill iron demands or the replacement of iron-containing proteins (Morrisey & Bowler, 2012; Kroh & Pilon, 2020).

In the case of oceans, the lack of iron is the main cause of the existence of oceanic areas with low levels of phytoplankton (and so chlorophyll, Chl), affecting around 40% of the surface of the oceans (Boyd et al., 2007; Boyd & Ellwood, 2010), which is known as the iron hypothesis (Field et al., 1998). Although iron concentrations of fresh waters can be relatively high (up to ≈10 µM), extremely limiting concentrations of this metal have been found in oceanic waters (< 1 nM) (Moore & Braucher, 2008). Actually, large-scale fertilization experiments for iron enrichment in the open sea have shown the occurrence of blooms of phytoplankton after this fertilization (Boyd et al., 2007). In relation to the objectives of this thesis, it should be noted that diatoms tend to dominate in the recollection of phytoplankton after these experiments of fertilization (Boyd et al., 2007).

The photosynthetic apparatus exhibits several adaptations to iron deficient conditions (Straus, 1994; Morrissey and Bowler, 2012). In particular, the diatom photosynthetic machinery undergoes, under the limitation of iron, a remodelling to adjust the use of light energy to a decrease in the content of photosynthetic complexes, especially the iron-rich PSI complex, resulting in an increase in the PSII:PSI ratio (Strzepek & Harrison, 2004; Lommer et al., 2012). Furthermore, in oceanic diatoms Fld can replace Fd (La Roche et al., 1996). In addition, some diatoms can also accumulate iron, by means of the production of the iron-storage protein ferritin (Marchetti et al., 2009).

1.4. The photosynthetic chain

As described in Section 1.1 and Figure 1.3, the photosynthetic chain comprises three large membrane complexes: PSII, Cb_6f and PSI, which are connected by mobile electron transporters (Hervás et al., 2003; Blankenship, 2014). Thus, the transfer of the electrons from PSII to Cb_6f is carried out through the membrane by PQ, whereas the transport of the electrons from the Cb_6f to the PSI is mediated in the lumen by the soluble metalloproteins Cc_6 and Pc. Finally, the electrons from PSI are accepted in the stroma by Fd or Fld and mainly used for the synthesis of NADPH catalysed by FNR (Hervás et al., 2003; Pierella Karlusich et al., 2014).

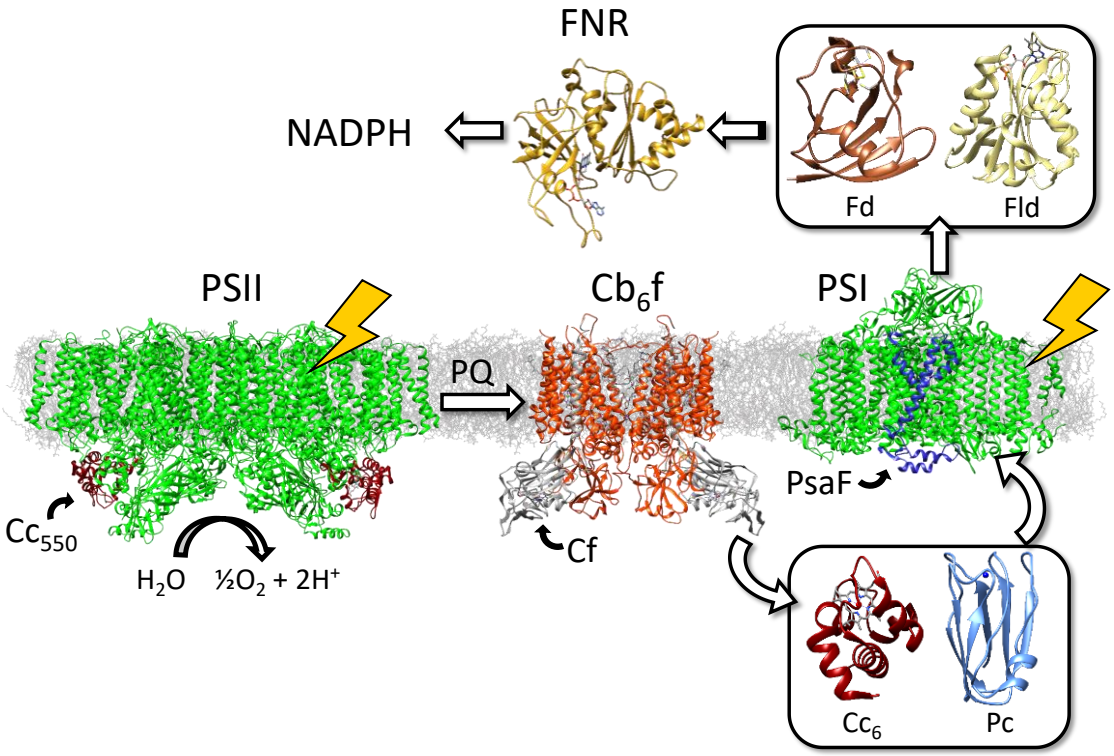

Figure 1.3. Photosynthetic chain of cyanobacteria. PDB codes used: PSII complex (PDB code, 2axt), Cb_6f complex (PDB code, 1vf5), Cc_6 (PDB code, 6tr1), Pc (PDB code, 1pcs), PSI complex (PDB code, 1jb0), Fd (PDB code, 1off), Fld (PDB code, 1czh) and FNR (PDB code, 1b2r). The cytochrome c_{550} (Cc_{550}, in PSII), cytochrome f (Cf, in Cb_6f) and PsaF (in PSI) subunits are highlighted.

1.4.1. The photosystem II

PSII is a large membrane-protein complex located in the thylakoid membrane of plants, algae and cyanobacteria, which catalyses the water-splitting reaction and the reduction of PQ by using light energy, generating oxygen as a by-product (Shen, 2015; Pi et al., 2019). The structure of the PSII complex of the thermophilic cyanobacterium *Thermosynechococcus elongatus* (*T. elongatus*) was the first to be solved (Zouni et al., 2001). The cyanobacterial PSII complex contains 20 subunits, including 17 transmembrane subunits and 3 extrinsic subunits, with a total molecular mass of 350 kDa (Figure 1.4) (Shen, 2015). The major intrinsic core proteins of PSII are largely conserved from prokaryotic cyanobacteria to eukaryotic algae and higher plants, meanwhile the extrinsic proteins can be significantly different (Enami et al., 2003; Nagao et al., 2010a).

The PSII core is organized into dimers, each containing the 17 transmembrane subunits, named according to their respective genes, from PsbA to PsbZ (encoded by the corresponding *psb* genes), of which 16 are conserved from cyanobacteria to higher plants. The PSII core also

binds different ligands, that together with Tyr Z results in a total of 13 active redox cofactors (Shen, 2015; Nagao et al., 2019). Each monomer of the dimeric PSII core contains 35 Chl *a* molecules, two pheophytins (Pheo), 12 β-carotene (Car), one non-heme iron, two hemes (cytochromes b_{559} and c_{550}), one Mn_4CaO_5 cluster, two PQ (PQ_A and PQ_B), 4 Ca^{2+} and 3 Cl^- ions and several lipids (Heinz et al., 2016).

Most redox centres involved in the photo-induced intra-complex ET are coordinated by the central transmembrane subunits D1 and D2 (PsbA and PsbD, respectively), which have five transmembrane helices each and constitute the reaction centre (RC) core of PSII. On the other hand, light collection is mediated mainly by Chl molecules bound to the intrinsic antenna proteins CP43 and CP47 (PsbB and PsbC, respectively) (Heinz et al., 2016). These subunits constitute the antenna complex, which, together with other small transmembrane polypeptide subunits, surrounds the PSII nucleus (Nixon et al., 2010).

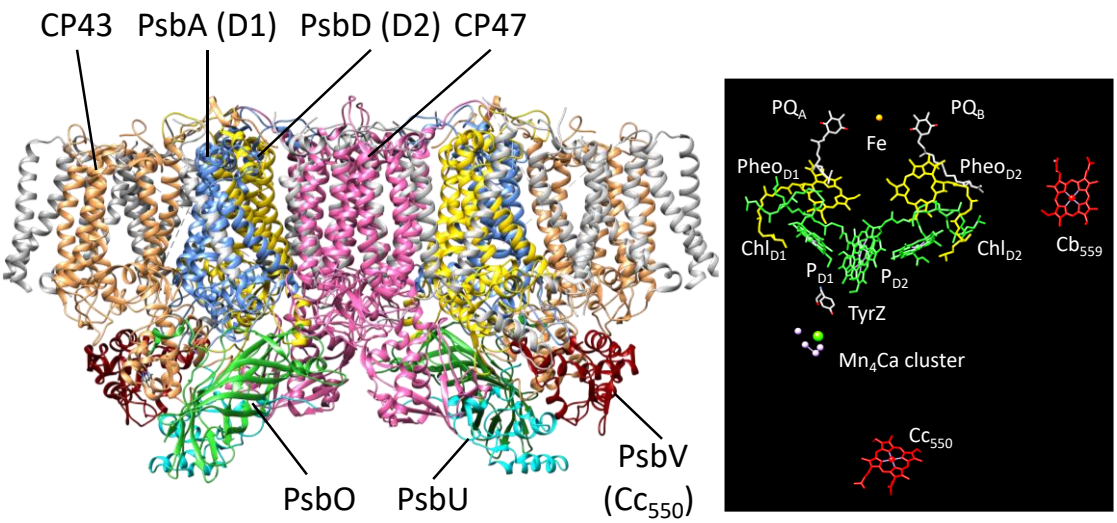

Figure 1.4. Cyanobacterial photosystem II complex. (Left) PSII dimer complex of the cyanobacterium *T. elongatus* (PDB code, 2axt). (Right) Redox components of the PSII reaction centre.

While most PSII core components are conserved from cyanobacteria to higher plants, photosynthetic organisms have developed a variety of light-harvesting pigment-protein complexes (LHCs). LHCs capture the solar energy and transfer it to the RC of the photosystem, to ensure fast and efficient charge separation and ET reactions. The LHCs of PSII (LHCII) are associated with the outer stromal part of the core and play an important role in absorbing unique spectral components that are not absorbed by the PSII cores (Crepin & Caffarri, 2018).

In the green lineage, LHCII binds Chl *a*/*b*, xanthophylls and carotenes (Neilson & Durnford, 2010; Crepin & Caffarri, 2018). The number of monomeric and trimeric LCHII associated to each reaction centre of PSII may vary, resulting in an extensive and flexible antenna supercomplex. In fact, LHCII is the most abundant membrane protein in nature. Moreover, the dynamic increase and decrease in its size plays an important role in the long-term adaptation to light intensity and protection of the photosynthetic apparatus against photooxidative damage (Nevo et al., 2012).

Cyanobacteria have a different light-harvesting complex, which is named the phycobilisome (PBS) (Bailey & Grossman, 2008; Chan et al., 2015). The PBS is a large, extrinsic membrane complex (over 100 polypeptides) that associates with the RC (Bailey & Grossman, 2008; Chan et al., 2015). However, unlike antenna complexes of higher plants and most algae, PBS does not bind chlorophyll. Instead, the phycobiliproteins have one α and β subunit that bind linear tetrapyrrole chromophores called phycobilins (Bailey & Grossman, 2008; Chan et al., 2015).

In the RC core of PSII is where the light-induced charge separation and the ET and water-splitting reactions occur. These primary processes in PSII are associated with a dimer of Chl *a*, named P_{680}, located in the luminal face (Shen, 2015). The global photochemical process in PSII consists of two different types of reactions. First, ET starts when light induces a charge separation in PSII by exciting P_{680}, that gives one excited electron to the first acceptor, a Pheo. Ultimately, this transferred electron comes from the water-oxidizing centre (WOC), and is extracted from H_2O (Loll et al., 2005; Shen, 2015). The Pheo rapidly reduces PQ_A, which subsequently gives the electron to PQ_B, the final and more stable acceptor of PSII, but loosely bound to the RC. PQ_B, after receiving two electrons from PQ_A, takes up two protons from the stroma. The resultant form, a plastoquinol (PQH_2), leaves its binding site in PSII and is replaced by another oxidized PQ. By its turn, oxidized P_{680} (P_{680}^+) is reduced by a nearby tyrosine residue (Tyr161 of the D1 subunit, or Tyr Z), which oxidizes a Mn_4CaO_5 cluster (the catalytic centre of water splitting). Once four electrons have been abstracted from the Mn_4CaO_5 cluster, two water molecules are split into four protons and one oxygen molecule (Shen, 2015; Cox et al., 2020). Two additional cofactors, one Chl and one iron atom, mediate the P_{680}/Pheo and PQ_A/PQ_B ET, respectively. Remarkably, the redox cofactors in PSII are organized in two similar branches, but only one is functional (Loll et al., 2005). The water oxidation mechanism is highly conserved across oxygenic photosynthetic organisms, ranging from cyanobacteria to higher plants (Shen, 2015; Ifuku & Noguchi, 2016).

In cyanobacteria, the three extrinsic proteins of PSII, associated at the lumenal side in the vicinity of the Mn_4CaO_5 cluster, are PsbV (cytochrome c_{550}, Cc_{550}), PsbU and PsbO. These extrinsic proteins play a protective role on the water-splitting cluster (Shen, 2015; Xiao et al., 2020). Cc_{550} only appears in cyanobacteria, red algae and other eukaryotic algae of the red lineage (Roncel et al., 2012; Xiao et al., 2020). In green algae and higher plants, the Cc_{550} and PsbU subunits are replaced by the non-iron containing PsbP and the PsbQ subunits, respectively (Roncel et al., 2012; Ifuku & Noguchi, 2016). PsbO is present in all oxygenic photosynthetic organisms and plays an important role in maintaining the stability and activity of the Mn_4CaO_5 cluster. Meanwhile, Cc_{550} and PsbU in cyanobacteria and red algae, or PsbP and PsbQ in green algae and higher plants, stabilize the binding of the Ca^{2+} and Cl^- ions, which are essential for the oxygen-evolving activity of PSII (Nagao et al., 2010a; Roncel et al., 2012).

Cc_{550} appears stoichiometrically bound to the luminal PSII surface in the proximity of the D1 and CP43 proteins, and close to the oxygen evolving complex (Shen, 2015; Ago et al., 2016). Cc_{550} is able to bind directly to the PSII core complex in a manner essentially independent of other extrinsic subunits, although PsbO is also required for a functional binding of the subunit (Nagao et al., 2010a). The structure of cyanobacterial Cc_{550} has been characterized, both in its free state (at 1.21 Å resolution) and bound to PSII (Frazão et al., 2001; Umena et al., 2011). Thus, the protein possesses a three-dimensional structure similar to that of Class I *c*-type cytochromes, although Cc_{550} exhibits both an unusual bis-histidine axial coordination and a hydrophobic extension in the C-terminal region that acts as the PSII anchoring domain (Frazão et al., 2001; Umena et al., 2011; Bernal-Bayard et al., 2017).

The main role of Cc_{550} in PSII appears to be the binding of Cl^- and Ca^{2+} ions, however it might also help with the stabilization of the Mn_4CaO_5 cluster and in the binding of the other extrinsic subunits (Shen et al., 1998; Enami et al., 2003; Nagao et al., 2010a; Bricker et al., 2012; Xiao at el., 2020). Crystal structures and theoretical calculations suggest that Cc_{550} could also contribute to entry/exit channels for water or protons from the Mn_4CaO_5 cluster (Umena et al., 2011; Vogt et al., 2015; Pi et al., 2019). Beyond a structural function, a redox role of the cytochrome heme cofactor in PSII has not been established, as PSII does not require the presence of Cc_{550} for the ET between the primary donor and oxidized chlorophylls (Shen et al., 1998; Li et al., 2004; Roncel et al., 2012).

Remarkably, since in many organisms a significant fraction of the Cc_{550} content is isolated unbound to PSII as a soluble protein (Evans & Krogmann, 1983; Navarro et al., 1995; Kerfeld & Krogmann, 1998; Bernal-Bayard et al., 2017), it would be possible that two different populations

of Cc_{550} are present, one bound to PSII and other free in the lumen (Kirilovsky et al., 2004). The soluble isolated Cc_{550} has a very low midpoint redox potential (ranging from -190 to -314 mV), incompatible with a redox function in PSII. However, it has been reported that Cc_{550} shows a much more positive potential when bound to PSII (from -80 to +200 mV) (Guerrero et al., 2011; Roncel et al., 2012). Several roles for a soluble Cc_{550} as a protein of low redox potential –beyond being an extrinsic subunit of PSII– have been proposed in cyanobacteria, mostly in anaerobic carbon and hydrogen metabolism (Krogmann, 1991; Kang et al., 1994; Morand et al., 1994), cyclic photophosphorylation (Kienzl & Pescheck, 1983) and in the reduction of nitrate to ammonia (Alam et al., 1984), but none of these possible functions have been clearly stablished (Roncel et al., 2012).

1.4.2. The cytochrome *b*$_6$*f* complex

Cb_6f is a protein complex located in the thylakoid membrane (Hasan et al., 2013; Tikhonov, 2018; Sarewicz et al., 2021). This complex has a plastoquinol:plastocyanin (or Cc_6) oxidoreductase activity, and occupies an electrochemically central position in the linear ET flow (Chi et al., 2000; Sarewicz et al., 2021), in which electrons move from PSII to PSI. Thus, it is associated with proton translocation through the thylakoid membrane and the generation of the transmembrane proton electrochemical potential gradient across the stroma (electro-negative side, n) to the lumen (electro-positive side, p) (Baniulis et al., 2008; Cramer, 2019; Sarewicz et al., 2021).

The Cb_6f is a dimeric complex (spinach Cb_6f, ca. 268 kDa) containing 7 prosthetic groups per monomer and 13 transmembrane α-helices (Cramer, 2019). The monomeric unit of the Cb_6f contains four large polypeptide subunits occupying a central position: PetA (Cytochrome *f*, Cf), PetB (Cytochrome b_6, Cb_6), PetC (Rieske iron-sulfur protein) and PetD (subunit IV). These polypeptide subunits are encoded by the genes *petA, petB, petC and petD*, respectively, and all of them provide binding sites for the prosthetic groups (Cramer, 2019). The complete complex contains four additional small subunits, each one consisting in a single transmembrane α-helix: PetG, PetL, PetM and PetN, encoded by the genes *petG, petL, petM and petN*, respectively (Hasan et al., 2013; Cramer, 2019).

The four main subunits of Cb_6f coordinate tightly the metallo-redox prosthetic groups, four of which, hemes b_p, b_n and c_1 and a [2Fe-2S] located in the Rieske protein, are conserved in the redox core of all cytochrome *bc* complexes. However, Cb_6f has differential cofactors, as Cf (equivalent to cytochrome c_1 in the bc_1 complex) and heme c_n, which does not exist in the

cytochrome bc_1 complex (Cramer, 2019). The hemes b_p and b_n, located on the p and n sides of the membrane, respectively, are non-covalently bound to the protein (Cramer, 2019). The heme c_n was firstly annotated as heme c_i or heme x in the *Chlamydomonas reinhardtii* (*C. reinhardtii*) green alga and cyanobacterial structures, respectively, but because of its location near the n side of the membrane, it turned out to be named as heme c_n (Cramer, 2019). Cb_6f also contains two exclusive additional cofactors, a ß-carotene and a Chl *a*, which function remains unsolved.

In each monomer (ca. 105 kDa), the redox cofactors are distributed in three subunits and arranged in two chains. The low potential chain is formed by Cb_6, which possesses two heme groups with bis-histidinyl axial coordination: hemes b_L ($E_{m,7}$, -150 mV) and b_H ($E_{m,7}$, -30 mV), also named as heme b_p and b_n, respectively, according to its position in the membrane (see above) (Hervás et al., 2003; Hasan et al., 2013; Sarewicz et al., 2021). The high redox potential chain is formed by the Rieske protein, which contains an unusual high potential [2Fe-2S] iron-sulphur cluster ($E_{m,7}$, +300 mV), and Cf ($E_{m,7}$, +350 mV) (Sarewicz et al., 2021).

The complex acts as a proton pump that uses the difference of redox potential between PQ and Pc/Cc_6 as driving force. The coupling between ET and proton translocation takes place through the so-called Q-cycle mechanism. This model assumes that electrons pass from plastoquinol (PQH_2) to Pc (or Cc_6) through sequential one-electron reactions and involves the translocation of protons from the stroma to the lumen with a stoichiometry of 2 H^+/e^-, with the concomitant formation of an electrochemical proton gradient (ΔpH) across the membrane (Tikhonov, 2018; Sarewicz et al., 2021).

Cf (ca. 290 amino acids) is one of the four large subunits of the complex and the exit point of electrons to the luminal soluble electron acceptors (Martínez et al., 1994). Thus, Cf takes electrons from the Rieske iron-sulfur subunit (*petC*) to be transferred to Pc or Cc_6 (Tikhonov, 2018; Cramer, 2019; Sarewicz et al., 2021). Cf has been structurally characterized in cyanobacteria and organisms from the green lineage, both as a part of the Cb_6f complex and in a truncated soluble form (Martínez et al., 1994; Chi et al., 2000; Kurisu et al., 2003; Stroebel et al., 2003). Cf is a *c*-type cytochrome, but the structure of its redox cofactor is unique as one of the heme iron ligands is the N-terminal tyrosine Y1 amino acid (Martínez et al., 1994; Chi et al., 2000). The overall protein fold is also unusual, as Cf is anchored to the membrane by a single transmembrane α-helix, whereas a large and elongated hydrophilic polypeptide (ca. 250 amino acids) with a β-barrel based structure is exposed to the thylakoid lumen (Figure 1.5) (Martínez et al., 1994; Kurisu et al., 2003; Stroebel et al., 2003). This lumen-exposed polypeptide exhibits a large and small flat domains connected by a bend, being the larger domain the one which

contains the heme cofactor and the Y1 ligand, both exposed to the solvent and acting as the ET point (Figure 1.5) (Martínez et al., 1994). In green-type organisms, several positive residues located in the interface of the large and small domains constitute a positively charged area on the surface of Cf, electrostatically complementary to the negative area of green-type Pc and Cc_6 (see below) (Martínez et al., 1994; Soriano et al., 1997; Haddadian & Gross, 2005). However, in cyanobacteria this area in Cf has negatively charged properties (Fedorov et al., 2019).

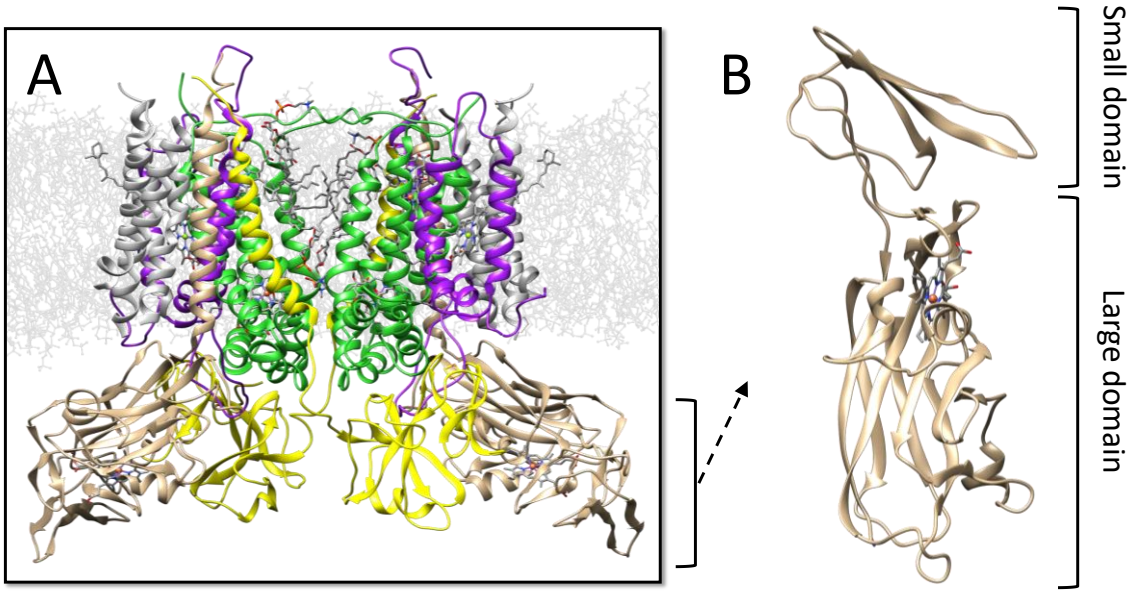

Figure 1.5. Cyanobacterial cytochrome *b_6f* complex. (A) Cb_6f dimer complex of the cyanobacterium *Mastigocladus laminosus*. The Cf (light brown), Cb_6 (green), Rieske protein (yellow) and subunit IV (purple) subunits are highlighted. (B) The truncated soluble Cf subunit showing the heme cofactor. PDB code, 1vf5.

1.4.3. The photosystem I

PSI is an integral, multi-subunit, protein-cofactor complex, embedded into the photosynthetic thylakoid membrane, which utilizes light energy to mediate ET from the luminal soluble electron carriers Pc or Cc_6 across the membrane to the stromal soluble acceptors Fd or Fld (Fromme et al., 2001; Hervás et al., 2003; Hippler & Drepper, 2006; Caspy et al., 2020). The number of cofactors in PSI, close to 130, is one of the largest found up to now in any protein-cofactor complex. PSI has been shown to be monomeric in plants and green and red algae (Busch & Hippler, 2011), but cyanobacterial PSI has been shown to exist in a trimeric form (Fromme et al., 2001).

The monomeric PSI core consists of 12–13 proteins –of which 9 subunits have transmembrane α-helices– and harbors the components for the light-driven charge separation and the subsequent ET reactions (Fromme et al., 2001; Hervás et al., 2003; Busch & Hippler, 2011). Each monomer of the PSI core (ca. 356 kDa) contains around 130 cofactors, of which approximately 100 are Chls, 6 of which are involved in the light-driven charge separation and comprise the terminal electron donor P_{700}. Other cofactors are 2 phylloquinones, 3 [4Fe-4S] clusters, 22 carotenoids and 4 lipids. The location and orientation of the core pigments, as well as the components of the PSI core, are highly conserved between cyanobacteria, green algae and higher plants, even after 1 billion years of evolution (Fromme et al., 2001; Su et al., 2019; Caspy et al., 2020). While structural information already exists for PSI from both cyanobacteria and higher plants for over two decades, no structures were available from eukaryotic algae of the red lineage until very recently (Antoshvili et al., 2019; Xu et al., 2020).

PSI contains different individual proteins, named according to their respective genes, from PsaA to PsaX (encoded by the corresponding *psa* genes) (Fromme et al., 2001). Among the 12-13 PSI core subunits, 9 are conserved from cyanobacteria to eukaryotic algae and higher plants, and they are responsible for charge separation and ET reactions and/or stabilization of the core structure (Fromme et al., 2001; Xu et al., 2020). The PSI core is formed by subunits PsaA and PsaB, with a molecular mass of 83 kDa and 11 transmembrane α-helices each. The PsaA/PsaB heterodimer coordinates most of the core ligands and ET cofactors (P_{700} Chl pair, Chls A_0, phylloquinones A_1 and the [4Fe-4S] iron-sulfur cluster F_X) (Fromme et al., 2001; Hervás et al., 2003; Caspy et al., 2020) (Figure 1.6). Bound at the stromal side are three hydrophilic subunits: PsaC, PsaD and PsaE. The subunit PsaC (9 kDa) harbors two [4Fe-4S] clusters (F_A and F_B), whereas subunits PsaD and PsaE are both surrounding subunit PsaC (Figure 1.6). ET to the soluble acceptors, Fd or Fld, is mediated by PsaC (Hippler & Drepper, 2006; Caspy et al., 2020).

Although the core of PSI is largely conserved in photosynthetic organisms, remarkable changes are found in the bound LHC proteins and pigments. Cyanobacterial PSI has no transmembrane LHC but sometimes it binds PBS antenna. By its turn, the PSI of eukaryotic organisms has membrane-spanning LHCs antenna, or LHCI (Croce & Amerongen, 2013; Qin et al., 2015; Xu et al., 2020), that differ remarkably in their sequences, stoichiometry of binding to the PSI core and the associated pigments (Xu et al., 2020). In green algae and higher plants, LHCI binds Chl *a*/*b* and carotenoids, but green algae PSI core contains up to ten LCHI subunits whereas higher plants PSI core contains four (Croce & Amerongen, 2013; Qin et al., 2015).

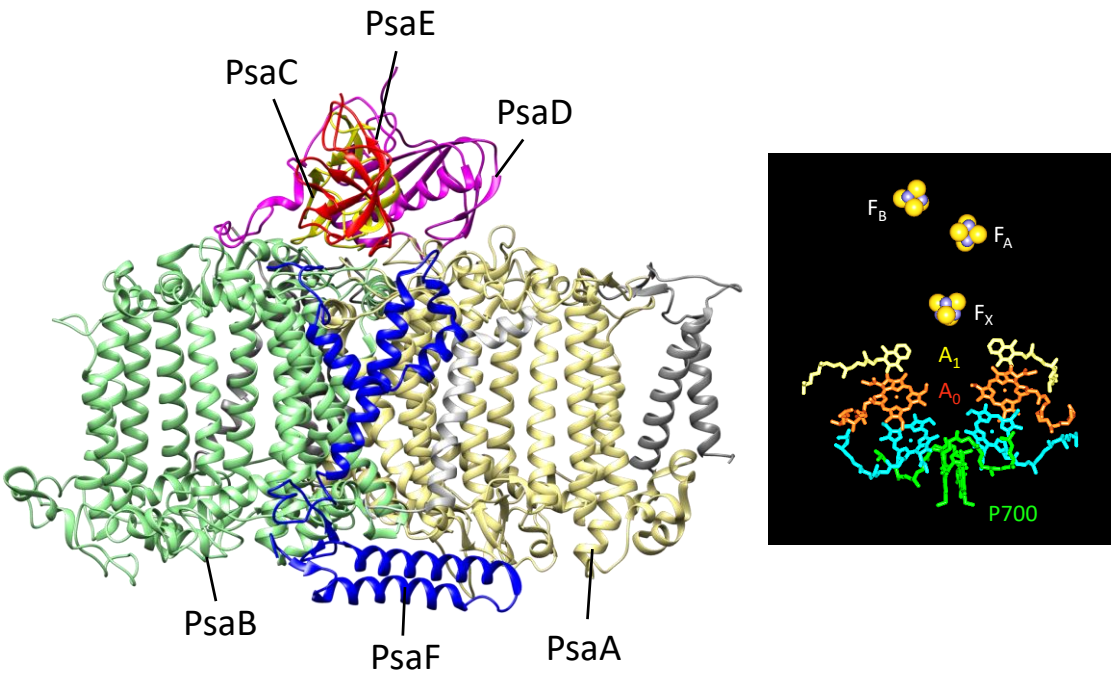

Figure 1.6. Photosystem I complex. (Left) PSI monomer of the green alga *C. reinhardtii*. PDB code, 6ijj. (Right) Redox components of the PSI reaction centre of the cyanobacterium *T. elongatus* (modified from Hervás et al., 2003).

The ET chain of the PSI reaction centre is formed by 6 Chl molecules (including the special pair, or $P_{700,}$ and the A_0 cofactor), 2 phylloquinones (A_1 cofactor) and the 3 [4Fe-4S] clusters F_X, F_A and F_B. The P_{700} special Chl pair is a heterodimer of Chl *a* and *a'*. Like in other photosystems, including PSII, the redox cofactors of PSI are distributed in two symmetric branches, A and B, in which electrons are transferred from P_{700}, close to the lumenal membrane side, to the first [4Fe-4S] cluster (F_X), on the stromal side (Hervás et al., 2003; Grotjohann & Fromme, 2005). Contrary to what happened in PSII, in PSI both branches seem to be functional and reduce F_x, but with the B branch being much faster (Guergova-Kuras et al., 2001; Grotjohann & Fromme, 2005).

Light-induced charge separation in PSI starts by the excitation of P_{700} and its oxidation to P_{700}^+. According to a simplified scheme, excited P_{700} (P_{700}^*) transfers the energized electron to the Chl primary electron acceptor (A_0). Electrons are then sequentially transferred to the phylloquinone A_1, the iron-sulfur centres F_X, F_A and F_B and finally to Fd or Fld. To allow a new redox cycle, P_{700}^+ is re-reduced by the transfer of one electron from Cc_6 or Pc (Hervás et al., 2003; De la Rosa et al., 2006; Hippler & Depper, 2006).

A hollow at the lumenal side of PsaA/PsaB seems to form a hydrophobic binding site for Pc or Cc_6 (Mazor et al., 2015; Caspy et al., 2020). This hydrophobic interaction site in the PSI core

is conserved between prokaryotic and eukaryotic organisms (Sommer et al., 2004). In addition, the subunit PsaF (15 kDa) (Figure 1.7), with one transmembrane α-helix and a globular domain protruding toward the lumenal side, seems to be involved in the correct docking of Pc (and Cc_6) in eukaryotic PSI, but not in cyanobacteria, by offering a positively charged electrostatic interaction site with Pc and Cc_6 (Figure 1.7; and see below). This subunit thus plays a critical role in the interaction of PSI with the two alternative electron donor proteins (Hippler et al., 1998; Sommer et al., 2006; Caspy et al., 2020).

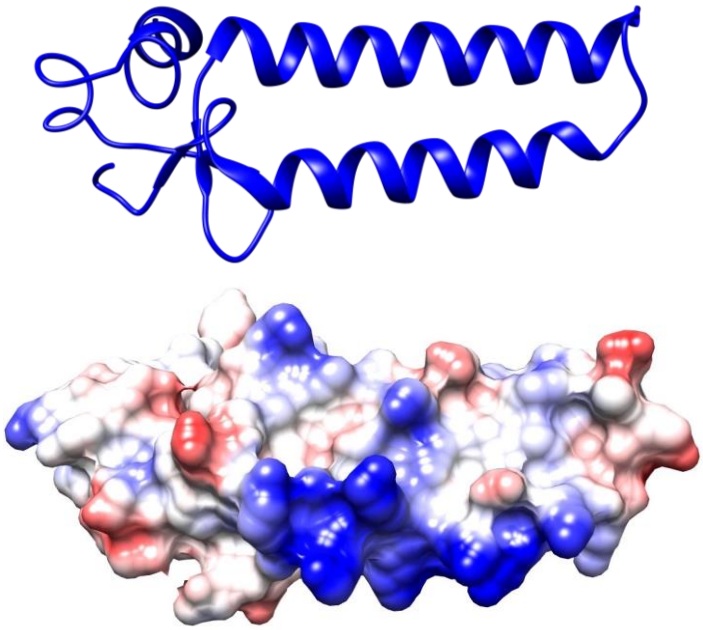

Figure 1.7. PsaF subunit of the green alga *C. reinhardtii*. Backbone representation (upper) and electrostatic properties (lower) of the luminal exposed part of PsaF of *C. reinhardtii* (PDB code, 6ijj).

1.4.4. The soluble carriers of the photosynthetic chain

In terrestrial plants, ET between the Cb_6f complex and PSI is carried out inside the thylakoidal lumen solely by Pc, whereas the output of electrons from PSI is directed to the iron-sulphur protein Fd (Caspy et al., 2020). However, this situation has to be taken as an end point in the evolutionary path of the green lineage that from cyanobacteria (considered the ancestors of the eukaryotic chloroplasts) and green algae leads to plants (Falkowski et al., 2004; De la Rosa et al., 2006; Sétif, 2006). Therefore, in aquatic systems photosynthetic microorganisms have maintained alternative redox protein couples, that can be understood as an adaptation to fluctuations and limitations in the bioavailability of metals in these ecosystems (specifically iron and copper) (De la Rosa et al., 2006; Moore & Braucher, 2008; Nouet et al., 2011; Marchetti et

al., 2012). In particular, in most cyanobacteria and unicellular green algae, Pc acts alternatively replacing Cc_6 as electron carrier between Cb_6f and PSI when copper is available, whereas the flavoprotein Fld can replace Fd during periods of iron deficiency (McKay et al., 1999; Hervás et al., 2003; De la Rosa et al., 2006; Sancho, 2006; Sétif, 2006). However, plants have lost Cc_6 and Fld as alternative proteins along their evolution within the green lineage, probably due to the particularities of metal availability in the process of land colonization (Pierella Karlusich et al., 2014). Remarkably, the functional and structural equivalence of Pc and Cc_6, and of Fd and Fld, has been well established (see below) (Hervás et al., 2003; Medina & Gómez-Moreno, 2004; Hippler & Drepper, 2006; Sétif, 2006; Pierella Karlusich et al., 2014; Bendall & Howe, 2016), representing in both cases an example of evolutionary convergence of structurally different proteins that have evolved to perform the same function (De la Rosa et al., 2006).

1.4.4.1. Ferredoxin and flavodoxin

Reduced Fd or Fld introduce low redox potential electrons into cell metabolism for the further assimilation of the primordial bioelements carbon, nitrogen and sulphur. Thus, both Fd and Fld play a critical role in the photosynthetic chain, either in the cyclic electron flow donating electrons to the Cb_6f complex (Pierella Karlusich et al., 2014; Shikanai, 2014; Nawrocki et al., 2019) or as electron donors for the $NADP^+$ reduction to NADPH catalysed by FNR (Medina & Gómez-Moreno, 2004).

Fd is a small (ca. 94 residues) soluble metalloprotein containing a [2Fe-2S] cluster as prosthetic group. By its turn, Fld is a soluble flavoprotein containing one flavin mononucleotide (FMN) as prosthetic group (Figure 1.8) (Bottin & Lagoutte, 1992; Sancho, 2006; Medina, 2009; Pierella Karlusich et al., 2014). In cyanobacteria and some microalgae both carriers can be present in the same genome. In this case, Fd is functionally replaced by Fld during periods of Fe limitation, reducing the global need of iron of these organisms (McKay et al., 1999; Medina & Gómez-Moreno, 2004; Marchetti et al., 2012; Pierella Karlusich et al., 2014). Consequently, Fd expression is repressed under conditions of iron limitation whereas the expression of Fld is repressed in iron-replete conditions (Bottin & Lagoutte, 1992; Pierella Karlusich et al., 2014). Fd and Fld do not share any structural similarity except being highly acidic proteins, but they can participate basically in the same oxido-reductive reactions with similar efficiency (Medina & Gómez-Moreno, 2004; Medina, 2009; Pierella Karlusich et al., 2014).

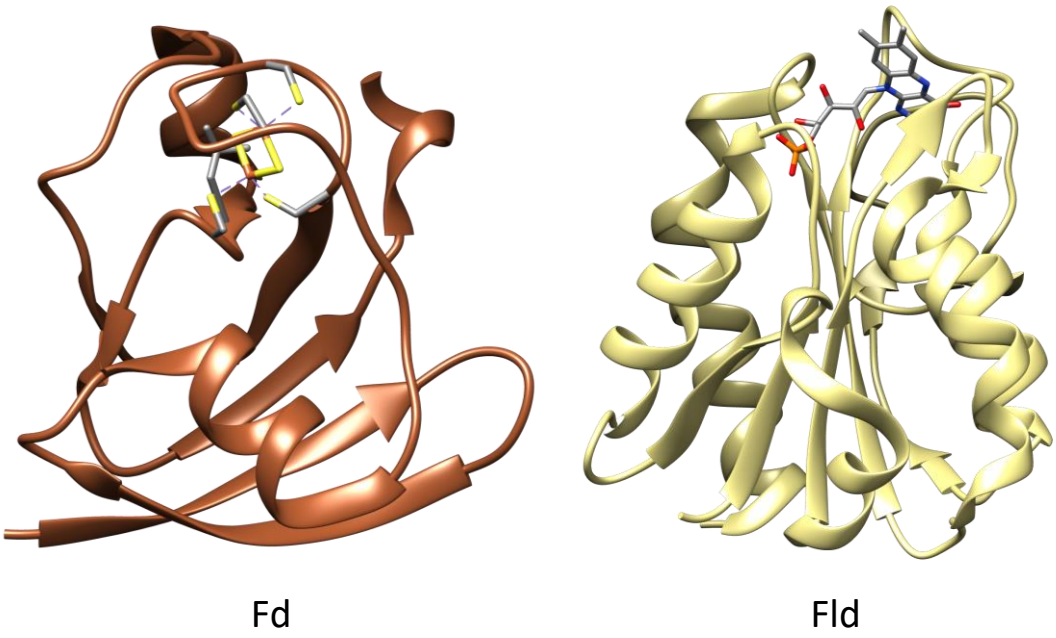

Figure 1.8. Structure of cyanobacterial ferredoxin and flavodoxin. Fd of *Synechocystis* sp. PCC 6803 (PDB code, 1off); Fld of *Synechococcus elongatus* (PDB code, 1czh). The [2Fe-2S] and FMN cofactors are shown.

Flds contain between 140 and 180 residues. They can be divided in two groups, short-chain and long-chain Flds, which differ in the presence of a 20-residue loop of an unknown function (Sancho, 2006; Pierella Karlusich et al., 2014). Only long-chain Flds have been associated to a role in photosynthesis (Pierella Karlusich et al., 2014).

Most cyanobacteria contain 3 or more isoforms of Fd with specific functions (Cassier-Chauvat & Chauvat, 2014). Among eukaryotes, a single Fd is usually found in glaucophytes and red algae, while green algae and plants contain numerous isoforms (Pierella Karlusich et al., 2014). By its turn, among eukaryotes, Flds are most common in algae, but are absent in higher plants. However, in bacteria, Flds are extensively distributed among many different groups (Sancho, 2006; Pierella Karlusich et al., 2015).

Although Flds can exchange one or two electrons, usually behave as one-electron carriers, switching between the semiquinone/hydroquinone states (half and fully reduced, respectively). The semiquinone/hydroquinone pair has a redox potential similar to that of Fd (ca. −400 mV), and in this way Fld can replace Fd in most functions (Medina & Gómez-Moreno, 2004; Medina, 2009).

1.4.4.2. Cytochrome c_6 and plastocyanin

In plants, Pc is the electron carrier between Cb_6f and PSI, while in most cyanobacteria and unicellular green algae, Pc acts by alternatively replacing Cc_6 when copper is available (Sandmann, 1986; De la Rosa et al., 2006). Because anoxygenic photosynthesis uses cytochromes as electron carriers and not Pc, it is considered that Cc_6 evolved as the ancestral carrier in primitive oxygenic organisms. However, as Pc is synthesized in the presence of copper whatever the iron levels, it could be concluded that Pc is the preferred protein.

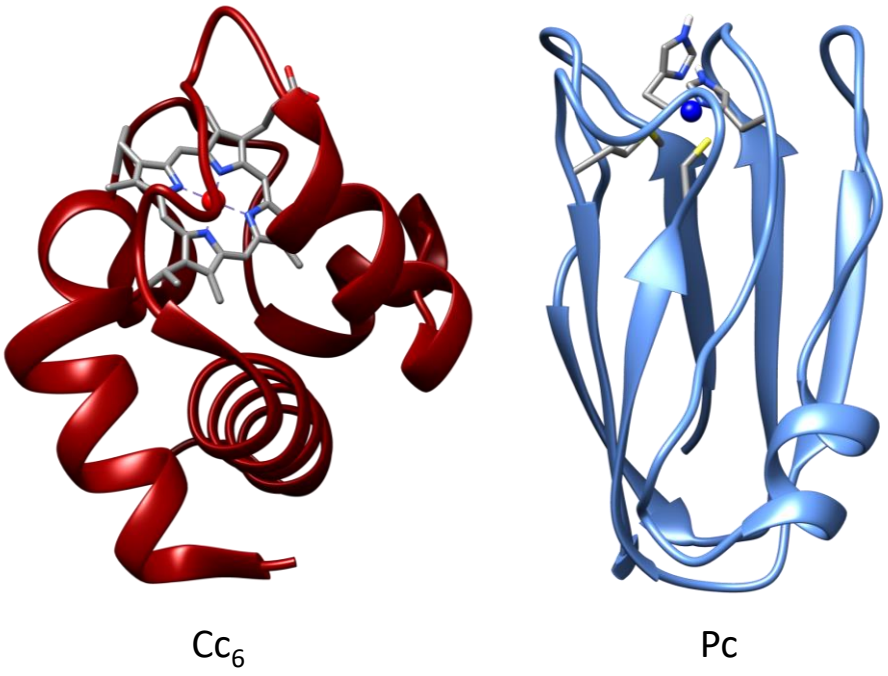

Figure 1.9. Structure of cyanobacterial cytochrome c_6 and plastocyanin. Cc_6 of *T. elongatus* (PDB code, 6tr1); Pc of *Synechocystis* sp. PCC 6803 (PDB code, 1pcs). The heme group, the copper (in blue) and the copper ligands are shown.

Although Pc and Cc_6 play the same function with similar efficiency, their structures are totally different, as it was the case of Fd/Fld, even though they share a similar size (around 100 amino acids) and redox potential (ca. +350 mV) (Díaz-Quintana et al., 2003) (Figure 1.9). Pc is a small soluble type I blue copper protein (molecular mass, ca. 10.5 kDa), containing a single metal atom. All Pc from plants, green algae and cyanobacteria have a similar folding pattern with a β-barrel tertiary structure formed by eight β strands with an additional loop forming in most cases a short α-helix (Redinbo et al., 1994; Navarro et al., 1997; De la Rosa et al., 2006). By its turn, Cc_6 is a typical Class I *c*-type cytochrome (molecular mass, ca. 9.5 kDa), with an α-helix-based tertiary

structure and a heme redox group covalently attached to a single polypeptide chain (Frazão et al., 1995; Navarro et al., 1997; De la Rosa et al., 2006) (Figure 1.9). However, both Pc and Cc_6 show a well-defined ET area determined by the accessibility to the solvent of their redox cofactors. In the case of Pc, this ET area contains a histidine residue (His87) that acts as one of the copper ligands (Guss & Freeman, 1983; Ubbink et al., 1998; Inoue et al., 1999), whereas in Cc_6 part of the heme group itself is exposed to the solvent (Figure 1.9) (Frazão et al., 1995; Sawaya et al., 2001).

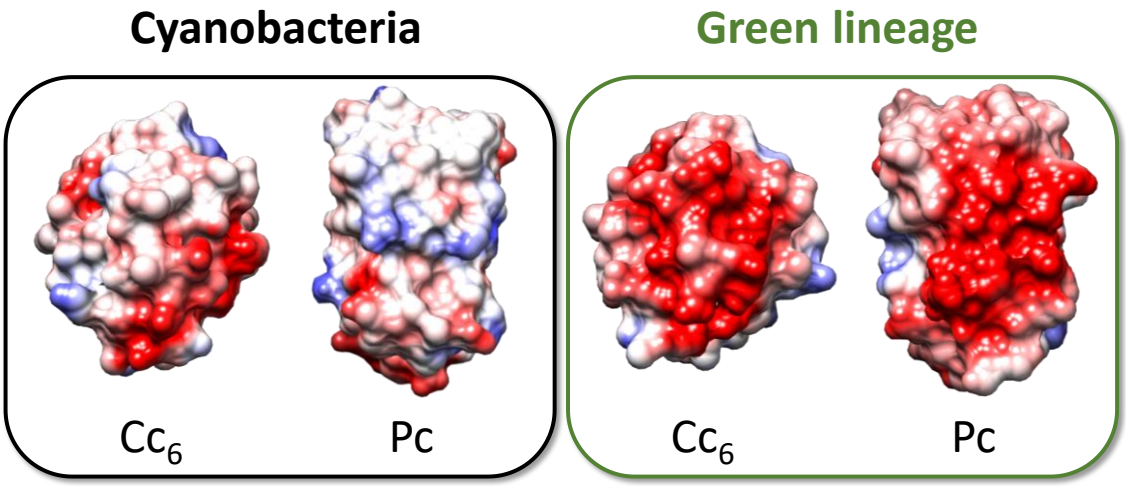

Figure 1.10. Electrostatic properties of cytochrome c_6 and plastocyanin from cyanobacteria and the green lineage. Cyanobacteria: *T. elongatus* Cc_6 (PDB code, 6tr1) and *Synechocystis* sp. PCC 6803 Pc (PDB code, 1pcs); Green lineage: *C. reinhardtii* Cc_6 (PDB code, 1cyi) and Pc (PDB code, 2plt).

A typical characteristic of Cc_6 and Pc, both prokaryotic and eukaryotic, is the existence of a hydrophobic area around the ET site. In addition, Cc_6 and Pc hold an electrostatically charged area in the surface of both proteins located in an equivalent position related to the ET sites and the hydrophobic patches (Frazão et al., 1995; De la Rosa et al., 2006; Díaz-Quintana et al., 2008) (Figure 1.10). Although in cyanobacteria the electrostatic patch can be relatively neutral or even strongly positive, in eukaryotic Cc_6 and Pc from the green lineage it has always a strong negative electrostatic charge (Figure 1.10) (De la Rosa et al., 2006; Hippler & Drepper, 2006; Díaz-Quintana et al., 2008). One interesting exception to this general description is fern Pc, whose acidic region is surrounding the hydrophobic patch, resulting in very distinct electrostatic properties as compared to typical eukaryotic Pc (Kohzuma et al., 1999).

1.4.4.2.1. Interaction of eukaryotic cytochrome c_6 and plastocyanin with photosystem I

Until very recently there were not solved 3D structures at atomic resolution for the intermolecular complexes of PSI with the electron donors Pc or Cc_6. However, from kinetic data, mutagenesis studies, mass spectrometry analyses and computational modelling, it has been possible to propose structural models for the binding of the two soluble electron donors to PSI in green organisms (Hippler et al., 1996; Sommer et al., 2004 & 2006). According to these models, long-range complementary electrostatic attractions, as well as more precise short-range hydrophobic contacts and specific interactions of charged groups, are essential for the fast and efficient ET (Sommer et al., 2004 & 2006; Busch & Hippler, 2011). Hydrophobic interactions involve the hydrophobic patches of Pc/Cc_6 and the lumenal loops i/j of PsaA/B in PSI, including the PsaA W651/PsaB W627 residues near P_{700} as part of the ET pathway (Sommer et al., 2004; Busch & Hippler, 2011). In addition to the hydrophobic binding pocket in the PSI core, in green algae and higher plants the strong positively charged luminal-exposed N-terminal extension (ca. 70 amino acids) of the PsaF subunit (Figure 1.7) would be responsible for the electrostatic interaction between PSI and the negatively charged Cc_6 and Pc donors (Farah et al., 1995; Hippler et al., 1996 & 1998; Sommer et al., 2006). This interaction particularly would involve several positive residues located in the 10-30 PsaF sequence positions, with a key role of a conserved lysine group in position 23 (Hippler et al., 1996 & 1998; Sommer et al., 2006), but also concerns negative groups in PsaB that are required for favouring the unbinding of the oxidized donor from PSI (Sommer et al., 2006; Busch & Hippler, 2011). The main features of the interaction between green PSI and Pc have been recently corroborated in the high-resolution structure of a triple complex of plant PSI with Fd and Pc, solved by cryo-electron microscopy (Caspy et al., 2020). The analysis of the PSI–Pc binding confirms that the association of Pc depends principally on hydrophobic interactions, mainly –but not only– around the two tryptophan residues of PSI near P_{700}, with the two copper-ligand His residues in Pc located adjacent to these tryptophan groups. In addition, stabilization of Pc binding occurs mostly through interactions between the positive patch in PsaF and negatively charged Pc residues (D42, D44, E43 and E45), although there are also other additional –but weaker– interactions of PsaF with other negative groups in Pc (Caspy et al., 2020).

The interaction between eukaryotic Cc_6 and Pc with PSI has been studied by time-resolved kinetic analysis in different algae and plants belonging to the green lineage (Bottin & Mathis, 1985; Haehnel et al., 1994; Hervás et al., 1995; Drepper et al., 1996; Sigfridsson et al., 1996; Hippler et al., 1998; Molina-Heredia et al., 2003; Navarro et al., 2004; Klughammer & Schreiber 2016). According to a proposal for a general ET mechanism to PSI, ET occurs in three different

detectable kinetic steps, which involve formation of an electrostatically-driven transient complex, further rearrangement or reorganization of redox partners inside the complex to an effective configuration and, finally, the ET step itself, followed by the dissociation of the reactants to allow a new redox cycle (Figure 1.11) (De la Rosa et al., 2006).

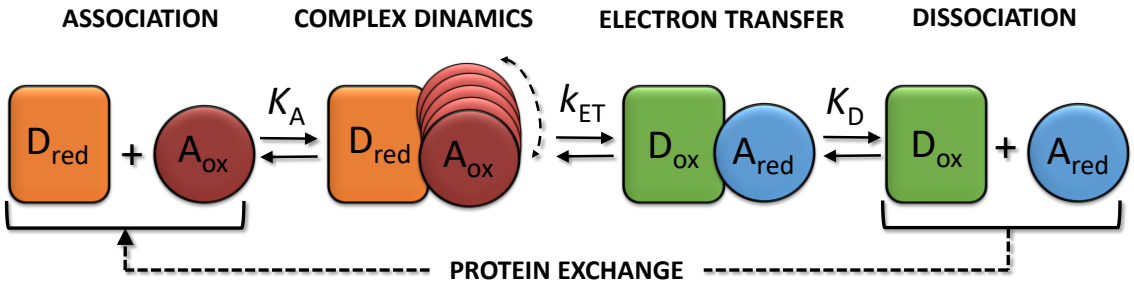

Figure 1.11. Electron transfer mechanism for the reduction of photosystem I.

According to the described mechanism and the electrostatic features of green-type Pc, Cc_6 and PsaF, long-range electrostatic attractions between strongly charged complementary patches (acidic in Pc and Cc_6 and basic in PsaF) are required for stable complex formation, whereas hydrophobic short-range interactions would be additionally involved in the complex reorganization to attain an efficient ET (Hippler et al., 1996 & 1998; Sommer et al., 2006). Actually, the structural properties of PSI and the electron donors in the green lineage ensure both efficient partner association ($K_A \approx 10^5\ M^{-1}$) and ET rates ($k_{ET} \approx 10^5\ s^{-1}$) (Haehnel et al., 1994; Hervás et al., 1995; Drepper et al., 1996; Sigfridsson et al., 1996; Hippler et al., 1998; Molina-Heredia et al., 2003; Klughammer & Schreiber 2016).

Globally, the high efficiency of the green lineage in the formation of the [donor:PSI] complex and in the ET step presents, however, a derived disadvantage, since a too strong electrostatic interaction necessarily implies a limitation to the dissociation of the complex after the ET, and therefore also limits the occurrence of a new redox cycle (Finazzi et al., 2005; Kuhlgert et al., 2012). In fact, the release of oxidized Pc (and probably Cc_6) from PSI represents the kinetic rate-limiting step in the ET from Cb_6f to PSI in eukaryotic "green" organisms (Drepper et al., 1996; Finazzi et al., 2005).

1.4.4.2.2. Interaction of eukaryotic cytochrome c_6 and plastocyanin with cytochrome *f*

Several NMR-based structures of plant [Cf:Pc] complexes have been described (Ubbink et al. 1998; Lange et al., 2005) (Figure 1.12). In addition, Brownian Dynamics (BD) simulations have studied the Cf interaction with the soluble electron acceptors in plants and in the green alga *C. reinhardtii* (Gross & Pearson, 2003; Musiani et al., 2005; Haddadian & Gross, 2006; Fedorov et al., 2019). However, these types of studies have been absent until now in organisms of the red lineage.

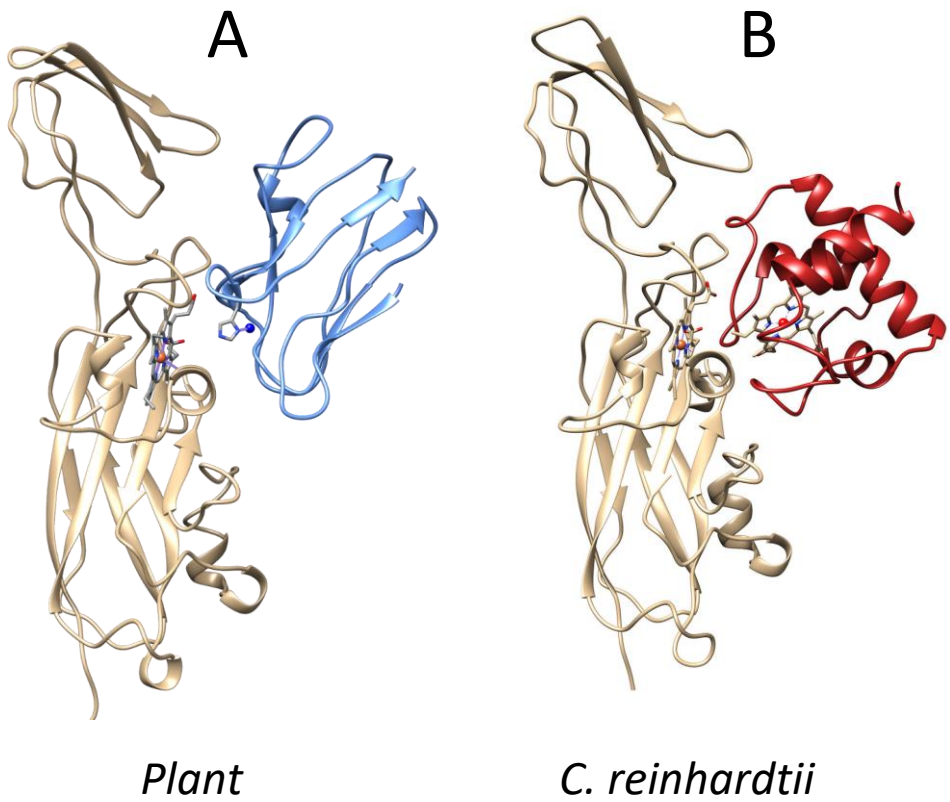

Figure 1.12. Representative eukaryotic structures of [Cf:Pc] and [Cf:Cc$_6$] complexes. (A) Representative structure for the plant [Cf:Pc] complex (turnip Cf and spinach Pc; obtained from PDB code 2pcf) (Ubbink et al., 1998). Pc is coloured in blue and the copper-ligand His87 is shown. (B) Representative structure for the green alga *C. reinhardtii* [Cf:Cc$_6$] modelled complex (drawn from data displayed in Haddadian & Gross, 2005). Cc$_6$ is coloured in red.

The NMR-based structure of the plant [Cf:Pc] complex (Figure 1.12A) shows a relatively large complex interface, involving both the large and small domains of Cf, forming the so-called "side-on" relative orientation (in contraposition to the "head-on" orientation that appears in some complexes of cyanobacteria based in hydrophobic forces) (Ubbink et al., 1998; Cruz-

Gallardo et al., 2012). As expected, the complex shows electrostatic interactions between positively charged residues in Cf and negatively charged groups in Pc, as well as interactions between both hydrophobic patches, thus providing an efficient ET pathway (Fe–Cu distance of 10.9 Å) (Ubbink et al. 1998) (Figure 1.12A).

Although a detailed analysis on NMR-based docking models of the [Cf:Cc_6] complex has been carried out in the cyanobacterium *Nostoc* sp. PCC 7119 (Díaz-Moreno et al., 2005 & 2014), in eukaryotic organisms the available data are limited to BD simulations applied to the green [Cf:Cc_6] (and [Cf:Pc]) complex of *C. reinhardtii* (Gross & Pearson 2003; Haddadian & Gross, 2005 & 2006). These studies demonstrated the functional equivalence of the hydrophobic and electrostatic areas in both green Pc and Cc_6. As described previously for the Cf:Pc interaction, hydrophobic residues around the heme of Cf (including Y1) interact with hydrophobic residues surrounding the Cc_6 heme. On the other hand, electrostatic attractive interactions involve positive groups in Cf –located in both the large and small domains– and negative groups in Cc_6. This results in a "side-on" orientation, which also shows a relatively large interface (Haddadian & Gross, 2005; and see Figure 1.12B). In conclusion, the comparison of the green [Cf:Pc] and [Cf:Cc_6] complexes confirms the key role of the electrostatic and hydrophobic areas in protein binding and, therefore, in achieving an efficient ET, but also the role of the small Cf domain in stabilizing the proper docking orientations of Pc and Cc_6.

Kinetic data for native proteins are only available for the Pc/Cf interaction (reviewed in Bendall & Howe, 2016) since the overlap between the absorbance spectra of Cc_6 and Cf prevents to accurately follow the kinetics of the ET reaction between both native cytochromes (Grove & Kostic, 2003). In eukaryotes, the Pc/Cf interaction has been studied in green algae and plants (Qin & Kostic, 1993; Meyer et al., 1993; Kannt et al., 1996; Soriano et al., 1997; Gong et al., 2000; Schlarb-Ridley et al., 2003). The final conclusion, obtained not only from kinetic data but also from computational and structural NMR studies (see above), is that ET from Cf to Pc occurs following a similar mechanism (binding, reorganization, and ET) to that described for PSI reduction (Figure 1.11) (Cruz-Gallardo et al., 2012; Schilder & Ubbink, 2013). Again, this mechanism involves long-range electrostatic attraction for initial binding and preorientation of the two partners, as well as short-range hydrophobic contacts to achieve a productive configuration for ET. Given that previous structural and functional data have established the general functional equivalence of Pc and Cc_6 (De la Rosa et al., 2006; Hippler & Drepper, 2006), the hypothesis that a similar mechanism controls the ET reaction of Cf with Cc_6 in green-type organisms seems reasonable.

1.5. Diatoms

Bacillariophyceae, commonly known as diatoms, are unicellular eukaryotic photosynthetic microalgae belonging to the division of Heterokontophyta (or Stramenopiles) in the red lineage of algae. Molecular-clock based estimations suggest that diatoms appeared around 250 million years ago (Armbrust, 2009; Not et al., 2012), although the earliest well-preserved diatom fossils are from 180 million years ago (Kroth & Strotmann, 1999; Kooistra et al., 2007). Diatoms can be found all over marine and freshwater ecosystems and they are responsible for around 20% of the annual global primary productivity, a contribution equivalent to all the tropical rainforests and grasslands of the world. Consequently, diatoms play a crucial role in the global maintenance of the biosphere, being essential contributors to photosynthetic carbon fixation and the subsequent capture of CO_2 (Falkowski et al., 1998; Bowler et al., 2008; Saade & Bowler, 2009; Daboussi et al., 2014). Nowadays diatoms constitute the most abundant and diversified group of oceanic eukaryotic phytoplankton, with more than 200 genera and between 100,000 and 200,000 different species (Kooistra et al., 2007; Armbrust, 2009; Bowler et al., 2010). Approximately 40% of the organic matter generated per year in the oceans is estimated to come from the photosynthetic productivity of diatoms, considered as major primary producers and main players in the biological carbon pump that sequesters carbon at the bottom of the ocean (Allen et al., 2008; Bowler et al., 2010).

Modern diatoms are diploid organisms in the vegetative state (Martin-Jézéquel & Tesson, 2012). A peculiar aspect of diatoms is that they contain genes from various sources, including horizontal gene transfer from bacteria and in their plastids via secondary endosymbiosis. This secondary endosymbiosis is thought to have taken place around 250 million years ago, between one eukaryotic red alga and one eukaryotic heterotrophic host cell, and the subsequent evolution of a red-type plastid (Scala et al., 2002; Kroth, 2007; Levering et al., 2016). Due to their secondary endosymbiotic origin, the plastids of diatoms are enclosed by four membranes, in contrast to the plastids of the green lineage, which are surrounded by only two membranes (Kroth & Strotmann, 1999; Falciatore et al., 2020).

Endosymbiotic processes usually involve massive losses or translocations of genes in the endosymbiont. In diatoms, most ancestral genes encoding plastid proteins were replaced by genes of the host or transferred to the nucleus of the new eukaryotic host (Oudot-Le Secq et al., 2007; Bowler et al., 2010; Benoiston et al., 2017). Due to this unique combination of organisms and genes, diatoms are taxonomically and functionally distinct from other algae and plants. As a result, diatoms possess an outstanding metabolic flexibility and the capacity to tolerate light

fluctuations, including occasional excessive exposure to light, which might be other of the reasons for their ecological success (Armbrust, 2009; Benoiston et al., 2017).

It is worth highlighting the use of eukaryotic microalgae, either as a direct source of food or in aquaculture and in the production of high value compounds, as pharmaceuticals, cosmetics, food and feed supplements or biofuels, acting as a sustainable alternative to mitigate the global warming and the climate change (Wijffels et al., 2013; Enzing et al., 2014). Among the group of eukaryotic microalgae, biotechnological applications of diatoms include their use as a source of phytoplankton in aquaculture, feed for animals, food and cosmetic supplements, since they are a natural source of polyunsaturated fatty acids, pigments and antioxidants. They can also be used as bioindicators of pollution and water quality, in technological applications like the production of biosensors or nanomaterials, and in the pharmaceutical industry. In addition, due to the increasing levels of CO_2 induced by the use of fossil fuels, a major potential probably lies in the production of biofuels (Kröger & Poulsen, 2008; Bozarth et al., 2009; Daboussi et al., 2014; Enzing et al., 2014).

1.5.1. Iron requirements and limitations in diatoms

It is well established that iron is a limiting nutrient for diatoms (Allen et al., 2008; Roncel et al., 2016). As it was mentioned previously, phytoplankton growth, and therefore that of diatoms, is mainly limited by iron availability in vast regions of the contemporary oceans, most notably in the so-called high nutrient-low chlorophyll regions (HNLC) (Boyd et al., 2007; Marchetti et al., 2009 & 2012). However, diatoms are often found in the most iron limited regions of the oceans, even though the lack of Pc as an alternative to Cc_6, and the presence of Cc_{550} in PSII, undoubtedly represents an extra requirement of iron that affects their adaptation to iron limitation (Guo et al., 2010 & 2012). It has been suggested that Cc_6 replacement by Pc can reduce iron requirements by up to 10% (Guo et al., 2010). More than 70% of blooms stimulated by iron fertilization experiments in HNLC areas are dominated by diatoms, suggesting that these microalgae have adaptations that allow survival in iron limited waters and a subsequent rapid multiplication when iron becomes available (Allen et al., 2008; Marchetti et al., 2009 & 2012; Lommer et al., 2012; Morrissey & Bowler, 2012). The tolerance of diatoms to iron limitation varies between species (Strzepek & Harrison, 2004; Allen et al., 2008; Lommer et al., 2012; Marchetti et al., 2012; Groussman et al., 2015). Different strategies have been developed by diatoms to minimize their iron requirements: the production of ferritin (an iron-storage molecule) (Marchetti et al., 2009), a decrease of the cellular pigment concentrations at

the cost of light capture efficiency, the biochemical alteration of the photosynthetic iron demand through decreased expression of the iron-rich PSI and Cb_6f components, or the substitution of iron-containing enzymes by iron-free equivalent proteins, as Fd by Fld (Allen et al., 2008; Marchetti et al., 2012; Groussman et al., 2015). In this sense, *petE* genes encoding Pc, closely related to those from green algae, have been found in the genomes of several strains of oceanic diatom species, probably due to the acquisition by horizontal gene transfer as an adaptation to iron limitation (Peers & Price, 2006; Marchetti et al., 2012; Groussman et al., 2015; Hippmann et al., 2017).

1.6. Particularities of the photosynthetic machinery of diatoms

The photosynthetic ET chain of diatoms owns some peculiarities acquired during its double endosymbiotic evolution. Although the RC cores of PSI and PSII are nearly identical in subunit composition to green algae and plant photosystems, LHCs have however specific properties (Neilson & Durnford, 2010). Thus, the pigment composition of diatoms differs from that of other photosynthetic organisms as they use Chl *a* and *c*, and the main carotenoids are β-carotene, fucoxanthins (Fx) and diadinoxanthin/diatoxanthin (Kuczynska et al., 2015). Furthermore, while the green-lineage possesses Chl *a*/*b* binding LHCs, the red lineage (diatoms, dinoflagellates and brown algae) has unique Fx Chl *a*/*c* binding proteins (FCPs), which bind 7 Chl *a*, 7 Chl *c*, 7 Fx and likely one diadinoxanthin within the protein scaffold (Veith & Büchel, 2007; Nagao et al., 2019; Falciatore et al., 2020; Xu et al., 2020). FCPs have prominent absorptions in the blue-green light region (400-550 nm), remarkably different from the green LHC, which enables diatoms and other related algae to survive efficiently in aquatic environments where red light is diminished and blue-green light is more available (Nagao et al., 2019; Pi et al., 2019; Wang et al., 2020; Xu et al., 2020).

1.6.1. The photosystem II

The recently solved structures of the PSII from the red alga *Cyanidium caldarium* (*C. caldarium*) (at 2.67 Å resolution) and the centric diatom *Chaetoceros gracilis* (*C. gracilis*) (at 3.0 Å resolution) have shown that the major intrinsic core proteins of the PSII are highly preserved in comparison to cyanobacteria or eukaryotic "green" organisms, implying a high conservation in both the green and red lineages (Figure 1.13) (Ago et al., 2016; Nagao et al., 2019; Pi et al., 2019). The PSII core of *C. gracilis* contains 40 Chl *a*, 2 Pheo, 10 β-carotenes, 2 hemes, 1 non-heme iron, 1 Mn_4CaO_5 cluster and several lipids (Nagao et al., 2019; Pi et al., 2019). However, in

spite of maintaining a similar PSII core, the diatom overall structure reveals a highly complicated protein–pigment network different from the green-type LHC apparatus. Thus, the PSII–LHC (or PSII–FCPII) supercomplex from *C. gracilis*, in particular, forms a homodimer, in which each PSII core of a monomer associates two FCP homotetramers and three FCP monomers. This PSII–FCPII structure reveals the arrangement of a huge number of Chls and Fxs that contribute to the energy transfer and dissipation.

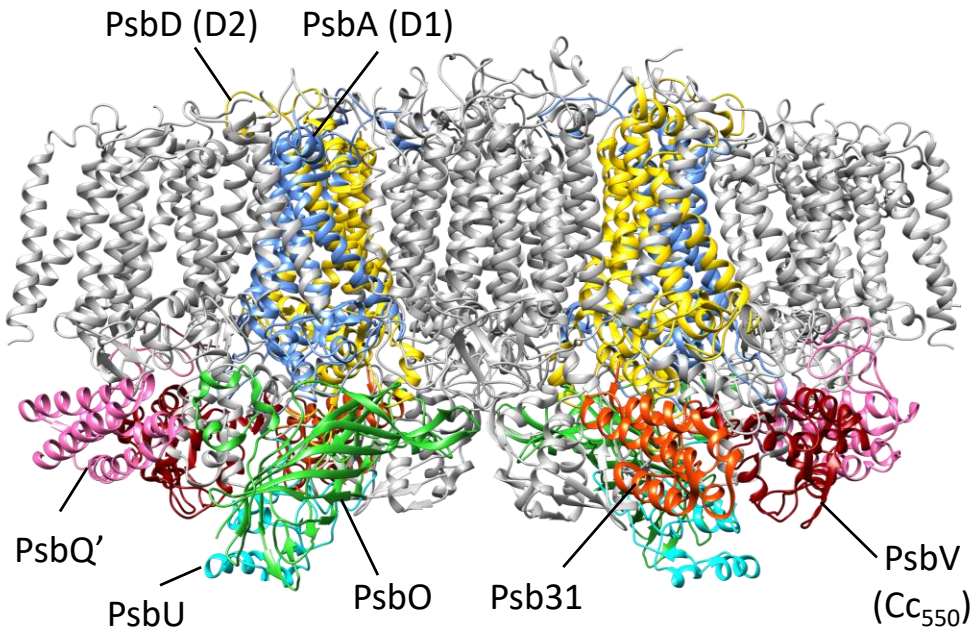

Figure 1.13. Photosystem II of the diatom *C. gracilis*. PDB code, 6jlu (Pi et al., 2019).

Another difference between the green and red lineages lies in the number and location of the extrinsic proteins at the lumenal side of the PSII core (Enami et al., 2003; Nagao et al., 2010a & 2019; Pi et al., 2019). In addition of 19 intrinsic subunits, diatom PSII contains five extrinsic proteins at the lumenal surface (Nagao et al., 2019; Pi et al 2019): PsbO, PsbU, and PsbV bind to the same positions as the equivalent subunits in the cyanobacterial PSII, whereas PsbQ' binds to the same position as in red algae and PsbQ in plant PSII (Ago et al., 2016; Nagao et al., 2019; Pi et al., 2019). The PsbQ' subunit is not involved directly in oxygen evolution but was previously described as required for effective binding of Cc_{550} and PsbU (Nagao et al., 2010a). The fifth extrinsic subunit, named Psb31, is only found in diatoms and has an overall structure similar to that of the green PsbQ subunit. It has been suggested that Psb31 originated via a secondary endosymbiotic event (Ifuku & Noguchi, 2016; Pi et al., 2019). This subunit, which binds directly to the PSII intrinsic proteins, could mitigate the chloride requirement for oxygen

evolution, maintain the stability of the Mn_4CaO_5 cluster and participate in the Y_Z proton channel that transfers protons from the Mn_4CaO_5 cluster to the lumenal surface (Nagao et al., 2010a; Ifuku & Noguchi, 2016; Pi et al., 2019).

From biochemical analyses, it was previously proposed that the binding of Cc_{550} to PSII would be different between cyanobacteria and diatoms. In cyanobacteria, the Cc_{550} binds directly to the PSII core (Section 1.3.1), whereas in diatoms the Cc_{550} could bind through its interaction with PsbO, PsbQ' and Psb31 (Nagao et al., 2010a). However, as mentioned above, the solved PSII structures of *C. caldarium* and *C. gracilis* have shown that Cc_{550} binds to the same position as in cyanobacteria, and no direct interactions are observed between Psb31 and the other extrinsic subunits, consistent with an indirect role of Psb31 in stabilizing the binding of PsbV to PSII (Pi et al., 2019). Moreover, the overall structure of Cc_{550} itself is similar to that described in cyanobacteria (Ago et al., 2016; Pi et al., 2019).

1.6.2. The photosystem I and the PsaF subunit

There were not available structures of the red PSI until very recently. However, the structures of the PSI of the red alga *Cyanidioschyzon merolae* (*C. merolae*) (at 4 Å resolution) (Antoshvili et al., 2019) and of the diatom *C. gracilis* (at 2.2 Å resolution for the PSI core) (Xu et al., 2020) have been recently solved. The *C. gracilis* PSI, in particular, has either three or five red alga-type LHC antenna subunits in which Chl *a* and zeaxanthins are the main light-harvesting pigments (Xu et al., 2020). Diatom PSI binds more than 20 FCPI antenna subunits with a huge variety of protein sequence and pigment binding, making it the largest antenna system found in the eukaryotic photosynthetic organisms and supporting the efficient survival of diatoms in the aquatic environment (Falciatore et al., 2020; Xu et al., 2020).

The structures of the PSI core of *C. merolae* and *C. gracilis* show both the conservation of the hydrophobic interaction site with the electron donors of PSI and the N-terminal extension in PsaF (Antoshvili et al., 2019; Xu et al., 2020). However, in red algae and diatoms this luminal extension presents a decrease in the number of positive groups (Bernal-Bayard et al., 2013; Castell et al., 2021a) (Figure 1.14). This evidences the existence of significant electrostatic differences in this PSI specific area between the organisms of the green and red lineages (Castell et al., 2021a).

1.6.3. The soluble carriers

The existence of alternative no-iron proteins is only partially maintained in the red lineage of photosynthetic organisms that diverged along evolution from the green lineage (Falkowski et al., 2004). Thus, Fld is present as an alternative to Fd in most algal taxa of the red lineage, including red algae, cryptophytes, stramenopiles (that include diatoms) and haptophytes (Pierella Karlusich et al., 2014; Gao et al., 2021). However, most diatoms lack Pc and only have Cc_6 as the soluble electron carrier between the Cb_6f and PSI complexes (Akazaki et al., 2009; Bernal-Bayard et al., 2013; Groussman et al., 2015). Cc_6 is the only soluble carrier available not only in diatoms, but in most algae from the red-plastid lineage, as demonstrated by direct protein characterization, genome sequences and transcriptomic analysis of different red algae and stramenopiles, including diatoms (Akazaki et al., 2009; Bowler et al., 2010; Blaby-Haas & Merchant 2012; Bernal-Bayard et al., 2013; Groussman et al., 2015). However, although all the stramenopiles whose genomes have been sequenced have *petJ* genes for Cc_6, *petE* genes encoding Pcs –closely related to those from green algae– have been found in the genomes of several strains of oceanic diatoms species, as *Thalassiosira oceanica* (*T. oceanica*) and *Fragilariopsis cylindrus* (*F. cylindrus*), as well as in the haptophyte *Emiliania huxleyi* (*E. huxleyi*) and the dinoflagellate *Karenia brevis* (*K. brevis*) (Nosenko et al., 2006; Peers & Price, 2006; Blaby-Haas & Merchant, 2012). In addition, transcripts encoding Pcs have been reported in at least once specie from each one of the principal diatom classes (Groussman et al., 2015), which can be explained by the acquisition from green algae by horizontal gene transfer as an adaptation to iron limitation in their natural habitats (Peers & Price, 2006; Marchetti et al., 2012).

1.6.3.1. Cytochrome c_6 and the "red" plastocyanin

In the red lineage, crystal structures of Cc_6 from red algae and diatoms have shown that this protein maintains the global folding pattern of the Cc_6 of green algae and cyanobacteria (Yamada et al., 2000; Akazaki et al., 2009). However, with respect to protein surface and functional areas, Cc_6 from red algae and diatoms still preserves the hydrophobic ET area but shows a significant decrease in the number of negative charges in the electrostatic patch, and thus the negative electrostatic character of this functional area is sensibly reduced, in agreement with the equivalent changes in the PSI partner (Figure 1.14) (Bernal-Bayard et al., 2013). Therefore, although the evolution of ET to PSI in red-type organisms has also led to complementary electrostatic interactions between acidic patches in Cc_6 and basic regions in PsaF, the electrostatic character of both partners is similarly reduced (Bernal-Bayard et al., 2013 & 2015; Castell et al., 2021a).

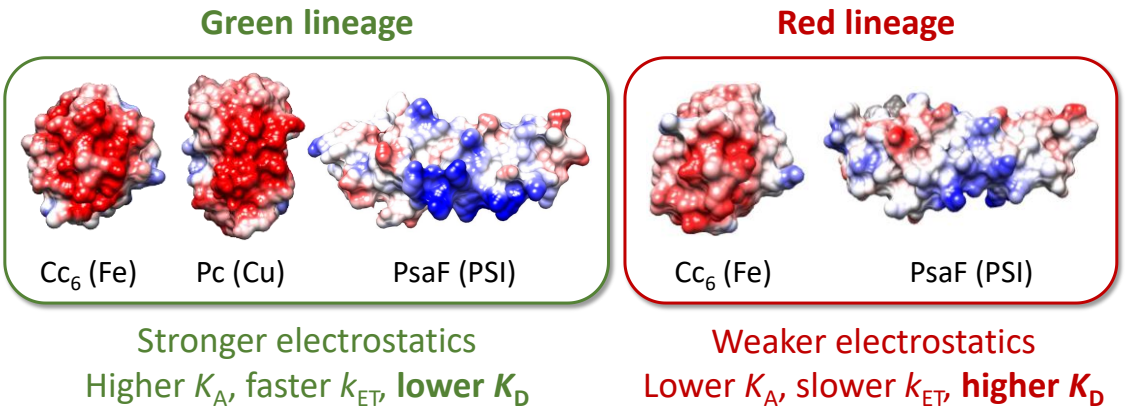

Figure 1.14. Electrostatic properties of cytochrome c_6, plastocyanin and the PsaF luminal part in the green and red lineages. Green lineage: *C. reinhardtii* Cc_6 (PDB code, 1cyi), Pc (PDB code, 2plt) and PsaF subunit (PDB code, 6ijj); Red lineage: *Phaeodactylum tricornutum* (*P. tricornutum*) Cc_6 (PDB code, 3dmi) and modelled PsaF (Bernal-Bayard et al., 2015).

Evidences for a functional "red" Pc have been reported in the case of *T. oceanica*, where a relatively small quantity of the Cu-containing protein was detected, partially purified and sequenced, although with a discrepancy between the expected size of the theoretical mature Pc (10,3 kDa) and the apparent molecular weight of the purified protein (18,2 kDa) (Peers & Price, 2006). Moreover, this diatom has been reported to replace constitutively Cc_6 by Pc, as the two Cc_6 encoding genes of its genome are weakly expressed, probably reducing their need of iron (Peers & Price, 2006; Lommer et al., 2012). However, the levels of Pc per cell reported in *T. oceanica* are around 7-10 times lower than the concentration previously described for Cc_6 in other diatoms under iron sufficient conditions (Peers & Price, 2006; Bernal-Bayard et al., 2013; Roncel et al., 2016; Kong & Price, 2020), which is also accompanied by lower PSI and Cb_6f complex concentrations, a typical characteristic of cells suffering iron limitation (Strzepek & Harrison, 2004). Another concerns lie in the unknown regulatory mechanisms by which a putative Pc could act as an alternative to Cc_6 in diatoms (Lommer et al. 2012; Kong and Price 2020; Merchant et al., 2020; García-Cañas et al., 2021), or the existence of a specific copper-transporting system to the thylakoid that has not yet been found (Guo et al., 2010 & 2015; Nouet et al., 2011; Blaby-Haas & Merchant, 2012). In any case, the Pc-translated region in diatoms is closely related to the Pc from green algae. Consequently, the "red" acquired Pc actually shows the typical strong negative electrostatics of a "green-type" Pc (Figure 1.14).

1.6.3.2. Interaction of cytochrome c_6 and green plastocyanins with photosystem I

Recent kinetic analysis, structural modelling and computational docking have provided new data on the ET mechanisms and protein characteristics in the red-plastid branch. These results suggest the development of different strategies in the evolution of the ET from Cf to PSI in the green and red lineages of eukaryotic photosynthetic organisms (Figure 1.14) (Bernal-Bayard et al., 2013 & 2015; Roncel et al., 2016).

The kinetic analysis of PSI reduction by Cc_6 in the diatom *P. tricornutum* indicated the occurrence of a mechanism similar to that previously described in the green lineage systems (Figure 1.11), ET taking place in a [protein:protein] transient complex undergoing a reorganization process from the initial encounter complex to the optimized final configuration (Bernal-Bayard et al., 2013). However, kinetic data made evident the weaker electrostatic nature of the interaction, in agreement with the weaker electrostatic character of both Cc_6 and PsaF/PSI. Consequently, and in comparison with the green-type systems, the red-type system of *P. tricornutum* showed lower values both for the binding affinity of Cc_6 to PSI ($K_A \approx 7 \times 10^3$ M^{-1} versus $\approx 10^5$ M^{-1}) and ET ($k_{ET} \approx 2 \times 10^4$ s^{-1} versus $\approx 10^5$ s^{-1}), in addition to a lower efficiency in the formation of the properly arranged [Cc_6:PSI] complex (Bernal-Bayard et al., 2013). Interestingly, the cross-reaction of *P. tricornutum* PSI with green algae Cc_6 showed to be more efficient kinetically than the native diatom system, with three-times and two-times higher K_A and k_{ET} values, respectively (Bernal-Bayard et al., 2013). This suggests that the native diatom Cc_6/PSI couple represents a compromise between a lower efficiency in ET and a facilitated turnover, due to a lower binding affinity (Figure 1.14). Finally, there are not functional data available for the interaction of the red lineage PSI with the native "green-type" acquired Pc (as in *T. oceanica*). However, kinetic data indicated that *P. tricornutum* PSI is able to react with the acidic Pc of green algae and plants, although it does much less efficiently than with *P. tricornutum* Cc_6 ($k_{ET} \approx 3 \times 10^2$ s^{-1} versus 2.2×10^4 s^{-1}, respectively), demonstrating the formation of less-optimal functional complexes (Bernal-Bayard et al., 2013 & 2015). Nevertheless, this efficiency was even doubled in Pc mutants of the green alga *C. reinhardtii* in which negative charges were replaced for positive ones, trying to mimic the electrostatics of diatom Cc_6 (Bernal-Bayard et al., 2015).

The structure of the transient ET complex between Cc_6 and PSI from the diatom *P. tricornutum* has been analysed by computational docking and compared to that of green lineage (Bernal-Bayard et al., 2015), the results explaining why the diatom redox couple shows a lower efficiency than the green systems, both in the formation of the properly arranged ET complex and in the ET itself. Thus, in the most energetically-favourable docking orientations of the diatom [Cc_6:PSI] complex, the two tryptophan residues in PSI forming the hydrophobic binding

site and the ET path to P_{700} were located at a relatively long distance from the Cc_6 heme. On the contrary, the [Cc_6:PSI] docking models showing the shortest distances for ET did not show electrostatic interactions with the positive patch in PsaF or favourable interactions at the binding interface. Altogether, this suggests that the more efficient ET orientations in the *P. tricornutum* [Cc_6:PSI] complex are not energetically optimized (Bernal-Bayard et al., 2015). In agreement with this model, it has been recently reported in the red algae *C. merolae* that the reduction of isolated PSI by the cyanobacterial *Synechocystis* sp. PCC 6803 Cc_6, which has a relatively neutral electrostatic patch, was not affected by the removal of the PsaF subunit (Antoshvili et al., 2019). However, similar experiments indicated that the reduction of PSI of *C. merolae* by an acidic plant Pc was strongly inhibited when depleting the PsaF subunit (Antoshvili et al., 2019).

To finish, it is worth saying that no kinetic, functional or structural information exists about the interaction of Cf with the soluble donors in the red lineage.

1.6.4. *Phaeodactylum tricornutum*

P. tricornutum is a pennate coastal marine diatom with a worldwide distribution (Martin-Jezequel & Tesson, 2012). Cells of this alga have a diameter of approximately 10 µm and a considerable part of their volume is occupied by a single chloroplast (3 – 9 µm) (Figure 1.15) (Flori, 2016). In comparison to other diatoms, *P. tricornutum* has an unusual life cycle, lacking an auxosporulation cycle. This diatom follows the general vegetative process, in which cell division allows each daughter cell to inherit one maternal valve as the epitheca, and to synthesize one new valve as the hypotheca, while there is a temporal and spatial rearrangement of the nuclear and cytoplasmatic material (Martin-Jezequel & Tesson, 2012).

P. tricornutum has the unusual property of being a pleiomorphic microalga, characterized by three different morphotypes (fusiform, triradiate and oval), which have been globally reported (De Martino et al., 2007; Martin-Jezequel & Tesson, 2012). This plasticity is related to the unusual nature of the cell wall, which is only poorly silicified (De Martino et al., 2007). In contrast to other species, *P. tricornutum* is the only diatom that can grow in the absence of silicon, even if its three morphotypes can assimilate this element (De Martino et al., 2007; Martin-Jezequel & Tesson, 2012). The ability to develop different morphotypes could be an adaptation to the changing environment found in coastal waters, as it is believed that the three morphotypes may represent distinct ecophenotypes, each one specifically adapted for growth under singular conditions (De Marino et al., 2007; Martin-Jezequel & Tesson, 2012). Numerous studies about the sensitivity of *P. tricornutum* to different physicochemical parameters have

demonstrated that stress conditions could affect cell morphometry or promote shape deformities and alterations (Martin-Jezequel & Tesson, 2012). The fusiform morphotype largely predominates in the usual laboratory conditions, but round-shape cells are formed under stress conditions. Moreover, the fusiform morphotype is affected in conditions of iron limitation by reducing cell diameter and volume (Martin-Jezequel & Tesson, 2012).

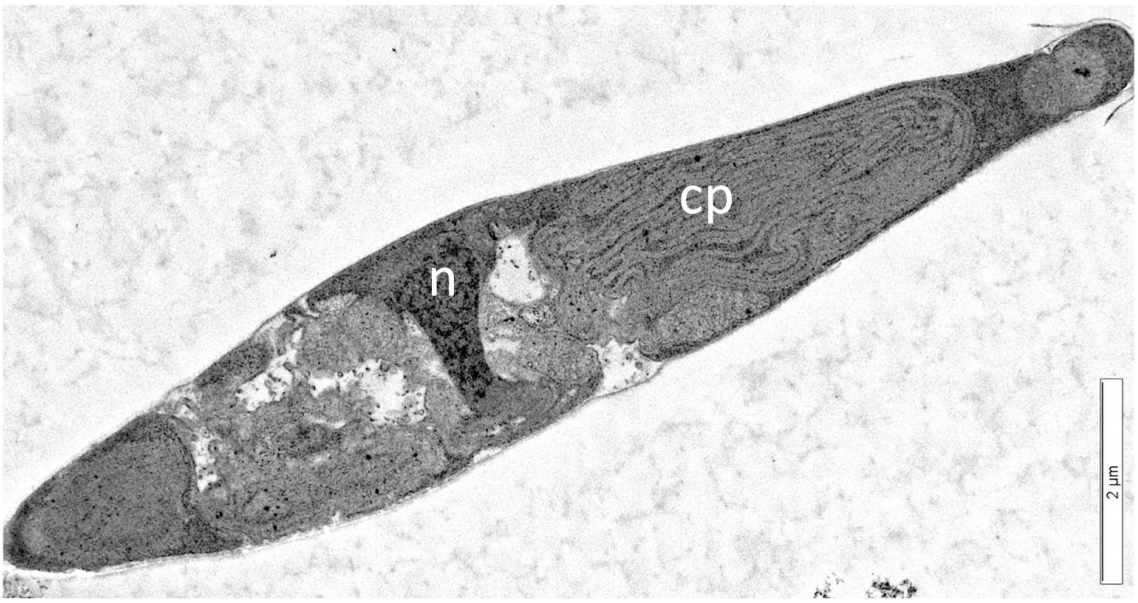

Figure 1.15. Electro microscopy image of a *P. tricornutum* cell. The image was obtained, in collaboratorio with Dr. Purificación Calvo, in the microscopy service of the CITIUS (University of Seville). Cp, chloroplast; n, nucleus.

P. tricornutum is one of the most widely used models in diatom research because of its relatively small genome (27.4 megabases), short generation time, ease of cultivation and flexibility to genetic engineering (Scala et al., 2002; Saade & Bowler, 2009; Levering et al., 2016; Buck et al., 2018). The entire sequence of its genome is available and is genetically manipulable (Allen et al., 2008; Bowler et al., 2008; Saade & Bowler, 2009). Different methods for the introduction of transgenes are available in this diatom, such as biolistic, conjugation with bacteria or electroporation. In addition, new genome editing methods, as TALEN or CRISPR, have been implemented recently in *P. tricornutum*, allowing the direct knockout or modification of specific nuclear genes (Buck et al., 2018).

Despite being sensitive to iron limitation, *P. tricornutum* is relatively tolerant to these conditions (Allen et al., 2008; Roncel et al., 2016). Even though this diatom shows a significant

reduction in Chl levels and photosynthetic efficiency, as a result of reduced carbon flux through the Calvin-Benson cycle, it has evolved novel strategies for acquiring different forms of iron (Allen et al., 2008). Moreover, *P. tricornutum* appears to use a different iron uptake system than other diatoms, making this diatom able to survive chronically to low iron concentration and to respond rapidly to iron stimulation (Allen et al., 2008; Morrissey & Bowler, 2012; Kazamia et al., 2018). Studies on this diatom have shown that it is also unusually resistant to damage by high light conditions, because a protective mechanism based in a xanthophyll-dependent non-photochemical quenching (NPQ). This photoprotective mechanism is induced very fast and can compete with excitation transfer to the PSII RC much more efficiently than does the analogous process in higher plants (Roncel et al., 2016), helping *P. tricornutum* to cope with the exposure to high light conditions in surface waters (Kayanja et al., 2021). In addition, this microalga is also known to have heterotrophic capacities, being able to grow with a vast range of organic sources, such as sugars, alcohols, amino acids, urea, etc. (Martin-Jezequel & Tesson, 2012).

P. tricornutum has been extensively used for physiological and biochemical research in diatoms for several decades, and as food source for the aquaculture industry, as it is rich in protein and fatty acid contents (De Martino et al., 2007; Daboussi et al., 2014; Butler et al., 2020). *P. tricornutum* has also a commercial potential as a natural source of fucoxanthin, which is used in human and animal food, health and cosmetic products (Dhaouadi et al., 2020; Runqing & Wei, 2020; Butler et al., 2020).

As previously said, diatoms have extra requirements of iron in their photosynthetic apparatus compared with the green lineage. First, these algae have Cc_{550} associated to PSII, this protein being absent in green algae and plants where it appears to have been replaced by the non-iron PsbP subunit (Roncel et al., 2012; Ifuku & Noguchi, 2016). Second, most diatoms lack Pc as an alternative to Cc_6 as electron carrier between Cb_6f and PSI. *P. tricornutum* fulfills both conditions: lacks Pc and produces Cc_{550} (Allen et al., 2008; Bernal-Bayard et al., 2013 & 2017), and therefore it has been considered as an adequate organism for the proposed study to be carried out in this PhD. Thesis.

2. Objectives

2.Objectives

The following specific objectives have been addressed in this Thesis:

1. Characterization of cytochrome c_{550} of the diatom *Phaeodactylum tricornutum* and the effects of iron deprivation on its function as a photosystem II extrinsic subunit.

2. Effects of the heterologous expression of a plastocyanin of green algae in the diatom *Phaeodactylum tricornutum*.

3. Modelling of the [cytochrome *f*:acceptor] electron transfer complexes in the diatoms *Phaeodactylum tricornutum* and *Thalassiosira oceanica*.

Part of the results presented in this Thesis has been included in the following publications:

- Bernal-Bayard, P., Álvarez, C., Calvo, P., Castell, C., Roncel, M., Hervás, M. & Navarro, J.A. (2019). The singular properties of photosynthetic cytochrome c_{550} from the diatom *Phaeodactylum tricornutum* suggest new alternative functions. *Physiologia Plantarum, 166*, 199-210.

- Bernal-Bayard, P., Puerto-Galán, L., Yruela, I., García-Rubio, I., Castell, C., Ortega, J.M., Alonso, P. J., Roncel, M., Martínez, J.I., Hervás, M. & Navarro, J.A. (2017). The photosynthetic cytochrome c_{550} from the diatom *Phaeodactylum tricornutum. Photosynthesis Research, 133*, 273-287.

- Castell, C., Bernal-Bayard, P., Ortega, J.M., Roncel, M., Hervás, M. & Navarro, J.A. (2021). The heterologous expression of a plastocyanin in the diatom *Phaeodactylum tricornutum* improves cell growth under iron deficient conditions. *Physiologia Plantarum, 171,* 277-290.

- Castell, C., Rodríguez-Lumbreras, L.A., Hervás, M., Fernández-Recio, J. & Navarro, J.A. (2021) New insights into the evolution of the electron transfer from cytochrome *f* to photosystem I in the green and red branches of photosynthetic eukaryotes. *Plant and Cell Physiology*, doi:10.1093/pcp/pcab044.

3. Experimental procedures

3. Experimental procedures

3.1. Organisms and culture conditions

3.1.1. *P. tricornutum* and other microalgae

3.1.1.1. *P. tricornutum*, *C. muelleri*, *N. gaditana* and *I. galbana* strains used in this work

Cells from the coastal pennate diatom *P. tricornutum* CCAP 1055/1 (obtained from the Culture Service of the "Centro de Investigaciones Científicas Isla de la Cartuja") were used as biological material. For the purification of big amounts of proteins, *P. tricornutum* cells from photobioreactors outdoor cultures (iron-replete conditions) were obtained as a frozen paste from Easy Algae (Cádiz, Spain).

Chaetoceros muelleri (C. muelleri), *Nannochloropsis gaditana (N. gaditana)* and *Isochrysis galbana* (*I. galbana*) were obtained from indoor cultures from the Centro Público Integrado de Formación Profesional Marítimo Zaporito (San Fernando, Spain).

In some experiments, extracts from the green alga *C. reinhardtii* were obtained to be used as controls for the detection of Pc by Werstern-blot.

3.1.1.2. Culture conditions

P. tricornutum was grown in Erlenmeyer flasks containing modified artificial seawater (ASW) medium (McLachlan, 1964; Goldman & McCarthy, 1978) in a rotatory shaker (50 rpm) at 20°C with regular transfer of the cells into fresh media. The cultures were illuminated by led white light (4500 K) lamps giving an intensity of 20 µmol m^{-2} s^{-1} (T8-150MWBL led lamps; Wellmax) under a light/dark cycle of 16/8 hours.

Table 3.1. "Dry" components of the medium.

Mineral salts	Concentration	g/L
NaCl	400 mM	23.4
$MgSO_4 \cdot 7\ H_2O$	20 mM	4.9
$CaCl_2 \cdot 2\ H_2O$	10 mM	1.11
NaBr	1.7 mM	0.19
KCl	10 mM	0.75
$MgCl_2 \cdot 6\ H_2O$	20 mM	4.1

High purity water (H_2O_{MQ}, resistivity of ≈18 MΩ cm; Mili-Q® Advantage A10 Water Purification System) was used to prepare culture media. ASW medium consists of two parts: the main salts that form the "basal seawater" and the enrichment solutions (McLachlan, 1964; Goldman & McCarthy, 1978; Andersen et al., 2005). One litre of the "basal seawater" (Table 3.1), made up of the "dry" components, was prepared and autoclaved.

There were five additional components, or enrichment solutions, added to the autoclaved "basal seawater". These enrichment solutions, referred to as the "wet components" (H_3BO_3, Tris-HCl, vitamins, nitrates and phosphates and trace elements) (Table 3.2), were prepared and sterilized as stock solutions, before being added to the "basal seawater". For iron-deplete cultures the trace elements were the same except that $FeCl_3 \cdot 6\ H_2O$ was eliminated and volumes of a stock solution of 10 µM Fe-EDTA (ethylenediaminetetraacetic acid) were added to the required concentrations. The following compounds: H_3BO_3, Tris-HCl, nitrates and phosphates and the trace elements, were autoclaved for sterilization, whereas the vitamins were sterilized by filtration with a sterile syringe filter qmax PES Ø30 mm, 0.22 µm (Syringe-driven filters FPE-204-030, Jet Biofil, Labotaq).

Table 3.2. "Wet" components of the medium.

Stock	Concentration	g/L	mL/L medium
H_3BO_3	0.2 M	12.4	1
Tris-HCl	0.4 M, pH 7.8	50	5
Vitamin Mix[a]	--	--	0.5
Nitrates and phosphates[b]	--	--	2
Trace elements[c]	--	--	1

[a] See Table 3.3; [b] See Table 3.4; [c] See Table 3.5.

Table 3.3. Vitamin mix.

Stock	mg/L	Final concentration (g/L)
Nicotinic acid	10	5×10^{-6}
p-amino-benzoic acid	10	5×10^{-6}
$NaHCO_3$	5	2.5×10^{-6}
Thiamine hydrochloride	5	2.5×10^{-6}
Biotin	1	5×10^{-7}
Vitamin B_{12}	0.35	1.8×10^{-7}

Table 3.4. Nitrates and phosphates.

Stock	g/L	Final concentration (g/L)
$K(Na)NO_3$	150	0.3
NaH_2PO_4	10	0.02

Table 3.5. Trace elements.

Stock	g/L	Final concentration (g/L)
EDTA-Na_2	4.4	0.0044
$FeCl_3 \cdot 6\ H_2O$	3.2	0.0032
$CuSO_4 \cdot 5\ H_2O$	0.01	10×10^{-6}
$ZnSO_4 \cdot 7\ H_2O$	0.022	22×10^{-6}
$CoCl_2 \cdot 6\ H_2O$	0.01	10×10^{-6}
$MnCl_2 \cdot 4\ H_2O$	0.18	2×10^{-4}
$NaMoO_4 \cdot 2\ H_2O$	0.006	6×10^{-6}

For the experiments to study the effects of iron deficiency, cells from cultures of 7 days were pelleted at 5,000 x*g* for 5 minutes and suspended and grown in modified ASW medium (10 µM Fe; iron-replete cultures) or modified ASW medium with only 10 nM Fe-EDTA (iron-deplete cultures) (McKay et al., 1999). Additional concentrations of 100 nM and 40 nM Fe-EDTA were used in some iron-deficiency experiments. All the material used for the iron-deplete cultures was thoroughly cleaned with 3.7% HCl and washed out with H_2O_{MQ}. The cells were transferred into fresh media after 7 days and they were grown for 15 days more. For most of the experiments, the initial optical density at 730 nm (OD_{730nm}) of the cultures was 0.1 (1.5×10^6 cells mL^{-1}). For the experiments of Pc expression under iron deficiency, a concentration of 0.3 mg L^{-1} (5 µM) of $CuSO_4$ was selected as the standard copper concentration to be added to the final culture media. Previous experiments with different copper contents were carried out in order to select this standard copper concentration.

For growth on solid media, cultures were grown in Petri dishes with modified ASW medium supplemented with 1% Bacto Agar (Difco) (McLachlan, 1964; Goldman & McCarthy, 1978).

C. muelleri, *N. gaditana* and *I. galbana* were grown and maintained in the same conditions as described above for *P. tricornutum*.

3.1.1.3. Growth measurements and cell collecting method

The cell density of the *P. tricornutum* cultures was measured at 730 nm by using a JASCO V-650 UV-Vis spectrophotometer. Cell concentrations were determined by cell counting with a Neubauer-Improved hemocytometer (Marienfeld-Superior), according to the manufacturer's instructions.

Cell specific growth rate (μ, day^{-1}) was calculated after 15 days of culture growth as: [$\mu = \ln (N_t/N_0)/\Delta t$] where N_t and N_0 are the final and initial cell concentration, respectively, and Δt is the days of growth (Li et al., 2017).

Depending on the culture volume, the cells were collected as follows. For culture volumes smaller than 1.5 mL, *P. tricornutum* cells were pelleted at 5,000 x*g* for 5 minutes in a Beckman Coulter® Microfuge®16 microcentrifuge. For volumes between 1.5 and 50 mL, an Eppendorf® 5804-R centrifuge was used at 5,000 x*g* for 5 minutes. Finally, for culture volumes bigger than 50 mL, *P. tricornutum* cells were pelleted at 5,000 x*g* for 10 minutes in a Beckman Coulter® Avanti J-25 centrifuge with a JA-25.50 (cultures up to 50 mL) or JA-16.250 (cultures up to 250 mL) rotor.

3.1.2. *Escherichia coli*

3.1.2.1. *E. coli* strains used in this work

Escherichia coli (*E. coli*) strains were obtained from the Culture Service of the "Centro de Investigaciones Científicas Isla de la Cartuja". The strains used in this work and the most relevant characteristics of their genotypes are shown in Table 3.6.

Table 3.6. Strains of *E. coli* used in this work.

Strain	Genotype	Reference
DH5α	F-, ϕ80/*acZ Δ*M15, *Δ*(*lacZYA-argF*)U169, deoR, *recA*1, *endA*1, *hsdR*17(rK-, mK+), *phoA, supE*44, λ-, *thi-1, gyrA*96, *relA*1	Hanahan, 1983
BL21(DE3) laclq	F'::Tn10 *proA+B+ laclq Δ(lacZ)M15/ ompT (lon) hsdS*(r_B-m_B-, an *E. coli* B) with DE3 (lambda prophage with the IPTG inducible polymerase)	Studier & Moffatt, 1986

3.1.2.2. Culture conditions and cell collecting method

E. coli was grown in Luria-Bertani (LB) medium (Sambrook & Russell, 2001) containing 10 g L^{-1} NaCl, 10 g L^{-1} Bacto-Tryptone and 5 g L^{-1} yeast extract. For growth on solid media, 1.5% agar (w/v) was added. The media were autoclaved for sterilization.

Liquid cultures were grown at 37°C in a rotatory shaker at 200 rpm for 16 hours. Solid agar cultures were grown in Petri dishes at 37°C.

When the presence of antibiotics was necessary in the medium, they were added at the following final concentrations: 100 µg mL^{-1} ampicillin (Ap), 50 µg mL^{-1} streptomycin (Sm), 50 µg mL^{-1} spectinomycin (Sp), 50 µg mL^{-1} kanamycin (Km) and 30 µg mL^{-1} chloramphenicol (Cm).

For culture volumes smaller than 1.5 mL, *E. coli* cells were pelleted at 16,000 x*g* for 1 minute in a Beckman Coulter® Microfuge®16 microcentrifuge. For volumes bigger than 15 mL, cells were pelleted at 10,000 x*g* for 10 minutes in a Beckman Coulter® Avanti J-25 centrifuge by using JA-25.15 (cultures up to 15 mL), JA-25.50 (cultures up to 50 mL) or JA-16.250 (cultures up to 250 mL) rotors.

3.2. Nucleic acids manipulation and analysis *in vitro*

3.2.1. Plasmids used in this work

The plasmids used in this work and its characteristics are shown in Table 3.7.

Table 3.7. Plasmids used in this work.

Plasmid	Features	Resistance	Reference
pPha_T1	Plasmid containing the zeocine resistance gene used for the selection of the transformed mutants	Zeocine	Gift of Prof. Chris Bowler's lab (IBENS, Paris, France)
Isip1::YFP	Plasmid with the promoter Pisip (inducible in absence of iron) and the YFP gene	Ap	Gift of Prof. Chris Bowler's lab (IBENS, Paris, France); Kazamia et al., 2018
pBS_PcE85K_Ptri	pBlueScript II SK (+) plasmid containing the *petE* gene of *C. reinhardtii* with the mutation E85K in *Eco*RV and *Pst*I sites, and the transit peptide of the ATPase gamma subunit (ATPC, directing the protein to the stroma)	Ap	Available in the lab; Castell, 2016, Master's thesis

pPisip1_PcE85K	Plasmid containing the *petE* gene of *C. reinhardtii* with the mutation E85K under the control of the promoter Pisip, and the transit peptide of the ATPC	Ap	Available in the lab; Castell, 2016, Master's thesis
pBS_pFld_PcE85K_Ptri	pBlueScript II SK (+) plasmid containing the *petE* gene of *C. reinhardtii* with the mutation E85K under the control of the *P. tricornutum* Fld promoter in *Eco*RV and *Pst*I sites, and the transit peptide of the ATPC	Ap	GeneCust. This work; Castell et al., 2021b
pFld_PcE85K	Plasmid containing the *petE* gene of *C. reinhardtii* with the mutation E85K under the control of the Fld promoter and the transit peptide of the ATPC	Ap	Constructed in this work; Castell et al., 2021b
pBS_pFld_PtCc6_PcE85K	pBlueScript II SK (+) plasmid containing the *petE* gene of *C. reinhardtii* with the mutation E85K, with the *P. tricornutum* full transit peptide of Cc_6 (directing the protein to the thylakoid lumen) and under the control of the *P. tricornutum* Fld promoter in *Eco*RV and *Pst*I sites	Ap	GeneCust. This work; Castell et al., 2021b
pFld_ptCc6_PcE85K	Plasmid containing the *petE* gene of *C. reinhardtii* with the mutation E85K, with the *P. tricornutum* full transit peptide of Cc_6 and under the control of the *P. tricornutum* Fld promoter	Ap	Constructed in this work; Castell et al., 2021b
pBS_pFld_PtVCc6_PcE85K	pBlueScript II SK (+) plasmid containing the *petE* gene of *C. reinhardtii* with the mutation E85K, with the *P. tricornutum* transit peptide of Cc_6 without an intron and under the control of the *P. tricornutum* Fld promoter in *Eco*RV and *Pst*I sites	Ap	GeneCust. This work; Castell et al., 2021b
pFld_ptVCc6_PcE85K	Plasmid containing the *petE* gene of *C. reinhardtii* with the mutation E85K, with the *P. tricornutum* transit peptide of Cc_6 without an intron and under the control of the *P. tricornutum* Fld promoter	Ap	Constructed in this work; Castell et al., 2021b
pSpark® I	Plasmid used for the maintenance of the *P. tricornutum FLDA1* gene in *E. coli* DH5α	Ap	Canvax Biotech
pSparkI_Fld	Plasmid containing the *P. tricornutum FLDA1* gene for its maintenance in *E. coli* DH5α	Ap	Constructed in this work; Castell et al., 2021b
pET-28 b (+)	Plasmid with His tag used for the construction of pET28b_Fld	Km	Novagen®
pET-28 b_Fld	Plasmid containing the *P. tricornutum FLDA1* gene, used for the overexpression of Fld in *E. coli*	Km	Constructed in this work; Castell et al., 2021b

3.2.2. DNA isolation

3.2.2.1. Isolation of plasmid DNA from *E. coli*

Plasmids were isolated by alkaline lysis as described in Ish-Horowicz & Burke (1981). First, cells were grown in 25 – 50 mL LB medium at 37ºC in a rotatory shaker at 200 rpm for 16 hours. Then, the cells were pelleted by centrifugation (Section 3.1.2.2) and resuspended in 100 µL of solution I [50 mM glucose, 25 mM Tris-HCl, pH 8.0, 10 mM EDTA]. Then, 200 µL of the solution II [0.2 N NaOH, 1% SDS] was added and the samples were mixed gently. After that, 150 µL of solution III [3 M potassium acetate, 2 M glacial acetic acid] was added, the samples were mixed gently, and after 5 minutes on ice the precipitated protein and chromosomal DNA were removed by centrifugation (10,000 x*g*) for 15 minutes at 4ºC. The supernatant was precipitated with 2 volumes of ethanol, incubated for 30 minutes at –20ºC and centrifuged at 10,000 x*g* for 5 minutes at 4ºC. The pellet was washed twice with 70% ethanol, dried under a laminar air flow cabinet and resuspended in 50 µL H_2O_{MQ}. Finally, the isolated plasmids were treated with 1 µg RNAse (MBiotech) at 37ºC for at least 15 minutes (Ish-Horowicz & Burke, 1981; Bernal-Bayard et al., 2015). After the RNAse treatment, the samples were purified with the Gel/PCR Purification Mini Kit (Favorgen Biotech Corp.), according to manufacturer's instructions. Then, the content of plasmid DNA in the samples was quantified with a Nanodrop ND-1000 spectrophotometer (Section 3.2.6).

Occasionally, the commercial DNA-spin™ Plasmid DNA Purification Kit (Intron Biotechnology) was used, according to the manufacturer's instructions.

3.2.2.2. Isolation of genomic DNA from *P. tricornutum*

The isolation of total genomic DNA (gDNA) of the diatom *P. tricornutum* was carried out according to a modified protocol of Murray & Thompson (1980). First, pelleted cells were ground with liquid N_2 in a mortar. The dry powder was gently dispersed in CTAB (Cetyl-trimethyl-ammonium bromide) buffer [2% (w/v) CTAB, 1.4 M NaCl, 100 mM Tris-HCl, pH 8.0, 20 mM EDTA] and incubated at 65ºC for at least 10 minutes. Then, the extract was mixed with an equal volume of chloroform and centrifugated at 13,000 x*g* for 1 minute; the aqueous phase was then removed to a new microcentrifuge tube. Afterwards, the DNA was precipitated by adding an equal volume of 2-propanol to the samples, mixed thoroughly and centrifuged again at 13,000 x*g* for 1 minute. Pellets were then washed with 70% ethanol, dried under a laminar air flow cabinet and resuspended in 50 – 100 µL H_2O_{MQ}. Finally, the gDNA was treated with 1 µg mL^{-1} RNAse (MBiotech) at 37ºC for at least 15 minutes (Ish-Horowicz & Burke, 1981; Bernal-Bayard

et al., 2015). The gDNA samples were quantified with a Nanodrop ND-1000 spectrophotometer (Section 3.2.6).

3.2.3. RNA isolation from *P. tricornutum*

For the isolation of total RNA of the diatom *P. tricornutum*, cell pellets were first frozen in liquid N_2 and crushed in a mortar (Siaut et al., 2007). The dry powder was thoroughly mixed with TRIzol™ Reagent (Thermo Fisher Scientific) and incubated at room temperature (RT) for 5 minutes. Then 200 µL of chloroform:isoamyl alcohol (24:1) was added and the samples were centrifuged at 4°C for 15 minutes at 10,000 x*g*. The aqueous phase was removed to a new microcentrifuge tube and mixed with an equal volume of 70% ethanol. The samples were mixed thoroughly, transferred up to the spin cartridge, previously inserted in the collection tube, of the PureLink® RNA Mini Kit (Ambion™) and centrifuged at 12,000 x*g* for 15 seconds at RT. Then, the flow-through was discarded, and the spin cartridge was reinserted into the same collection tube. Afterwards, for DNA-free total RNA samples, the On-column PureLink® DNase Treatment and Purification Protocol was used (Ambion™), according to the manufacturer's instructions. RNA integrity was verified by electrophoresis in agarose gel (Section 3.2.4) and by an OD_{260}/OD_{280} nm absorption ratio > 1.95 (PfaffI, 2001). Finally, the RNA content of the samples was quantified with a NanoDrop ND-1000 spectrophotometer (Section 3.2.6).

3.2.4. DNA electrophoresis on agarose gels

The separation of DNA fragments was carried out using 0.7 – 2% (w/v) agarose gels prepared in TBE buffer [10.8 g L^{-1} Tris, 5.5 g L^{-1} boric acid, 0.1 M EDTA (pH 8)] (Sambrook & Russell, 2001). To visualize the DNA, the RedSafe™ Nucleic Acid Staining Solution (20,000x; iNtRON Biotechnology, Inc.) was added to the agarose gels. Before loading the samples in the agarose gels, 1/10 DNA loading buffer [60% glycerol, 0.5% bromophenol blue, 0.5% Xylene Cyanol FF] was added to each sample. The electrophoresis was held in a DNA Mini-Sub Cell GT Horizontal Electrophoresis System (Bio-Rad) with TBE buffer, with a voltage of 80 – 120 V for 40 – 60 minutes.

To determine the size of the DNA fragments, 100 pb or 1 kb molecular weight markers (Invitrogen) were used, depending on the size to be determined. After the electrophoresis, gels were illuminated with ultraviolet light (312 nm) and photographed with the Gel Doc XR Imaging System (Bio-Rad) through the Quantity One 4.6.8. software.

3.2.5. Purification of DNA fragments

To purify DNA fragments from agarose gels, the Gel/PCR Purification Mini Kit (Favorgen Biotech Corp.) was used, according to manufacturer's instructions. To purify DNA fragments in solution, the DNA-spin™ Plasmid DNA Purification Kit (Intron Biotechnology) was used, according to manufacturer's instructions.

3.2.6. Nucleic acids quantification

DNA or RNA concentrations were quantified by absorbance measurements at 260 nm, with a NanoDrop ND-1000 spectrophotometer and using the ND-1000 V.3.5.2 software, according to manufacturer's instructions (Sambrook & Russell, 2001; Siaut et al., 2007).

3.2.7. Polymerase Chain Reaction (PCR)

3.2.7.1. Standard PCR

The amplification of DNA fragments was carried out with a T100™ Thermal Cycler (Bio-Rad). The reaction was performed in a final volume of 20 – 50 µL, in a reaction mixture containing 1 – 10 ng of DNA template, 0.2 mM of each deoxyribonucleotide triphosphate (dNTP), 0.5 µM of each oligonucleotide primer and the DNA polymerase with its own buffer. Different pairs of oligonucleotides were used for the genomic PCR analysis (Table 3.8). The isolated gDNA of the diatom *P. tricornutum* or the isolated plasmidic DNA of *E. coli* were used as templates. The amplification program consisted in an initial denaturalization step of 0.5 – 3 minutes at 95°C or 98°C, depending on the DNA polymerase used, followed by 30 – 35 cycles of amplification. Each amplification cycle consisted in a denaturalization step of 30 seconds at 95°C or 98°C, an annealing step of 30 seconds at a different temperature (depending on the oligonucleotides used), and a last step of extension or elongation at 72°C for a certain time, depending on the size of the fragment to amplify and the DNA polymerase used. The program had a final elongation step of 10 minutes at 72°C. The final amplified product was visualized by agarose (0.7%) gel electrophoresis to confirm the expected product size (Section 3.2.4). Different DNA polymerases were used depending on the purpose of each experiment. So, for routine experiments the enzyme MyTaq™ Polymerase (Bioline) was used, whereas the enzyme iProof™ High-Fidelity DNA Polymerase (Bio-Rad) was used for experiments requiring a higher fidelity.

Table 3.8. Oligonucleotides used in this work.

Name	Sequence 5'-3'	Use
pPisipF	TCTCGTGTGGTCATGGGTTG	Forward amplification of a fragment of the promoter isip1 of the isip1::YFP plasmid used for routine PCRs of plasmids with PcE85K
pPisipR	GGCGGACTTGAAGAAGTCGT	Reverse amplification of a fragment of the YFP target of the isip1::YFP plasmid used for routine PCRs of plasmids with PcE85K
pDest_Pc_F	TTGTCTTCGACGAAGACGCC	Forward amplification of a fragment of the PcE85K gene used for routine PCRs of plasmids with PcE85K
pDest_Pc_R	TGTTCGTGCACCATGAGAGC	Reverse amplification of a fragment behind the YFP target of the isip1::YFP plasmid used for routine PCRs of plasmids with PcE85K
Flavo_Tri_F	GCAGTCGAC**ATG**TTTGTCAATACCCATCG	Forward amplification of the *FLDA1* gene with the *Sal*I site and a start codon used to produce Fld antibodies
Flavo_Tri_R	GCACTCGAG**TCA**AAAGAATCCTTCGCTTTTG	Reverse amplification of the *FLDA1* gene with the *Xho*I site and a termination codon used to produce Fld antibodies
CCC_F1	CGTCAGATATCTTGTTGATGG	Forward amplification of a fragment of the promoter isip1 of the isip1::YFP plasmid used for the construction of the pPisip1_pcE85K plasmid
CCC_R1	GCTGGGTC**TTATTA**CTGGAC	Reverse amplification located at the end of *petE* gene with the mutation E85K, including a termination codon, used for the construction of the pPisip1_pcE85K plasmid
CCC_F2	GTCCAG**TAATAA**GACCCAGC	Forward amplification located at the end of the *petE* gene with the mutation E85K, including a termination codon, used for the construction of the pPisip1_pcE85K plasmid
CCC_R2	GCGAAGCACTGCAGGCCG	Reverse amplification located in the middle of the YFP target of the isip1::YFP plasmid used for the construction of the pPisip1_pcE85K plasmid
CCC_F4	ATGCGTTCCTTCTGCATTGCC	Forward amplification of the *petE* gene with the mutation E85K used for the RT-PCR of mutants with the plasmids containing the PcE85K, to check the correct transcription of the gene
CCC_R4	CTGGACAATAATCTTTCCGACCATTC	Reverse amplification of the *petE* gene with the mutation E85K used for the RT-PCR of mutants with the plasmids containing the PcE85K, to

		check the correct transcription of the gene
CCC_F5	TCAACGCCGACGCCATTTC	Forward amplification of the *petE* gene with the mutation E85K used for the qPCR of mutants with the plasmids containing the PcE85K, to check the number of copies of PcE85K
CCC_R5	TGGGGTTTGCAGTAGTATCCGTATT	Reverse amplification of the *petE* gene with the mutation E85K used for the qPCR of mutants with the plasmids containing the PcE85K, to check the number of copies of PcE85K
PsbOqPCR_F	CCAGGAACAGGAAGGCATTGATT	Forward amplification of the *psbO* gene used as control for the qPCR of mutants with the plasmids containing the PcE85K
PsbOqPCR_R	GACGGTAAAAAGGAAAGGAACACG	Reverse amplification of the *psbO* gene used as control for the qPCR of mutants with the plasmids containing the PcE85K
FlavoqPCR_F	TTGGGGATGCTACGAACGAAGAAG	Forward amplification of the *FLDA1* gene used as control for the qPCR of mutants with the plasmids containing the PcE85K
FlavoqPCR_R	TAGAGCCAGTCATCCCACGAGGTT	Reverse amplification of the *FLDA1* gene used as control for the qPCR of mutants with the plasmids containing the PcE85K
C1-F	ATGTTAAAAAAATATTCAAAATTTTGTGCG	Forward amplification of the *psbV* gene of *C. muelleri*. Oligonucleotide designed from *Chaetoceros gracilis* (*C. gracilis*) sequence
C2-R	TTAGTAATAAATTTTTCCACCACCCCAT	Reverse amplification of the *psbV* gene of *C. muelleri*. Oligonucleotide designed from the *C. gracilis* sequence
11-F	CCWGAAGCWTTAAGTTTAGC	Forward amplification of the 3'-end of the *psbV* gene of *I. galbana*. Degenerate oligonucleotide designed from a consensus sequence from *C. gracilis*, *P. tricornutum* and the five closest *psbV* genes (according to a BLAST search)
12-R	GAAAAATGGGGTGGTGGAAAAATTTA	Reverse amplification of the 3'-end of the *psbV* gene of *I. galbana*. Degenerate oligonucleotide designed from a consensus sequence from *C. gracilis*, *P. tricornutum* and the five closest *psbV* genes (according to a BLAST search)
13-F	ATGGCACTAAAAAGTAAATTTTTAGTCG	Forward amplification of the 5'-end of the *psbV* gene of *I. galbana*. Degenerate oligonucleotide designed from the *E. huxleyi* sequence

14-R	TTATCACGGGGCGGGGTTGC	Reverse amplification of the 5'-end of the *psbV* gene of *I. galbana*. Degenerate oligonucleotide designed from the *E. huxleyi* sequence

3.2.7.2. Colony PCR

The amplification of DNA fragments from individual transformants was also carried out using the T100™ Thermal Cycler (Bio-Rad). The reaction was executed in a final volume of 20 µL, in a reaction mixture containing biomass of the selected colony of *P. tricornutum* or *E. coli* as the template source, the enzyme MyTaq ™ Polymerase (Bioline), its own buffer (containing each dNTP, $MgCl_2$ and enhancers at optimal concentrations) and 0.5 µM of each oligonucleotide primer. Different pairs of oligonucleotides were used for the genomic PCR analysis (Table 3.8). The amplification program consisted in an initial denaturalization step of 5 minutes at 95ºC, followed by 30 – 35 cycles of amplification. Each amplification cycle consisted in a denaturalization step of 30 seconds at 95ºC, an annealing step of 30 seconds at a different temperature depending on the oligonucleotides used, and a last step of extension or elongation at 72ºC for a certain time, depending on the size of the fragment to amplify. The program had a final elongation step of 10 minutes at 72ºC. The final amplified product was visualized by agarose (0.7%) gel electrophoresis to confirm the expected product size (Section 3.2.4).

3.2.8. Reverse Transcription PCR (RT-PCR)

Reverse Transcription was used to check the Pc gene transcription in the transformed strains. After RNA extraction (Section 3.2.3), the cDNA of *P. tricornutum* was obtained by using the QuantiTect® Reverse Transcription Kit (Qiagen), following the manufacturer's instructions. The possible DNA contamination in RNA samples was eliminated using the gDNA Wipeout Buffer of the same Kit.

A standard PCR protocol and program were carried out to amplify the cDNA (Section 3.2.7.1). The different pairs of oligonucleotides used are described in Table 3.8.

3.2.9. Quantitative PCR (qPCR)

Real time qPCR was used to determine the number of copies of the Pc gene integrated in the genome of the transformed strains. The qPCR mixtures (final volume 20 µL) contained 1 ng of cDNA obtained after reverse transcription (Section 3.2.8), 250 nM of each oligonucleotide

(forward and reverse), and 10 µL of the iTaq Universal SYBR Green Supermix (Bio-Rad). Reactions were optimised and run in a IQ5 Real-Time PCR Detection System (Bio-Rad), according to manufacturer's instructions. The qPCR started with 3 minutes at 95ºC, followed by 40 cycles of amplification, each one consisting of a step of 10 seconds at 95ºC and a step of 30 seconds at 55 – 60ºC.

3.2.10. Design of synthetic genes

The new synthetic genes were designed with the codon usage of either *E. coli* or *P. tricornutum* and with the restrictions sites required for the subsequent cloning. The codon usages of both organisms were taken from the Codon Usage Database (https://www.kazusa.or.jp/codon/) (Nakamura et al., 2000). The nucleotide sequences of *P. tricornutum* and *C. reinhardtii* chloroplast encoded wild-type (WT) genes were retrieved from the GenBank-NCBI database (National Center for Biotechnology Information: http://www.ncbi.nlm.nih.gov) with the accession numbers EF067920.1 and NC_005353.1, respectively. The amino acid sequences were reversely translated with the online-tool "Reverse Translate" of the Sequence Manipulation Suite (SMS, http://www.bioinformatics.org/sms2/rev_trans.html) (Stothard, 2000). Homology comparisons and prediction of conserved domains were performed using BLAST-N and P (Basic Local Alignment Search Tool; Nucleotide BLAST or Protein BLAST, respectively) programs (https://blast.ncbi.nlm.nih.gov/Blast.cgi). Proteins physical and chemical parameters were predicted using the ProtParam tool of the ExPASy server (http://expasy.ch/tools/protparam.html/). Multiple sequence alignments of nucleotide and predicted protein sequences were carried out with the Clustal Omega program (http://www.ebi.ac.uk/Tools/msa/clustalo/) (Sievers et al., 2011). Synthetic genes were obtained from the Custom Services for Research of GeneCust (France), and the genes were inserted in the pBlueScript II SK (+) or pSpark®I vectors.

3.2.11. Enzymatic manipulation of DNA

3.2.11.1. DNA restriction

Restriction enzymes from New England Biolabs (USA) or Takara (France) were used to excise the fragment of interest from DNA samples. Usually, the restriction reaction was held at 37ºC for 12 – 15 hours, in a final volume of 20 – 50 µL, with 100 – 500 ng of DNA and the

appropriate amount of enzyme, according to manufacturer's instructions. In those occasions when the enzymes were High-Fidelity (HF®) type, the incubation was carried out for 1 – 2 hours. When necessary, the enzymes were inactivated by heating at 65°C or 80°C for 20 minutes in a thermoblock.

3.2.11.2. DNA ligation

The T4 DNA ligase enzyme (Promega) was used for the ligation of DNA fragments. The reaction was held in a final volume of 10 µL with 20 ng of DNA vector and DNA insert, in a 1:5 vector:insert molar ratio. The mixture was supplemented with the buffer, as indicated in the manufacturer's instructions, and with 1 U of the enzyme. Afterwards, the mixture was incubated at 22°C for 2 hours and used for the transformation of *E. coli* (Section 3.3.1).

3.2.12. DNA sequencing

DNA sequencing was carried out by the DNA Sequencing Service of NZYtech (GATC Biotech AG).

3.3. Methods of genetic transformation

3.3.1. *E. coli* transformation

3.3.1.1. *E. coli* DH5α transformation by heat shock

For the transformation by heat shock, 50 – 100 µL of *E. coli* DH5α competent cells, previously thawed on ice, were mixed with DNA (20 – 50 µg) in a maximal volume of 10 µL and incubated on ice for 30 minutes. The mixture was heated without agitation at 42°C for 2 minutes and placed on ice for 5 minutes. Afterwards, 1 mL of LB medium was added to the samples, and they were incubated at 37°C for 1 hour. Finally, the cells were spread gently into a Petri dish with LB agar medium with the appropriate antibiotic and the plates were incubated at 37°C overnight (Hanahan, 1983).

When the plasmid and the *E. coli* strain used allowed the selection of positive clones through the *lacZ* gene interruption, 40 µg mL^{-1} X-gal (5-bromo-4-chloro-3-indolyl-β-D-galactopyranoside) and 0.4 mM IPTG (Isopropyl-β-D-1-thiogalactopyranoside) were added to the medium (Sambrook & Russell, 2001). In this case, positive colonies (transformed with the

plasmid) appeared in white colour, whereas the negative colonies, those which did not have the insert, appeared in blue colour.

The transformation of positive colonies was confirmed by colony PCR (Section 3.2.7.2).

3.3.1.2. *E. coli* BL21 transformation by electroporation

For the transformation by electroporation, 50 – 100 µL of BL21 competent cells, previously thawed on ice, were mixed with DNA (20 – 50 µg) in a maximal volume of 10 µL. The mixture was transferred to an electroporation cuvette of 2 mm of separation between the electrodes (Cell Projects), previously cooled on ice. The electroporation was carried out with a MicroPulser Electroporator (Bio-Rad). Immediately, 1 mL of LB medium was added to the cells and they were incubated at 37°C for 1 hour. Finally, the cells were spread gently into a Petri dish with LB agar medium with the appropriate antibiotic, and the plates were incubated at 37°C overnight (Hanahan, 1983).

The transformation of colonies grown after the overnight incubation was confirmed by colony PCR (Section 3.2.7.2).

3.3.2. *P. tricornutum* transformation by biolistic

The different vectors used in this thesis were introduced into *P. tricornutum* cells by biolistic bombardment using a Biolistic PDS-1000/He Particle Delivery System (Bio-Rad) (Apt et al., 1996; Falciatore et al., 1999). *P. tricornutum* cell cultures were harvested at mid-logarithmic phase (OD_{730nm} of 0.3 to 0.4). Approximately 5 x 10^7 cells were spread on ASW/1% (w/v) agar plates and allowed to dry under a sterile hood. After 24 hours of incubation, cells were co-transfected with the pPha_T1 vector (Table 3.7), to enable selection of transformants with zeocine (InvivoGen), and with the plasmid with the selected gene. M17 tungsten microcarrier particles (1.1 µm diameter; Bio-Rad) were coated with 3 µg of each plasmid DNA (pPha_T1 and the plasmid with the selected gene) using 1.7 µL of 6.2 M spermidine and 50 µL of 2.5 M $CaCl_2$. The particles were washed out twice with ethanol 100% and suspended in a final volume of 80 µL of ethanol 100%. Agar plates containing *P. tricornutum* cells were positioned at level two within the chamber (target distance of 6 cm from the stopping screen) and a burst pressure of 10.7 MPa was used for the bombardment (Apt et al., 1996; Falciatore et al., 1999; Siaut et al., 2007). The cells were then incubated for 48 hours in the dark, before being spread onto new ASW agar plates supplemented with 100 µg mL^{-1} zeocine, 100 µg mL^{-1} Ap, 34 µg mL^{-1} Cm and

100 µg mL^{-1} Sm. The plates were maintained under led white light lamps giving an intensity of 20 µmol m^{-2} s^{-1} under a light/dark cycle of 16/8 h at 20°C (Section 3.1.1.2). Individual resistant colonies appearing 3 – 4 weeks after the bombardment were restreaked on new ASW agar plates containing zeocine.

To determine whether the Pc gene was successfully introduced into the zeocine-resistant colonies, the region containing this gene was amplified by using the cells as a template source (section 3.2.7.2). As a control of the possible effects of the zeocine resistance, an experiment in which *P. tricornutum* cells were transformed only with the zeocine resistance vector (pPha_T1) was also carried out (B1 mutants).

3.4. Methods of manipulation and analysis of proteins

3.4.1. Protein extraction methods

Cells from *P. tricornutum* cultures of 25 – 50 mL were pelleted by centrifugation at 5,000 x*g* for 5 minutes. Subsequently, the cells were washed with TE Buffer (50 mM Tris-HCl, pH 8, 100 mM EDTA), distributed into microcentrifuge tubes and centrifuged at 5,000 x*g* for 5 minutes. Cell pellets were frozen and stored at –20°C until use.

Protein extraction was carried out by following basically the protocol described by Hippmann et al (2017). During protein extraction, all samples and buffers were kept on ice. Proteins were extracted by adding 100 – 150 µL of lysis buffer [50 mM Tris-HCl, pH 7.5, 2% SDS, 10 mM EDTA, and a protease inhibitor cocktail (cOmplete™ ULTRA Tablets, Mini, EDTA-free, *EASYPack*, Roche)] to the frozen pellet. Cells were then incubated at 37°C for 30 minutes with occasional vortexing. Soluble protein fractions were obtained by centrifugation at 15,000 x*g* for 30 min at 4°C and transferred to new microcentrifuge tubes.

3.4.2. Protein quantification methods

Total protein contents were quantified by a modification of the Lowry Method (Lowry et al., 1951; Markwell et al., 1978). Each sample was mixed with H_2O_{MQ} (final volume of 200 µL), supplemented with 50 µL of 0.5 N NaOH and 750 µL of the reagent C (prepared by mixing 100 parts of reagent A [2% Na_2CO_3 (w/v), 0.4% NaOH (w/v), 0.16% sodium tartrate (w/v) and 1% SDS (w/v)] and 1 part of reagent B [4% $CuSO_4 \cdot 5\ H_2O$ (w/v)]). The samples were mixed by vortexing and incubated for 5 minutes at 37°C. A volume of 75 µL of 1:1 diluted Folin-Ciocalteu reagent

(Merck) was then added. Samples were mixed vigorously by vortexing and incubated again for 5 minutes at 37ºC. Finally, absorbances at 750 nm were measured in a JASCO V-650 UV-Vis spectrophotometer.

To determine the protein concentration of each sample, a standard curve was previously established by using samples with known concentrations of bovine serum albumin (BSA).

3.4.3. Protein electrophoresis in SDS-PAGE gels

Proteins were analyzed by denaturing sodium dodecyl sulphate-polyacrylamide gel electrophoresis (SDS-PAGE) as described in Laemmli (1970), using the system Mini-Protean II (Bio-Rad) according to manufacturer's instructions. The separating gel solution contained 1.9 mL of 40% acrylamide/bis-acrylamide (29:1), 1.25 mL of 1.5 M Tris-HCl buffer (pH 8.8) and 1.8 mL H_2O_{MQ}. The stacking gel solution contained 0.5 mL of 40% acrylamide/bis-acrylamide (29:1), 1.25 mL of 0.5 M Tris-HCl buffer (pH 6.8) and 3.2 mL H_2O_{MQ}. The final concentration of polyacrylamide in the separating and stacking gels was 15% and 5%, respectively. Both gel solutions contained 50 µL of 0.1% SDS (w/v), 35 µL of 0.7% ammonium persulfate (APS) (w/v) and 5 µL of 0.1% N,N,N',N'-tetramethylethylenediamine (TEMED) (v/v) as catalysts of the polymerization reaction. Gels were polymerized between two glass plates (10.2 x 7.3 cm) fitted with 1 mm spacers.

The separating gel was first added and, when polymerized, the stacking gel was added until to complete the gel volume. After polymerization, the gel was ready for electrophoresis. Samples were prepared with Laemmli Sample Buffer, in a final volume of 20 µL, and were boiled 5 minutes at 100ºC. The Page Ruler™ Prestained Protein Ladder (Thermo Scientific) was used as the molecular weight marker. The electrophoresis was carried out in a Miniprotean II System (Bio-Rad), filled with running buffer (30 g L^{-1} Tris, 144 g L^{-1} glycine, 10 g L^{-1} SDS) at RT with a constant voltage of 100 – 120 V for 60 – 90 minutes.

3.4.4. Protein gel staining methods

Once the electrophoresis was ended, proteins were stained using Coomassie blue staining solution [450 mL L^{-1} methanol (v/v), 100 mL L^{-1} acetic acid (v/v), 2.5 g Brilliant Blue R (w/v)] (Sambrook & Russell, 2001) for 15 minutes at RT. Then, gels were washed with a destaining solution [40% methanol, 10% acetic acid], shaking gently 1 – 2 hours at RT until a clear

background is obtained. After all this process, protein bands could be visualized in blue colour (Sasse & Gallagher, 2009).

3.4.5. Protein analysis methods

3.4.5.1. Protein purification methods

3.4.5.1.1. Fld purification from *E. coli* transformed cells

For the overproduction and purification of *P. tricornutum* Fld, the pET-28 b_Fld construction was introduced into *E. coli* BL21 (DE3 lalq) (Akazaki et al., 2008; Bernal-Bayard et al., 2015). *E. coli* transformed with the Fld gene was grown overnight at 37°C in 1 L of LB medium (supplemented with 50 µg mL^{-1} Km and 2% glucose), in a rotatory shaker at 200 rpm. Three aliquots of 300 mL of the culture were harvested by centrifugation for 10 minutes at 5,000 x*g* and each pellet was resuspended and diluted 10 times in 3 L of LB medium supplemented with 50 µg mL^{-1} Km. Cell density measurements were made during approximately 1 hour, until the OD_{600nm} was around 0.5 – 0.6. Then, 1 mM of IPTG and 10 µM FMN were added, and the culture was incubated for 3 hours at 37°C. Samples of 1 mL were collected at time 0 h and at 3 h.

The main part of Fld in the cells of *E. coli* was concentrated in the inclusion bodies. Thus, we followed, with minor modifications, protocols previously described for protein purification from the inclusion bodies (Purifying Challenging Proteins, Principles and Methods, Chapter 3: Inclusion Bodies, GE Healthcare Life Science; and Rogl et al., 1998). Cells were first collected by centrifugation for 10 minutes at 5,000 x*g* and resuspended in 50 mL of 20 mM Tris-HCl (pH 8.0), supplemented with DNase, 1 mM of the protease inhibitors phenylmethylsulfonyl fluoride (PMSF), benzamidine, ε-aminocaproic acid, and a tablet of the cOmplete™ Protease Inhibitor Cocktail (Roche), followed by disruption in a French press G-M® model 11 (GlenMills Inc.) at 138 MPa for three rounds. Triton 1% was then added to the lysate followed by centrifugation in a Beckman Coulter® Optima™ XPN 100 ultracentrifuge at 30,000 x*g* for 20 minutes. The pellet was suspended and washed in 20 mM Tris-HCl (pH 8.0) supplemented with Triton 1%. Afterwards, this mixture was centrifuged again at 30,000 x*g* for 20 minutes and the pellet, which contained the inclusion bodies, was collected.

To continue with the Fld purification, the inclusion bodies were solubilized with 50 mM Tris-HCl (pH 8.0) and 8 M urea for 60 minutes at RT. From this point, Fld was purified by FPLC (Fast Protein Liquid Chromatography, IBVF Chromatography Service), by using a HisTrap Fast Flow Crude column (GE Healthcare Life Science). The protein was eluted with a linear gradient

of elution buffer (20 mM Tris-HCl, pH 8.0, 0.5 M NaCl, 0.5 M Imidazole). Protein fractions with an A_{464}/A_{280} ratio close to 1.0 were pooled and dialysed overnight in 20 mM Tris-HCl (pH 8.0) and 10 µM FMN to eliminate the imidazole. The sample was then centrifuged at 30,000 x*g* for 20 minutes, concentrated in an Amicon pressure filtration cell fitted with a 3 kDa cut-off membrane, and finally frozen at –80ºC until use. The purity of the protein was determined by 15% (w/v) polyacrylamide gel electrophoresis (Section 3.4.3), the protein being visualized by Coomassie Blue staining (Section 3.4.4).

3.4.5.1.2. Cc_{550} purification from *P. tricornutum, C. muelleri*, *N. gaditana* and *I. galbana*

For the purification of truncated Cc_{550} from *P. tricornutum,* ≈80 g of frozen paste from Easy Algae (Cádiz, Spain) were resuspended in 300 mL of buffer B [10 mM MES (2-(*N*-morpholino)ethanesulfonic acid), pH 6.5, 2 mM KCl and 5 mM EDTA], supplemented with DNase, 1 mM of the protease inhibitors PMSF, benzamidine and ε-aminocaproic acid, and a tablet of the cOmplete™ Protease Inhibitor Cocktail (Roche). Cells were then broken by three cycles of disruption in a French press at 138 MPa. Unbroken cells were separated by centrifugation at 5,000 x*g* for 5 minutes and the supernatant was centrifuged at 170,000 x*g* for 20 minutes. The resulting supernatant was treated with 0.1 M streptomycin sulfate pH 7, at a final ratio of 1:10 (v/v), gently stirred for 1 hour and allowed to rest for 2 hours. After centrifugation at 12,000 x*g* for 20 minutes, the precipitated material was discarded and the supernatant was first clarified by precipitation with 30% ammonium sulfate, later precipitated with 60% ammonium sulfate, resuspended in Tris-HCl 10 mM, pH 7.5, buffer and dialyzed against the same buffer. From this point, Cc_{550} was purified by FPLC, first by using a DEAE Sepharose® Fast Flow (GE Healthcare Life Sciences) column, from which Cc_{550} was eluted by applying a 0.01-0.2 M NaCl linear gradient in Tris-HCl 10 mM, pH 7.5 buffer, and further by gel filtration using a Sephacryl S-200 HR column (GE Healthcare Life Sciences). Protein fractions with an A_{550}/A_{275} ratio close to 1.0 were pooled, dialyzed against Tris-HCl 10 mM, pH 7.5 buffer, concentrated in an Amicon pressure filtration cell, and finally frozen at –80ºC until use. The concentration of Cc_{550} was calculated using an extinction coefficient at 550 nm of 26 mM^{-1} cm^{-1} for the reduced form (Navarro et al., 1995; Bernal-Bayard et al., 2017).

The purification of the truncated form of Cc_{550} from *C. muelleri*, *N. gaditana* and *I. galbana* cells was carried out from ≈10 g of wet pellets following essentially the protocol described above.

For the purification of the complete Cc_{550} from *P. tricornutum*, wet cell pellets (≈10 g) were first resuspended in 50 mM MES, pH 6.5, 5 mM $MgCl_2$ and 5 mM EDTA buffer (buffer A), supplemented with proteases inhibitors and 1 M betaine, and disrupted three times in a French pressure cell at 104 MPa. Unbroken cells were separated by centrifugation at 5,000 x*g* for 5 minutes and the supernatant was centrifuged at 170,000 x*g* for 30 minutes. The resultant pellet, consisting mainly in thylakoids membranes, was washed twice with the same buffer by centrifugation at 170,000 x*g* as before and resuspended in buffer A supplemented with 0.2 M sucrose at 1 mg Chl mL^{-1}. Cc_{550} was solubilized from this membrane fraction by dilution to 0.5 mg Chl mL^{-1} with the same volume of β-DM (β-dodecyl-maltoside) 3% (w/v), prepared in buffer A, and further incubation during 45 minutes in the dark at 4°C. Samples were then centrifuged at 170,000 x*g* for 30 minutes and the resulting supernatant was loaded onto a continuous density gradient from 0.17 to 0.3 M sucrose, prepared in buffer A plus 0.03% β-DM, and centrifuged at 135,000 x*g* for 16 hours. The complete Cc_{550} (as determined by Mass Spectrometry, Section 3.4.7) was collected from the top gradient band, corresponding to the free protein (Bernal-Bayard et al., 2019).

Protein samples for in-gel peptide fingerprint analysis of *P. tricornutum* Cc_{550} were obtained from crude cell extracts resolved on polyacrylamide gel electrophoresis (Bernal-Bayard et al., 2019). Fresh *P. tricornutum* cells were washed twice in ice-cold PBS 20 mM buffer (pH 8.0), and resuspended in 25 mM Tris–HCl (pH 8.5), 50 mM NaCl buffer, supplemented with 0.5% Triton X-100, DNase and the protease inhibitors PMSF, benzamidine and ε-aminocaproic acid. Samples were incubated for 5 minutes at 70°C followed by a cycle of French-press disruption (138 MPa). Samples were then centrifuged at 170,000 x*g* for 15 minutes. The resultant supernatant was resolved on 20% (w/v) SDS-PAGE and visualized by Coomassie blue staining (Section 3.4.3).

3.4.5.1.3. Antibodies

Polyclonal antibodies raised against *P. tricornutum* Fld and Cc_{550} were generated using standard procedures at the Animal Experimentation Facility (University of Seville, Spain) by subcutaneous injection of 1 mg of purified proteins into a white New Zealand rabbit (Bernal-Bayard et al., 2017; Castell et al., 2021b). Similarly obtained antibodies against *C. reinhardtii* Pc and *P. tricornutum* Cc_6 were already available in the lab (Bernal-Bayard et al., 2015; Roncel et al., 2016), whereas antibodies against D1, PsbO and the RubisCO large subunit were purchased

from Agrisera (products no. AS05 084A, AS06 142-33 and AS03 037, respectively). Finally, antibodies against PsaB were kindly provided by Dr. Anna M. Lindahl (IBVF).

3.4.5.2. Protein quantification methods

3.4.5.2.1. Cc_6, Cc_{550} and Pc determination in *P. tricornutum* cells

The Cc_6 and Pc E85K content in *P. tricornutum* cells were carried out following a modification of the method described in Bernal-Bayard et al. (2017). *P. tricornutum* cells were collected by centrifugation at 5,000 x*g* for 5 minutes. Wet pellets (1 – 3 g) were weighed and resuspended in 20 mL of 20 mM Tris-HCl buffer, pH 7.5, supplemented with DNase and 1 mM of the proteases inhibitors PMSF, benzamidine and ε-aminocaproic acid. At this point, cells were homogenized using a Potter-Elvehjem system and broken by three cycles of French press disruption at 138 MPa. Unbroken cells were separated by centrifugation at 5,000 x*g* for 5 minutes and the supernatant (crude extract) was centrifuged at 170,000 x*g* for 30 minutes. Samples were then clarified by precipitation with 55% ammonium sulfate, further precipitated with 100% ammonium sulfate and finally resuspended in 2 – 3 mL of 20 mM Tris-HCl buffer, pH 7.5. Cc_6 and Pc concentrations were determined in these final solutions by differential absorbance measurements (JASCO V-650 UV-Vis spectrophotometer) between the fully reduced (sodium ascorbate) and fully oxidized (potassium ferricyanide) states at 552 nm (Cc_6, reduced minus oxidized) or 600 nm (Pc, oxidized minus reduced) (Bernal-Bayard et al., 2015; Roncel et al., 2016; Castell et al., 2021b). To reduce interferences from Cc_6 absorbance in the determination of Pc, the concentration of Cc_6 was first determined and an equivalent concentration of purified Cc_6 was used as baseline to measure Pc concentration more precisely (Castell et al., 2021b). The final concentrations of both proteins were calculated using the published differential extinction coefficients of 15 mM^{-1} cm^{-1} at 552 nm for Cc_6 and 4.9 mM^{-1} cm^{-1} at 600 nm for Pc (Navarro et al., 2011; Bernal-Bayard et al., 2015).

The determination of the Cc_{550} content in *P. tricornutum* cells was carried out using as starting point crude extracts obtained as described before. The crude extracts were centrifuged at 170,000 x*g* for 30 minutes, and the resultant supernatants were successively precipitated with 30% and 60% ammonium sulfate. The final pellets of the 60% ammonium sulfate precipitation were resuspended in 2 – 3 mL of 20 mM Tris-HCl buffer, pH 7.5, and the Cc_{550} content was estimated from the absorbance difference at 550 nm between the reduced (sodium dithionite, 1 mM) and oxidized state (in the presence of sodium ascorbate, 1 mM), using a differential extinction coefficient (reduced minus oxidized) of 15 mM^{-1} cm^{-1} at 550 nm (Navarro et al., 1995).

In some cases, a faster alternative method for Cc_6 and Cc_{550} determination in *P. tricornutum* cultures was carried out. A volume of 30 – 100 mL culture was collected by centrifugation at 5,000 x*g* for 5 minutes, resuspended in 1 mL of 10 mM Tris-HCl, pH 7.5, and disrupted by six cycles of freezing in liquid nitrogen and thawing at 25ºC in a thermoblock. Unbroken cells and cell debris were separated by centrifugation at 16,000 x*g* for 10 minutes and the supernatant was collected. The Cc_6 and Cc_{550} content was measured in a JASCO V-650 UV-Vis spectrophotometer as described above.

3.4.5.2.2. Determination of photosynthetic proteins in whole cells and membrane fractions of *P. tricornutum*

To estimate the amount of several photosynthetic proteins in whole cells or associated to membrane (in the case of Cc_{550} and PsbO PSII subunits), *P. tricornutum* cells from 75 mL cultures were collected and resuspended in 25 mL of 50 mM MES, pH 6.5, buffer supplemented with 10 mM $MgCl_2$, 1 M betaine, proteases inhibitors (1 mM) and DNase, and disrupted by three French press cycles at 48 MPa. Unbroken cells were separated by centrifugation at 5000 x*g* for 5 min and the supernatant was centrifuged at 170,000 x*g* for 25 minutes. The resultant supernatant was considered as the soluble fraction, whereas the pellet was resuspended in the same buffer to obtain the membrane extract. The soluble and membrane fractions were used for Western-blot analyses (section 3.4.6).

3.4.6. Immunological detection of proteins by Western-blot analysis

After the protein extracts (2.5 – 30 µg of total protein) were resolved on 15% (w/v) SDS-polyacrylamide gel electrophoresis, as described in section 3.4.3, separated proteins were transferred to a 0.2 µm nitrocellulose membrane included in the Trans-Blot® Turbo™ RTA Midi Nitrocellulose Transfer Kit (Bio-Rad), through the Trans-Blot® Turbo™ Transfer System (Bio-Rad) and following the manufacturer's instructions. Usually, the transfer was carried out by electroblotting following the Mixed MW protocol, defined in the transfer-blot system, with an intensity of 1.3 A for 7 minutes.

After the transfer, the membrane with the proteins was incubated with blocking buffer [5% skimmed milk powder, TBS (20 mM Tris-HCl, pH 7.5, 150 mM NaCl) and 0.1% Tween-20 (v/v)] for 1 hour at RT in a rotatory shaker. Subsequently, the membrane was incubated with blocking buffer overnight at 4ºC in a rotatory shaker with a 1:500 – 1:50000 dilution of the

selected primary antibody. After this step, the membrane was washed out four times for 5 minutes at RT with washing buffer [TBS and 0.1% Tween-20 (v/v)] and incubated with blocking buffer at RT for 1 hour with a 1:10000 dilution of the secondary antibody (Goat Anti-Rabbit IgG [H+L]-HRP Conjugate, from Bio-Rad). The membrane was then washed out again with washing buffer four times for 5 minutes at RT.

Finally, the membrane was treated with the reagents of the kit Immobilon Western Chemiluminescent HRP Substrate (Millipore), according to the manufacturer's instructions, and visualized with a ChemiDoc™ Imaging System (Bio-Rad). In some cases Western-blot bands were quantified using the Quantity One® 1-D analysis software (Bio-Rad), Ponceau total protein stainings being used as loading controls in the immunoblottings.

3.4.7. Matrix-assisted laser desorption/ionization time-of-flight mass spectrometry

Matrix-assisted laser desorption/ionization time-of-flight (MALDI-TOF) mass spectrometry (MS) analyses were performed at the Proteomic Service (IBVF, Seville, Spain), in an Autoflex model analyser (Bruker Daltonics, Germany) operated in lineal (protein molecular weight) or reflector (peptide mass fingerprint) positive modes. Mass spectra were previously calibrated with appropriate standards to the range of mass under study. The molecular weights (MW) of the proteins purified in this work were determined with sinapinic acid as matrix, whereas HCCA (α-cyano-4-hydroxy-cinnamic acid) was used as the matrix for peptide mass fingerprint. Protein samples for in-gel peptide fingerprint analysis were obtained from crude cell extracts resolved on polyacrylamide gel electrophoresis (Section 3.4.5.1.2) by cutting gel slices in the Cc_{550} location zone. Tryptic digestion and BrCN cleavage were carried out as described elsewhere (Sechi & Chait, 1998; Crimmins et al., 2005; Martínez-Fábregas et al., 2014) and the peptide fingerprint was obtained by MALDI-TOF MS. Protein identification was carried out by comparing the obtained peptide fingerprint with the NCBI database using the MASCOT software programs (Bernal-Bayard et al., 2017 & 2019).

3.5. Analytical methods

3.5.1. Methods of pigments determination

Pigments content in the cells of the diatom *P. tricornutum* was determined following a modification of the procedure described in Kong & Price (2020), by acetone extraction and

differential absorbance measurements. A volume of 1 mL of cells was pelleted at 16,000 x*g* for 5 minutes and the supernatant was discarded. The wet pellet was weighed, suspended in 1 mL of acetone 90% (v/v), heated at 70°C for 30 minutes and then incubated overnight in the dark at 4°C to allow pigment extraction. The suspensions were then cleared by centrifugation at 16,000 x*g* for 5 minutes and the Chl and carotenoids concentrations were measured spectrophotometrically (JASCO V-650 UV-Vis spectrophotometer) as follows. The total Chl content in *P. tricornutum* cells was determined according to Arnon (1949). Chl *a* and Chl *c* concentrations were measured using the following equations as described by Jeffrey & Humphrey (1975), whereas carotenoids concentration was determined by the equation given by Strickland & Parsons (1972):

$$\text{Chl } \textit{total} \text{ (mg mL}^{-1}\text{)} = A_{652} / 34.5$$

$$\text{Chl } \textit{a} \text{ (µg mL}^{-1}\text{)} = 11.47 \times (A_{664} - A_{750}) - 0.40 \times (A_{630} - A_{759})$$

$$\text{Chl } \textit{c} \text{ (µg mL}^{-1}\text{)} = 24.34 \times (A_{630} - A_{750}) - 0.40 \times (A_{664} - A_{759})$$

$$\text{Carotenoids (µg mL}^{-1}\text{)} = 7.6 \times [(A_{480} - A_{750}) - 1.49 \times (A_{510} - A_{750})]$$

3.5.2. Redox potential measurements

Redox titrations were performed as described previously (Molina-Heredia et al., 1998; Guerrero et al., 2014), using 10 µM of Cc_{550} purified as described in Section 3.4.5.1.2., in potassium phosphate 50 mM (pH 7) or acetic acid/MES (25:25 mM, pH 5-6) buffers, in the presence of 10 µM of anthraquinone-2-sulfonate, 2-hydroxy-1,4-naphthoquinone and duroquinone as redox mediators. The accuracy of the potential-measuring system was first tested by redox titration of a FMN solution as a standard ($E_{m,7}$ = –220 mV).

3.5.3. Dephosphorylation

The occurrence of protein phosphorylation was investigated by using the Cc_{550} purified as described in Section 3.4.5.1.2. A volume of 15 µL of 1.45 mM Cc_{550} was diluted in 300 µL of H_2O_{MQ}. Then, 50 µL of dephosphorylation solution [10 mM NaCl, 1 $MgCl_2$, 10 µM dithiothreitol (DTT) and 100 µL of alkaline phosphatase (Roche) (or H_2O in the control sample)] were added. The mixture was incubated at 37°C for 30 minutes and diluted in 2.5 mL of H_2O. Finally, the solution was concentrated in a centricon (Merck Millipore Amicon™ Ultra, 3 kDa, centrifugal filter units) and analyzed by MALDI-TOF MS (Section 3.4.3).

3.5.4. Protein sequencing

The N-terminus of purified Cc_{550} was sequenced in a Precise TM 494 Protein Sequencer (Applied Biosystems) at the Protein Chemistry Service (CIB-CSIC, Spain).

3.6. Microscopy analysis

3.6.1. Microscopy

Cells were observed and photographed using a Leica Microscope DM6000 B apparatus (Leica Microsystem) for differential interference contrast (DIC) and fluorescence microscopy. Images were captured with the Leica software and processed with the ImageJ Fiji software (v. 1.46) (Schindelin et al., 2012).

The morphology of WT and transformed cells of *P. tricornutum* was imaged *in vivo* by fluorescence microscopy. Cell volumes and surfaces were calculated from images measurements of longitudinal and transversal cell dimensions from at least 30 cells, and treating *P. tricornutum* as a two cones model (Levy et al., 2008). In addition, cells aspect ratio ([Major Axis]/[Minor Axis]) and circularity (4π x ([Area]/[Perimeter]^2)) shape descriptors were measured with ImageJ Fiji (v. 1.46; Schindelin et al., 2012).

3.6.2. Immunostaining and fluorescence microscopy

To monitor the Pc expression and localization in *P. tricornutum* transformed strains, cells were extended in a slide, let dry and fixed with 70% ethanol for 30 minutes at –20^{o}C. After washing three times for 5 minutes with washing buffer (Section 3.4.6), the cells were blocked with blocking buffer (Section 3.4.6) for 45 minutes. Subsequently, the cells were incubated with rabbit polyclonal anti-Pc antibody for 90 minutes at RT in darkness. Afterwards, the cells were washed again three times for 5 minutes with washing buffer and incubated with anti-rabbit FITC secondary antibody (Sigma), in darkness, for 90 minutes. Then, they were washed three more times for 5 minutes with washing buffer and mounted in mounting buffer (6 mL 100% glycerol, 1 mL 10x TBS, 2 mL H_2O) (Szabo & Colman, 2007). Finally, the coverslip was placed in the slide and the immunolabelling was performed using a Leica Microscope DM6000 B (Section 3.6.1.).

3.6.3. Flow cytometry

Flow cytometry experiments were carried out in the Flow Cytometry Core Unit of the Centro Andaluz de Biología Molecular y Medicina Regenerativa (CABIMER, Seville, Spain), by using a FACSCalibur cytometer equipped with an argon-ion laser (488 nm) and the CellQuest Pro software (Becton Dickinson, USA). Forward scatter (FSC), side scatter (SSC) and fluorescent signal detectors allowed to simultaneously determine mean values per count, corresponding respectively to cell size, internal complexity and chlorophyll fluorescence parameters (Franklin et al., 2001). 10^4 cells were analyzed in each experiment.

3.7. Biophysical methods

3.7.1. Time-resolved *c*-type cytochromes oxidation/reduction measurements by an optical parametric oscillator

The time-resolved oxidation/reduction of *c*-type cytochromes in *P. tricornutum* cells was measured *in vivo* at 420 nm using a home-built Optical Parametric Oscillator-based spectrophotometer (OPO), in the 1 to 500 milliseconds range. At this wavelength there is an optical contribution of P_{700}, but after 1 millisecond post-flash P_{700} is completely rereduced and the 420 nm signal corresponds mainly to *c*-type cytochromes. This spectrophotometer is able to measure *in vivo* small absorbance changes in a time window ranging from 10 nanoseconds to 100 seconds (Bailleul et al., 2015; Viola et al., 2019). In this equipment, whose operating principle is a frequency conversion process called parametric optical amplification, the monochromatic flashes are produced by an OPO pumped by the third harmonic of a pulsed Nd:Yag laser (6 nanoseconds pulse duration), providing continuously tunable flashes in a wide range of wavelengths (Joliot et al., 1998; Bailleul et al., 2015). These experiments were carried out at the Laboratory of Computational and Quantitative Biology (Institute de Biologie, Sorbonne University, Paris), during a stay in the group of Prof. Angela Falciatore and under the supervision of Dr. Benjamin Bailleul.

3.7.2. Thermoluminescence

Thermoluminescence (TL) glow curves of *P. tricornutum* cell suspensions were obtained using a home-built apparatus designed by Dr. Jean-Marc Ducruet for luminescence detection from 1°C to 80°C (standard thermoluminescence, STL) and from 20°C to 160°C (high temperature thermoluminescence, HTL). A detailed description of the system can be obtained elsewhere

(Roncel et al., 2016; García-Calderón et al., 2019; Castell et al., 2021b). Temperature regulation, signal recording and flash sequences were driven by a computer through a National Instrument DAQ-Pad1200 interface, using a specific acquisition program developed by Dr. Ducruet. An electrically insulated resistor heater (Thermocoax), powered by a variable (0 to 5 A) computer-driven power supply, was mounted below the chamber for temperature regulation. Luminescence emissions were detected by a H5701-50 Hamamatsu photomultiplier module. Illumination was performed through a light guide parallel to the photomultiplier, both of them being attached to the same stand sliding horizontally from the illumination to the measuring position. Single turnover flashes were provided by a xenon white light lamp (Walz XST-103).

STL and HTL measurements were carried out basically as described in Roncel et al. (2016) and Castell et al. (2021b). TL experiments were carried out in parallel cultures for each strain under iron-replete and iron-deficient conditions. Most of the experiments were performed using cultures with a cellular concentration of ≈1.5 x 10^8 and ≈5 x 10^7 cells mL^{-1} for STL and HTL, respectively. For STL measurements, cultures were dark-incubated for 2 minutes at 20ºC, then cooled to 1ºC for 1 minute and illuminated at the end of this period with different numbers of saturating single turnover flashes (separated by 1 second). Luminescence emission was then recorded while warming samples from 1 to 80ºC at a heating rate of 0.5ºC per second. For HTL measurements, cultures were filtered in Millipore filters of 0.45 µm, that were pressed against a copper film and dark-incubated for 10 minutes at 20ºC under N_2 atmosphere. Luminescence emission was then recorded whilst warming samples from 20 to 160ºC at a heating rate of 0.1ºC per second. N_2 gas was flushed on the sample during HTL experiments in order to desiccate samples and prevent any oxidation induced by high temperatures.

Data acquisition, signal analysis and graphical simulation were performed as previously described (Ducruet & Miranda, 1992; Zurita et al., 2005; Ducruet et al., 2011).

3.7.3. Photosynthetic measurements

To study photosynthetic global activity, cells from different cultures were collected by centrifugation and resuspended in fresh ASW medium. Oxygen intake or evolution was then determined in 2.5 mL samples by using a Clark-type oxygen electrode (Oxylab$^+$, Hansatech) at 20ºC, both in the dark and under illumination (176 µmol m^{-2} s^{-1}), to establish the net photosynthetic activity per cell. In some cases, the cells from different culture conditions were resuspended to a similar cell density for the oxygen intake or evolution experiments, in order to compare net photosynthetic activity per cell.

The Chl *a* fluorescence of PSII and the redox state of P_{700} from intact cells were determined at RT using a pulse-amplitude modulation fluorometer (DUAL-PAM-100, Walz, Effeltrich, Germany). The photosynthetic parameters were obtained from five independent experiments. Prior to measurements, cell suspensions with a cellular concentration of 1.1 x 10^8 cells mL^{-1} were dark adapted for 30 minutes. The maximum quantum yield of PSII was assayed after incubation of the cell suspension in the dark for 30 minutes by calculating the ratio of the variable fluorescence, F_v (F_m - F_o), to maximal fluorescence, F_m, (F_v/F_m). Relative linear electron transport rates (rETR) were determined in pre-illuminated cell suspensions applying stepwise increasing red actinic light (635 nm) intensities up to 1292 µmol m^{-2} s^{-1}. The effective PSII quantum yield, Y(II), for each actinic light intensity was measured using saturating pulses of red light at 10,000 µmol m^{-2} s^{-1} intensity and 0.6 seconds duration. Y(II) and rETR values were calculated by the DUAL-PAM-100 software, according to the equations by Kramer et al. (2004).

The relative PSII content of cells on a chloropyll basis was estimated from the total yield of variable chlorophyll a fluorescence (F_v= F_m– F_0). F_o (minimum fluorescence in dark adapted state) was measured when Q_A is fully oxidized (achieved by incubating cells in darkness with *p*-benzoquinone and ferricyanide). F_m was determined when Q_A is fully reduced [achieved by illuminating cells in the presence of 3-(3,4-dichlorophenyl)-1,1-dimethylurea (DCMU)] and an exogenous electron donor such hydroxylamine). The samples were incubated in darkness for 30 minutes and afterwards it was followed an incubation step with 0.3 mM *p*-benzoquinone and 1 mM ferricyanide for 5 minutes. DCMU was then added up to a concentration of 40 µM and incubated for 1 minute in darkness. Then, hydroxylamine was added to a concentration of 20 mM from a freshly-made 1 M stock solution (pH 6.5). The fluorescence measuring light was turn on 20 seconds after the last addition to record F_0. Later, F_m was determined after one single saturating flash. The difference between F_m - F_0 was used as a measure of the relative PSII content in the cells (Chu et al., 1994; Hung et al., 2007).

The redox state of P_{700} was monitored by following the changes in absorbance at 830 nm versus 875 nm in cells dark-adapted for 30 minutes prior to measurements. Most of the experiments were carried out using cultures with a cellular concentration of ≈5.5 x 10^7 and ≈4.5 x 10^8 cells mL^{-1} for iron-replete and iron-deplete cultures, respectively. The level of maximal P_{700}^+ signal observed upon P_{700} full oxidation, P_m, was determined by pre-illumination of cell suspensions with far-led light (730 nm) for 10 seconds. Thereafter a saturating pulse of red light (635 nm) at 10,000 µmol m^{-2} s^{-1} intensity was applied during 0.2 seconds. Following P_m determinations, P_{700}^+ reduction kinetic decays were recorded in darkness. The average of at least three individual traces from different cultures was taken. The half-life time ($t_{1/2}$) of the P_{700}^+

absorption decay was determined by fitting the curves to a single exponential function. The quantum yields of PSI photochemistry, Y(I), donor side limitations, Y(ND), and acceptor side limitations, Y(NA), were measured by the DUAL-PAM-100 software (Roncel et al., 2016; Castell et al., 2021b).

3.8. Bioinformatics analyses

3.8.1. Molecular structures and modelling

Molecular structures were visualized with the ICM-Browser (Molsoft ICM Browser Software) (Abagyan et al., 2006) or the UCSF Chimera (http://www.rbvi.ucsf.edu/chimera/) (Pettersen et al., 2004) programs.

All the sequence alignments were performed using BLAST (Altschul et al., 1990) and ClustalW (Sievers et al., 2011).

The 3D structure of *P. tricornutum* Cc_6 was obtained from the Protein Data Bank, PDB code: 3dmi (Akazaki et al., 2009). Homology models were built in this work as described in Castell et al. (2021a) by using MODELLER version 9v23 (Sali & Blundell, 1993; https://salilab.org/modeller/) with default settings (Eswar et al., 2007). The Cf truncated forms of *P. tricornutum* (UniProtKB-A0T0C9 CYF_PHATC) and *T. oceanica* (UniProtKB-E7BWE1_THAOC) were modelled based on the X-ray structure of the Cf truncated form of *C. reinhardtii* (PDB code, 1cfm), with which they share 58.2% and 44.6% sequence identity, respectively. The coordinates for the cofactors (heme and Cu ion) were taken from the template structures. The structure of the small domain deletion variant of *P. tricornutum* Cf was generated by removing residues 171–229 from the intact protein structure with the ICM Browser Software (http://www.molsoft.com) (Abagyan et al., 2006).

The structure of *T. oceanica* Pc, corresponding to the theoretical Pc-translated sequence (UniProtKB-D2Z0I2_THAOC), was modelled based on the X-ray structure of the Pc from *C. reinhardtii* (PDB code, 2plt), with which they share 53% sequence identity.

The different Cc_{550} structures from *P. tricornutum* (UniProtKB-A0T0C6 CYC550_PHATC), *I. galbana* (UniProtKB-A0A3G2CHS9_ISOGA), *N. gaditana* (UniProtKB-K9ZXJ9_9STRA) and *C. muelleri* (UniProtKB-A0A3G2CHW3_9STRA) were modelled based on the X-ray crystal structure of the Cc_{550} from the red alga *Cyanidium caldarium* (*C. caldarium*) (PDB code, 4yuu).

A total of 100 homology models were built and the model with the best DOPE (Discrete Optimized Protein Energy) score was finally selected (Shen & Sali, 2006) as previously described in Bernal-Bayard et al. (2015). Representation of the protein surface electrostatic potentials was performed using the UCSF Chimera program. The Cu atom in Pc was assigned a charge of +2, whereas the heme charges for both Cf and Cc_6 (–2) were assigned as: Fe (+2), two ring nitrogen atoms (–1 each), and the two propionic acid side chains (–1 each) (Haddadian & Gross, 2006).

3.8.2. Protein-protein docking simulations

3.8.2.1. Docking simulations

Protein-protein docking simulations were performed by the pyDock scheme (Cheng et al., 2007; Jiménez-García et al., 2013), as previously described (Bernal-Bayard et al., 2015). A total of 10,000 rigid-body docking poses were generated by FTDock (Gabb et al., 1997), and evaluated by the energy-based pyDock 3.0 scoring function (Cheng et al., 2007; Jiménez-García et al., 2013), based on desolvation and electrostatics, with limited van der Waals energy contribution. Cofactors and ions were both included during the FTDock sampling and the pyDock scoring calculations. For this, AMBER topology files were built with the AmberTools package and the LEaP program (Case et al., 2019). The heme atomic coordinates were downloaded from the supplementary data of Shahrokh et al. (2012) and they were translated into a common frame of reference and saved with the UCSF Chimera program. The mass and the non-bonded parameters from the iron (frcmod.hemall file) were extracted from the AMBER Parameter Database (https://personalpages.manchester.ac.uk/staff/Richard.Bryce/amber/cof/frcmod.hemall) adapted from previously reported parameters (Giammona, 1984). When required, incomplete side chains were built with SCWRL 3.0, an efficient program for the prediction of protein side chain conformations (Canutescu et al., 2003).

Atomic distances and clashes were computed with the ICM-Browser program (Molsoft ICM Browser Software) (Abagyan et al., 2006). Protein surface electrostatic potential was calculated with the UCSF Chimera program, based on Coulomb's electrostatics with default parameters.

3.8.2.2. Normalized Interface Propensity (NIP)

All docking poses were ranked together, based on an optimised scoring function formed by electrostatics and desolvation energy, as implemented in the pyDock algorithm. All the

solutions were analyzed by patch prediction (pyDockNIP), which is an implementation of a method able to predict interface propensities from the distribution of docking poses. The NIP (Normalized Interface Propensity) value represents the frequency of a given residue to be located at the interface among the 100 lowest-energy solutions of docking. A NIP value of 1 would indicate that the corresponding residue is involved in all predicted interfaces of the docking solutions, meanwhile a value of 0 would mean that it appears as expected by a random distribution. A negative value would mean that the residue appears at the interface less often than expected by random. Those residues with NIP values higher or equal to 0.2 were those that appear significantly more often than expected by random (Grosdidier & Fernández-Recio, 2008).

3.8.2.3. Minimization of the protein-protein docking poses

In order to improve the quality of the docking models and reduce their interatomic clashes, they were minimized with the Sander program from AMBER (Case et al., 2019), using AMBER ff99SB and GAFF force field parameters (Cheatham et al., 1999), with implicit solvent. The protocol consisted in a 300-cycle steepest descent (SD) minimization, with harmonic restrains applying a force constant of 1000 kcal (mol $Å^2$)$^{-1}$ to the heme group and the coordinated atoms (Fe, Cu) and residues (Tyr, His, and Cys) to optimize the coordination states and the side chain conformations, followed by a 500-cycle conjugate gradient (CG) minimization with the same harmonic restrains.

4. Results

4.1. Chapter I

The photosynthetic cytochrome c_{550} from the diatom *Phaeodactylum tricornutum*

4. Results

4.1. Chapter I. The photosynthetic cytochrome c_{550} from the diatom *Phaeodactylum tricornutum*

4.1.1. Characterization of a truncated form of Cc_{550}

It was established previously in the group (Bernal-Bayard et al., 2017) that the Cc_{550} from *P. tricornutum* could be obtained as a modified form, with a lower MW than expected from the gene sequence, indicating some type of protein modification. The Cc_{550} purified from *P. tricornutum* presents a MW value of ca. 15.110 Da as analyzed by MALDI-TOF (Bernal-Bayard et al., 2017; and Figure 4.2). After subtracting the mass of the heme group (616 Da), a MW of ca. 14,495 Da for the polypeptide chain was consequently deduced. This value is lower than the theoretical value inferred from the *psbV* gene sequence (ca. 14,822 Da for the polypeptide chain, and 15,438 Da for the heme containing holoprotein). The modified Cc_{550} not only appeared as the final purified protein, but also in the initial clarified crude extract from the purification process (Bernal-Bayard et al., 2017). Actually, no MS signal corresponding to the theoretical sequence was detected in any case. In this work, the modified/truncated form of Cc_{550} was purified from *P. tricornutum* cells following the protocol described in section 3.4.5.1.2, and some of its physicochemical properties, as well as the nature of the protein modification, have been determined.

Visible absorption spectra of purified Cc_{550}, both in the native oxidized and dithionite reduced forms, showed absorption bands (549.5, 521 and 417 nm, reduced; 405.5 and 528.5 nm, oxidized) similar to those previously described for Cc_{550} (Shimazaki et al., 1978; Navarro et al., 1995) (Figure 4.1). The absorbance ratio A_{275} (oxidized)/A_{550} (reduced) was 1.07 for the final purest protein samples obtained. Redox titration of the *P. tricornutum* Cc_{550} established a midpoint redox potential ($E_{m,7}$) value of –190 ± 12 mV (Figure 4.1) which did not significantly change in the pH range 5–7 (data not shown). This potential value, although maintaining the typical negative redox potential of this protein, is significantly more positive than those described in cyanobacteria for Cc_{550} in solution (–250 to –300 mV) (Navarro et al., 1995; Roncel et al., 2003; Guerrero et al., 2011).

The determined MW of the purified protein agrees with a truncated protein in the two last tyrosine residues of the C-terminus (14,495.5 Da for the polypeptide chain and ca. 15,111 Da for the holoprotein). Even a smaller band of much lower intensity was also identified, whose MW (14,997.6 Da) could fit with an additional small fraction of a truncated protein in the last three residues of the C-terminus (14,998.4 Da for the polypeptide chain) (Figures 4.2 and 4.3).

However, other modifications of the protein are also possible, as it could be an alternative processing of the N-terminus and/or specific protein chemical modifications. Taking into account these different possibilities, various experiments have been further carried out with the purified protein in order to confirm the nature of the changes resulting in the modified protein.

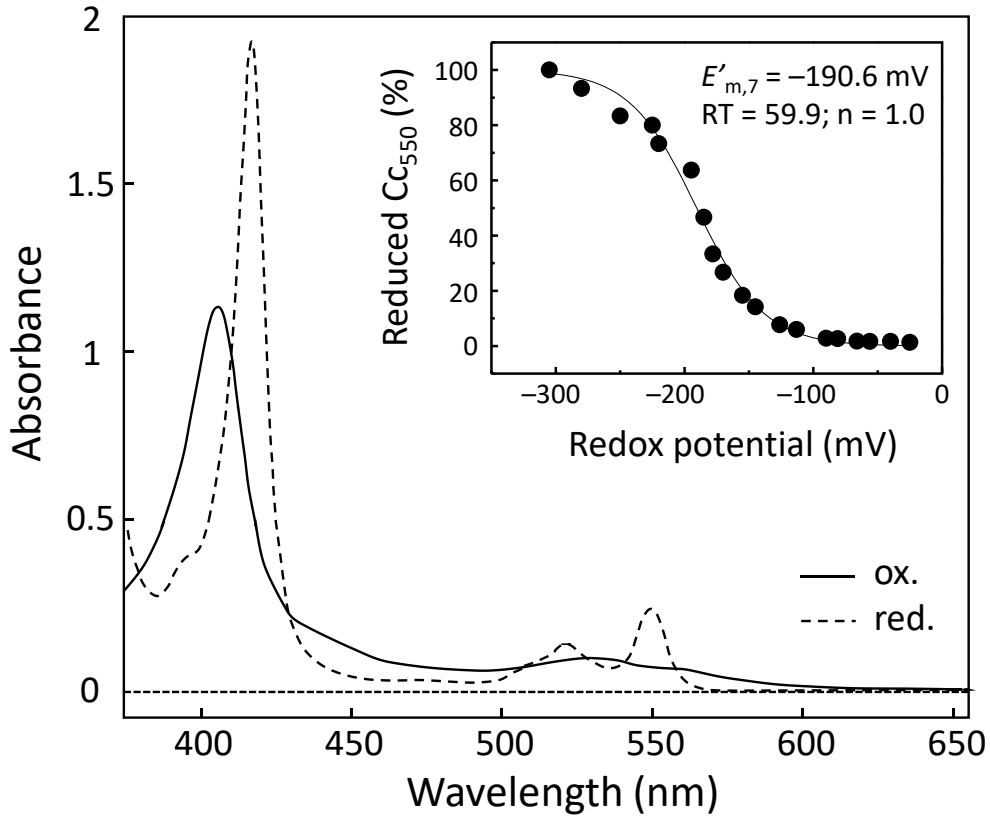

Figure 4.1. Absorption spectra of purified cytochrome c_{550} from *P. tricornutum* in its oxidized form and after reduction with dithionite. Oxidized form is shown in continuous line; reduced form in dashed line. (Inset) Reductive potentiometric redox titration of purified Cc_{550} in potassium phosphate 50 mM, pH 7, buffer. Continuous line corresponds to the theoretical fit according to the Nernst equation and n = 1. In all cases the concentration of the protein was 10 µM.

First, in order to explore possible deviations from the theoretical protein sequence due to the processing of the target transit-peptide, we started by sequencing the N-terminal part of the purified Cc_{550}. However, this N-terminal part showed the correct sequence according to the predicted processing of the *psbV* gene (`IDLDEATRTV`, Figure 4.2).

Experimental MW = 15,110 Da

Theoretical protein sequence:

IDLDEATRTV VVDSSGKTIV LTPEQVKRGK RLFNATCGAC
HVGGVTKTNP NVGLDPEALS LATPRRDNIA GLVDFLKNPT
TYDGLESIAE VHPSIKSADI YPRMRSVTDE DLTAMAGHIL
LQPKIVTEKW GGGKIYY

Complete protein	**MW = 15,438 Da; *psbV* gene sequence**
LQPKIVTEKW GGGKI	**MW = 15,111 Da; truncated 2-C-terminal**
LQPKIVTEKW GGGK	**MW = 14,998 Da; truncated 3-C-terminal**

Figure 4.2. Different molecular weights of cytochrome c_{550}. (Upper) Experimental MW of the purified Cc_{550}. (Middle) Protein sequence of *P. tricornutum* Cc_{550} as translated from the *psbV* gene. (Lower) Theoretical MW of the complete protein and of different predicted truncated forms, according to the indicated C-terminus.

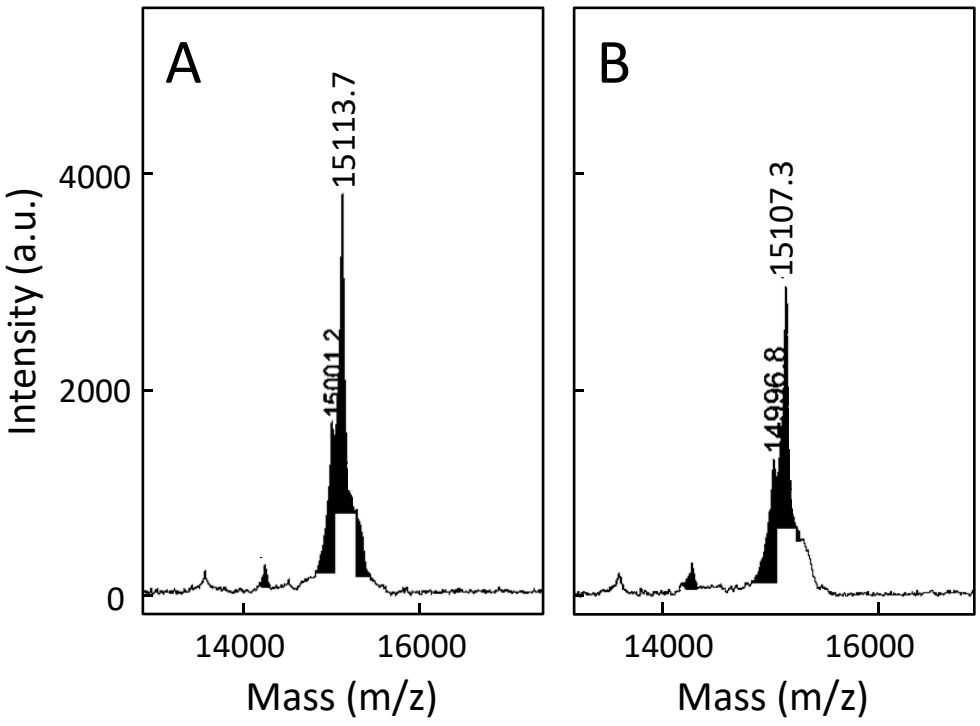

Figure 4.3. MALDI-TOF analysis of the molecular weight of cytochrome c_{550} in samples subjected to dephosphorylation. (A) No treatment. (B) Sample treated with phosphatase.

To discard protein chemical modifications that could modify the MW of purified Cc_{550}, dephosphorylation experiments were carried out to check the occurrence of this alteration. As it is shown in Figure 4.3, there was no difference in the MW between the control sample and the sample treated with phosphatase, indicating that no such post-translational modification was present in the protein.

A

IDLDEATRTV VVDSSGKTIV LTPEQVKRGK RLFNATCGAC HVGGVTKTNP
NVGLDPEALS LATPRRDNIA GLVDFLKNPT TYDGLESIAE VHPSIKSADI
YPR**M**RSVTDE DLTA**M**AGHIL LQPKIVTEKW GGGKIYY

B

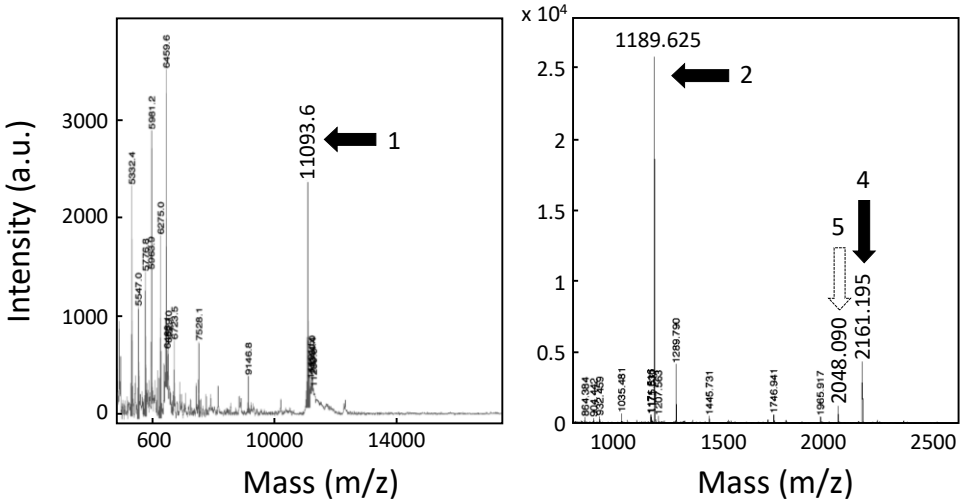

C

1. IDLDEATRTV VVDSSGKTIV LTPEQVKRGK RLFNATCGAC HVGGVTKTNP
   NVGLDPEALS LATPRRDNIA GLVDFLKNPT TYDGLESIAE VHPSIKSADI
   YPRM
2. RSVTDE DLTAM
3. AGHIL LQPKIVTEKW GGGKIYY
4. AGHIL LQPKIVTEKW GGGKI
5. AGHIL LQPKIVTEKW GGGK

Figure 4.4. BrCN cleavage and peptide analysis of cytochrome c_{550} purified from *P. tricornutum.* (A) Theoretical protein sequence as deduced from the translation of the *psbV* gene. Methionine targets for BrCN are underlined. (B) Molecular weight MS-analysis of the different peptides obtained after BrCN digestion of Cc_{550}. Arrows indicate the peptides fitting the expected results from the digestion of the truncated Cc_{550}. (C) Expected main peptides from the Cc_{550} cleavage by BrCN in methionine positions, either in the theoretical complete protein (1–3) or the truncated form (1, 2, 4, 5). Peptide 3 was not detected.

To study more accurately which forms of Cc_{550} were present in the purified samples, a trypsin or BrCN cleavage and further peptide analysis by MALDI-TOF was carried out. Tryptic

digestion and peptide analysis unequivocally identified the sample as the pure Cc_{550} protein, without the observation of additional peptides arising from alternative proteins (data not shown). However, the presence of lysines 129 and 134 in Cc_{550} (targets for trypsin; Figure 4.4A) prevented the possible identification of the protein C-terminus part when using this protease, due to the small size of the peptides rendered, and thus BrCN was alternatively used. BrCN cleavage allowed the identification of peptides covering residues 1–115, but the expected peptide corresponding to the 116–137 residues in the C-terminus (peptide 3, MW = 2,471.9 Da) was absent. Conversely, peptides compatible with the lack of the 2–3 C-terminus groups appeared (Figure 4.4), although peptide 5 is sensibly less abundant, thus confirming the occurrence of C-terminus truncated species.

Names	Confidence	Sequence
Cytochrome c-550 OS=Phaeodactylum tricornutum	99,00	IDLDEATRTVVVDSSGK
Cytochrome c-550 OS=Phaeodactylum tricornutum	99,00	IDLDEATRTVVVDSSGKTIVLTPEQVK
Cytochrome c-550 OS=Phaeodactylum tricornutum	99,00	IDLDEATRTVVVDSSGKTIVLTPEQVKR
Cytochrome c-550 OS=Phaeodactylum tricornutum	99,00	IVTEKWGGGKIYY ←
Cytochrome c-550 OS=Phaeodactylum tricornutum	99,00	LFNATCGACHVGGVTK
Cytochrome c-550 OS=Phaeodactylum tricornutum	99,00	MRSVTDEDLTAMAGHILLQPK
Cytochrome c-550 OS=Phaeodactylum tricornutum	99,00	NPTTYDGLESIAEVHPSIK
Cytochrome c-550 OS=Phaeodactylum tricornutum	99,00	RDNIAGLVDFLK
Cytochrome c-550 OS=Phaeodactylum tricornutum	99,00	RLFNATCGACHVGGVTK
Cytochrome c-550 OS=Phaeodactylum tricornutum	99,00	SVTDEDLTAMAGHILLQPK
Cytochrome c-550 OS=Phaeodactylum tricornutum	99,00	TDEDLTAMAGHILLQPK
Cytochrome c-550 OS=Phaeodactylum tricornutum	99,00	TIVLTPEQVK
Cytochrome c-550 OS=Phaeodactylum tricornutum	99,00	TIVLTPEQVKR
Cytochrome c-550 OS=Phaeodactylum tricornutum	99,00	TIVLTPEQVKRGK
Cytochrome c-550 OS=Phaeodactylum tricornutum	99,00	TNPNVGLDPEALSLATPR
Cytochrome c-550 OS=Phaeodactylum tricornutum	99,00	TNPNVGLDPEALSLATPRR
Cytochrome c-550 OS=Phaeodactylum tricornutum	99,00	TVVVDSSGKTIVLTPEQVK
Cytochrome c-550 OS=Phaeodactylum tricornutum	99,00	TVVVDSSGKTIVLTPEQVKR
Cytochrome c-550 OS=Phaeodactylum tricornutum	98,52	SADIYPR
Cytochrome c-550 OS=Phaeodactylum tricornutum	99,00	VTEKWGGGKIYY ←
Cytochrome c-550 OS=Phaeodactylum tricornutum	99,00	PEALSLATPR
Cytochrome c-550 OS=Phaeodactylum tricornutum	76,45	SADIYPRMR
Cytochrome c-550 OS=Phaeodactylum tricornutum	99,00	TEKWGGGKIYY ←

Figure 4.5. Summary for the in-gel peptide fingerprint analysis of *P. tricornutum* cytochrome c_{550} obtained from crude cell extracts resolved on polyacrylamide gel electrophoresis. Only the peptides that have contributed to the protein identification are shown, which cover 100% of the cytochrome mature protein. Arrows indicate peptide fitting for a complete (no truncated) C-terminal end. Peptides corresponding to the truncated protein could not be correctly fitted to the obtained data.

A truncated form could be the result of a specific physiological protein modification or can be caused by the exposure of Cc_{550} to cellular proteases during the purification procedure. As stated above, no MS signal corresponding to the theoretical sequence was detected in any case in different cell extracts from *P. tricornutum*, including the protein obtained from detergent extraction of membrane fractions (Bernal-Bayard et al., 2017). Therefore, a fast method was here carried out to check if the truncated species is the physiological form of Cc_{550}. To shorten the process of protein separation as much as possible, crude cell extracts from *P. tricornutum* cells heated at 70°C, in order to inactivate possible proteolytic enzymes, were directly resolved on polyacrylamide gel electrophoresis. Extracted gel spots in the MW range corresponding to Cc_{550} were analyzed by tryptic digestion and MW peptide fingerprint (Figure 4.5). The fingerprint peptide analysis accurately covered 100% of the amino acid sequence corresponding to the complete non-truncated protein, whereas the theoretical peptide fingerprint for the truncated protein could not be correctly fitted to the obtained data (Figure 4.5). These data indicate that the truncation of Cc_{550} is a non-physiological process.

4.1.2. Design of a protocol for the purification of the complete Cc_{550}

The truncated form of Cc_{550} was purified as a soluble protein from whole crude extracts of broken cells (Bernal-Bayard et al., 2017), thus exposing the protein to cell proteases. Consequently, we designed a protocol for the purification of Cc_{550} from membrane fractions. A complete cocktail of protease inhibitors, including specific inhibitors for carboxypeptidase, was added to the breaking buffer, as well as 1 M betaine to stabilize the Cc_{550} binding to PSII (see section 3.4.5.1.2). After detergent solubilization of the separated membrane fraction, the solubilized supernatant was loaded onto a sucrose gradient and the free protein was isolated from the top of this gradient and identified by its differential absorption spectrum (Figure 4.6A). The MALDI-TOF MW analysis of the solubilized Cc_{550} showed a MW (approximately 15,433 Da) that confirmed the obtention of the complete protein (MW deduced from the *psbV* gene sequence = 15,438 Da; Figure 4.6B).

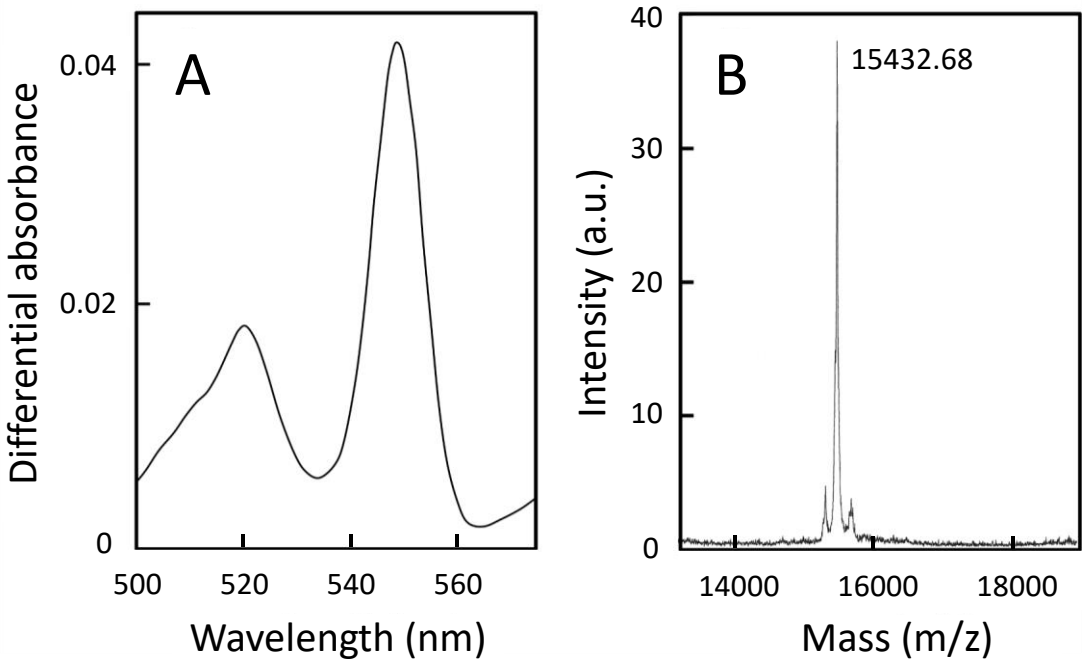

Figure 4.6. Differential absorption spectrum and molecular weight MS analysis of cytochrome c_{550}. (A) Differential absorption spectrum (dithionite minus ascorbate) of Cc_{550} from *P. tricornutum* extracted by solubilization from membrane fractions. The concentration of cytochrome was 3 μM. (B) Molecular weight MS analysis of the complete holocytochrome.

Remarkably, the enzymatic activity responsible of Cc_{550} truncation seems to be widespread among several lines of the red lineage of eukaryotic algae, as truncated Cc_{550} forms were purified from *C. muelleri* (a marine centric diatom), *N. gaditana* (Eustigmatophyte) and *I. galbana* (Haptophyte, Isochrysidales). However, this activity seems to be absent in cyanobacteria, as Cc_{550} from *Synechocystis* sp. PCC 6803, used as a control, showed the expected MW for the complete protein (Table 4.1).

In the case of *C. muelleri* and *I. galbana*, previous sequencing of their *psbV* genes was required in order to establish the MW of both complete proteins. The sequencing of these genes was carried out after PCR amplification using degenerate oligonucleotides designed from a consensus sequence from several *psbV* genes (Table 3.8, Section 3.2.7.1). The *C. muelleri psbV* gene showed only 11 nucleotide variations as compared with the already reported gene of *C. gracilis*, but this resulted only in two amino acid changes in the protein transit peptide (not shown). The *I. galbana psbV* gene showed 83% identity with the equivalent gene of the also Isochrysidal alga *E. huxleyi*, and the protein alignment (94% identity) is shown in Figure 4.7.

Table 4.1. Molecular weight of cytochrome c_{550} and cytochrome c_6 of different strains of microalgae, measured by MALDI-TOF MS analyses.

	Experimental MW	Theoretical MW	MW (–YY)	MW (–IYY)
***I. galbana* Cc_6**	9,678 (–616) = 9,062	9,037	--	--
***I. galbana* Cc_{550}**	15,172 (–616) = 14,556	14,964	14,637	**14,557**[b]
***C. muelleri* Cc_6**	9,889 (–616) = 9,273	9,273	--	--
***C. muelleri* Cc_{550} (1)**[a]	15,164 (–616) = 14,548	14,876	**14,549**	14,436
***C. muelleri* Cc_{550} (2)**	15,052 (–616) = 14,436	14,876	14,549	**14,436**
***N. gaditana* Cc_6**	9,850 (–616) = 9,234	9,234	--	--
***N. gaditana* Cc_{550}**	15,186 (–616) = 14,570	15,010	14,684	**14,571**
***Synechocystis* Cc_{550}**	15,737 (–616) = 15,121	15,120	--	--

[a]The number indicates the order of peaks found in the same experiment. [b]Considering an oxidation modification (+32).

```
I. galbana      LELDEDTRTVTLDPKGNTVVLSVEQIKRGKRLFNNACAICHVGGLTKTNPNVGLDVEALS
E. huxleyi      LELDEDTRTVTLDGKGNTVVLSVEQIKRGKRLFNNACAICHVGGLTKTNPNVGLDVEALS
                ************* **********************************************

I. galbana      LATPPRDNIANLVAYLKDPMTYDGADSIAELHPSIKSADIFPKMRSLTDEDLFAISGHIL
E. huxleyi      LATPPRDNVSSLVSYLKDPMTYDGADSIAELHPSIKSADIFPKMRSLTDEDLFAISGHIL
                ********:::.**:**********************************************

I. galbana      VQPKVVNEKWGGGKIYY
E. huxleyi      VQPKVVNEKWGGGKIYY
                *****************
```

Figure 4.7. Alignment of the sequences of cytochrome c_{550} from the Isochrysidal algae *E. huxleyi* (NCBI accession YP_277399.1) and *I. galbana*, as deduced from the *psbV* gene sequences.

4.1.3. Effects of iron deprivation on the content of photosynthetic cytochromes and PSII parameters in *P. tricornutum*

A down-regulation under iron limitation of several iron-containing proteins has been previously reported in *P. tricornutum* (Allen et al., 2008). In fact, previous results obtained in our lab indicated a decrease to ≈30% of the Cc_6 protein content in iron-deplete *P. tricornutum* cells as compared with iron-replete conditions (Roncel et al., 2016). In this work, we have extended

this preliminary study to analyse the effects of iron deprivation on the content of both photosynthetic cytochromes, Cc_6 and Cc_{550}, in *P. tricornutum*. Moreover, in the case of Cc_{550} a decrease in the cellular content of this protein would have effects on cell growth and photosynthetic activities, mainly related with its role as a subunit of PSII. Consequently, we have also explored the possible specific consequences related to the iron-promoted changes in the level of Cc_{550}.

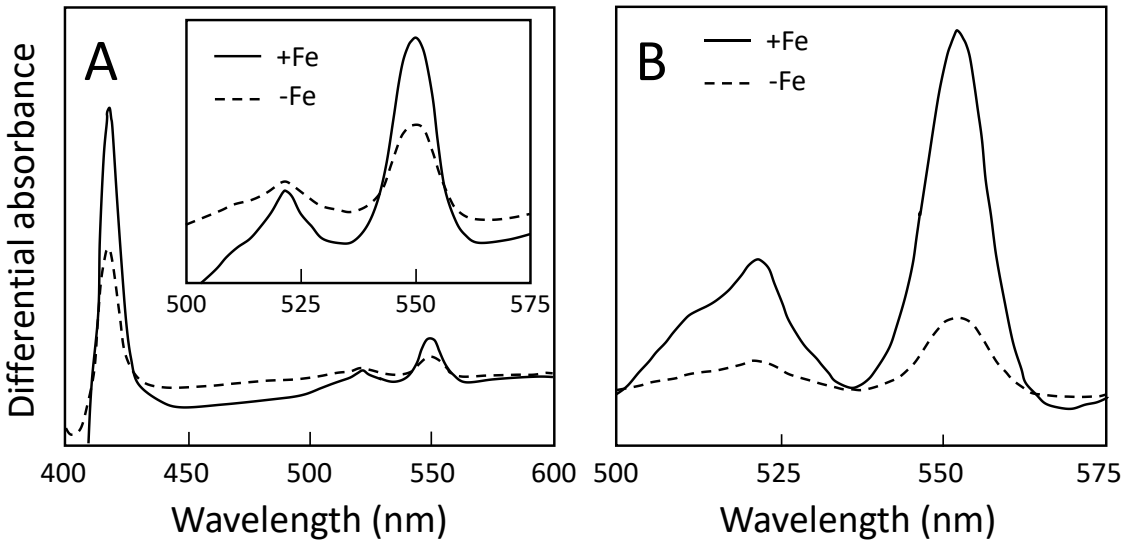

Figure 4.8. Cytochromes content in *P. tricornutum* cultures. Content of (A) Cc_{550} and (B) Cc_6 in *P. tricornutum* cultures grown under iron-replete (10 µM Fe, +Fe) or iron-deplete (0.01 µM Fe, -Fe) conditions, estimated by specific redox differential absorbance changes (dithionite minus ascorbate or ascorbate minus ferricyanide, respectively). (A, inset) Expanded spectra in the region of the Cc_{550} α-band. The Figures shown are representative examples of individual cultures.

First, we have investigated the evolution of the Cc_{550} content when changing iron availability as compared with that of Cc_6, the obtained results indicating that iron deficiency induced an important decrease in the relative content of both Cc_{550} and Cc_6 (Figures 4.8 and 4.9). The changes in the amount of Cc_{550} and Cc_6 were determined by measuring the differential absorbance spectra of soluble cell fractions after 15 days of growth (Figure 4.8). Different concentrations of iron in the culture media were used: iron-replete (10 µM) and three different iron-deficient conditions (0.1, 0.04 and 0.01 µM of added iron).

As shown in Figure 4.9, the content of Cc_{550} and Cc_6 decreased as the amount of iron is lowered in the cultures. Cultures grown under low iron availability (0.01 µM Fe) showed levels

of Cc_6 and Cc_{550} of ≈15 and 25%, respectively, compared with iron-replete conditions (10 µM Fe), (Figure 4.8). The decrease in the content of both cytochromes is not directly proportional to the iron concentrations. Thus, a more pronounced decrease was appreciated when lowering iron concentration from 10 to 0.1 µM Fe, whereas the variation was less marked at lower Fe levels (Figure 4.9). As previously indicated, the decrease in Cc_6 content is more pronounced than that of Cc_{550}, but both cytochromes reached a similar intracellular level (≈4 µM) at the lowest Fe concentration used.

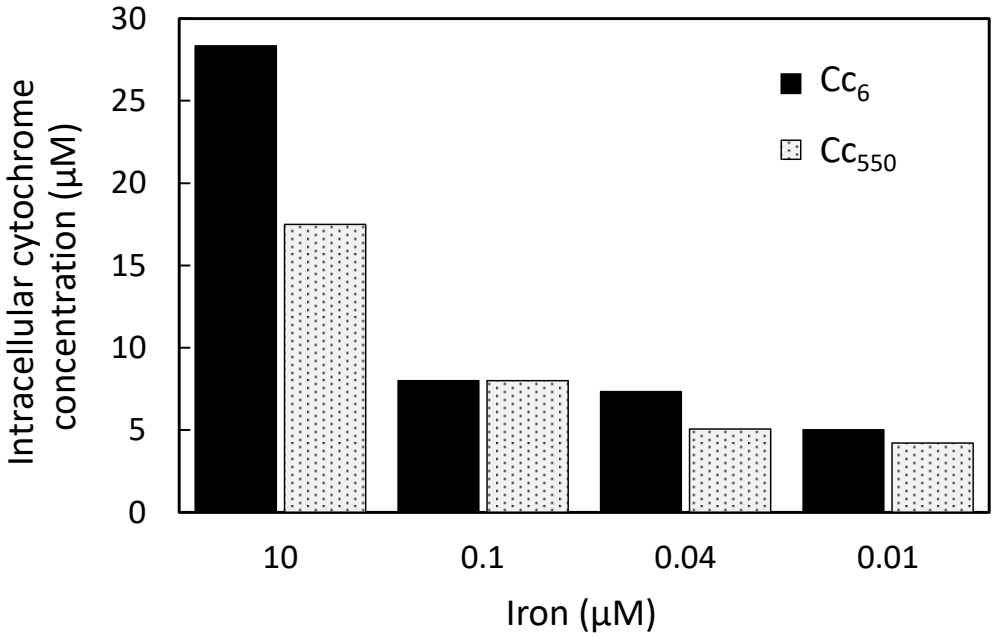

Figure 4.9. Intracellular cytochrome concentration measured by differential absorbance changes of *P. tricornutum* WT cells grown under different iron concentrations. Cc_6, cytochrome c_6; Cc_{550}, cytochrome c_{550}. Data represent mean values of two independent measurements.

We have also analyzed the effect of different levels of iron starvation on the growth of *P. tricornutum* WT cells. Figure 4.10 shows that the growth of the cultures decreased as the amount of iron in the medium diminished. As previously observed for the content of cytochromes, this effect is not directly proportional to the iron concentration. A more pronounced decrease in growth can be appreciated when lowering Fe concentration from 10 to 0.1 µM, the variation being less marked at lower Fe concentrations (Figure 4.10).

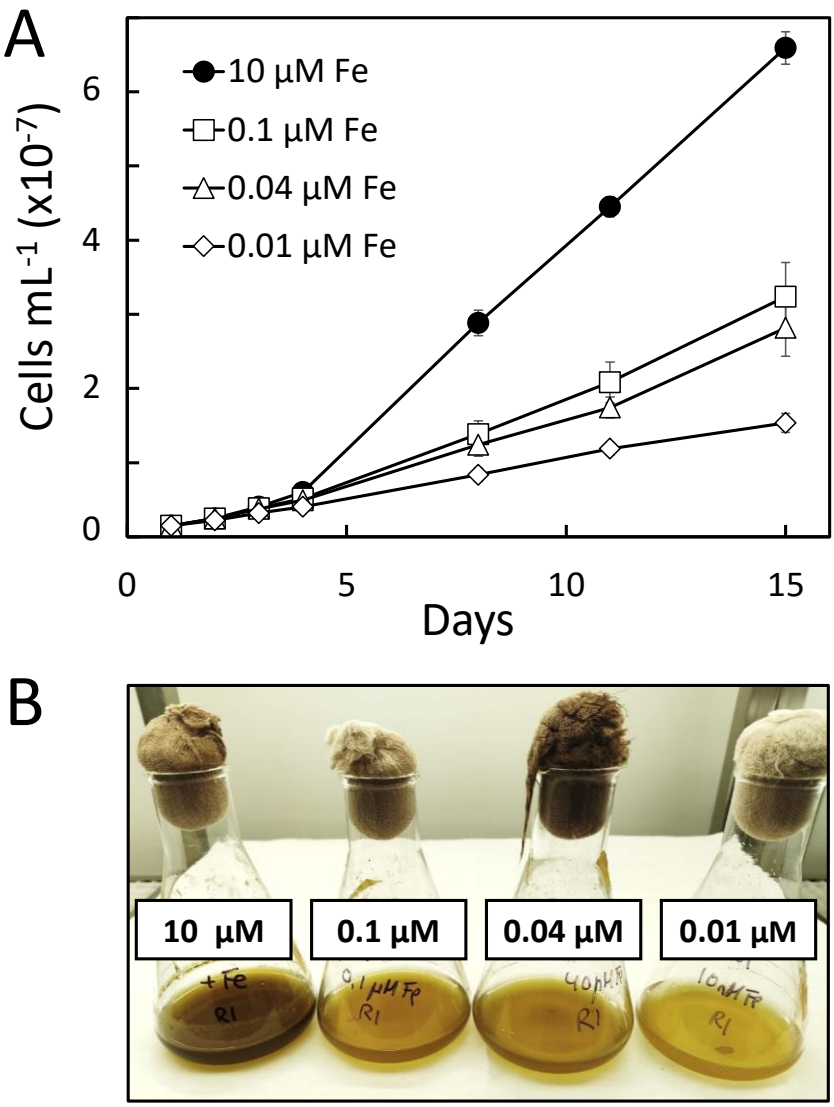

Figure 4.10. Growth of *P. tricornutum* WT and mutant cultures. (A) Growth curves of *P. tricornutum* cultures under different iron concentrations. Mean values ± SD of measurements from 10 independent cultures are presented. (B) Representative examples of the cultures after 15 days of growth.

To further characterize the effect of the decrease in the levels of Cc_{550} in *P. tricornutum*, induced by iron starvation, we have analyzed different parameters related to PSII activity. First, a decrease in the overall photosynthetic activity of PSII per cell is appreciated when iron concentration is reduced in the media. This global PSII activity was measured as the net photosynthetic oxygen evolution per cell using DCBQ as electron acceptor (that allows to estimate the PSII activity from water to quinones). This decrease reaches levels of ≈30% of activity in the presence of 0.01 µM Fe when comparing with the iron-replete condition (Figure 4.11A).

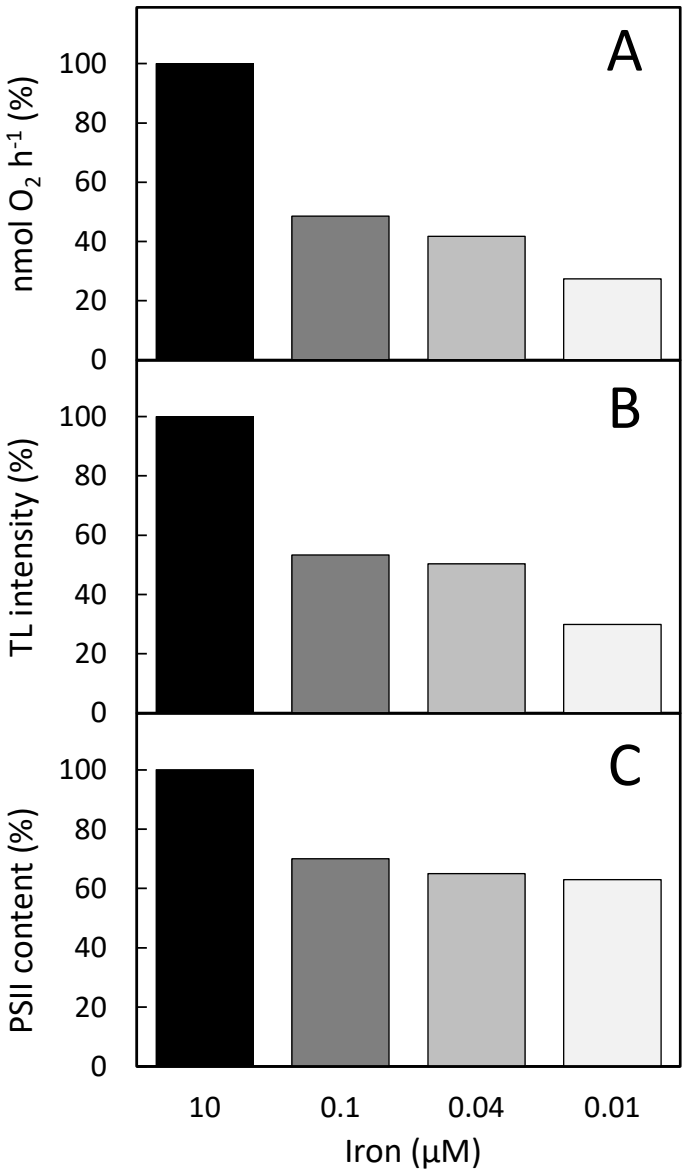

Figure 4.11. Effect of iron deficiency on different PSII-related photosynthetic parameters of *P. tricornutum* WT cells. (A) photosynthetic oxygen evolution, (B) TL intensity, and (C) quantum yield of PSII photochemistry, Y(II). Values are referred to as the percentage per cell of that of WT under iron-replete conditions (Fe 10 µM).

The effect of iron deficiency on the electron transfer PSII activity of *P. tricornutum* WT cells was further investigated using the STL technique. Excitation of iron-deficient *P. tricornutum* WT cells with two flashes at 1°C induced the appearance of typical TL glow curves, but with a significant decrease of the total signal intensity as compared with iron-replete conditions (Figure 4.11B). The decomposition analysis of these emission curves allowed obtaining two components with similar t_{max} values of 14 and 28°C for the different iron conditions. These two components can be assigned to the well-known B1 and B2 TL bands, originated from the recombination

reactions of $S_3Q_B^-$ and $S_2Q_B^-$ charge pairs, respectively, in the PSII water-splitting system (Rutherford et al., 1984). The comparison between conditions of iron sufficiency or limitation indicated that the signal intensity in the lowest iron-deficiency condition (0.01 µM Fe) drops to about 30% of the values obtained under iron-replete conditions (Figure 4.11). Therefore, STL data are both in agreement and confirm the results obtained from the photosynthetic net oxygen evolution (Figure 4.11A). However, the data of PSII content obtained by dual-PAM, showed a minor iron-dependent decrease as compared with the oxygen evolution and STL data. This estimated PSII content is a direct measure of the photochemically active PSII, capable of charge separation (from P_{680} to quinones). With this technique, a decrease only to 60% of PSII content is observed with 0.01 µM Fe as compared with the iron-replete condition (Figure 4.11C).

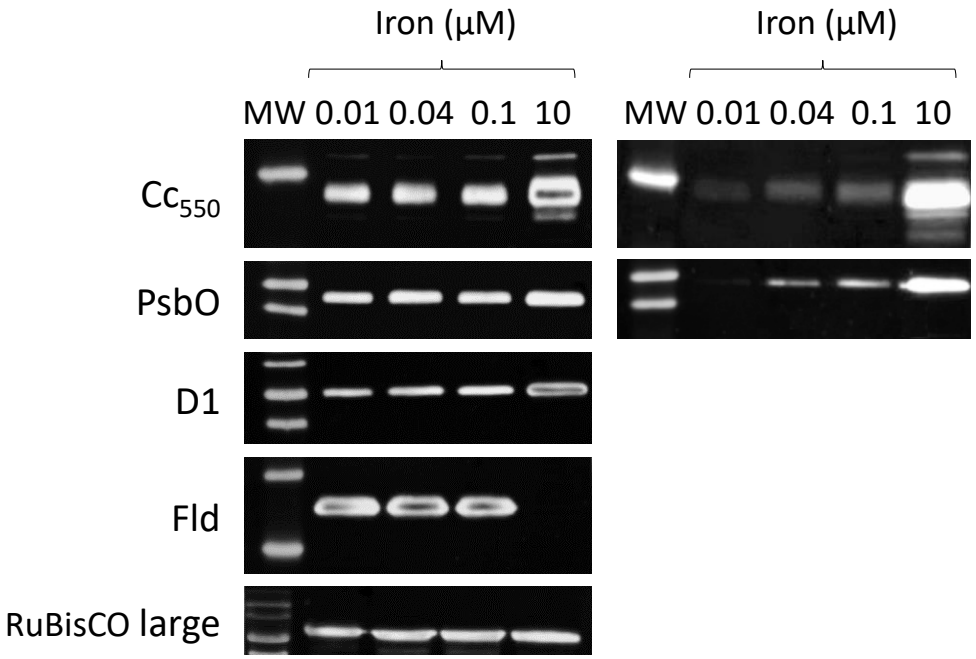

Figure 4.12. Western-blot analysis of different photosynthetic proteins. Western-blot analysis in samples of WT cells (Left) and membrane extracts (Right) from *P. tricornutum* grown under iron-replete (10 µM) and iron-deficient (0.1, 0.04 and 0.01 µM iron) conditions. MW: molecular weight standard; Cc_{550} and PsbO, the extrinsic cytochrome c_{550} and PsbO subunits of PSII; D1, the intrinsic D1 subunit of PSII; Fld, flavodoxin; RuBisCO large, control with the RuBisCO large subunit. Protein extracts: 20 µg for RuBisCO large; 10 µg for PsbO and D1; 5 µg for Fld; 2.5 µg for Cc_{550}. Membranes were incubated overnight with the following dilutions of the selected primary antibody: 1:1000 anti-Cc_{550} and anti-RuBisCO large; 1:2000 anti-PsbO; 1:10000 anti-D1; 1:50000 anti-Fld.

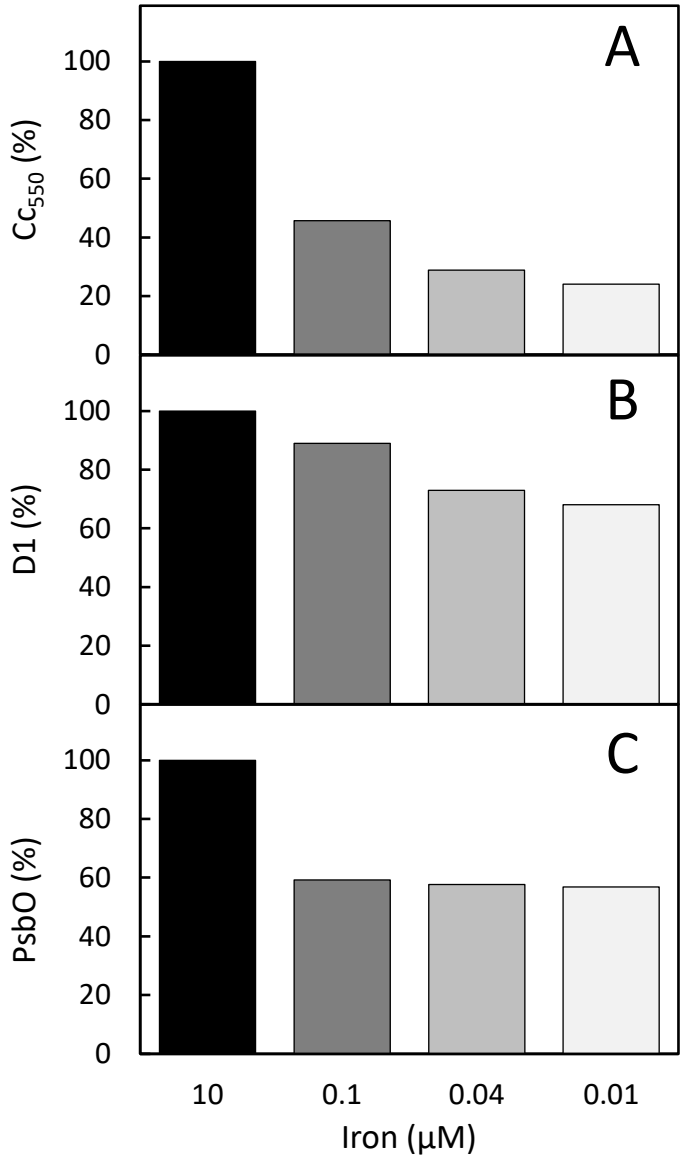

Figure 4.13. Effect of iron deficiency on the content of PSII subunits in *P. tricornutum* WT cells. (A) Intracellular Cc_{550} measured by differential absorbance. (B) D1 and (C) PsbO subunits of PSII quantified by Western-blot analyses. Values are referred to as the percentage of that of WT under iron-replete conditions (Fe 10 µM).

When comparing the changes of decreasing iron concentrations on the Cc_{550} content (determined both by the spectral changes and Western-blot) and the global PSII activity, a parallel decrease was observed (Figures 4.11, 4.12 and 4.13A). On the other hand, a similar reduction was found in the content of both the D1 and PsbO subunits of PSII measured by Western-blot analysis (Figures 4.12 and 4.13). However, this decrease is sensibly less pronounced than that of Cc_{550} (and the oxygen/TL data) but similar to that of the photoactive PSII content obtained by dual-PAM (Figures 4.11 and 4.13). From these data it can be concluded

that under iron limitation a specific decay in the functioning of the water-splitting system occurs, as compared with the lower decrease in the total amount of photochemically active PSII. This specific decay of the water-splitting system is parallel to the decay in the Cc_{550} content.

A specific effect of the lack of Cc_{550} on PSII activity could be related with its role in stabilizing the water-splitting system and/or the binding of the other PSII extrinsic subunits, causing a lower water-splitting activity (Pi et al., 2019; Xiao et al., 2020). Consequently, we have also investigated the content of the extrinsic subunits Cc_{550} (PsbV) and PsbO in membrane fractions of *P. tricornutum* when decreasing the iron concentration in the media. As shown in Figure 4.12, the Cc_{550} and PsbO content, measured by Western-blot, was sensibly lower in the membrane extracts compared with whole cells, preventing a reliable estimation of the content of both proteins at the lower iron levels. However, whereas the decrease in Cc_{550} can be explained by the existence of an intracellular free soluble population not bound to PSII (Kirilovsky et al., 2004; Bernal-Bayard et al., 2017), the PsbO decay indicates a lower affinity of this protein for the binding to PSII at low iron concentrations.

4.1.4. Structural modelling of Cc_{550} from different algae of the red lineage

Modelled structures of *P. tricornutum*, *C. muelleri*, *I. galbana* and *N. gaditana* Cc_{550} were obtained from the available sequences by using MODELLER version 9v23 (Figure 4.14) (Sali & Blundell, 1993). In all cases the solved structure of Cc_{550} of the red alga *C. caldarium* was used as template (Ago et al., 2016). The modelled structures displayed a common folding pattern, very similar to that described in other cyanobacterial and red algae Cc_{550}. Therefore, the structures conserved the hydrophobic northern finger (according to the orientation presented in Figure 4.14) previously described (Frazão et al., 2001), that is part of the interaction area with PSII (Shen, 2015; Pi et al., 2019). However, the surfaces of eukaryotic Cc_{550} show exclusive electrostatic features as compared with the cyanobacterial Cc_{550}. Thus, whereas in the prokaryotic protein the cofactor exposed area holds a negatively charged electrostatic character (Frazão et al., 2001), in the eukaryotic Cc_{550} the area around the heme group is mainly hydrophobic, and the negative electrostatic potential is restricted to the southern area, opposite to the hydrophobic northern protuberance (Figure 4.14 & 4.15).

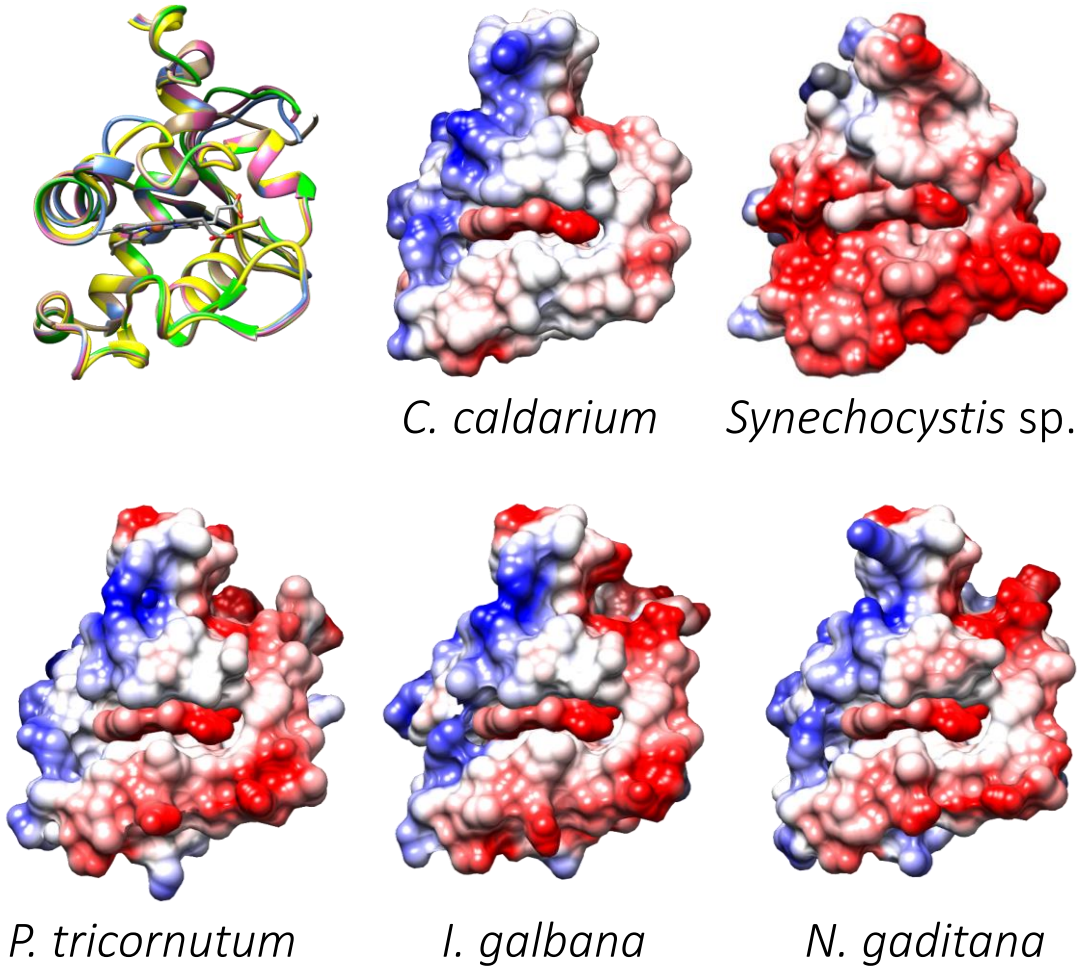

Figure 4.14. Superimposition of backbones and surface electrostatic potential distribution of cytochrome c_{550}. Superimposition of backbones of Cc_{550} from *C. caldarium* (PDB code 4yuu; yellow) and Cc_{550} models of *P. tricornutum* (light brown), *C. muelleri* (green), *I. galbana* (pink) and *N. gaditana* (blue), and surface electrostatic potential distribution in the Cc_{550} of *C. caldarium* and *Synechocystis* sp. PCC 6803 and in the structural models of *P. tricornutum*, *I. galbana* and *N. gaditana*, as indicated. The view displays the proteins in the same orientation, showing in front the heme cofactor exposed area, and in the top the protein C-terminal hydrophobic protuberance. Simulations of surface electrostatic potential distribution were performed using the UCSF Chimera Program. Positively and negatively charged regions are depicted in *blue* and *red*, respectively.

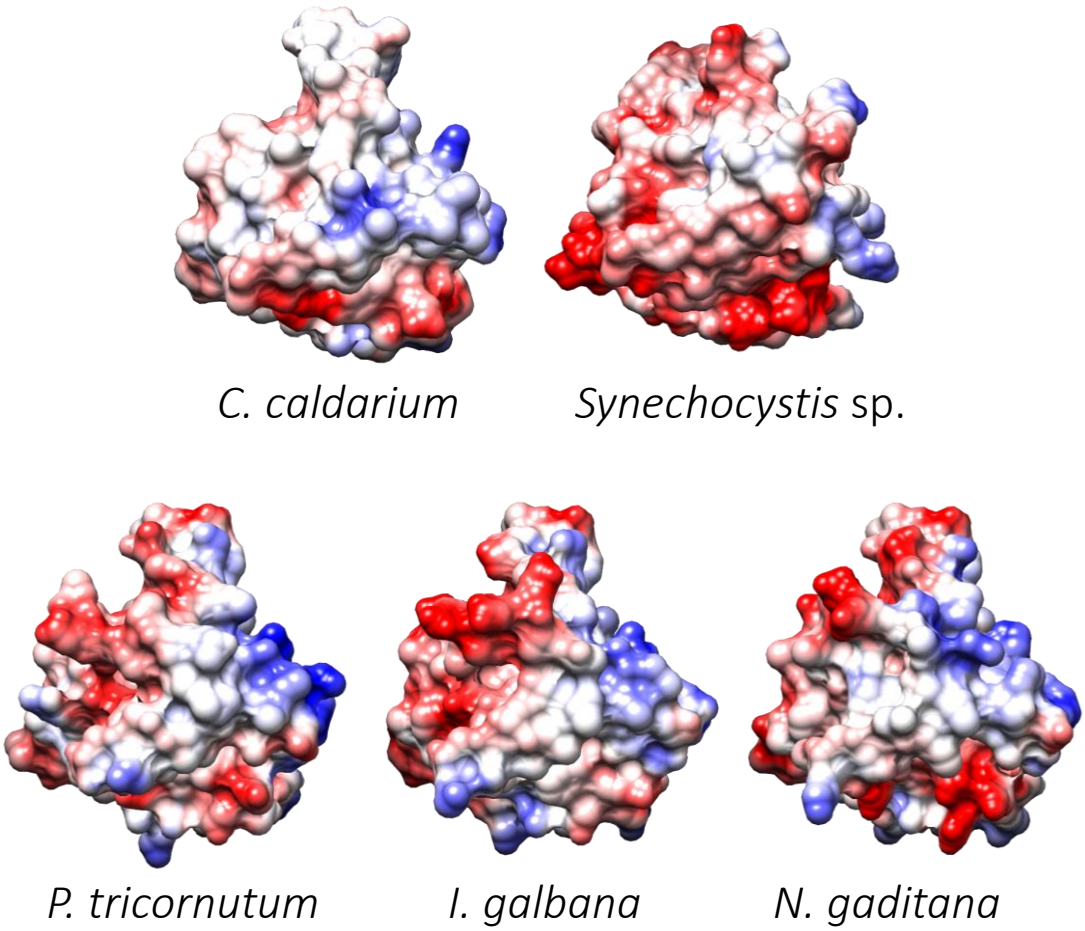

Figure 4.15. Surface electrostatic potential distribution in cytochrome c_{550}. Surface electrostatic potential distribution in the Cc_{550} of *C. caldarium* and *Synechocystis* sp. PCC 6803 and in the structural models of *P. tricornutum*, *I galbana* and *N. gaditana*, as indicated. The view displays the proteins after a 180^{o} rotation on the Y axis from the orientation shown in the Figure 4.14.

4.2. Chapter II

The effects of the heterologous expression of a plastocyanin in the diatom *Phaeodactylum tricornutum*

4.2. Chapter II. The effects of the heterologous expression of a plastocyanin in the diatom *Phaeodactylum tricornutum*

4.2.1. Heterologous expression in the chloroplast of *P. tricornutum* of the E85K mutant Pc of *C. reinhardtii*

The expression of native Pc in some oceanic species of diatoms has been proposed to constitute an alternative replacement of Cc_6, similar to what occurs in cyanobacteria and green algae (Peers & Price, 2006; Moore & Braucher, 2008; Lommer et al., 2012; Marchetti et al., 2012; Groussman et al., 2015; Hippmann et al., 2017). However, there are no available data about the *in vivo* functional effects of expressing Pc in the thylakoidal lumen of diatoms under iron-limiting conditions. Thus, here we investigated the effects of the heterologous expression of a Pc in *P. tricornutum*, a diatom that naturally only produces Cc_6. We have selected the E85K mutant of the Pc from the green alga *C. reinhardtii* to be expressed in *P. tricornutum*, as this mutant has previously shown to be the most effective Pc in reducing diatom PSI *in vitro* (Bernal-Bayard et al., 2015).

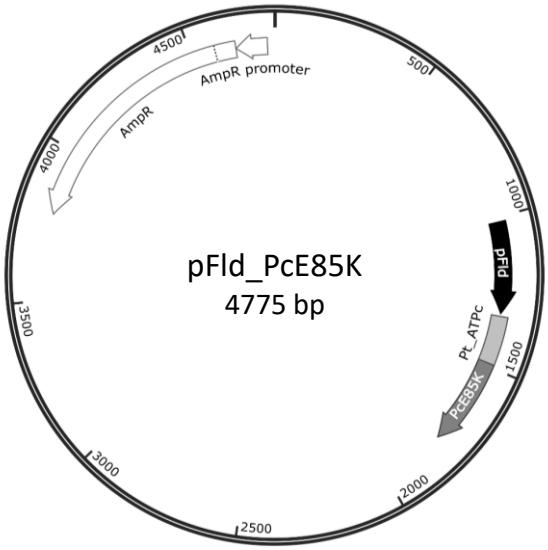

Figure 4.16. pFld_PcE85K plasmid used to transform *P. tricornutum* cells. The pFld_PcE85K plasmid contained the transit peptide of the ATPase gamma subunit (ATPC). The picture was generated by using the SnapGene® program.

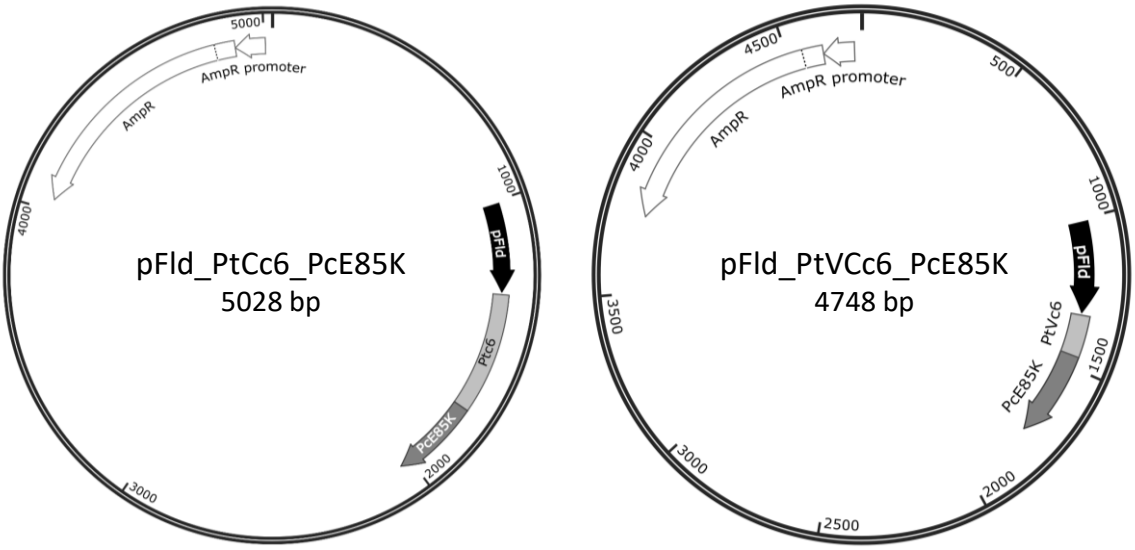

Figure 4.17. pFld_PtCc6_PcE85K and pFld_PtVCc6_PcE85K plasmids used to transform *P. tricornutum* cells. The pFld_PtCc6_PcE85K plasmid contained an intron (280 nucleotides) within the N-terminal plastid targeting sequence, present in the native Cc_6 gene (Kilian & Kroth, 2004), whereas the pFld_PtVCc6_PcE85K plasmid was designed without the intron. Pictures were generated by using the SnapGene® program.

The synthetic *C. reinhardtii* Pc *petE* gene, with the E85K mutation (Bernal-Bayard et al., 2015), was designed with the codon usage of *P. tricornutum* (see Section 3.2.10 in Experimental Procedures). Different plasmids were constructed containing this Pc gene: pFld_PcE85K, pFld_PtCc6_PcE85K and pFld_PVCc6_PcE85K (Figures 4.16 and 4.17). Synthetic plasmids were generated by GeneCust, by inserting the Pc *petE* E85K constructions into the pBlueScript II SK (+) vector in *EcoR*V and *Pst*I sites. The constructions were then subcloned in the *P. tricornutum* transformation vector Isip1::YFP, kindly provided by the group of Prof. Chris Bowler (IBENS, Paris, France) (Kazamia et al., 2018). All constructions were checked by sequencing (NZYTech) using the oligonucleotides pPisipF and pPisipR (Table 3.8, Section 3.2.7.1).

In all plasmids, the Pc gene was placed under the control of the Fld promoter (induced in absence of iron), to ensure its expression under low iron conditions (Figures 4.16 and 4.17), in which the levels of native Cc_6 drastically decrease and become limiting for the photosynthetic activity (Roncel et al., 2016; and see also Section 4.1.3). Different transit peptides were used. The pFld_PcE85K plasmid contained the bipartite transit peptide of the ATPC, which directs the protein to the stroma. This plasmid was used as a control of the possible unspecific effects of the expression of Pc out of its location for a physiological function (the lumen). The plasmids

pFld_PtCc6_PcE85K and pFld_PtVCc6_PcE85K contained the tripartite transit peptide of the native Cc_6 added to the Pc gene sequence, directing the protein to the thylakoid lumen (Killian & Kroth, 2004). However, as the native Cc_6 gene of *P. tricornutum* has an intron (280 nucleotides) located within the region coding for the N-terminal plastid targeting sequence (Killian & Kroth, 2004), two constructions with alternative versions of the transit peptide of Cc_6 were designed, with or without the sequence corresponding to the intron (Figures 4.17 and 4.18).

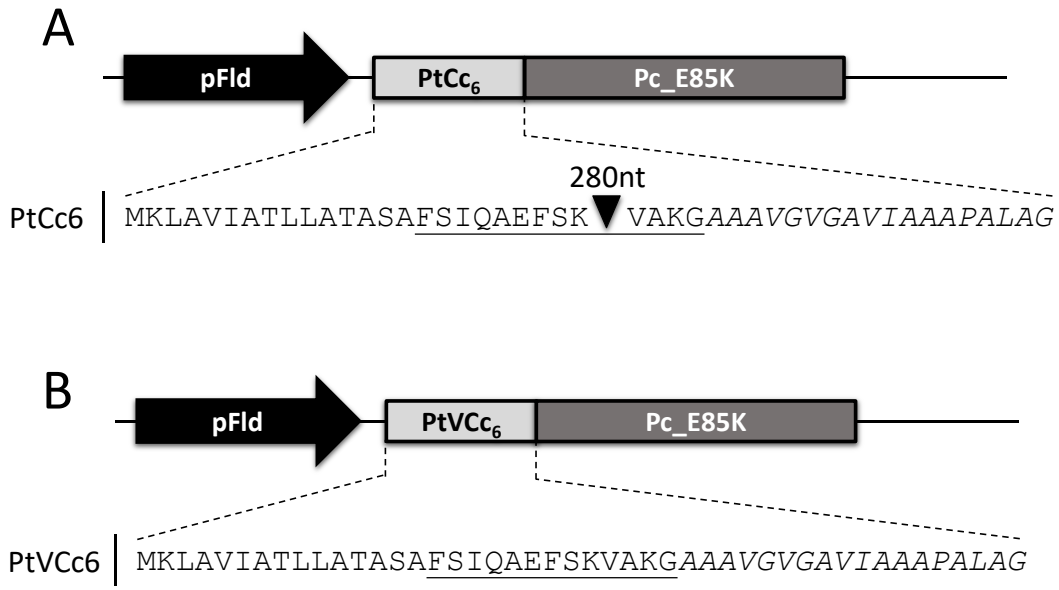

Figure 4.18. Construction of the plasmids pFld_PtCc6_PcE85K and pFld_PtVCc6_PcE85K. (A) Construction of the plasmid pFld_PtCc6_PcE85K, containing the intron (280 nucleotides) within the N-terminal plastid targeting sequence present in the native Cc_6 gene. (B) Construction of the plasmid pFld_PtVCc6_PcE85K, without the sequence corresponding to the intron of the transit peptide of Cc_6.

The presence of the Pc gene in zeocine-resistant transformed colonies was checked by colony PCR and DNA electrophoresis in agarose gels. Moreover, gDNA of these "positive" colonies was extracted and analyzed by PCR for a further and more precise evaluation. The final amplified product was examined by agarose gel electrophoresis to confirm the expected product size, thus corroborating the correct insertion of the Pc gene in several strains (Figure 4.19). The correct transcription of the Pc gene in the mutant strains was checked by RT-PCR, using the oligonucleotides indicated in Table 3.8.

The number of copies of the Pc gene inserted in the genome of *P. tricornutum* in the different mutant strains was estimated by qPCR, using the oligonucleotides indicated in Table

3.8 and the genes of Fld and PsbO as control, the results showing a great variability. Among the strains analyzed, mutant #1 contained around 25 copies of the gene, mutant #30 1–2 copies, mutant #45 3–4 copies and mutant #79 10 copies.

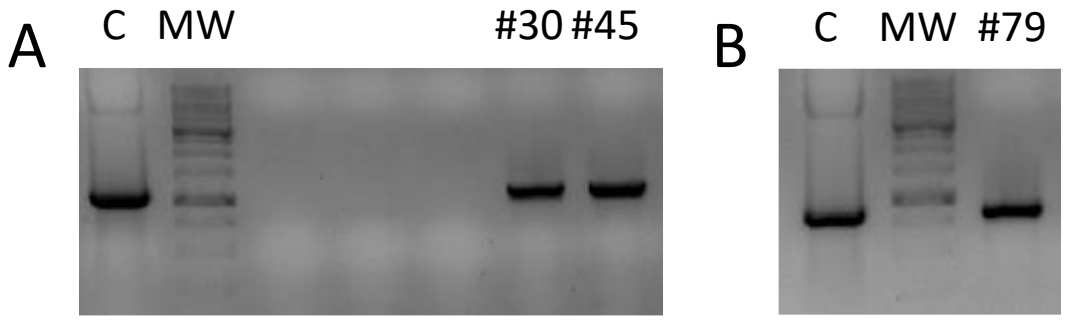

Figure 4.19. PCR analyses of gDNA. PCR analyses of the gDNA extracted from the cells transformed with plasmids (A) pFld_PtCc6_PcE85K and (B) pFld_PtVCc6_PcE85K. MW, molecular weight standard; C, control: purified plasmids pFld_PtCc6_PcE85K and pFld_PtVCc6_PcE85K, used for the transformation of *P. tricornutum* cells, were used as a PCR control for (A) and (B), respectively.

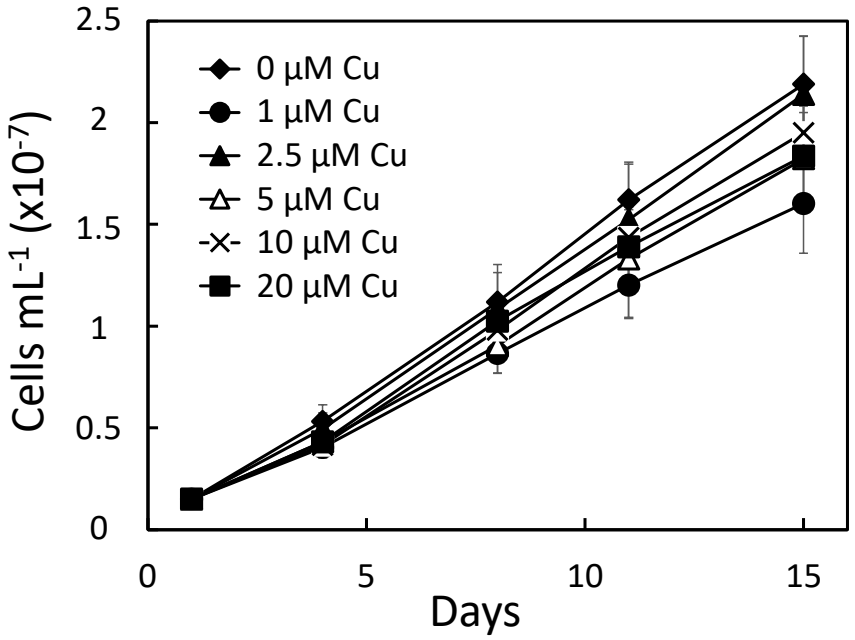

Figure 4.20. Growth curves of *P. tricornutum* WT cells with different concentrations of $CuSO_4$. Mean values ± SD of measurements from 10 independent cultures are presented.

Before starting the analysis of the selected mutants, growth curves of WT cells in the presence of different amounts of copper were made to stablish the metal concentration to be used in additional experiments, avoiding toxicity effects (Figure 4.20). From these data, a standard concentration of 5 µM of copper was selected for further experiments.

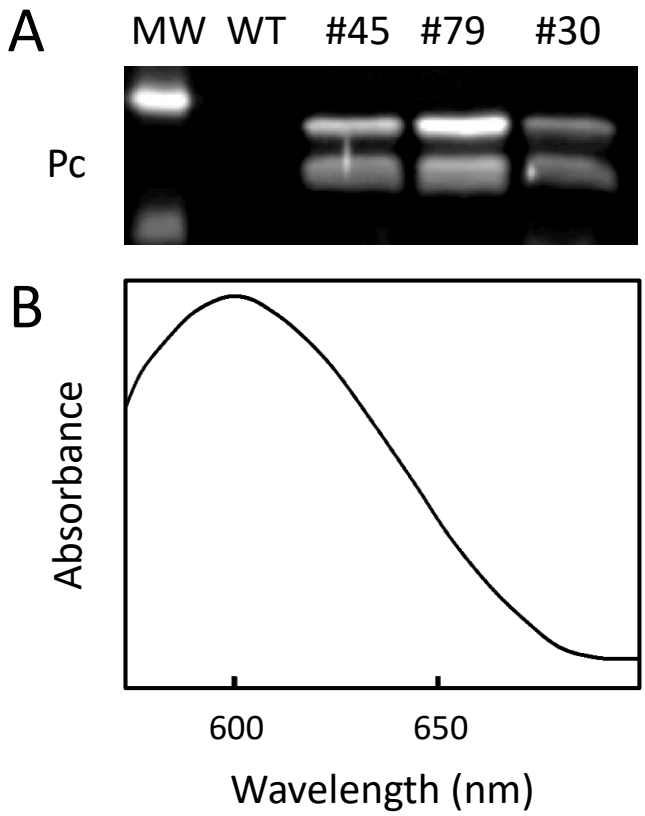

Figure 4.21. Western-blot analysis and spectroscopic measurement of plastocyanin. (A) Western-blot analysis of the presence of Pc in samples from *P. tricornutum* WT and #30, #45 and #79 mutant cells grown under iron-deficient conditions. MW, molecular weight standard. 30 µg of protein extracts were used. Membranes were incubated overnight with anti-Pc primary antibody (1:500). (B) Spectroscopic monitoring of holo-Pc (ferricyanide minus ascorbate) in cell extracts from mutant #45 grown under iron-deficient conditions.

The nuclear transformation of *P. tricornutum* is random, which can result in a great variability in the level of expression of a protein in different clones. Consequently, several *P. tricornutum* strains with different levels of Pc expression were selected (clones #30, #45 and #79), as shown by the presence in Western-blot analysis of a band corresponding to the expected size of Pc (10.2 kDa; Figure 4.21A). The following apparent progression in the levels of expression was observed: #30 < #45 < #79 (Figure 4.21A). Whereas mutants #30 and #45 were

transformed with the construction that contained the intron in the plastid targeting gene sequence, mutant #79 was transformed with the construction that lacked the intron (Figures 4.17 and 4.18), indicating that both constructions can be correctly processed to the lumen. However, in the three mutant strains an additional band of an apparent higher size (12.6 kDa) was also observed (more abundant in the clone #79; Figure 4.21A). This band can be tentatively assigned to unprocessed Pc molecules still containing the Cc_6 thylakoid transit peptide (24 extra amino acids; Killian & Kroth, 2004) and that would be considered as apo-Pc.

The presence of the Pc holoprotein (i.e., with the copper active cofactor) was directly detected by its differential absorption spectrum in cell extracts (Figure 4.21B). From the recorded differential spectra, analogous amounts of intracellular holo-Pc were estimated for mutants #45 (≈3.8 µM) and #79 (≈4.4 µM), whereas the lower levels of Pc detected in the mutant #30 did not allow obtaining a reliable estimate of the holoprotein content. On the other hand, a similar amount of ≈3.6 µM of intracellular Cc_6 was estimated for the WT and mutant strains under iron-deficient conditions, following the procedure previously described (Figure 4.8 in Section 4.1.3).

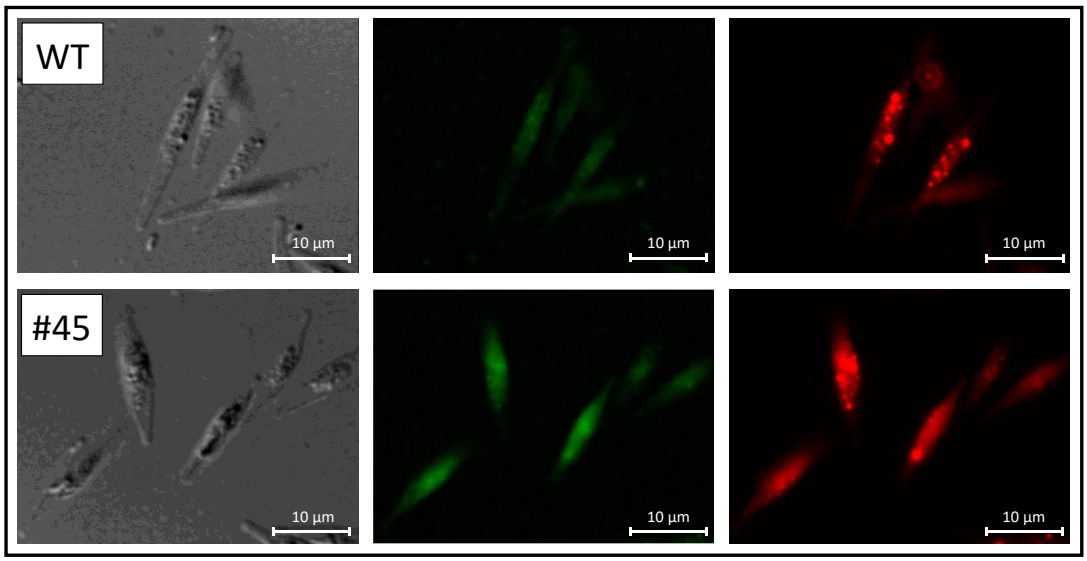

Figure 4.22. Fluorescence microscopy of WT and #45 mutant immunolabeled cells. *P. tricornutum* cells were incubated with rabbit polyclonal anti-Pc antibody for 90 minutes and, afterwards, they were incubated with anti-rabbit FITC secondary antibody, in darkness, for 90 minutes. The cells were visualized using a Leica Microscope DM6000 B. Differential interference contrast (left), green fluorescence associated to the immunodetection of Pc (middle) and chlorophyll red auto-fluorescence (right) were observed.

Finally, fluorescence microscopy monitoring of immunolabeled cells confirmed the detection of the heterologous Pc in the chloroplast, as the green fluorescence associated to the immunodetection of Pc merged with the red fluorescence of photosynthetic pigments (Figure 4.22).

4.2.2. Effects of the heterologous expression of Pc on the growth of *P. tricornutum* cells under iron-deficient conditions

It should be noted that, under iron-replete conditions, the transformed strains did not show significant differences in cell growth with the WT strain (Figure 4.23), nor did the B1 strain (with the resistance to zeocine but without Pc) under iron-deficient conditions (Figure 4.25B).

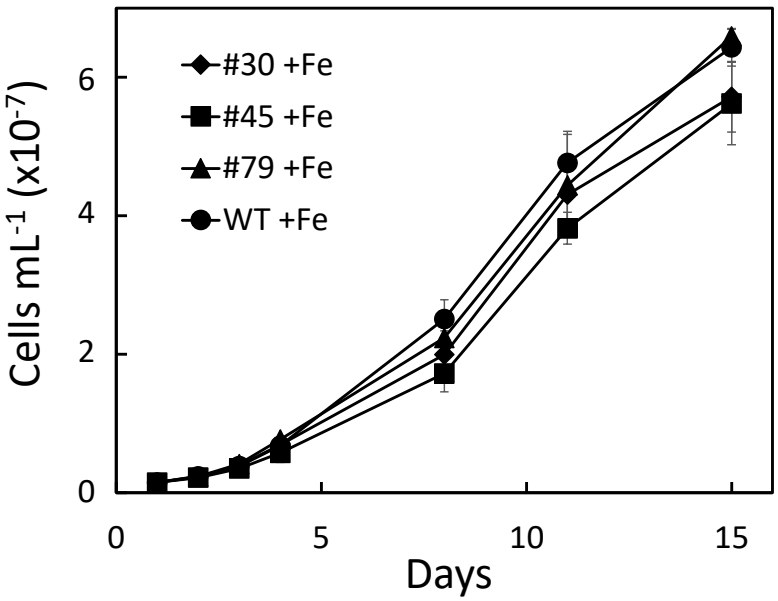

Figure 4.23. Growth curves of *P. tricornutum* WT, #30, #45 and #79 strains cultures under iron-replete conditions. Mean values ± SD of measurements from 10 independent cultures are presented.

Similarly, the transformed strain with the plasmid pFld_PcE85K, used as control of the growth when Pc is located in the stroma, did not show significant differences with the WT strain under iron-deficient conditions (Figure 4.24). Moreover, the MW of the expressed Pc corresponded to the expected size of the processed protein (10.2 kDa; Figure 4.24, inset).

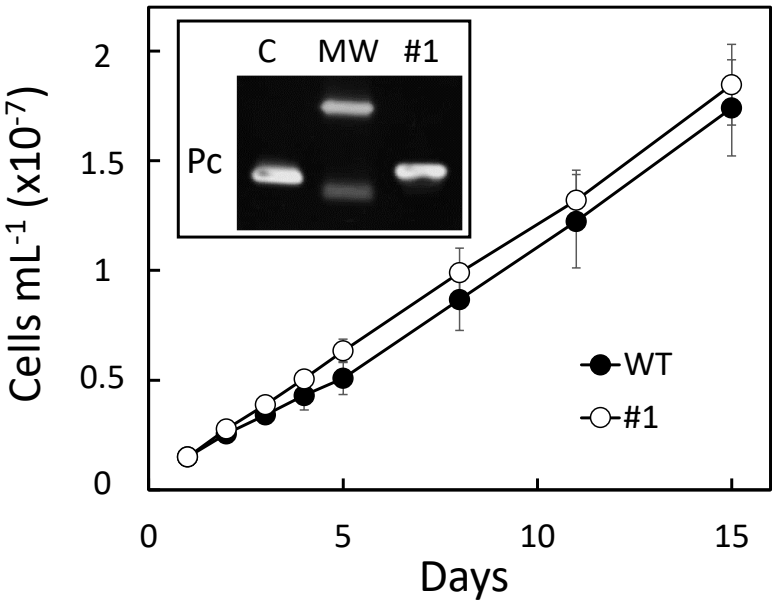

Figure 4.24. Growth curves under iron-deficient conditions of *P. tricornutum* WT and the mutant #1, expressing plastocyanin in the chloroplast stroma. Mean values ± SD of measurements from 10 independent cultures are presented. (Inset) Western-blot analysis of Pc in samples of the mutant strain #1 grown under iron-deficient conditions (1.25 µg of protein extract were used). MW, molecular weight standard; C, purified *C. reinhardtii* Pc used as control. The membrane was incubated overnight with anti-Pc primary antibody (1:1000).

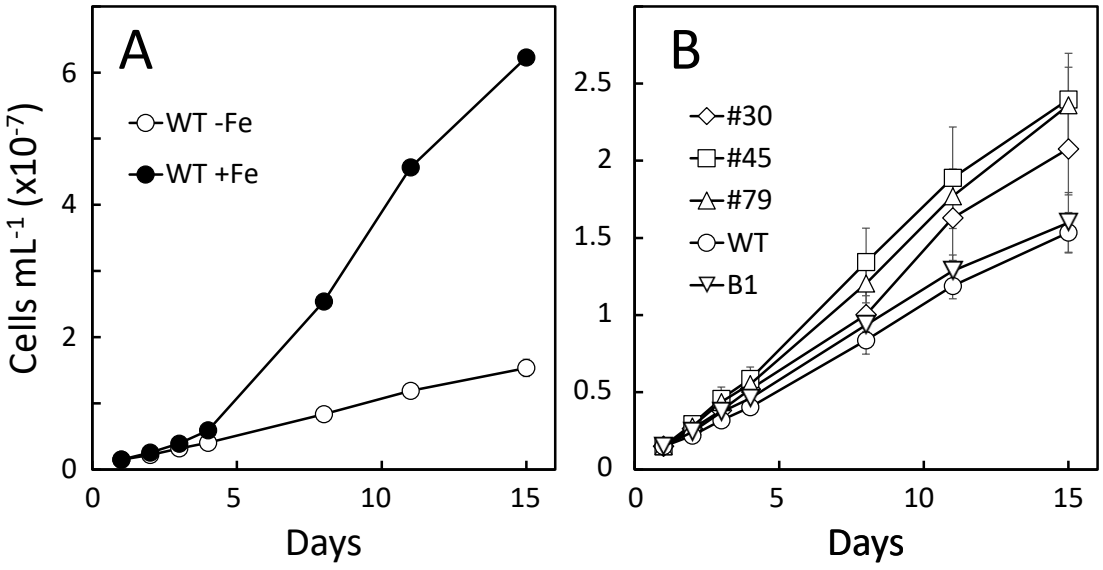

Figure 4.25. Growth curves of *P. tricornutum* WT and mutant cultures under iron-deficient conditions. (A) Growth curves of *P. tricornutum* WT cultures under iron-replete (+Fe) or iron-deficient (–Fe) conditions as a control. (B) Growth curves of WT, B1, #30, #45 and #79 strains cultures under iron-deficient conditions. Mean values ± SD of measurements from 10 independent cultures are presented.

The three selected transformed strains that express the Pc in the thylakoid lumen showed however an increased cell growth under iron-deficient conditions compared with the WT (and B1) strain (Figure 4.25). This increase was about 40% in the mutant #30, but up to 60% in the case of the #45 and #79 mutants (Figure 4.25B and Table 4.2) although the growth of the three transformed strains was still sensibly lower as compared with iron-replete conditions (Figure 4.25 and 4.26A).

The absorption spectra of pigments extracts of *P. tricornutum* WT, #30, #45 and #79 cultures under iron-deficient conditions showed comparative similar results to that obtained with the growth curves. The WT strain exhibited the lowest pigment content, followed by the #30 mutant, whereas the #45 and #79 mutants showed a similar higher pigment content (Figure 4.26A).

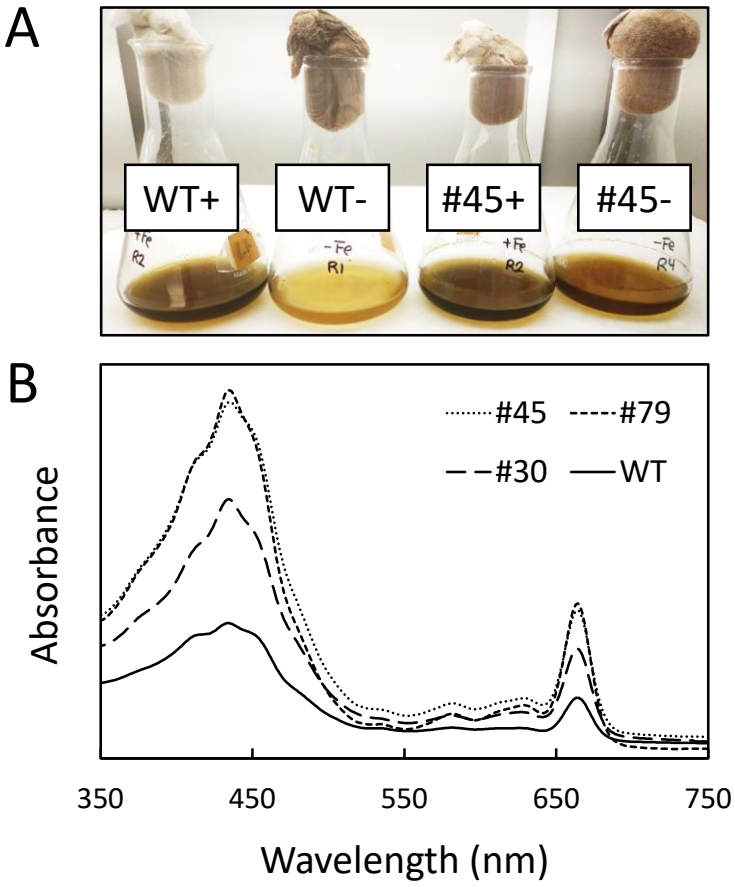

Figure 4.26. Examples of *P. tricornutum* WT and mutant cultures and absorption spectra of pigment extracts. (A) Examples of WT and mutant #45 individual cultures under iron-replete (+) and iron-deficient (-) conditions. (B) Absorption spectra of pigments extracts of *P. tricornutum* WT and #30, #45 and #79 mutant cells under iron-deficient conditions. In all cases cultures with 15 days of growth were taken.

Table 4.2. General physiological and biochemical parameters of *P. tricornutum* transformed cells and cultures under iron-deficient conditions.

Parameter (after 15 days of growth)	WT	#30	#45	#79
Cells per mL	(1.5 ± 0.1) x 10^7 (100%)[a]	(2.1 ± 0.3) x 10^7 (140%)	(2.4 ± 0.3) x 10^7 (159%)	(2.5± 0.2) x 10^7 (163%)
Specific growth rate (μ, day^{-1})	0.155 ± 0.005 (100%)	0.175 ± 0.008 (113%)	0.183 ± 0.010 (118%)	0.185 ± 0.013 (119%)
Total Chl per mL (μg Chl mL^{-1})	4.19 ± 0.23 (100%)	6.05 ± 0.06 (144%)	8.13 ± 0.07 (194%)	8.14 ± 0.06 (194%)
Chl *a* per mL (μg Chl mL^{-1})	2.97 ± 0.03 (100%)	4.45 ± 0.09 (150%)	6.12 ± 0.05 (206%)	6.30 ± 0.02 (212%)
Chl *c* per mL (μg Chl mL^{-1})	1.49 ± 0.04 (100%)	2.24 ± 0.02 (150%)	3.22 ± 0.04 (216%)	3.14 ± 0.06 (211%)
Total carotenoids per mL (μg Car mL^{-1})	2.04 ± 0.07 (100%)	3.50 ± 0.15 (172%)	4.81± 0.65 (236%)	4.34 ± 0.41 (213%)
Total Chl per cell (pg Chl $cell^{-1}$)	0.27 (100%)	0.32 (120%)	0.38 (140%)	0.37 (137%)
Total carotenoids per cell (pg Car $cell^{-1}$)	0.13 (100%)	0.16 (125%)	0.20 (150%)	0.18 (135%)
Cell circularity	0.33 ± 0.04 (100%)	0.43 ± 0.07 (130%)	0.44 ± 0.05 (133%)	0.38 ± 0.05 (115%)
Cell volume (μm^3)	40.2 ± 8.6 (100%)	35.3 ± 9.5 (90%)	55.8 ± 14.8 (139%)	53.2 ± 10.9 (132%)
Cell surface (μm^2)	85.1 ± 12.8 (100%)	71.4 ± 13.6 (84%)	92.8 ± 13.8 (110%)	95.2 ± 11.4 (112%)
Net photosynthetic rate per 10^6 cells (nmol O_2 h^{-1})	37.2 ± 0.6 (100%)	45.4 ± 2.5 (122%)	78.5 ± 8.8 (213%)	87.0 ± 1.6 (235%)

[a]Below, in parentheses, values referred to as the percentage of that of WT cells.

Accordingly, the three transformed strains also showed higher values in the specific growth rate (μ, from 0.155 day^{-1} in the WT to 0.175–0.185 day^{-1} in the mutants), as well as in the total Chl, Chl *a* and *c* and carotenoid estimated contents per mL, as compared with WT cells under iron-deficient conditions (Table 4.2). Higher levels of pigments are still observed in the three mutants when normalized per cell, particularly in the mutants #45 and #79 (up to 40%, Table 4.2). Regarding global photosynthetic activity, the three transformed strains presented a significant enhancement in the net photosynthetic oxygen evolution rate normalized per cell

compared with the WT strain, with the highest values observed again for the #45 and #79 clones (Table 4.2).

Chl per cell was also determined by fluorescence measurements by flow cytometry (FL3-H mean parameter) (Figure 4.27), resulting in a slight increase (≈10–15%) of this parameter in the mutant strains as compared with the WT under iron deficiency conditions (Table 4.3). Possible morphological changes in the Pc-expressing strains were also monitored by flow cytometry (Figure 4.27). Regarding cell complexity (SSC-H parameter), under iron-limiting conditions no clear differences between the WT and the mutant strains were observed (Table 4.3). However, an apparent smaller cell size (FSC-H parameter) was determined for the mutant strains (average values ≈75% as compared with the WT strain, Table 4.3).

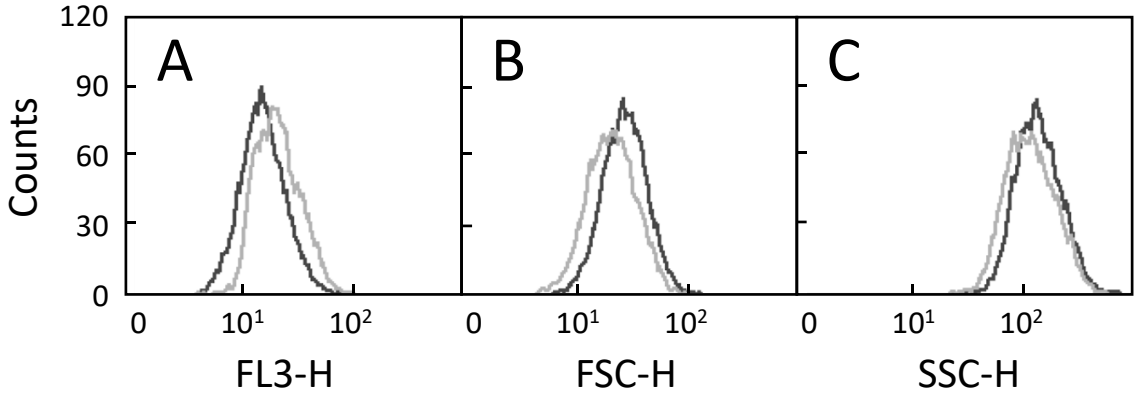

Figure 4.27. Flow cytometry results of *P. tricornutum* WT and #45 mutant cultures under iron-deficient conditions. Examples of flow cytometry results under iron-deficient conditions of individual cultures of *P. tricornutum* WT (black) and mutant #45 (grey) strains. Different parameters were measured: (A) FL3-H, chlorophyll; (B) FSC-H, cell size; and (C) SSC-H, cell complexity.

Table 4.3. Flow cytometry parameters under iron-deficient conditions of *P. tricornutum* #30, #45 and #79 strains as compared with the WT strain. Different parameters were measured: FL3-H, chlorophyll; FSC-H, cell size and SSC-H, cell complexity. Values referred to as the percentage of that of WT cells.

Parameters (after 15 days of growth)	WT	#30	#45	#79
FL3-H	100%	112%	115%	110%
FSC-H	100%	73%	77%	75%
SSC-H	100%	78%	94%	110%

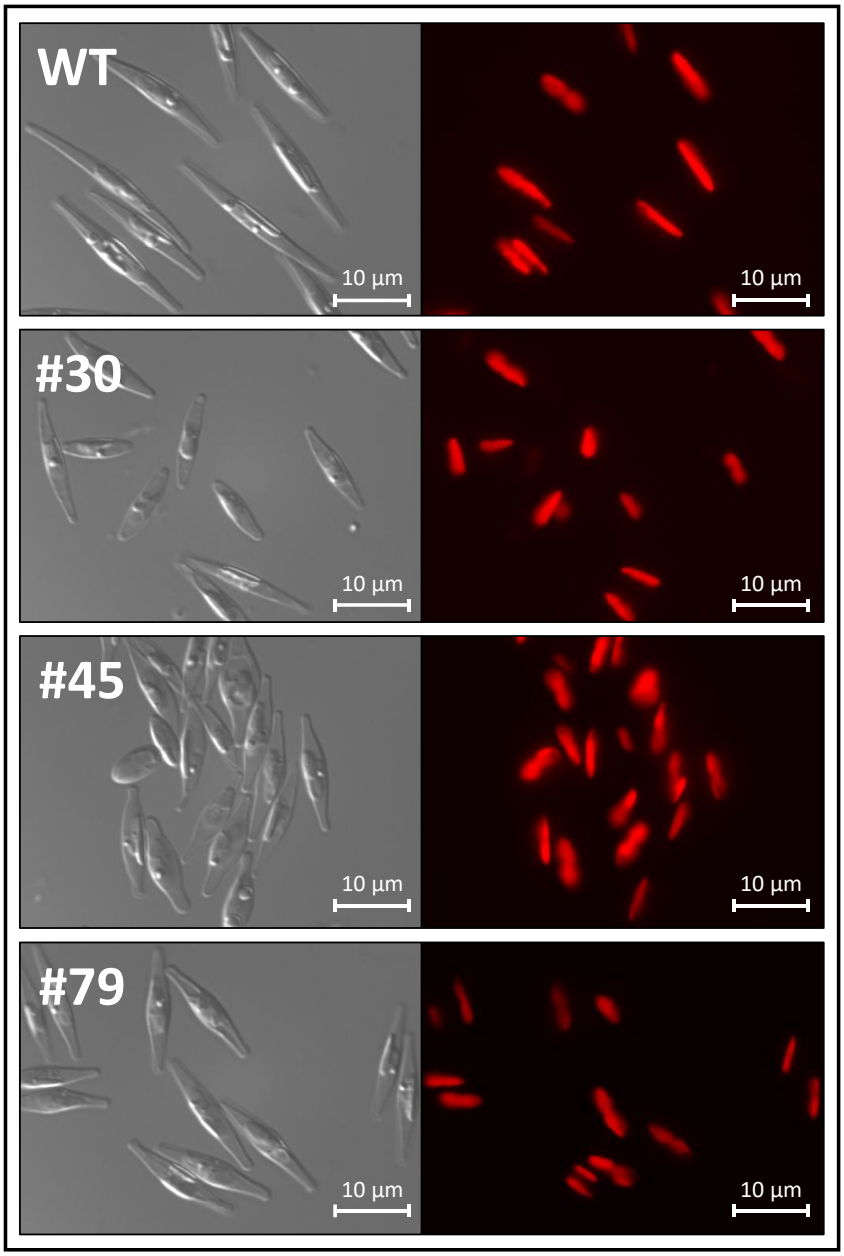

Figure 4.28. Examples of microscopy images of *P. tricornutum* WT and mutant cells. Microscopy images of (left) differential interference contrast or (right) chlorophyll auto-fluorescence of *P. tricornutum* fusiform cells from cultures of the WT, #30, #45 and #79 strains grown under iron-deficient conditions.

Morphological changes were also observed by fluorescence microscopy. Microscopy analysis showed that the differences in cell size arise from changes in the cell morphology more than from a decrease in cell size and volume (Figure 4.28; and compare Table 4.2 and 4.3). Thus, under iron-deficient conditions, WT fusiform cells showed to be more elongated than in the mutant strains (aspect ratio of 6.52, 4.89, 4.25 and 5.15 for WT, #30, #45 and #79 cells, respectively). Consequently, the mutant strains also appeared with an increased circularity,

which actually resulted in an increased cell volume (Table 4.3) and chloroplasts with a thicker shape, as detected by red auto-fluorescence (Figure 4.28).

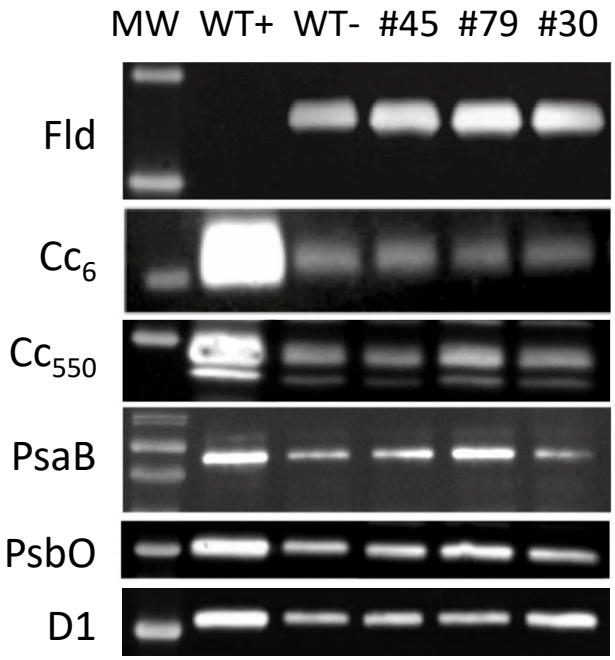

Figure 4.29. Western-blot analysis of different photosynthetic proteins in samples from *P. tricornutum* WT and #30, #45 and #79 mutant cells grown under iron-deficient conditions. MW: molecular weight standard; WT+ and WT-, WT control cells under iron-replete and iron-deficient conditions, respectively; Fld, flavodoxin; Cc_6, soluble cytochrome c_6; Cc_{550}, the extrinsic cytochrome c_{550} subunit of PSII; PsaB, the PsaB membrane intrinsic subunit of PSI; PsbO, the PsbO extrinsic subunit of PSII; D1, the D1 membrane intrinsic subunit of PSII. Protein extracts: 20 µg for PsaB; 10 µg for Cc_6, PsbO and D1; 5 µg for Fld; 2.5 µg for Cc_{550}. Membranes were incubated overnight with the following dilutions of the selected primary antibody: 1:1000 anti-Cc_6, Cc_{550} and PsaB; 1:2000 anti-PsbO; 1:10000 anti-D1; 1:50000 anti-Fld.

The changes in the levels of some photosynthetic proteins under low iron conditions were visualized by Western-blot analysis. In addition to Fld (used as a control of iron deficiency), the studied proteins included soluble Cc_6, PSII subunits (the intrinsic D1 subunit and the luminal extrinsic subunits Cc_{550} and PsbO), as well as the intrinsic PsaB subunit of PSI. The deficiency of iron promotes a drastic decrease in the levels of the two luminal cytochromes, Cc_6 and Cc_{550}, more particularly in the case of Cc_6, as described in the previous chapter (Figure 4.29). Western bands quantification allowed estimating a similar value of ≈10% in the levels of Cc_6 and ≈30% in Cc_{550} in all the strains as compared with iron-replete conditions, in good agreement with the

spectroscopic measurements (Figure 4.9). Regarding other PSII components, the levels of PsbO and D1 were basically analogous in the WT and mutant strains under iron deficiency (Figure 4.29). However, in the case of the PsaB subunit of PSI, the decrease observed in the WT strain under iron-deficient conditions (to ≈40% of the iron-replete levels) seems to be somewhat recovered in the #45 and more clearly in the #79 mutant strains (Figure 4.29). Nevertheless, it is important to note that an increased level of PsaB does not necessarily imply an equivalent amount of active PSI, since other PSI iron-containing subunits are required to form functional PSI complexes.

4.2.3. *In vivo c*-type cytochromes oxidation observed by flash-induced kinetics

An Optical Parametric Oscillator-based spectrophotometer (OPO) was used to measure the time-resolved redox changes associated to *c*-type cytochromes at 420 nm in *P. tricornutum* WT and #30, #45 and #79 strains (Figure 4.30). One millisecond after flash excitation, P_{700} is fully re-reduced, and so the 420 nm signal corresponds to redox changes related to cytochromes.

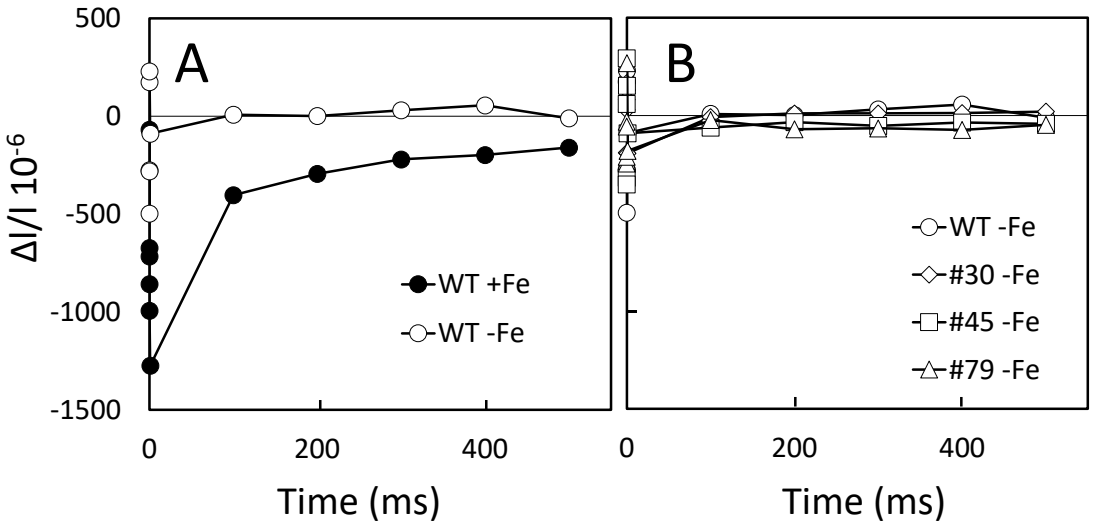

Figure 4.30. Flash-induced measurements of *c*-type cytochromes oxidation/reduction determined at 420 nm. (A) *P. tricornutum* WT cultures under iron-replete (+Fe) and iron-deficient (-Fe) conditions. (B) *P. tricornutum* WT and #30, #45 and #79 strains cultures under iron-deficient conditions.

Under iron-replete conditions, the WT and mutant strains (Figures 4.30A and 4.31) show a comparable initial oxidation of cytochromes at 1ms after flash excitation (detected as a decrease in the absorbance at 420 nm), which relaxes in about 500 ms. These signals can be

mainly assigned to the initial Cc_6 oxidation and further slow re-reduction. However, under iron-deficient conditions the changes associated to cytochromes oxidation are very low (Figures 4.30B and 4.31), in agreement with the decreased content in Cc_6 detected both by absorbance changes and Western-blot analysis.

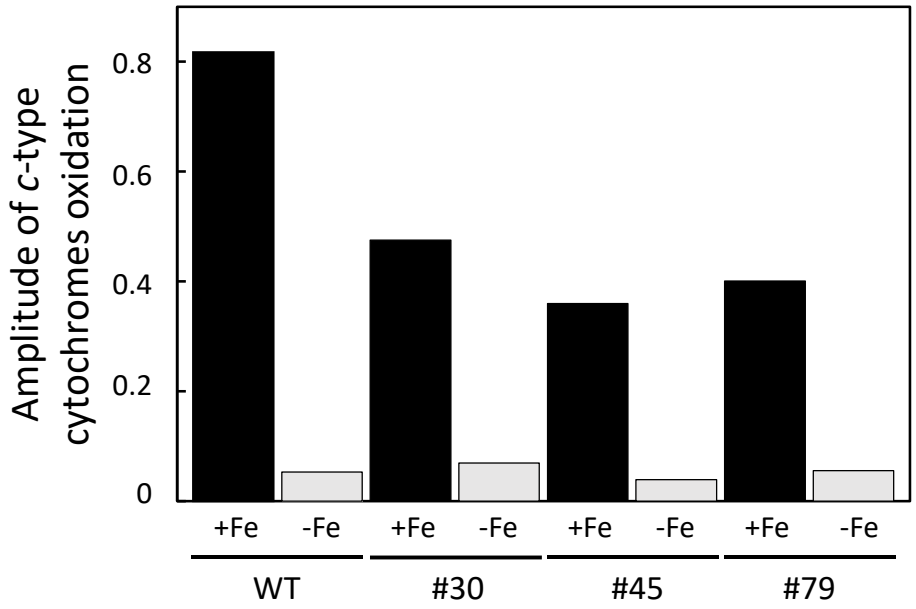

Figure 4.31. Amplitude of *c*-type cytochromes oxidation. Amplitude of the flash-induced initial absorbance changes at 420 nm (corresponding to *c*-type cytochromes oxidation) in *P. tricornutum* WT and #30, #45 and #79 mutant cells under iron-replete (+Fe) and iron-deficient (-Fe) conditions. Data represent mean values of two independent measurements.

4.2.4. Thermoluminescence analysis of *P. tricornutum* cells expressing Pc

The effects of iron deficiency on the PSII electron transfer activity of *P. tricornutum* WT and mutant strains were investigated using the STL technique (Figure 4.32). Excitation of iron-deficient *P. tricornutum* WT cells with two flashes at 1°C induced the appearance of a TL glow curve with a very significant decrease in the total TL signal intensity (about 65%) in comparison with the curves obtained in iron-replete cells (Figure 4.32). The decomposition analysis of these emission curves allowed obtaining two components with similar t_{max} values of 14 and 28°C for both iron conditions. As previously said (Section 4.1.3), these two components can be assigned to the well-known B1 and B2 TL bans, originated from the recombination reactions of $S_3Q_B^-$ and $S_2Q_B^-$ charge pairs in PSII, respectively (Rutherford et al., 1984).

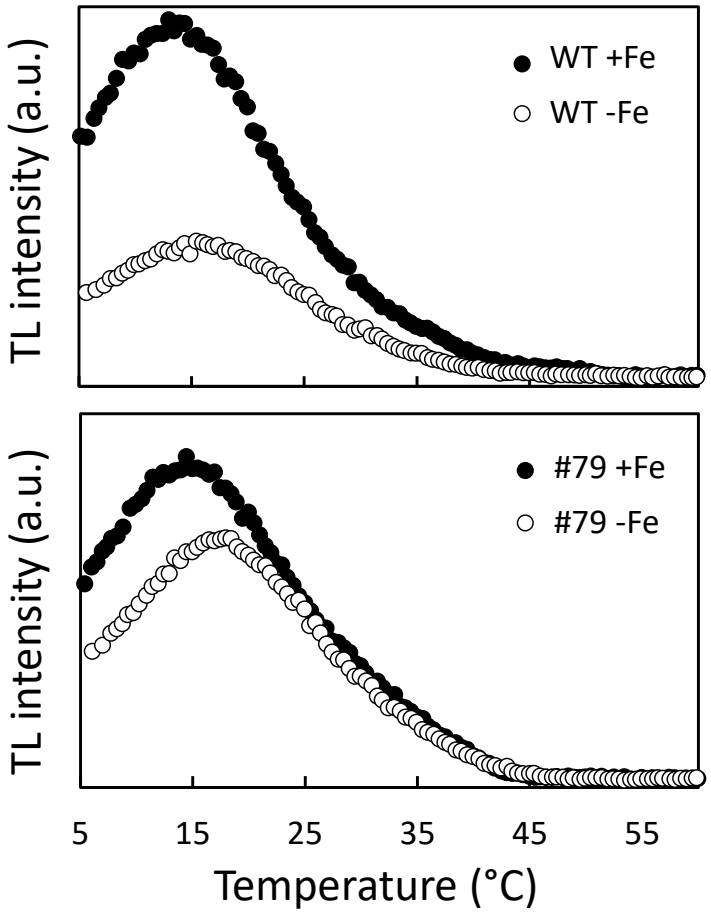

Figure 4.32. Effects of iron deficiency on the photosystem II activity of *P. tricornutum* cells measured by the STL technique. Representative standard TL glow curves of the WT and #79 strains for iron-deficient (-Fe) and iron-replete (+Fe) conditions are shown. Intensities were obtained from the component analysis of the curves of TL.

The TL glow curves obtained for the #79 (Figure 4.32), #30 and #45 (not shown) mutant strains could be also decomposed in two TL components: B1 and B2 bands. The t_{max} values for these components were similar to WT in all strains and for the two iron conditions. The TL glow curves obtained in iron-deficient cells also showed a decrease in the total TL signal intensity with respect to iron-replete conditions (Figures 4.32 and 4.33). However, the comparison between conditions of iron sufficiency or limitation for each strain indicated a much lower decrease in intensity in the mutants compared with the WT strain: 39%, 56% and 18% for #30, #45 and #79 mutant strains, respectively (Figure 4.33), indicating an increased amount of functional PSII in the mutant cells compared with the WT under iron-deficient conditions.

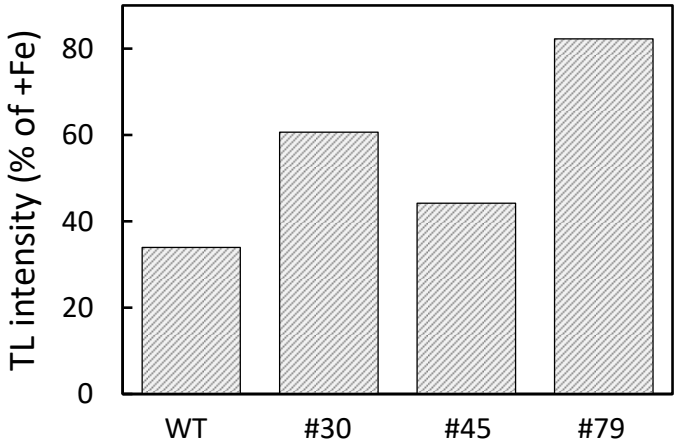

Figure 4.33. Intensities of TL B1 and B2 bands for all the strains investigated under iron-deficient conditions determined by the STL technique. In each case it is shown the percentage referred to iron-replete condition as 100%. Intensities were obtained from the component analysis of the curves of TL. Data represent mean values of three independent measurements.

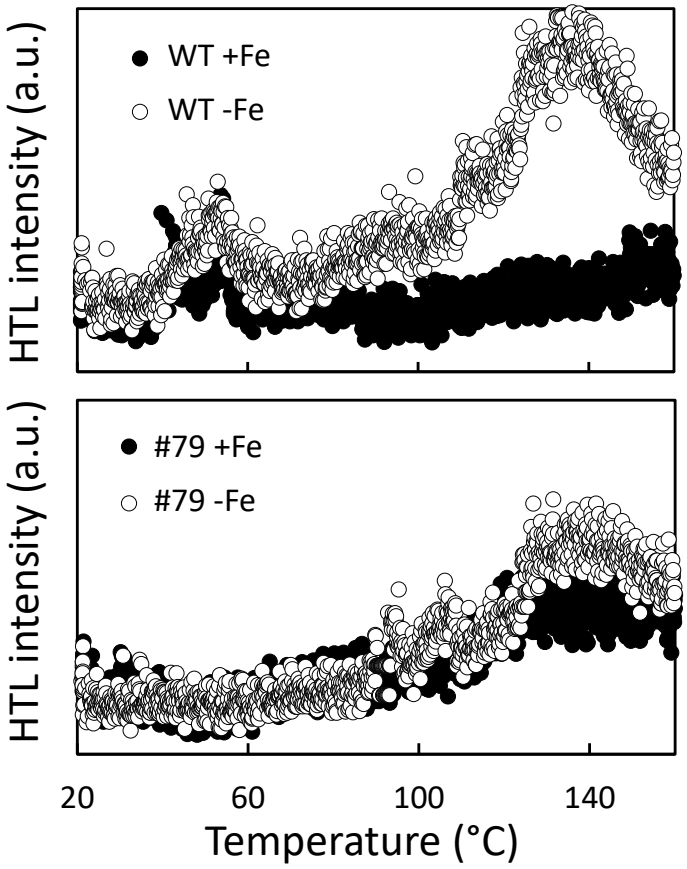

Figure 4.34. Effects of iron deficiency on the lipid peroxidation in *P. tricornutum* WT and mutant strains measured by the HTL technique. Representative high-temperature TL glow curves (HTL2 band) of WT and #79 mutant strains for iron-replete (+Fe) or iron-deficient (-Fe) conditions are shown. Intensities were obtained from the component analysis of the curves of HTL.

The HTL technique was applied to detect lipid peroxidation in *P. tricornutum* WT and mutant cells, cultured in both iron-replete and iron-deficient conditions. Lipid peroxidation is a well-known marker of redox stress and the subsequent generation of reactive oxygen species. Figure 4.34 shows that a broad HTL2 band with a maximum between 130–140^{o}C was present in iron-deficient WT cells. This band was significantly lower in iron-replete cells.

Thus, an important level of lipid peroxidation was observed in WT cells grown under iron-deficient conditions under the relatively low light intensity used. Nonetheless, for the three mutant strain cultured under iron-deficient conditions, the level of lipid peroxidation was significantly lower (Figure 4.35).

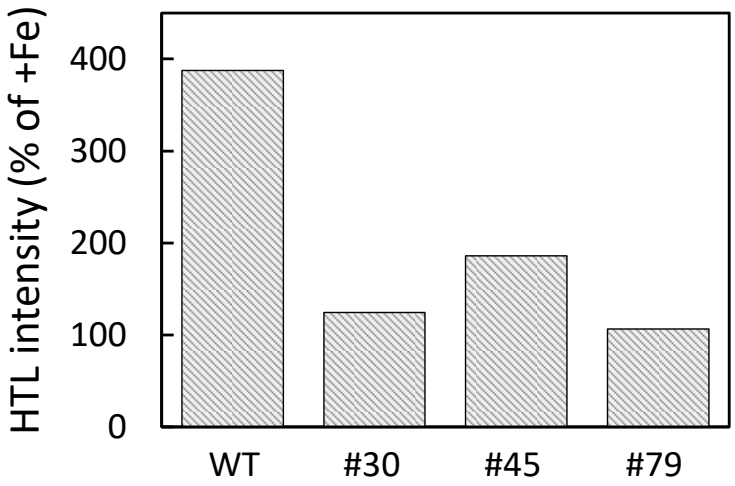

Figure 4.35. Intensities of HTL2 bands for the WT and mutant strains measured by the HTL technique under iron-deficient conditions. In each case it is shown the percentage referred to iron-replete condition as 100%. Intensities were obtained from the component analysis of the curves of HTL. Data represent mean values of three independent measurements.

4.2.5. Photosynthetic measurements by chlorophyll fluorescence analysis in *P. tricornutum* cells expressing Pc

The effects of iron deficiency on PSII photochemistry in the mutants expressing Pc have been further investigated by Chl *a* fluorescence measurements. The maximum quantum yield of PSII, F_v/F_m, was significantly decreased in iron-deficient WT cells (F_v/F_m = 0.331) in comparison with iron-replete cultures (F_v/F_m = 0.632) (Table 4.4). However, the three mutants showed a partial recovery (≈15–30%) of the F_v/F_m values as compared to WT cells under conditions of iron

deficiency, with higher values being obtained for the #45 (0.384) and #79 mutants (0.425) (Table 4.4).

Table 4.4. Photosynthetic measurements obtained by DUAL-PAM. Maximum quantum yield of PSII (F_v/F_m), photosynthetically active radiation intensity (PAR) for relative maximum electron transport rate ($rETR_{max}$), relative electron transport rate (rETR) at the maximum photosynthetically active radiation intensity (PAR_{max}), maximal P_{700}^+ signal upon full oxidation (P_m), and half-life time ($t_{1/2}$) of the P_{700}^+ re-reduction in iron-replete (+Fe) WT and iron-deficient (-Fe) WT cells and the #30, #45 and #79 mutants.

Parameter	WT +Fe	WT -Fe	#30 -Fe	#45 -Fe	#79 -Fe
F_v/F_m	0.632 ± 0.004	0.331 ± 0.014	0.381 ± 0.055	0.384 ± 0.036	0.425 ± 0.044
PAR for $rETR_{max}$ (µmol m^{-2} s^{-1})[a]	500	150	200	350	350
rETR (at PAR_{max})[b]	28.32	3.90	5.65	7.27	7.67
P_m	0.683 ± 0.043 (--)	0.093 ± 0.011 (100%)[c]	0.110 ± 0.008 (118%)[c]	0.105 ± 0.003 (113%)[c]	0.112 ± 0.007 (120%)[c]
$t_{1/2}$ (ms)	4.45 ± 0.23	11.82 ± 0.93	5.35 ± 0.35	6.06 ± 0.37	5.84 ± 0.35

[a]Light intensity for $rETR_{max}$.
[b]rETR values at 1292 µmol m^{-2} s^{-1} light intensity.
[c]Values as percentage of that of WT-Fe cells.

It has been previously shown in cultures of *P. tricornutum* (Roncel et al., 2016) that the effective quantum yield of PSII, Y(II), is significantly lower in iron-deficient cultures as compared with iron-replete conditions at the range of irradiances used; iron-deficient cells being more sensitive to photoinhibition (Roncel et al., 2016; and see Figure 4.36A). In our case, PSII light saturation curves carried out under iron deficiency have shown Y(II) values of a similar magnitude for the mutant strains compared to WT cells, although slightly higher values were observed in the mutants at lower light intensities (Figure 4.36B).

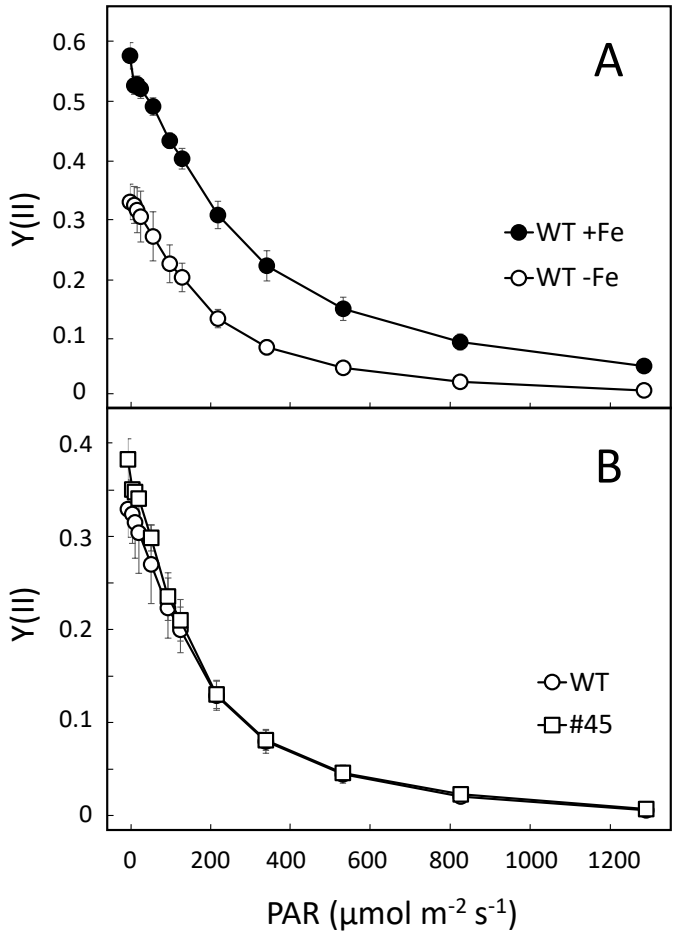

Figure 4.36. Quantum yield of photosystem II photochemistry of WT and mutant #45 strains. (A) Quantum yield of PSII photochemistry, Y(II), in *P. tricornutum* WT cells under iron-replete (+Fe) and iron-deficient (-Fe) conditions. (B) Y(II) in the WT and #45 mutant strains of *P. tricornutum* cells under iron deficiency. Chlorophyll fluorescence was measured with a pulse-amplitude modulation fluorometer. Y(II) values were determined as a function of irradiance derived from steady-state light curves during stepwise increases of photosynthetically active radiation (PAR), from 0 up to 1292 µmol m^{-2} s^{-1} light intensity. Data represent the mean ± SD of five independent experiments.

It has also been previously reported that *P. tricornutum* cells showed differences in the relative electron transport rate (rETR, i.e., the ratio between absorbed light quanta and transported electrons) under iron-replete and iron-deficient conditions (Roncel et al., 2016; and see Figure 4.37A). In cells exposed to gradually increasing light intensities, the electron transport increases in parallel up to its limit capacity. Beyond this point, increasing light intensity induces photoinhibition, that is, a decrease of the rETR (Bailleul et al., 2015; Roncel et al., 2016; and see Figure 4.37A). In this work, iron-deficient WT cells reached its maximum electron transport rate ($rETR_{max}$) at 150 µmol m^{-2} s^{-1} showing inhibited rETR values at higher light intensities (about 30% of the maximum value at ≈1300 µmol m^{-2} s^{-1}; Figure 4.37 and Table 4.4). In contrast, iron-replete

WT cells have shown a $rETR_{max}$ at 500 µmol m^{-2} s^{-1} (Table 4.4 and Figure 4.37A) and, under these conditions, the rETR value measured at the higher light intensity remained at about 85% of the maximum value (Figure 4.37A). Therefore, these results confirmed a substantially higher sensitivity to light for *P. tricornutum* WT cells grown under low iron concentration (Roncel et al., 2016).

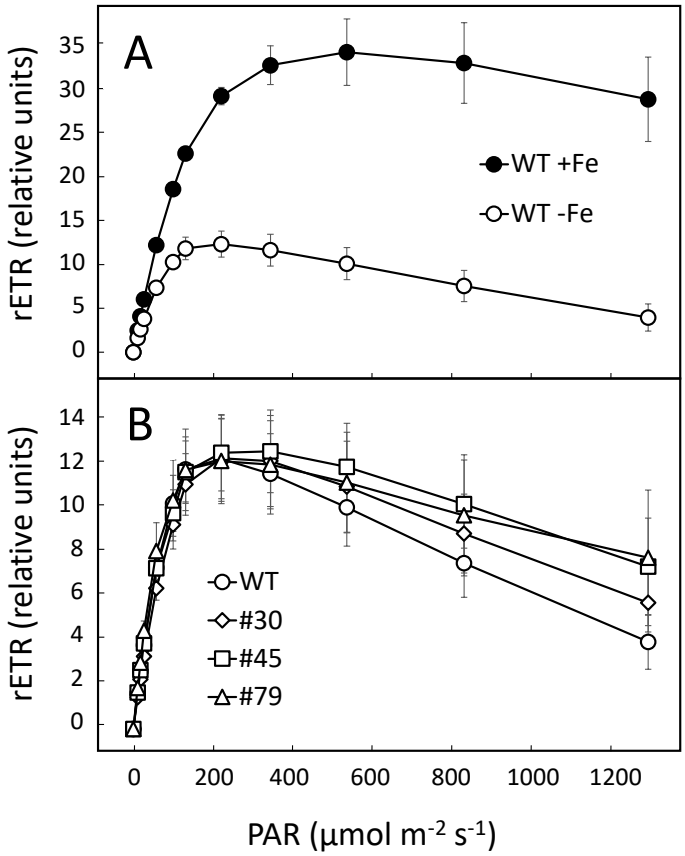

Figure 4.37. Relative linear electron transport rates in *P. tricornutum* WT and mutant #45 strains
(A) Relative linear electron transport rate (rETR) in *P. tricornutum* WT cells under iron-replete (+Fe) and iron-deficient (-Fe) conditions. (B) rETR in the WT and #30, #45 and #79 mutant strains of *P. tricornutum* cells under iron deficiency. Chlorophyll fluorescence was measured with a pulse-amplitude modulation fluorometer, and rETR values were determined as a function of irradiance derived from steady-state light curves during stepwise increasing photosynthetically active radiation (PAR) from 0 up to 1292 µmol m^{-2} s^{-1} light intensity. Data represent mean values ± SD of five independent measurements.

Table 4.4 shows the higher values of photosynthetically active radiation (PAR) observed for the $rETR_{max}$ for the three mutants (reached at 200–350 µmol m^{-2} s^{-1}), as compared to that obtained in the WT (150 µmol m^{-2} s^{-1}) under the same conditions. In addition, the three mutants showed higher rETR values at light intensities above 500 µmol m^{-2} s^{-1} and up to ≈1300 µmol m^{-2}

s^{-1}, at which the rETR values still remained at about 50–65% of the maximum value. Higher values were again observed for the #45 and #79 mutants (Figure 4.37B and Table 4.4). Our results suggest that under iron deficiency, the three mutant strains exhibit better light tolerance, confirming the specific effect of expressing Pc in preventing earlier photoinhibition. This is also in line with the observed faster growth rate of the three mutants.

4.2.6. Analysis of the PSI photochemistry monitored by changes in absorbance in *P. tricornutum* cells expressing Pc

The effects of Pc expression on PSI activity under iron deficiency were also investigated by measuring the P_{700} redox state changes during illumination. In dark-adapted cultures, P_{700} is reduced since the acceptor side of P_{700}, that is, the Calvin-Benson cycle and subsequent reactions, is deactivated. Under actinic light, P_{700} is first oxidized and re-reduced by electrons coming from the PQ pool; thus, by applying saturating pulses, its ability to become oxidized and re-reduced can be determined (Roncel et al., 2016; and see Figure 4.38). Induction-recovery curves were performed in iron-replete and iron-deficient cultures showing that the calculated quantum yield of PSI photochemistry (Y(I); Figure 4.38A) increased in the three mutants compared to WT cells under the same conditions of iron deficiency. On the other hand, the high degree of donor side limitations, Y(ND), observed in iron-deficient WT cells, was slightly reversed in all the mutants (Figure 4.38B).

The higher Y(I) of the three mutants indicates a recovery of the PSI activity missing in the WT cells as a result of the lack of availability of electron donors for PSI (Roncel et al., 2016), as indicated by the OPO results. In contrast, similar acceptor-side limitations, Y(NA), were observed in all the cultures (Figure 4.38C). Thus, the presence of Pc in the three mutants seems to compensate for the deficiency in PSI activity by providing electrons to PSI in the light. To confirm this hypothesis, P_{700} reduction kinetics after saturating light pulses were recorded to obtain the maximal P_{700}^+ signal upon full oxidation (P_m) and the half-life time ($t_{1/2}$) parameters for P_{700}^+ re-reduction (Table 4.4). After illumination with far-red (FR) light and thereafter with a saturating light pulse, P_{700} became oxidized and reached a maximal level of P_{700}^+ (Figure 4.39). As expected, the P_m signal amplitude was significantly lower in WT iron-deficient cells than in iron-replete conditions (Table 4.4). Nevertheless, under conditions of iron deficiency, the three mutants exhibited a slightly higher P_m signal compared to WT cells, thus indicating a somewhat higher amount of active P_{700} (Table 4.4). Following P_m determinations, P_{700}^+ reduction kinetic decays were recorded in darkness, and $t_{1/2}$ for the P_{700}^+ absorption decay could be calculated (Figure 4.39 and Table 4.4). The estimated value of $t_{1/2}$ in WT iron-deficient cultures was ≈3 times higher

compared with iron-replete conditions (11.82 versus 4.45 ms; Table 4.4). However, under iron deficiency, $t_{1/2}$ values were ≈2 times lower in the three mutants (≈5.8 ms) in comparison with WT cells (Table 4.4), thus indicating an acceleration of P_{700}^{+} re-reduction in the three mutants as compared with iron-deficient WT cells (Table 4.4) that can be explained as the result of the presence of a higher amount of electron donors to PSI.

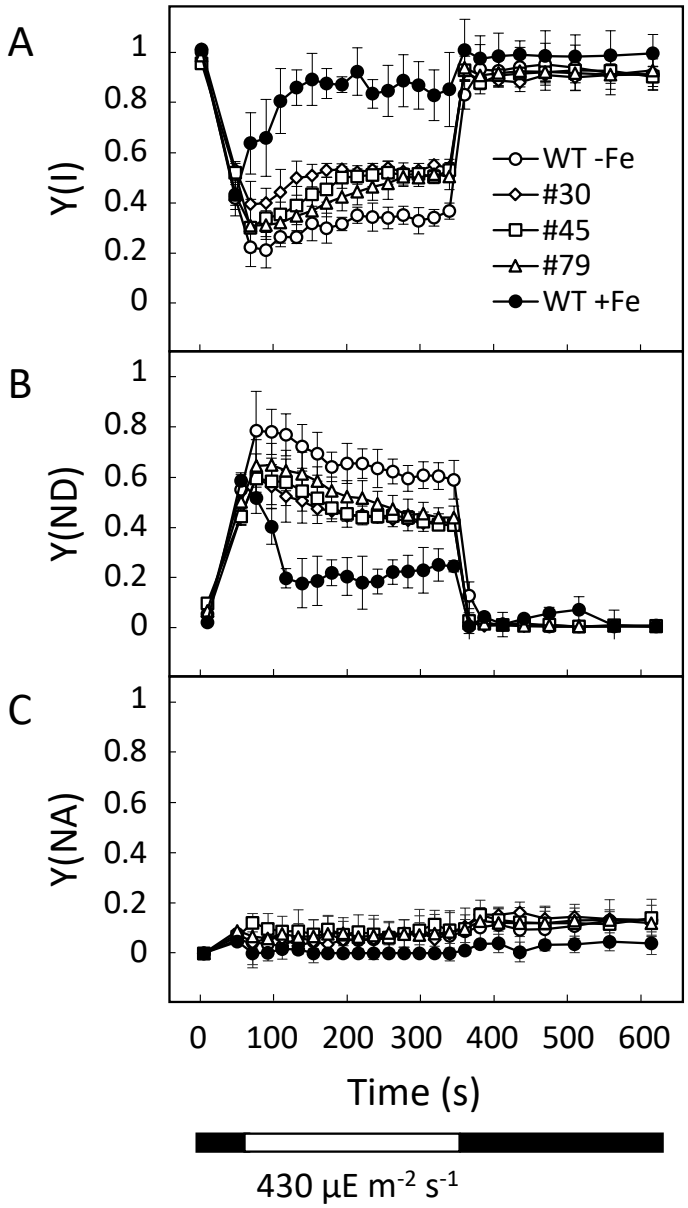

Figure 4.38. Photosystem I activity of *P. tricornutum* WT and mutant strains under iron-deficient conditions. (A-C) PSI activity of WT (WT -Fe) and #30, #45 and #79 mutant cells of *P. tricornutum* under iron-deficient conditions. Values of WT cells in iron-replete conditions (WT +Fe) are also included as a control. The redox state of the PSI reaction centre, P_{700}, was monitored through the changes in absorbance at 830 nm versus 875 nm, measured with a pulse-amplitude modulation fluorometer. Cultures of the different strains were kept in the dark for 30 minutes prior to the measurements. After the initial

determination of the maximal oxidation of P_{700}, actinic light was turned on at an intensity of 430 µmol m^{-2} s^{-1} and saturating pulses were applied every 20 seconds. After 5 minutes, the actinic light was switched off and measurements continued for another 5 minutes. Changes of (A) quantum yields of PSI, Y(I), (B) donor side limitations, Y(ND), and (C) acceptor side limitations, Y(NA), during the course of the induction curve are displayed. Data represent the mean values ± SD of five independent measurements. White and black bars below graphs indicate periods of illumination with actinic light and darkness, respectively.

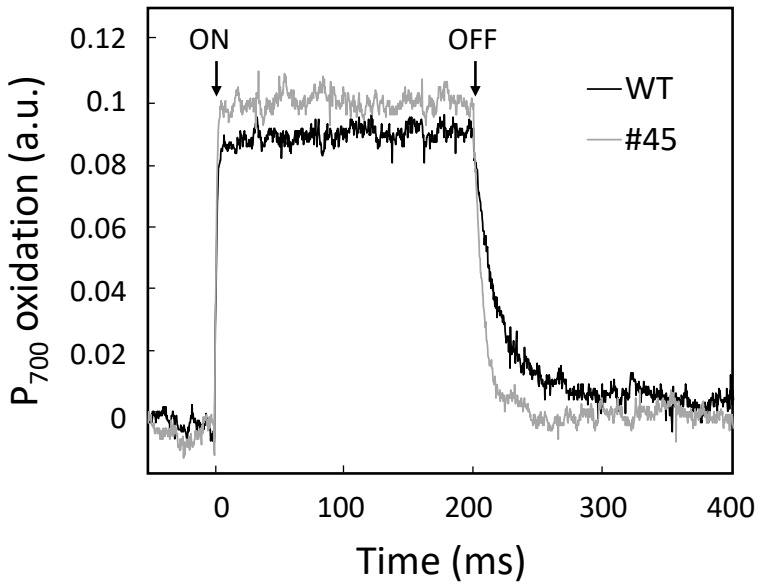

Figure 4.39. Comparison of fast oxidation-reduction kinetics of photosystem I in WT and #45 mutant cells of *P. tricornutum* under iron deficiency. The redox state of the PSI reaction centre, P_{700}, was monitored through the changes in absorbance at 830 nm versus 875 nm. Complete P_{700} oxidation was achieved by preillumination with far-red light (730 nm, 75 W m^{-2}) and a saturating pulse (635 nm, 10,000 µmol m^{-2} s^{-1}) of 200 ms.

4.3. Chapter III

Modelling of the [cytochrome *f*:acceptor] electron transfer complexes in *Phaeodactylum tricornutum* and *Thalassiosira oceanica*

4.3. Chapter III. Modelling of the [cytochrome *f*:acceptor] electron transfer complexes in *Phaeodactylum tricornutum* and *Thalassiosira oceanica*

4.3.1. Structural modelling of Cf and Pc of different algae of the red lineage

Modelled structures of *P. tricornutum* and *T. oceanica* Cf, and *T. oceanica* Pc, were obtained from the available sequences (Figures 4.40 and 4.41) by using MODELLER version 9v23 (Sali & Blundell, 1993) using the Cf (PDB code, 1cfm) and Pc (PDB code, 2plt) of *C. reinhardtii* as templates, respectively. The surface electrostatic potential computed on the structural models of *P. tricornutum* and *T. oceanica* Cf (Figure 4.40) shows the conservation of the ET exposed area around the Y1 and the heme, as well as a positive area placed in an equivalent position relative to the green-type Cf (Figure 4.40). However, due to the substitution of positive groups in the interface of the large and small domains, in the red lineage the positive electrostatic potential of this area in the Cf surface is sensibly reduced (Figure 4.40), which is in accordance with the decreased electrostatic character of Cc_6. However, in the case of *T. oceanica* Cf, it is interesting to note the presence of positive groups in the southern part of the protein, outside the usual ET region around the heme-exposed area (Figure 4.40).

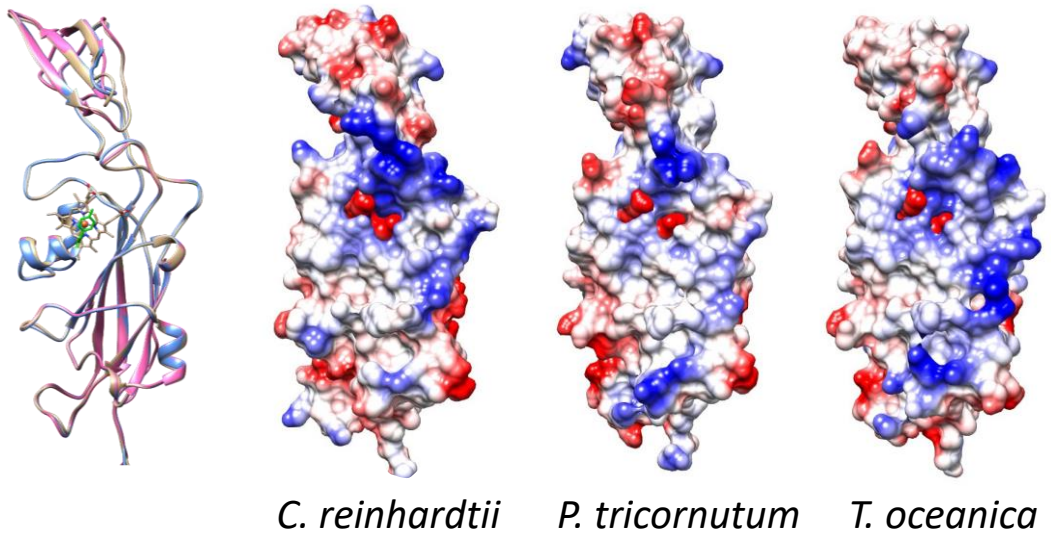

Figure 4.40. Superimposition of backbones and surface electrostatic potential distribution of cytochromes *f*. (Left) Superimposition of backbones of Cf from *C. reinhardtii* (PDB code, 1cfm; light brown), and Cf models of *P. tricornutum* (blue) and *T. oceanica* (magenta), obtained using the Cf of *C. reinhardtii* as a template. The view displays in front both the heme group and the bound Tyr1 (in green). (Right) Surface electrostatic potential distributions of *C. reinhardtii* Cf and the structural models of *P. tricornutum* and *T. oceanica* Cf. The proteins are oriented as shown in the backbone representation on the left. Electrostatic potential values are shown on a scale from red to blue, corresponding to –10.0 and +10.0 kcal/(mol·e), respectively, at 298K.

The Pc-translated region in diatoms is closely related to the Pc from green algae. Consequently, the “red” acquired Pc of *T. oceanica* actually shows the typical strong negative electrostatics of a "green-type" Pc (Figure 4.41).

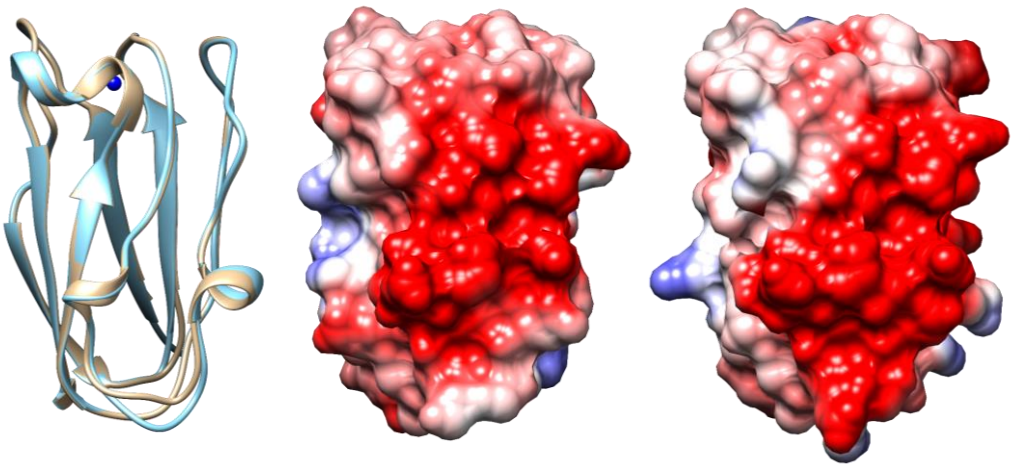

Figure 4.41. Superimposition of backbones and surface electrostatic potential distribution of plastocyanins. (Left) Superimposition of backbones of Pc from *C. reinhardtii* (PDB code, 2plt; light brown) and the *T. oceanica* model (blue), obtained using the Pc of *C. reinhardtii* as a template. The copper atom is depicted in dark blue. (Right) Surface electrostatic potential distribution of *C. reinhardtii* Pc and the structural model of *T. oceanica* Pc. The proteins are oriented as shown in the backbone representation on the left, displaying their electrostatic areas in front and with the hydrophobic patches at the top. Electrostatic potential values are shown on the same scale as Figure 4.40.

4.3.2. Modelling of the interaction of Cf with the soluble carriers in the red lineage

There are no structural data available about the [Cf:Cc_6] (and [Cf:Pc]) complexes in organisms of the red lineage. Here we have carried out docking simulations to study the [Cf:Cc_6] complex in diatoms by using pyDock, a protein-protein rigid-body protocol that uses electrostatics and desolvation energy to score the generated docking poses (Jiménez-García et al., 2013). To validate our analysis, the same approach has also been used to explore the [Cf:Cc_6] complex of the green alga *C. reinhardtii*, previously studied by BD simulations (Gross & Pearson, 2003; Haddadian & Gross, 2005, 2006). Our results indicate that the best-energy docking models for the *C. reinhardtii* complex converge towards an orientation with the shortest cofactors distance (Figure 4.42A). This orientation is basically identical to the models previously described (Haddadian & Gross, 2005, 2006). The Figure 4.43 also shows, as an example of the green [Cf:Pc] complex, the NMR-solved structure of the [Cf:Pc] complex of plants (Ubbink et al., 1998).

In the case of *P. tricornutum*, the energy-distance landscape of the docking models of the native [Cf:Cc_6] complex also shows that the lowest-energy models converge towards orientations with a short distance between the heme iron in Cf and the heme group in Cc_6 (Figure 4.42B).

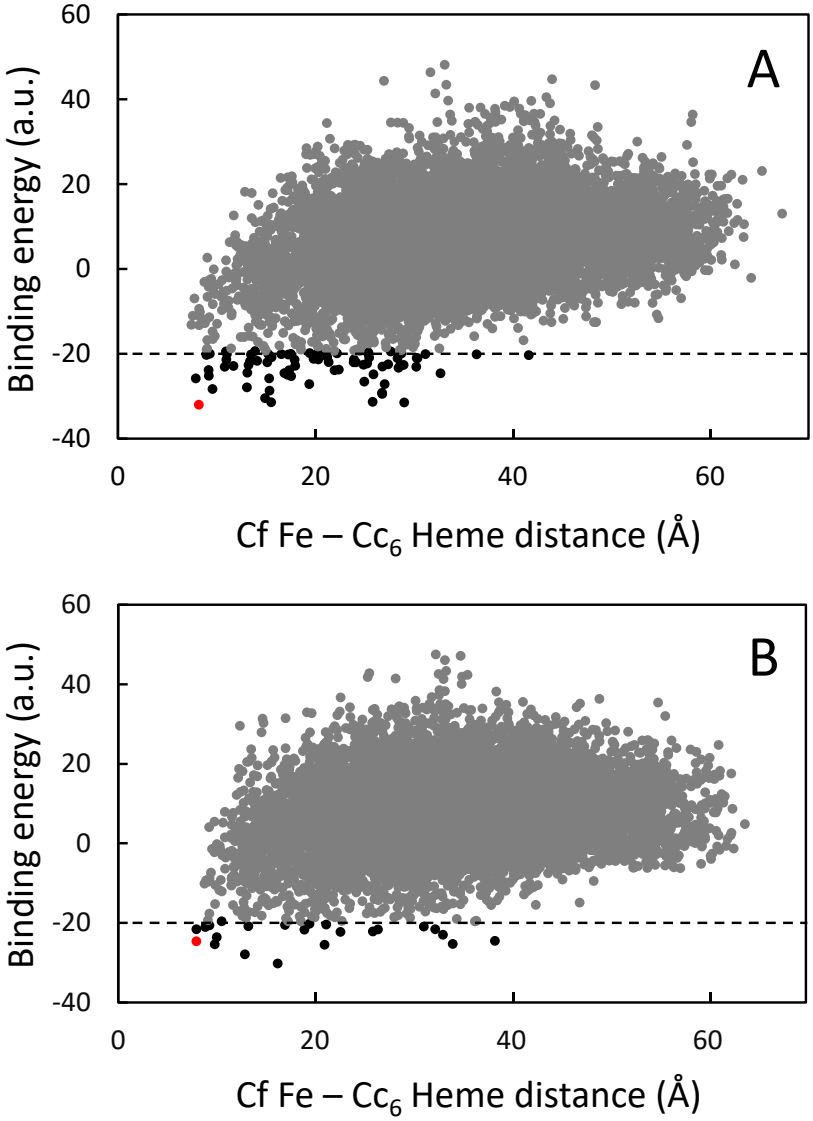

Figure 4.42. Landscapes for the computational docking results of the [Cf:Cc_6] complex of (A) *C. reinhardtii* and (B) *P. tricornutum*. The distances between the iron atom of Cf and the heme group of Cc_6 were considered. The lowest-energy and best distance docking orientations, showed in the next Figure, are highlighted in red.

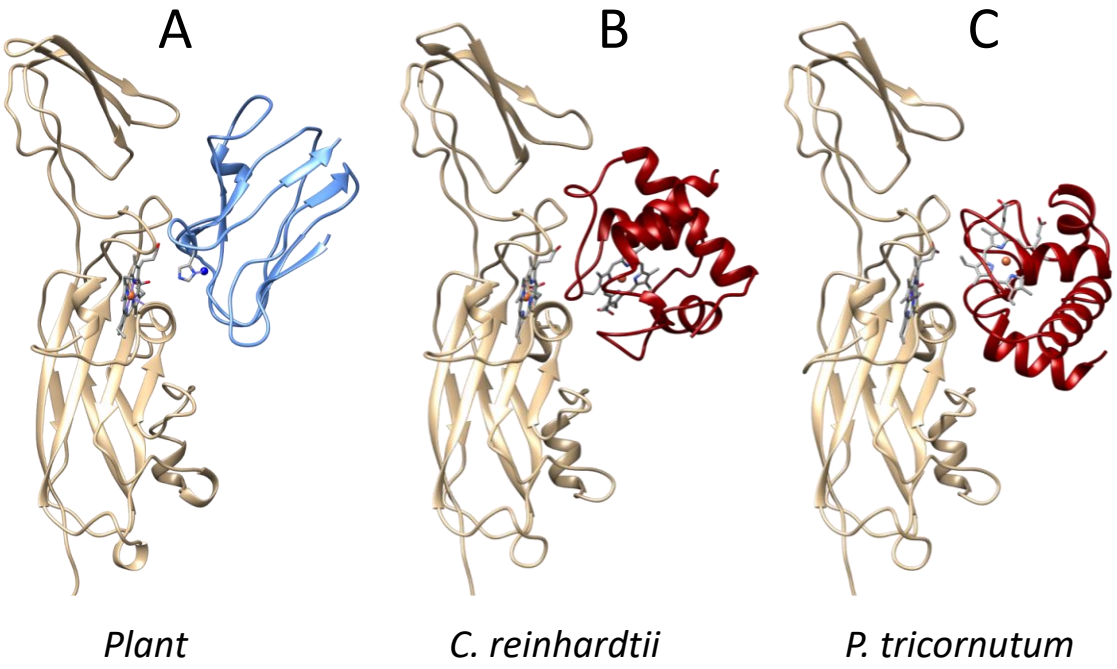

Figure 4.43. Representative structures for the [Cf:Pc] complex of plants and best-energy docking models for the [Cf:Cc_6] complexes of *C. reinhardtii* and *P. tricornutum*. (A) Representative structure for the plant [Cf:Pc] complex (turnip Cf and spinach Pc; PDB code, 2pcf) (Ubbink et al., 1998). Pc is coloured in blue and the copper-bound His87 is shown. (B, C) Best-energy docking models for efficient ET between Cf (in light brown) and Cc_6 (in red) of the green alga *C. reinhardtii* (rank 1, docking energy –32.0 a.u., distance between Fe in Cf to heme in Cc_6 of 8.2 Å) and *P. tricornutum* (rank 6, docking energy –24.7 a.u., distance between Fe in Cf to heme in Cc_6 of 8.0 Å, the shortest distance model).

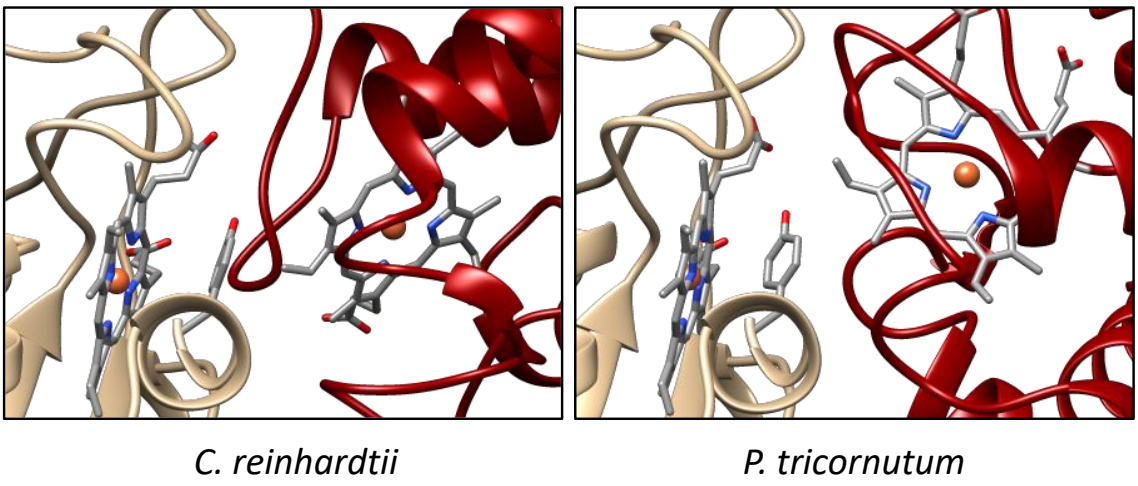

Figure 4.44. Zoom of the heme areas of the docking models for the [Cf:Cc_6] complex of *C. reinhardtii* and *P. tricornutum*. Zoom of the heme areas of the best-energy docking models, shown in the previous Figure, for efficient ET between Cf (in light brown) and Cc_6 (in red) of *C. reinhardtii* (left) and *P. tricornutum* (right). The Tyr1 groups in Cf are also shown.

However, the *P. tricornutum* [Cf:Cc_6] docking complex has a different orientation compared with the model of the equivalent green complex in *C. reinhardtii* (Haddadian & Gross, 2005) (Figures 4.43 and 4.44). Thus the docking models of the *P. tricornutum* [Cf:Cc_6] complex with the lowest –most favourable– energies and optimal distances between the Fe in Cf and the heme cofactor in Cc_6 (energies from –25 to –22 a. u.; distances between 8 and 10 Å) have a "head-on" orientation (Figures 4.42B and 4.43), more similar to that described previously in cyanobacterial systems. These orientations display smaller interfaces and weaker electrostatic interactions, with hydrophobic interactions being more relevant (Crowley et al., 2001; Cruz-Gallardo et al., 2012) (Figure 4.43). Consequently, although both *C. reinhardtii* and *P. tricornutum* complexes present a similar distance (≈8 Å) between the two cofactors (Figure 4.44), the green alga complex has a lower and more favourable energy (–32 *versus* –24.7, a.u.), indicating higher binding affinities as a result of the stronger electrostatics in this complex. Remarkably, in the *P. tricornutum* complex the small domain of Cf appears to have only a minor role in the interaction with Cc_6 (Figure 4.43). In fact, the simulated deletion of the Cf small domain did not significantly affect the docking to Cc_6 (Figure 4.45). This latter result is in contrast with the docking simulation in *C. reinhardtii*, in which the deletion of the Cf small domain affected the binding positions on Cf of both Pc and Cc_6 (Haddadian & Gross, 2006).

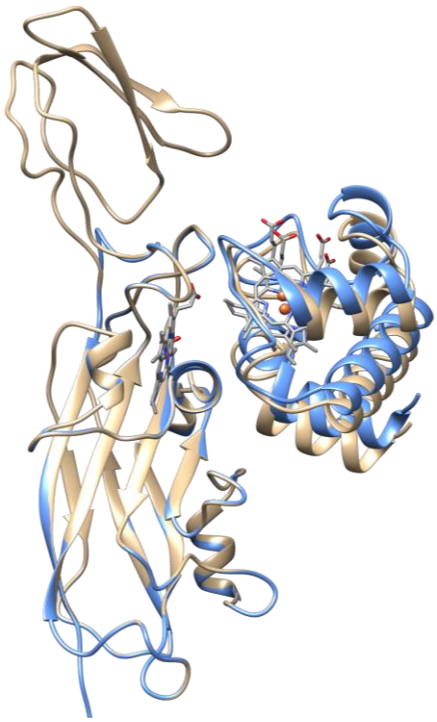

Figure 4.45. Superimposed docking models of *P. tricornutum*. Superimposed docking models of the *P. tricornutum* [Cf:Cc_6] complex and the model (in blue) corresponding to a truncated Cf without the small domain (rank 2, docking energy –31.0 a.u., distance between Fe in Cf to heme in Cc_6 of 8.4 Å).

Interestingly, the energy-distance landscape of the docking models of the native [Cf:Cc_6] complex of *P. tricornutum* shows alternative docking orientations either with a cofactors' short distance (ca. 9 Å) or a lower energy (ca. –30 a.u.) (Figure 4.46A-B), but in the first case with unfavourable binding energies (ca. –2 a.u.), and in the second with longer distances (ca. 16 Å) between the cofactors. Moreover, "side-on" docking orientations can be found in *P. tricornutum* that are relatively similar to the best-energy models obtained in *C. reinhardtii* (Figure 4.46C). However, although these orientations have short distances between the Fe in Cf and the heme cofactor in Cc_6 (between 9.0 to 10.5 Å) they have unfavourable higher energies (from –15 to –9 a.u.).

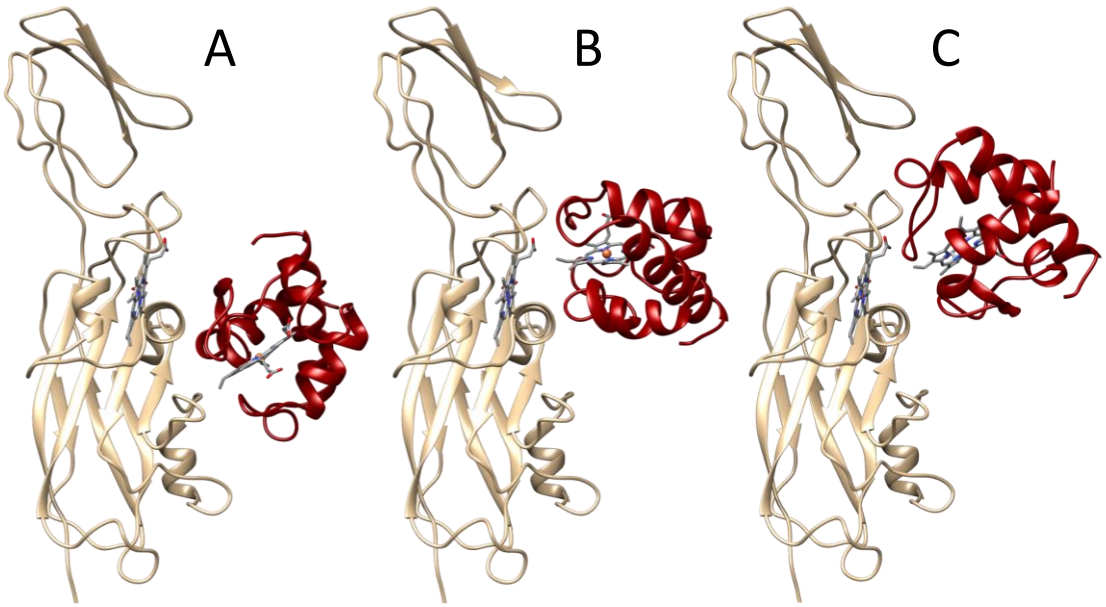

Figure 4.46. Alternative docking orientations of the [Cf:Cc_6] complex. Alternative docking orientations for the *P. tricornutum* [Cf:Cc_6] complex with (A) a cofactors' long distance but favourable energy (docking energy –30 a.u., distance between Fe in Cf to heme in Cc_6 of 16 Å), (B) a cofactors' short distance but unfavourable energy (docking energy –2 a.u., distance between Fe in Cf to heme in Cc_6 of 9 Å) and (C) a docking orientation similar to the best-models obtained with *C. reinhardtii* (docking energy –15.3 a.u., distance between Fe in Cf to heme in Cc_6 of 9.9 Å).

Finally, we have also analyzed the modelled [Cf:Pc] complex of *T. oceanica* and compared it with the above described [Cf:Cc_6] complex of *P. tricornutum*, as well as with the equivalent [Cf:Pc] complex of *C. reinhardtii* in the green lineage. Remarkably, the docking between *T. oceanica* Cf and Pc produced a much larger population of low-energy docking orientations than the *P. tricornutum* [Cf:Cc_6] complex. This indicates higher binding affinities, possibly as a result

again of the stronger electrostatics of the acquired "green-type" Pc (Figure 4.47). However, in *T. oceanica* the energy-distance landscape does not converge towards a single prevalent low-energy orientation with a short distance between Cu (in Pc) and Fe (in the Cf heme). On the contrary, it results in a series of different orientations in a similar range of energies and distances (Figures 4.47 and 4.48). Therefore, different protein-protein orientations might be functionally possible and could coexist. The best energy/distance balanced dockings of the *T. oceanica* [Cf:Pc] modelled complex (Figure 4.47) include: (i) a "head-on" configuration, relatively similar to some cyanobacterial complexes, involving the hydrophobic patches of both Cf and Pc with no interactions between the electrostatic areas or the Cf small domain (energy of –24.2 a.u. and the shortest Fe–Cu distance of 11.1 Å) (Figure 4.48A); (ii) a "side-on" configuration, more similar to the green complexes (Figures 4.43A and 4.48B), involving the electrostatic and hydrophobic patches of both proteins and the small domain of Cf (energy of –31.1 a.u.; Fe–Cu distance of 12.7 Å) (Figure 4.48B); and (iii) an intermediate configuration, which includes the hydrophobic patches and some residues of the electrostatic patches (energy of –30.1 a.u.; Fe–Cu distance of 12.2 Å) (Figures 4.48C and 4.49).

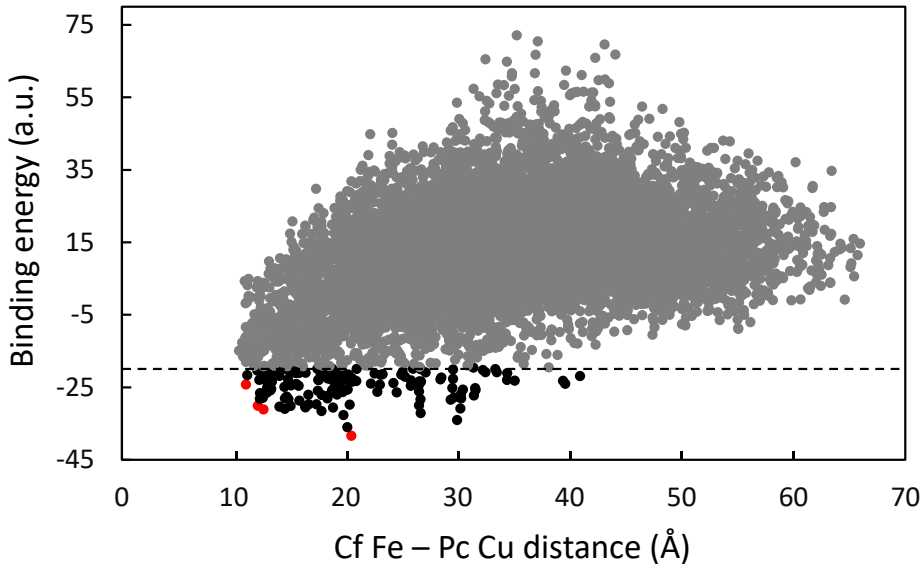

Figure 4.47. Landscape for the computational docking results of the [Cf:Pc] complex of *T. oceanica*. The docking orientations showed in the next Figure are highlighted in red. The distances between the iron in Cf and the copper in Pc were considered.

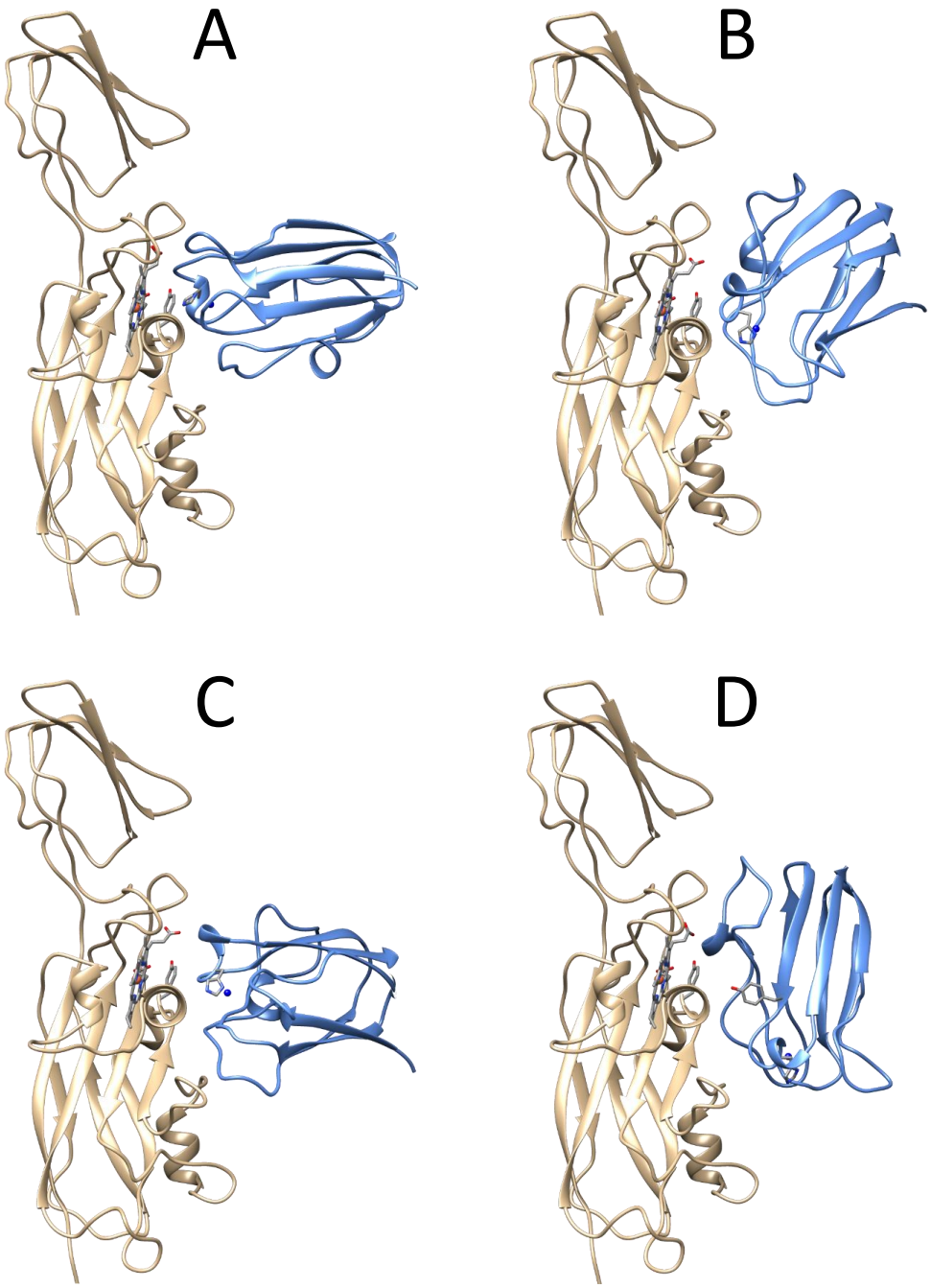

Figure 4.48. Docking models for the [Cf:Pc] complex of *T. oceanica*. (A-C) Representative best-energy docking models for efficient ET between the modelled Cf (in light brown) and Pc (in blue) of the diatom *T. oceanica* (selected by the shorter distances between Fe in Cf and Cu in Pc). The Cf heme, the iron-bound Tyr1 and the copper-bound His88 in Pc are shown. (A) Rank 62, docking energy –24.2 a.u., distance between Fe in Cf to Cu in Pc of 11.1 Å (the shortest distance model). (B) Rank 8, docking energy –31.1 a. u., distance between Fe in Cf to Cu in Pc of 12.7 Å. (C) Rank 16, docking energy –30.1 a.u., distance between Fe in Cf to Cu in Pc of 12.2 Å. (D) Best-energy docking model, showing the Tyr84 group in Pc (rank 1, docking energy –38.4 a.u., distance between Fe in Cf to Cu in Pc of 20.5 Å).

Surprisingly, the clearly more favorable energies (energy of –38 to –36 a.u.) correspond to a cluster of very similar orientations (Figures 4.47 and 4.48D), in which the electrostatic patches of both proteins establish strong interactions, also involving the additional positive groups outside the usual region of ET in Cf. However, in these orientations the Cu and the Fe are located at a long distance from each other (Fe–Cu distance of ≈20 Å) (Figures 4.48D and 4.49). Obviously, these orientations also show a long distance from the Fe in Cf to the groups that form the hydrophobic patch of Pc, and in particular to the Cu-binding H87 residue (H88 in the sequence of *T. oceanica*) (Figure 4.49). However, in the apparently unproductive orientations of lowest energy in *T. oceanica*, the highly conserved Y84 residue in Pc (typically referred to as Y83 in cyanobacterial and eukaryotic Pc) points directly towards the heme-binding Y1 of Cf (Y1–Y84 distance of 5.1 Å; Fe–Y84 distance of 9.9 Å) (Figures 4.48D and 4.49).

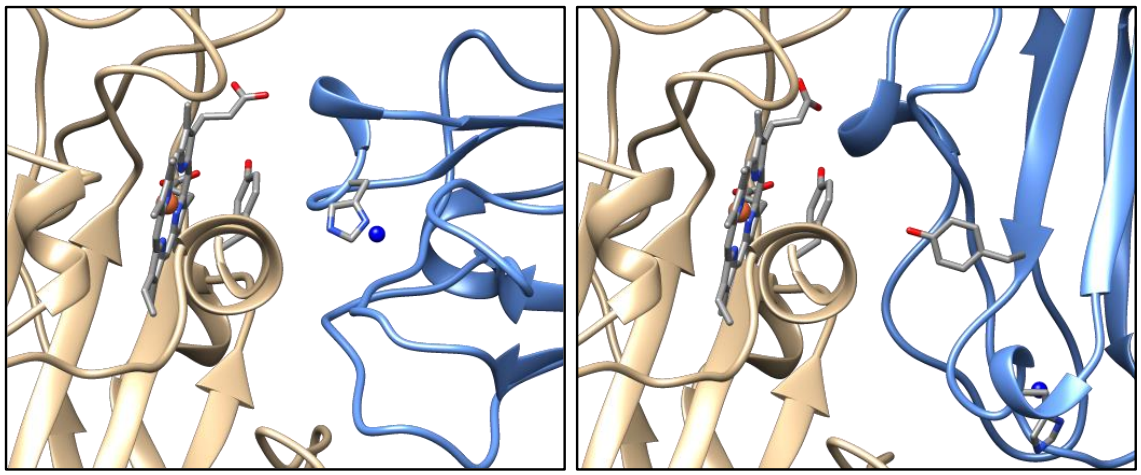

Figure 4.49. Zoom of the cofactors areas of the docking models for the [Cf:Pc] complex of *T. oceanica*. The docking models C (left) and D (right), of the [Cf:Pc] complex of *T. oceanica* shown in the Figure 4.48 are depicted.

5. Discussion

5. Discussion

5.1. Chapter I. The photosynthetic cytochrome c_{550} from the diatom *Phaeodactylum tricornutum*

Cc_{550} is an extrinsic component in the luminal side of PSII in cyanobacteria, but also in eukaryotic algae from the red photosynthetic lineage, which comprises diatoms. This protein is however absent in the green lineage, which comprises green algae and plants (Enami et al., 2008; Roncel et al., 2012; Ifuku & Noguchi, 2016). The role of Cc_{550} in PSII appears to be stabilizing the Mn_4CaO_5 cluster, mainly through the binding of Cl^- and Ca^{2+} ions or by facilitating the binding of other extrinsic subunits (Shen & Inoue, 1993; Enami et al., 1998, 2008; Kerfeld & Krogmann, 1998; Shen et al., 1998; Nagao et al., 2010a,b; Bricker et al., 2012; Xiao et al., 2020) and to contribute to entry/exit channels for water or protons from the Mn_4CaO_5 cluster in the proton-coupled electron transfer via Y_z (Umena et al., 2011; Vogt et al., 2015; Pi et al., 2019; Xiao et al., 2020). In many organisms Cc_{550} can be easily purified as a soluble protein (Navarro et al., 1995; Kerfeld & Krogmann, 1998; Bernal-Bayard et al., 2017), and the existence of two different populations of Cc_{550} (bound to the PSII or free in the lumen) has been described (Kirilovsky et al., 2004). Recently, the photosynthetic Cc_{550} from *P. tricornutum* has been purified in our group from algal cells (Bernal-Bayard et al., 2017). In addition to a relatively weaker affinity of Cc_{550} for the diatom PSII complex, the purified protein was described as being truncated/modified, as the observed MW was lower than that expected from the gene sequence (Bernal-Bayard et al., 2017). In this work, we have purified and further characterized the Cc_{550} from the diatom *P. tricornutum*.

The general spectral and redox properties of *P. tricornutum* Cc_{550} are similar to the cyanobacterial protein. The estimated $E_{m,7}$ value of ca. –190 mV for the purified protein is at least 60 mV more positive than values described in cyanobacteria at pH 7 for the protein in solution (Navarro et al., 1995; Roncel et al., 2003; Guerrero et al., 2011). In the cyanobacterium *T. elongatus* the redox potential of isolated Cc_{550} is pH-dependent, and varies from –150 to –350 mV as the pH increases from 5 to 10 (Roncel et al., 2003). However, in *P. tricornutum* the redox potential remains basically constant in the pH range from 5 to 7, which, as will be discussed below, can be related to the hydrophobic character of the heme solvent-exposed area compared to the negative electrostatic area of the cyanobacterial Cc_{550}.

Our results demonstrate that *P. tricornutum* Cc_{550} is purified in a truncated form when using standard purification protocols, lacking the last two C-terminal tyrosines and discarding other possible protein modifications. The physiological relevance of this fact, *i.e.*, if the

truncated Cc_{550} is the result of a specific processing or arises from the unspecific exposition of the protein to cell proteases during the purification course, has been answered in this Thesis. The fast resolution of crude extracts of *P. tricornutum* heated cells on polyacrylamide gel electrophoresis, and the in gel tryptic digestion and MS peptide fingerprint, demonstrated the presence of the complete protein. In addition, a protocol designed for the purification of Cc_{550} from the membrane fractions indicated that the truncation is a non-physiological process. This is a very remarkable result, because in spite of the relatively high amount of Cc_{550} in the initial crude extracts, no traces of the theoretical complete protein were previously detected in any case in the different fractions and steps of purification (Bernal-Bayard et al., 2017). Moreover, the enzymatic activity responsible of Cc_{550} truncation seems to be widespread among several lines of the red lineage of eukaryotic algae, but it is absent in cyanobacteria. In this sense, several serine and zinc carboxypeptidases are annotated in the *P. tricornutum* genome (Bowler et al., 2008). Moreover, thylakoid proteolytic activities are also associated to PSII turnover, related to photochemical oxidative effects and to dynamic adaptations under different environmental conditions (Aro et al., 1993; Kato & Sakamoto, 2010). In *C. gracilis*, in particular, the PSII complex was described to be remarkably unstable, and rapid protein degradation was observed (Nagao et al., 2007 & 2012). In addition, at least four new proteases were detected in the thylakoid membranes of this diatom (Nagao et al., 2012). However, the identification of the specific protease responsible of Cc_{550} truncation remains to be established.

Iron limitation is known to affect the intracellular levels of iron-containing proteins in *P. tricornutum*, including those with a function in photosynthesis (Allen et al., 2008; Nunn et al., 2013). This down-regulation includes Fd (replaced by Fld), PSI and some subunits of the Cb_6f complex (Allen et al., 2008; Morrissey & Bowler, 2012; Nunn et al., 2013). In particular, previous results obtained in our lab indicated a drastic decrease of the Cc_6 content in iron-depleted *P. tricornutum* cells (0.12 µM Fe) as compared with iron-replete conditions (Roncel et al., 2016). In this work, we have extended this preliminary study to analyse in detail the effects of iron deprivation on the content of both Cc_6 and Cc_{550} in *P. tricornutum*. Our results suggest a similar iron-regulation process for these two main luminal heme proteins. It is interesting to note that although Cc_6 is more abundant under iron-replete conditions, under iron limiting conditions the content of Cc_6 and Cc_{550} is similar because the more pronounced decrease of the former. Thus, *P. tricornutum* somewhat "prefers" to decrease the content of the soluble electron carrier between the Cb_6f and PSI complexes while trying to maintain the level of the extrinsic subunit of PSII as much as possible.

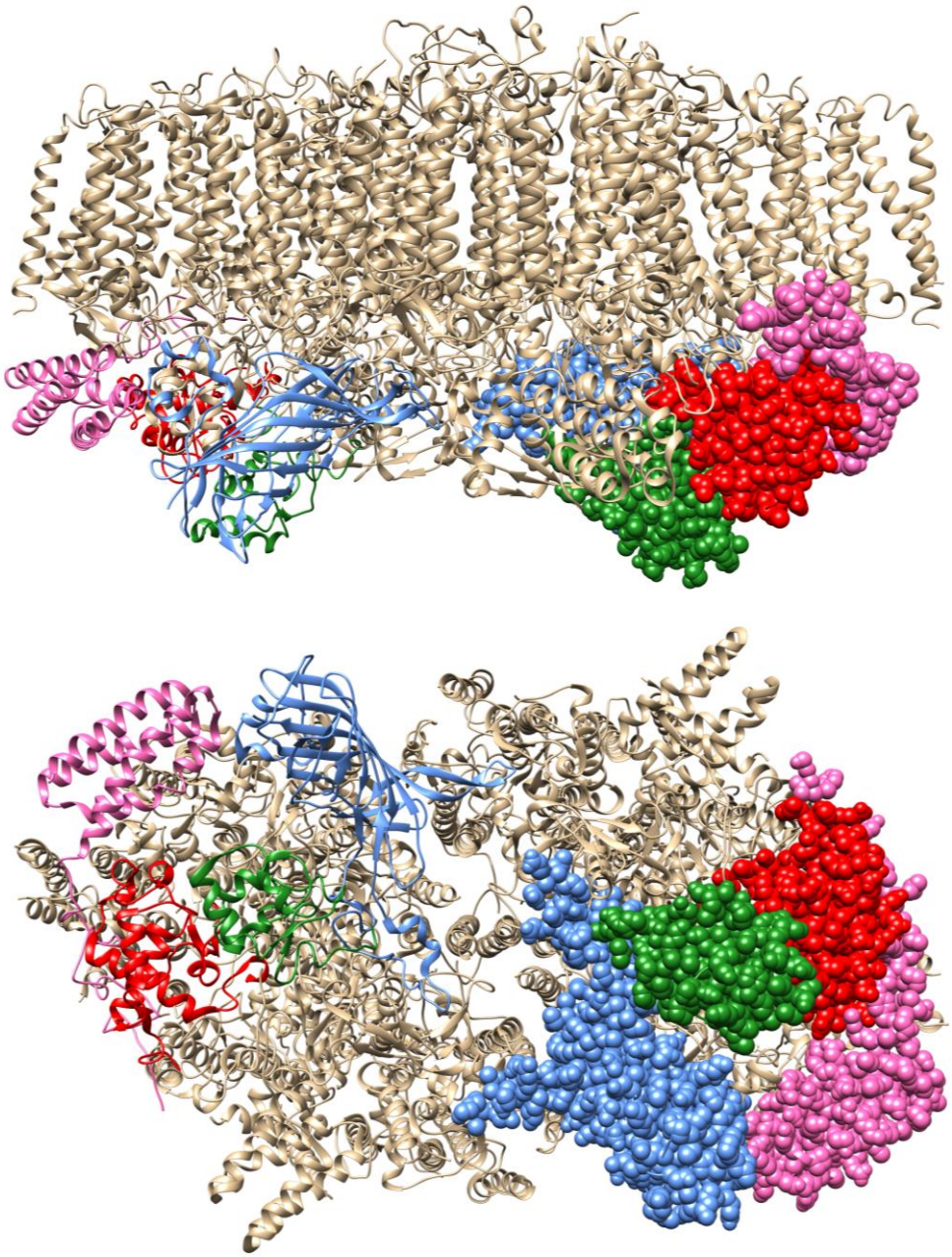

Figure 5.1. Photosystem II core of the diatom *C. gracilis.* The extrinsic subunits are highlighted: PsbO (blue), Cc_{550} (red), PsbU (green), PsbQ' (pink). PDB code, 6jlu (Pi et al., 2019). (Upper) Membrane lateral view; (Lower) bottom luminal view (90^{o} rotation).

In addition to Cc_{550}, PSII contains two other iron components, and iron deficiency can disturb PSII activity by affecting either the cytochrome b_{559} or the non-heme iron. However, the presence of these two components is essential for PSII activity, as cytochrome b_{559} is strictly required for PSII assembly (Chu & Chiu, 2016) and the lack of the non-heme iron results in disruption of the electron flow between Q_A and Q_B and the loss of PSII activity (Müh & Zouni,

2013). On the other hand, it has been demonstrated in cyanobacteria, both *in vitro* and in ΔpsbV mutants *in vivo* (Shen et al., 1998; Li et al., 2004; Xiao et al., 2020), that the absence of Cc_{550} indeed affects PSII activity but its presence is not strictly required, indicating an accessory role of Cc_{550} in the stabilization and functioning of the Mn_4CaO_5 cluster. Our results indicate that iron limitation induces a drastic decrease in the total activity of PSII transferring electrons from water to quinones. This decreased activity is parallel to the specific decay in the content of Cc_{550} under iron-deficient conditions compared to other PSII components. However, the photochemical activity of PSII, defined as the capacity of charge separation between P_{680} and the quinones, is less affected by the iron limitation, in a similar and parallel manner to the measured levels of other proteins of the PSII complex, both intrinsic (D1) and extrinsic (PsbO). The conclusion is that although the lack of iron exerts a negative effect on PSII, it affects more specifically to the water-splitting activity, related to the Mn_4CaO_5 cluster, than the photochemical activity, related to the PSII core and the charge separation.

The specific effect of the lack of Cc_{550} on PSII activity can be explained by its role stabilizing the water-splitting system and, in particular, in the binding of the other extrinsic subunits of PSII. Diatoms have an extra extrinsic protein, Psb31, in addition to the other four subunits also present in red algae: PsbO, PsbU, PsbQ' and PsbV/Cc_{550} (Enami et al., 1998; Okumura et al., 2008; Nagao et al., 2010a). Earlier reconstitution experiments of PSII samples had suggested that the binding of PsbV (and PsbU) required previous binding of PsbO, PsbQ' and, particularly, Psb31, the last three proteins being able to bind directly to PSII intrinsic proteins (Enami et al., 1998, 2003; Nagao et al., 2010a). This was in contrast to the situation in cyanobacteria, where Cc_{550} is reported to bind directly to the PSII core, in a manner essentially independent of the other extrinsic proteins, although the binding of Cc_{550} alone renders a non-functional PSII (Shen & Inoue, 1993; Enami et al., 2003; Nagao et al., 2015). However, the recent crystal structure of the PSII of the diatom *C. gracilis* (Pi et al., 2019) (Figure 5.1) has confirmed an overall structure similar to that of cyanobacterial PSII, which includes the position of Cc_{550} in the complex. Thus, PsbV/Cc_{550} interacts both with PsbU and PsbQ', which by its turn stablish contacts with PsbO (Figure 5.1). No direct interactions were observed between Psb31 and the other extrinsic subunits, indicating in any case an indirect role of Psb31 in stabilizing the binding of PsbU and PsbV to PSII (Pi et al., 2019). In addition, it has been recently described in Cc_{550} mutants in cyanobacteria that the weakening of the binding of PsbV to PSII not only promoted low levels of oxygen-evolving activity, but also debilitated the binding of the extrinsic proteins PsbO and PsbU to PSII (Xiao et al., 2020). The observed decrease in PSII activity was not caused by a lower amount of PSII core centres but for the

impairment of the water-splitting system because the lack of the extrinsic subunits. The conclusion was that the loss of PsbV and the subsequent weakening of binding of PsbO and PsbU resulted in the incomplete assembly of fully functional PSII complexes and, consequently, a lower water-splitting activity (Xiao et al., 2020). According to the results obtained in this Thesis, a similar situation seems to occur in *P. tricornutum* under strong iron limitations, in which an insufficient amount of Cc_{550}, compared to the total amount of PSII core complexes, should specifically affect PSII activity, not only because the direct role of Cc_{550} in the water-splitting function, but also by affecting the binding of other extrinsic subunits equally required.

The modelled structures of *P. tricornutum*, *C. muelleri*, *I. galbana* and *N. gaditana* eukaryotic Cc_{550} show a common folding pattern similar to that described in cyanobacteria, including the hydrophobic northern finger, involved in PSII binding and proton exit during water oxidation (Frazão et al., 2001; Xiao et al., 2020). However, whereas in the prokaryotic protein the cofactor exposed area holds a negatively charged electrostatic character (Frazão et al., 2001, Bernal-Bayard et al., 2017), in the eukaryotic Cc_{550} the area around the heme group is mainly hydrophobic, and the negative electrostatic potential is restricted to the southern area, opposite to the hydrophobic northern protuberance. According to the PSII known structures, the facing surface of Cc_{550} displayed in Fig. 5.2, that includes the cofactor exposed area, is also involved in the binding to the photosystem, maintaining close contacts with the PSII surface (Pi et al. 2019). Consequently, the distinctive surface charge distribution of eukaryotic Cc_{550} could be significant in defining the binding affinity to PSII, as suggested for the *P. tricornutum* Cc_{550} (Bernal-Bayard et al., 2017). Although Cc_{550} can be obtained from soluble cell extracts in different organisms (Evans & Krogmann, 1983; Navarro et al., 1995; Kerfeld & Krogmann, 1998; Bernal-Bayard et al., 2017 & 2019), this fact is particularly significant in *P. tricornutum,* where about 60-85% of total Cc_{550} can be solubilized during the process of cell disruption in the absence of added detergents (Bernal-Bayard et al., 2017). A similar result has been here observed during the purification of this protein from *C. muelleri*, *N. gaditana* and *I. galbana* cells. These results could be justified by a combination of a weaker affinity for PSII and an enhanced PSII turnover, as previously suggested in diatoms (Lavaud et al., 2016), both resulting in a higher fraction of unbound Cc_{550}. In this sense, most of the protein still attached to membrane fractions in *P. tricornutum* has been shown to be released by relatively weak detergent extraction procedures, thus suggesting a comparatively weaker affinity of Cc_{550} for PSII (Bernal-Bayard et al., 2017), and opening the possibility of new functions for an increased fraction of unbound Cc_{550} (Bernal-Bayard et al., 2019).

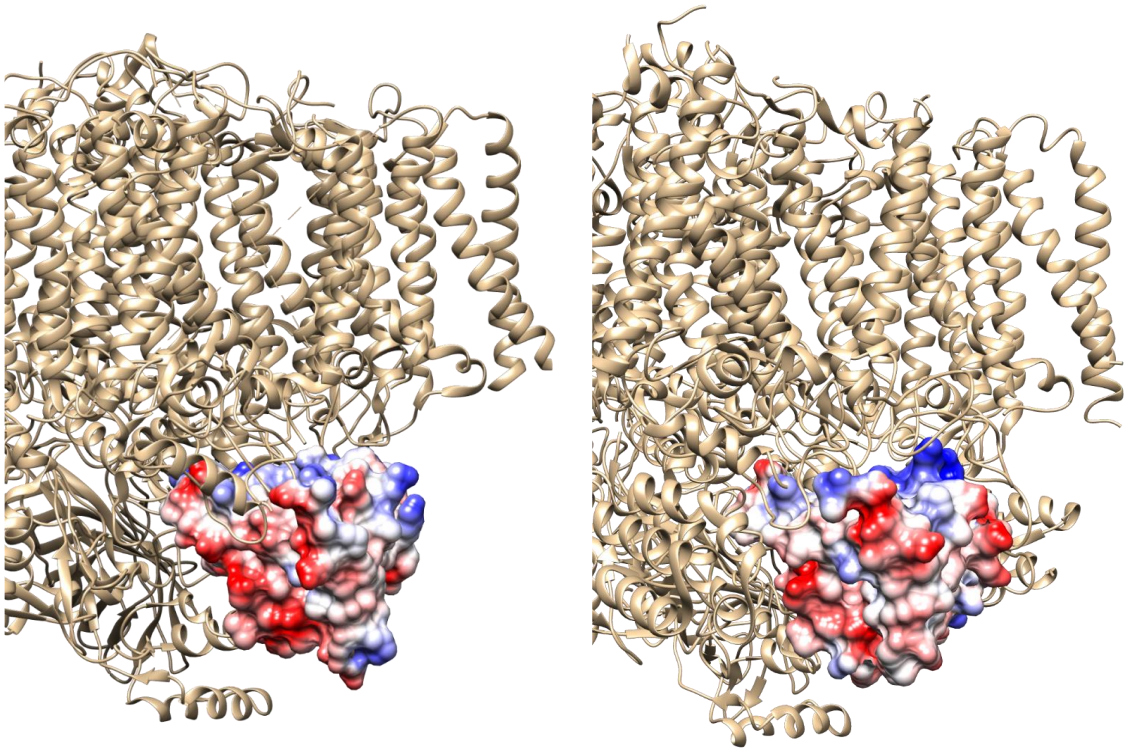

Figure 5.2. Photosystem II showing the cytochrome c_{550} binding site. PSII of (left) the cyanobacterium *T. elongatus* and (right) the diatom *C. gracilis*, showing the Cc_{550} binding and the protein surface electrostatic potential.

5.2. Chapter II. The effects of the heterologous expression of a plastocyanin in the diatom *Phaeodactylum tricornutum*

Diatoms are key contributors to the phytoplankton biomass and carbon sequestration in the oceans, but their growth is limited by iron deficiency in the environment (Boyd et al., 2007). Actually, iron enrichment by massive large-scale iron fertilization in the open sea has been proposed as a strategy to increase phytoplankton growth, global oceans' productivity and CO_2 sequestration, as a way to mitigate the global climate change (de Baar et al., 2005). However, this approach has significant technical and ecological disadvantages [Editorial, Nature Geosci 2:153 (2009)]. As previously stated, adaptations of diatoms to natural oceanic low-iron environments include, among other strategies, the induction of specific iron-uptake systems and the lowering or replacement of iron-containing photosynthetic proteins. In particular, a decrease in the levels of Fd (replaced by Fld) and the PSI and Cb_6f iron-rich complexes has been reported (Strzepek & Harrison, 2004; Lommer et al., 2012). On the other hand, Cc_6 is the only soluble donor available in red algae and most algae of the red-plastid lineage. A widespread predominance of the *petJ* gene encoding Cc_6 has been confirmed, validating this protein as the

electron carrier from Cb_6f to PSI in the majority of organisms within the red-plastid lineage (Blaby-Haas & Merchant, 2012; Groussman et al., 2015; Gao et al., 2021). However, the presence of *petE* Pc genes in the genomes of some oceanic diatoms has been explained by their acquisition from green algae by horizontal gene transfer, as an adaptation to chronic iron limitations in these environments (iron concentration <1 nM) (Moore & Braucher, 2008). Thus, Pc acquisition and expression in oceanic diatoms has been considered to represent an alternative (or even constitutive) substitution of Cc_6, as it occurs in cyanobacteria and green algae (Peers & Price, 2006; Moore & Braucher, 2008; Lommer et al., 2012; Marchetti et al., 2012; Groussman et al., 2015; Hippmann et al., 2017).

Evidences for a functional Pc have been reported in the case of *T. oceanica*, where the holoprotein was detected and partially purified and sequenced (Peers & Price, 2006). However, the intracellular levels of Pc reported in *T. oceanica* are remarkably low compared to those reported for Pc in cyanobacteria, green algae and plants (Peers & Price, 2006; Navarro et al., 2011; Kong & Price, 2020). The expression of a functional Pc in diatoms raises, however, the question about the mechanism regulating a putative Cc_6/Pc replacement in diatoms. In cyanobacteria and green algae, copper levels radically determine the expression of one protein or another through precisely regulated mechanisms, including transcription regulators, metal sensors and proteases that have not been found in diatoms (Merchant & Bogorad, 1986; Sandmann, 1986; Kropat et al., 2005; Merchant et al., 2020; García-Cañas et al., 2021). In cyanobacteria, this precise mechanism has been recently unveiled (García-Cañas et al., 2021). Thus, in *Synechocystis* sp. PCC 6803, the regulatory system is composed of a BlaI/CopY-family transcription factor (PetR) and a BlaR-membrane protease (PetP). PetR represses Pc expression and activates Cc_6, while PetP controls PetR levels *in vivo* in response to copper concentration (García-Cañas et al., 2021). In *C. reinhardtii* a different system ensures the precise regulation of the synthesis of either Pc or Cc_6. In fact, the accumulation of Pc vs. Cc_6 is controlled by different mechanisms for each protein. For Pc, copper stabilizes the protein both *in vitro* and *in vivo*; in the absence of copper the apoprotein is unfolded and then more susceptible to protease degradation. However, *in vivo* this degradation requires the expression of a protease whose identity is not yet known (Merchant et al., 2020). For Cc_6, the *petJ* gene is under tight transcriptional control by a transcriptional activator, or copper response regulator 1 (CRR1), which works through copper response elements (CuREs) (Merchant et al., 2020). In diatoms, however, both low copper and sufficient iron conditions have been reported to induce a decrease in Pc transcripts which, on the contrary, can be detected under iron limiting conditions (Lommer et al., 2012; Marchetti et al., 2012; Hippmann et al., 2017; Rizkallah et al., 2020).

Recently, a 3-fold decrease in the Pc protein content under copper deficiency has been reported in *T. oceanica* (Kong & Price, 2020). This is in contrast to the drastic changes in Pc content in response to changes in copper concentration observed in cyanobacteria and green algae (Merchant & Bogorad, 1986; Sandmann, 1986; Durán et al., 2005). By its turn, our results confirm that Cc_6 levels in *P. tricornutum* depend on the availability of iron (Roncel et al., 2016; Castell et al., 2021b), although iron uptake itself is connected to copper availability (Maldonado et al., 2006).

According to previous results (Roncel et al., 2016), and the severe decrease here observed of the Cc_6 content, the iron-limited growth of *P. tricornutum* can be in part ascribed to the exclusive use of Cc_6 as electron carrier to PSI, and the absence of Pc as alternative donor. In this context, the expression of heterologous proteins can be a way to improve cellular functions and implement new capabilities or adaptations in the transformed host organism. In particular, the expression of algal Fld or Cc_6 in plants has shown to enhance plant growth and CO_2 assimilation, as well as tolerance to stress and iron deficiency (Chida et al., 2007; Blanco et al., 2011; Lodeyro et al., 2012; Yadav et al., 2018). Thus, here we have investigated the effects of the heterologous expression under iron limiting conditions of a functional Pc in *P. tricornutum*, a diatom that naturally only produces Cc_6, as a possible way to increase photosynthetic efficiency and cell growth. The *C. reinhardtii* E85K Pc gene was placed under the control of the Fld promoter, to ensure its expression in low iron conditions, in which the levels of native Cc_6 drastically decrease and become limiting for the photosynthetic activity (Roncel et al., 2016; and see above). This mutant Pc was selected to be introduced into *P. tricornutum* based on previous *in vitro* kinetic analysis of the interaction of *P. tricornutum* PSI with green algae and plants Pc (Bernal-Bayard et al., 2015). These previous data indicated that diatom PSI is able to react with the very acidic Pc from these organisms, although with lower efficiency than with *P. tricornutum* Cc_6. However, in the *C. reinhardtii* E85K Pc mutant, designed trying to mimic the electrostatics of diatom Cc_6, this efficiency doubled as compared with the WT protein (Bernal-Bayard et al., 2015). Monitoring of immunolabelled cells confirmed the detection of the heterologous Pc in the chloroplast. Moreover, the presence of the Pc holoprotein (*i.e.*, with the copper active cofactor) was directly detected by its absorption spectrum in cell extracts, and intracellular levels of heterologous holo-Pc of ≈4 μM were determined.

The reported holo-Pc concentration per cell in *T. oceanica* under copper sufficient conditions (≈3 μM) is about 10 times lower than that usually described for Cc_6 under iron sufficient conditions, including reported values in *P. tricornutum* (≈28 μM) (Peers & Price, 2006; Bernal-Bayard et al., 2013; Kong & Price, 2020). Pc levels in *T. oceanica* are, however,

comparable to the Cc_6 content found here under iron-deficient conditions in *P. tricornutum* (≈4-7 µM) and, interestingly, to the Pc levels here detected (≈4 µM). In this sense, although inducible copper uptake pathways have been recently described in *T. oceanica* (Kong & Price, 2019), the functional expression of Pc requires a specific copper-transporting system into the thylakoid that has not yet been found in red-type organisms (Figure 5.3). A copper-trafficking system should be expected to include chaperones for copper transport and, in particular, a P-type ATPase transporter located in the thylakoid membrane, delivering copper to the lumen to be incorporated into Pc (Guo et al., 2010 & 2015; Nouet et al., 2011; Blaby-Haas & Merchant, 2012; Kong & Price, 2019; Merchant et al., 2020). In this sense, it has been established that cyanobacteria have two P-type ATPases, CtaA and PacS, that efflux copper from inside the cell either to the periplasm or the thylakoid (Figure 5.3A) (Huertas et al., 2014). In *Synechocystis* sp. PCC 6803, PacS and CtaA have been localized in the plasma and the thylakoid membrane, respectively (Baers et al., 2019). In addition, a copper metallochaperone, Atx1, is able to interact and exchange copper with both CtaA and PacS (Figure 5.3A) (Tottey et al., 2012). Similar systems for copper trafficking exist in the green alga *C. reinhardtii*, with different copper-transporting ATPases involved (Merchant et al., 2020) (Figure 5.3B). Two CTR active copper transport systems located in the periplasmic membrane have been described (CTR1 and 2; Figure 5.3B), although its functions *in vivo* in *C. reinhardtii* are not yet unveiled. In addition, two copper-transporting ATPases are located in the chloroplast (Ctp2) and thylakoid (Ctp4) membrane (Figure 5.3B; Merchant et al., 2020). These two last proteins pump copper ions into the chloroplast stroma and lumen, respectively, for assembly of Pc. An ortholog of Atx1 has also been identified. In addition, Pcc1 is a luminal copper chaperone in *C. reinhardtii*, with orthologues in other algae expressing Pc, which is consistent with a possible function in copper delivery to Pc (Figure 5.3B; Merchant et al., 2020). As stated before, none of these genes have been found in the genome of red algae or diatoms (Figure 5.3C). This is an important point, since in the absence of specific mechanisms of copper import into the thylakoid lumen, the copper available to be incorporated into Pc would probably be limited (Ho et al., 2003; Levy et al., 2008; Twining & Baines, 2013; Castell et al., 2021b), which is furthermore hampered in diatoms because the existence of additional plastid membranes (Figure 5.3C). Thus, it is possible that, in the absence of specific mechanisms of copper import, the limitation in the copper available in the lumen to be incorporated into Pc restrains the amount of a functional holoprotein to the levels described in *T. oceanica* and found in this work (Ho et al., 2003; Levy et al., 2008; Twining & Baines, 2013).

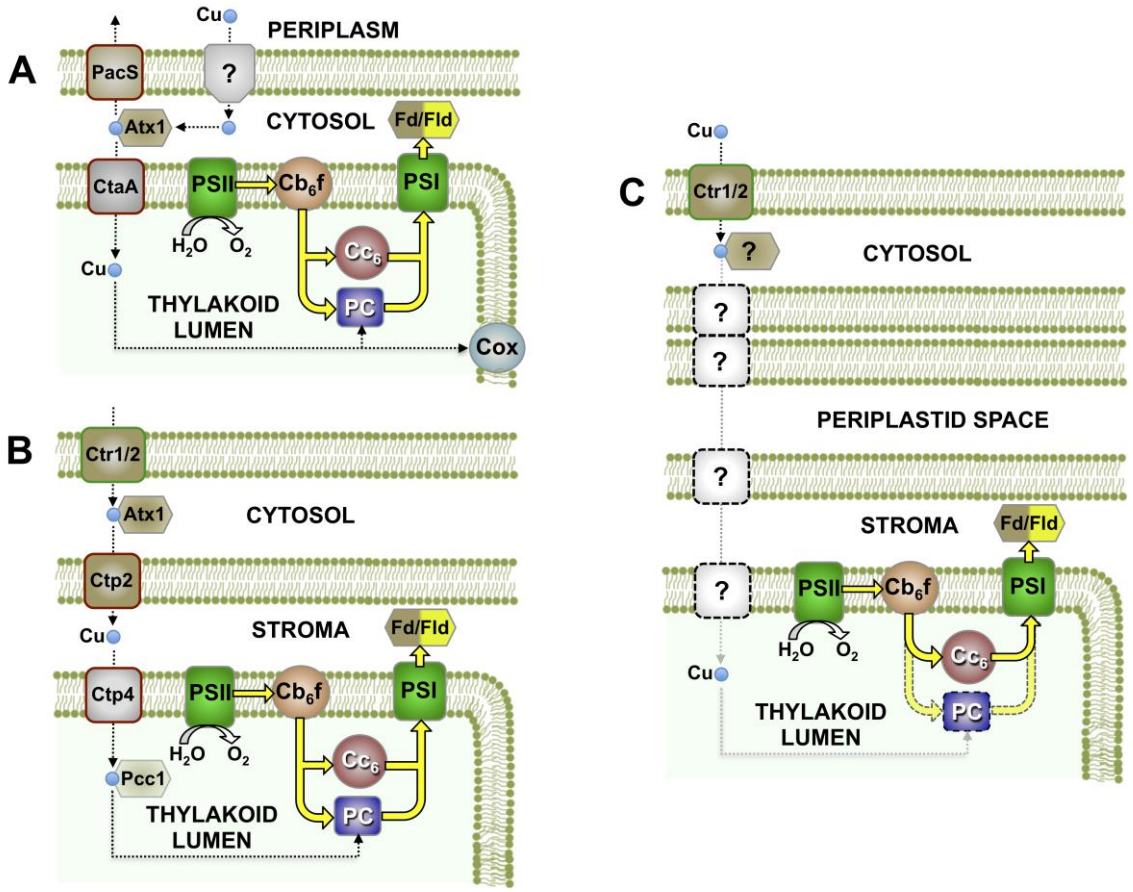

Figure 5.3. Mechanisms of copper import into the thylakoid lumen. Mechanisms of copper import into the thylakoid lumen established in (A) cyanobacteria (modified from Huertas et al., 2014) and (B) green algae (modified from Blaby-Haas & Merchant, 2012). (C) Putative mechanism of copper import into the chloroplast in diatoms. See the text for more details.

However, our results indicate that even the relatively low concentrations of holo-Pc detected are enough to promote an increased growth (up to 60% in the case of the #45 and #79 mutants) under iron-deficient conditions as compared with the WT strain. This increased growth can be measured as higher cell densities, content in pigments (chlorophylls and carotenoids), global photosynthetic rates per cell and even cell volume. Moreover, although the apparent partially recovered levels of psaB –more evident in mutant #79– does not allow to directly inferring an equivalent increase of active PSI, a slightly higher PSI activity has been also observed in the mutants in PAM experiments. Previous studies have proposed that in *P. tricornutum* the iron-rich PSI is degraded under iron-deficient conditions, mobilising this element for other metabolic activities, as respiration (Allen et al., 2008). The presence of Pc should not modify the extent of PSI degradation, as it does not alter the cell metabolic demand for iron. Thus, the observed data suggest that the balance of PSI synthesis/degradation, under iron-limiting

conditions, is perhaps not only affected by iron requirements, but also by the limitations at the PSI donor side or the global redox stress status of the chloroplast. Finally, the Pc-expressing strains also show changes in cell morphology, as the presence of less-elongated fusiform cells with an increased circularity and chloroplasts with a thicker shape, which indeed reflects changes in the physiological and metabolic status of cells (Levy et al., 2008; Martin-Jézéquel & Tesson, 2012).

In addition, PSII activity of *P. tricornutum* cells was affected by low iron concentration in a different manner in the WT and mutant strains. The partial blocking of ET between PSII and PSI in cells cultured under iron-deficient conditions can generate the over-reduction of the PQ pool. Under iron-deficient conditions, P_{700} cannot become reduced, possibly due to fewer available iron-containing ET proteins downstream of the PQ pool, such as the Cb_6f complex or the Cc_6 soluble carrier (Bruce & Malkin, 1991; Greene et al., 1992; Allen et al., 2008; Roncel et al., 2016). In particular, in *P. tricornutum* cells grown under low iron conditions, the Cc_6 concentration is reduced to ≈10-15% of the protein present in iron-replete cells, thus presumably disfavouring the PQ pool re-oxidation (Roncel et al., 2016; Castell et al., 2021b). An over-reduction of the PQ pool may induce the appearance of the acceptor side photoinhibition process, which can decrease PSII activity. The existence of an alternative electron carrier in the mutant strains, the E85K Pc, could improve the ET to PSI, and partially eliminate the over-reduction of the PQ pool and the concomitant lack of activity of PSII. This hypothesis can explain the significant lower decrease of the TL intensity signal in the mutant strains, as well as the higher maximum quantum yield of PSII obtained by fluorescence measurements in the mutants compared to the WT. Higher values for $rETR_{max}$ were also determined in the three mutants with respect to the WT, which indicates that the aforementioned occurrence of the acceptor side photoinhibition process is delayed due to the presence of Pc.

In chloroplasts, the reducing side of PSI and the oxidizing side of PSII are the major generation sites of reactive oxygen species (Sgherri et al., 2018), although recently it has been reported that superoxide can also be produced by Cb_6f and at the acceptor side of PSII (Roach & Krieger-Liszkay, 2014). On the other hand, the major source of singlet oxygen appears to be PSII (Krieger-Liszkay, 2005; Murata et al., 2007), the generation of this reactive oxygen species being enhanced as a consequence of the photoinhibition of the acceptor side in PSII. The formation of singlet oxygen can initiate the peroxidation of unsaturated lipids in membranes (Vavilin & Ducruet, 1998). The level of lipid peroxidation in photosynthetic membranes can be measured by the HTL technique (Roncel et al., 2007; Ortega & Roncel, 2021). Several luminescence high temperature bands (HTL bands) have been observed without prior illumination at temperatures

above 60°C (Ducruet & Vavilin, 1999; Roncel et al., 2007). A broad HTL band centred near 130°C (known as the HTL2 band) is generated because of the thermal radiative decomposition of lipid peroxides that, in turn, leads to the formation of carbonyl groups in a triplet state followed by migration of excitation energy toward chlorophylls (Vavilin & Ducruet, 1998; Ducruet & Vavilin, 1999; Vavilin et al., 2002). The amplitude of this band has been well correlated with the accumulation of malondialdehyde, an indicator of lipid peroxidation in standard chemical tests (Vavilin & Ducruet, 1998; Vavilin et al., 2002).

Analysis of HTL2 bands of TL obtained in *P. tricornutum* cells clearly showed a much higher level of lipid peroxidation under iron-deficient conditions in the WT strain. However, in the three mutant strains the level of peroxidation did not significantly increase under iron-restricted conditions. These results suggest a higher rate of generation of reactive singlet oxygen under iron-deficient conditions in the WT strain. As previously said, the low levels of Cc_6 probably induce the over-reduction of the PQ pool and the concomitant acceptor side photoinhibition in PSII, and thus singlet oxygen production. The presence of Pc in the mutant strains under iron-deficient conditions could partially eliminate the over-reduction of the PQ pool and the concomitant generation of singlet oxygen, thus decreasing oxidative stress and lipid peroxidation.

On the other hand, it has been shown that PSI activity is more sensitive than PSII activity to iron-limitation (Pushnik & Miller, 1989; Roncel et al., 2016). The significant decrease in the quantum yield of PSI, Y(I), observed in iron-deficient WT cells can be ascribed to a deficiency of PSI donors, which causes that P_{700} cannot become reduced (Bruce & Malkin, 1991; Greene et al., 1992; Allen et al., 2008; Roncel et al., 2016). An increase of Y(I) and a lower degree of limitation on the donor side of PSI, Y(ND), have been here observed in the three mutants. The existence of Pc as an additional electron carrier in the mutant strains seems to improve ET to PSI and, consequently, to partially increase Y(I), as well as to decrease the over-reduction of the PQ pool and the concomitant donor-side limitation of PSI.

In summary, our results show that the presence of Pc as an additional electron carrier in *P. tricornutum* under iron-limiting conditions seems to decrease the over-reduction of the PQ pool. This consequently promotes an improvement in the maximum quantum yield of both PSII and PSI, together with a decrease in the acceptor side photoinhibition of PSII and oxidative stress, the peroxidation of lipids and a lower degree of limitation on the donor side of PSI. As a result, the mutants expressing Pc in *P. tricornutum* exhibit an enhancement in cell growth under iron limiting conditions as compared to WT cells.

5.3. Chapter III. Modelling of the [cytochrome *f*:acceptor] electron transfer complexes in *Phaeodactylum tricornutum* and *Thalassiosira oceanica*

Several NMR-based structures of plant [Cf:Pc] complexes have been described and even taken as a model of the type of transient complexes involved in ET reactions (Ubbink et al., 1998; Crowley & Ubbink, 2003; Lange et al., 2005; Cruz-Gallardo et al., 2012). In addition, BD simulations have studied the Cf interaction with the soluble electron acceptors in plants and in the green alga *C. reinhardtii* (Gross & Pearson, 2003; Musiani et al., 2005; Haddadian & Gross, 2006; Fedorov et al., 2019). From these structural data, as well as from extensive kinetic analyses (Meyer et al., 1993; Qin and Kostic, 1993; Kannt et al., 1996; Soriano et al., 1997; Gong et al., 2000; Schlarb-Ridley et al., 2003), it has been concluded that long-range electrostatic attraction between the positively charged surface patch at the interface of the large and small domains in Cf and the negative region of Pc or Cc_6 drives the formation of an initial transient complex in green algae and plants. Further short-range hydrophobic interactions between both hydrophobic patches are also involved in the reorganization of the complex and its fine tuning, to reach an effective configuration leading to an efficient ET (Cruz-Gallardo et al., 2012; Schilder & Ubbink, 2013; Bendall & Howe, 2016). The structure of the plant [Cf:Pc] complex shows a relatively large complex interface, forming the so-called "side-on" relative orientation (in contraposition to the "head-on" orientation that appears in some complexes of cyanobacteria) (Ubbink et al., 1998; Cruz-Gallardo et al., 2012; Bendall & Howe, 2016). Thus, the comparison of the green [Cf:Pc] and [Cf:Cc_6] complexes confirms the role of the small Cf domain in stabilizing the proper docking orientations of Pc and Cc_6. However, neither structural nor kinetic data are available for the [Cf:acceptor] complex in the red lineage of eukaryotic algae.

The surface electrostatic potential computed on the structural model of *P. tricornutum* Cf shows the conservation of the ET exposed area around the Y1 and the heme. However, the model also shows a sensibly reduced positively charged surface patch at the interface of the large and small domains, in accordance with the decreased electrostatic character of Cc_6 (Bernal-Bayard et al., 2015; Castell et al., 2021a). Remarkably, in the case of *T. oceanica* it is interesting to note both the presence in Cf of positive groups outside the usual ET region around the heme-exposed area and the typical strong negative electrostatics of a "green-type" Pc.

As mentioned above, there are no structural data available for the [Cf:Cc_6] (and [Cf:Pc]) complexes in organisms of the red lineage. However, ET proteins, and in particular *c*-type cytochromes, have been shown to be structurally quite rigid, and thus BD and docking approaches treating Cf and Cc_6 as rigid bodies have been widely used (Haddadian & Gross, 2005

& 2006; Cruz-Gallardo et al., 2012; Bernal-Bayard et al., 2015). Here we have carried out docking simulations to study the [Cf:Cc_6] complex in the red lineage by using pyDock, a protein-protein rigid-body docking protocol that uses electrostatics and desolvation energy to score the generated docking poses. Our results indicate that the lowest-energy models for both the *C. reinhardtii* and *P. tricornutum* [Cf:Cc_6] complexes converge towards orientations with a short distance between the heme iron in Cf and the heme group in Cc_6. However, the *P. tricornutum* [Cf:Cc_6] docking complex has a different orientation compared with the equivalent green complex in *C. reinhardtii* (Haddadian & Gross, 2005). Thus the best docking models of the *P. tricornutum* [Cf:Cc_6] complex have a "head-on" orientation, more similar to that described previously in cyanobacterial systems (Díaz-Moreno et al., 2014). These orientations display smaller interfaces and weaker electrostatic interactions, with hydrophobic forces being more relevant (Crowley et al., 2001; Cruz-Gallardo et al., 2012). In the "side-on" configuration observed in the complex of *C. reinhardtii*, negatively charged residues of Cc_6 (D2, E54, K57, D65, R66, E70 and E71) have significant contacts with positive residues in Cf, in particular with the K65, K188 and K189 groups. However, in *P. tricornutum* the E54 and D65 groups in Cc_6 and K189 in Cf are not conserved, and cannot stabilize this "side-on" orientation. On the contrary, the orientation in *P. tricornutum* involves relevant electrostatic interactions between E28 in Cc_6 and residues K65 and K187 in Cf, as well as between residues R66 and K57 in Cc_6 and residues E108 and E164 in Cf. As a consequence, the small domain of *P. tricornutum* Cf appears to have only a minor role in the interaction with Cc_6. Interestingly, "side-on" docking orientations can be found in *P. tricornutum* that are relatively similar to the best-energy models obtained in *C. reinhardtii*. However, although these orientations have short distances between the Fe in Cf and the heme cofactor in Cc_6 they have unfavourable higher energies.

Finally, it is interesting to analyse the modelled [Cf:Pc] complex of *T. oceanica* in comparison with the [Cf:Cc_6] complex of *P. tricornutum*, as well as with the equivalent [Cf:Pc] complex of the green lineage. The docking between *T. oceanica* Cf and Pc suggests stronger electrostatics as compared to the [Cf:Cc_6] complex of *P. tricornutum*, in agreement with the strong negative character of the electrostatic patch in this Pc. However, in *T. oceanica* the Cf:Pc interaction is not optimized in a single group of solutions with a favourable combination of energies and distances for ET. Therefore, different protein-protein orientations might be functionally possible and could coexist, including "head-on" configurations based in hydrophobic forces, similar to some cyanobacterial complexes, and "side-on" configurations, more similar to the green complexes involving strong electrostatics and the small domain of Cf. The fact that Pc is not present in many diatom species suggests that its heterologous acquisition

may be relatively recent, and therefore the [Cf:Pc] complex in *T. oceanica* would not have yet achieved a prevalent configuration optimized for ET.

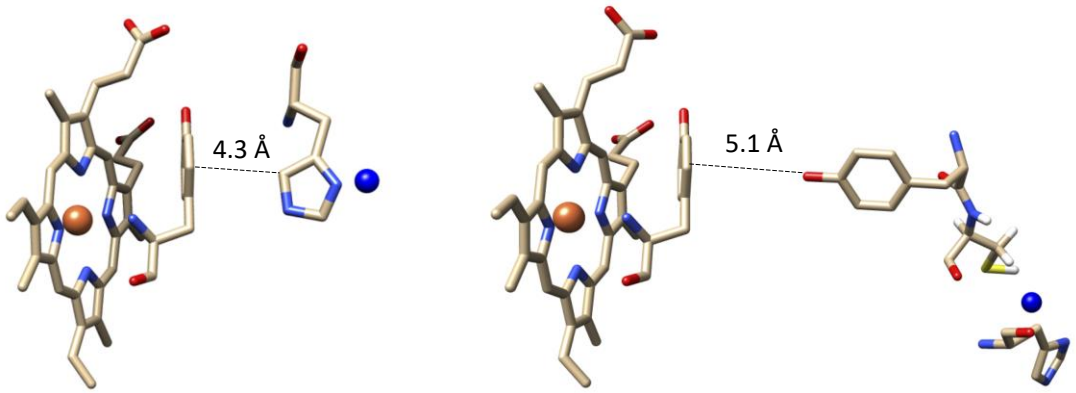

Figure 5.4. Electron transfer pathways in docking models of [Cf:Pc] complexes of *T. oceanica*. (Left) ET pathway in the best balanced energy-distance docking orientation, and (Right) putative ET pathway in the best-energy docking [Cf:Pc] complex of *T. oceanica*. The Heme and Y1 groups in Cf and H87, Y83, C84 and Cu in Pc are highlighted. Lines indicate the distance between different groups.

Surprisingly, the clearly more favourable energies correspond to novel orientations in which the electrostatic patches of both proteins establish strong interactions, but the Cu-binding H87 residue (H88 in the sequence of *T. oceanica* Pc) and the Fe are located at long unproductive distances from each other. The imidazole of H87 defines the shortest path from the copper atom to the protein surface (≈6 Å) and forms the ET pathway in Pc from Cf and to PSI in cyanobacteria, green algae and plants, as clearly demonstrated by kinetic and structural data (Ubbink et al., 1998; Hippler & Drepper, 2006; Caspy et al., 2020). However, in the apparently unproductive orientations of lowest energy in *T. oceanica*, the widely conserved Y84 residue in Pc (typically referred to as Y83 in cyanobacterial and eukaryotic Pc) points directly towards the heme-binding Y1 of Cf (Figure 5.4). Based on the reactivity of Pc with inorganic complexes, as well as on theoretical studies, it was previously proposed that Y83 could act as another potential ET pathway in Pc (reviewed in Redinbo et al., 1994). However, this hypothesis was later discarded in the interaction of Pc with Cf and PSI (Ubbink et al., 1998; Hippler & Drepper, 2006; Caspy et al., 2020). Although Y83 is located in the electrostatic patch of Pc, and ≈19 Å away from the copper, ET at this site would involve a through-bond pathway to C84, which is coordinating the copper atom (Redinbo et al., 1994) (Figure 5.4). Therefore, it could be a matter of discussion whether this ET pathway involving Y83 –not active in green Pcs–, and alternative to the more

canonical docking models here described, is active or not in the heterologously acquired diatom Pc.

To conclude, based on the models presented here and the extensive body of previous structural and kinetic data on the green complexes, it seems that in eukaryotic organisms the evolution of the ET from Cb_6f (and to PSI) has developed conserved negative electrostatic patches in the soluble carriers, parallel to positive complementary areas of interaction in the Cb_6f membrane complex (and in PsaF-PSI). However, within this general framework, our data suggest that different strategies have been developed in the evolution of the ET from Cb_6f to PSI in the green and red branches of eukaryotic photosynthetic organisms. Thus, the green line has developed areas of interaction with a stronger electrostatic charge, with a higher affinity between partners and a more efficient ET, at the cost of limiting the turnover of the complexes. On the other hand, the red line seems to have developed areas of interaction with a weaker electrostatic charge, with a lower affinity between partners and a less efficient ET, favouring instead the exchange of proteins, and thus increasing the turnover of the process. Finally, in diatoms the interaction of the acquired green-type Pc with Cf (and PSI) may not yet be optimized.

6. Conclusions

6. Conclusions

1. Cytochrome c_{550} from the diatom *Phaeodactylum tricornutum* is purified as a truncated form lacking the last two carboxy-terminal tyrosine residues when using standard purification protocols, and showing no other post-translational modifications.

2. A protocol has been designed to purify the complete cytochrome c_{550} from membrane fractions, thus indicating that the truncation is a non-physiological process.

3. Iron limitation induces a drastic and parallel decrease in the content of both cytochrome c_{550} and the total activity of photosystem II. The specific effect of the lack of cytochrome c_{550} on the activity of photosystem II can be explained by its role stabilizing the water-splitting system and, in particular, in the binding of the other extrinsic subunits of the photosystem.

4. A single mutant plastocyanin of the green alga *Chlamydomonas reinhardtii* has been heterologously expressed in *Phaeodactylum tricornutum*. The protein is correctly processed and targeted to the chloroplast.

5. Relatively low intracellular concentrations of the heterologous holoplastocyanin are enough to promote an increased growth in *Phaeodactylum tricornutum* under iron-deficient conditions.

6. *Phaeodactylum tricornutum* cells expressing plastocyanin under low iron concentration show a lower decrease in photosystem II activity due to a diminished acceptor side photoinhibition, higher maximum quantum yields of photosystem II and relative electron transport rates, as well as a lower level of lipid peroxidation, compared with wild-type cells.

7. The heterologous expression of plastocyanin in *Phaeodactylum tricornutum* promotes an increase in the maximum quantum yield of photosystem I and faster P_{700} reduction kinetics.

8. The best docking model of the [cytochrome *f*:cytochrome c_6] complex of *Phaeodactylum tricornutum* has a different orientation compared with the equivalent green complex in *Chlamydomonas reinhardtii*. The diatom complex shows a “head-on” orientation, more similar to that described previously in cyanobacterial systems, with smaller contact interfaces and weaker electrostatic interactions.

9. Docking models show that the [cytochrome *f*:plastocyanin] complex of *Thalassiosira oceanica* is not optimized in a single group of solutions, with a favourable combination of energies and distances for electron transfer, indicating that this complex would not have yet achieved a prevalent configuration optimized for electron transfer.
10. The most favourable energies in the [cytochrome *f*:plastocyanin] complex of *Thalassiosira oceanica* correspond to apparently unproductive orientations, in which the conserved Tyrosine-84 of plastocyanin could form part of a potential alternative electron transfer pathway from cytochrome *f*.

7. References

7.References

Abagyan, R., Lee, W.H., Raush, E., Budagyan, L., Totrov, M., Sundstrom, M. & Marsden, B.D. (2006). Disseminating structural genomics data to the public: from a data dump to an animated story. *Trends in Biochemical Science, 31*(2), 76-78.

Ago, H., Adachi, H., Umena, Y., Tashiro, T., Kawakami, K., Kamiya, N., Tian, L., Han, G., Kuang, T., Liu, Z., Wang, F., Zou, H., Enami, I., Miyano, M. & Shen, J-R. (2016). Novel features of eukaryotic photosystem II revealed by its crystal structure analysis from a red alga. *Journal of Biological Chemistry, 291*(11), 5676-5687.

Akazaki, H., Kawai, F., Chida, H., Matsumoto, Y., Hirayama, M., Hoshikawa, K., Unzai, S., Hakamata, W., Nishio, T., Park, S-Y. & Oku, T. (2008). Cloning, expression and purification of cytochrome c_6 from the brown alga *Hizikia fusiformis* and complete X-ray diffraction analysis of the structure. *Acta Crystallographica Section F: Structural Biology and Crystallization Communications, 64*(8), 674-680.

Akazaki, H., Kawai, F., Hosokawa, M., Hama, T., Chida, H., Hirano, T., Boon-Keng, L., Sakurai, N., Hakamata, W., Park, S-Y., Nishio, T. & Oku, T. (2009). Crystallization and structural analysis of cytochrome c_6 from the diatom *Phaeodactylum tricornutum* at 1.5 Å resolution. *Bioscience, Biotechnology, and Biochemistry, 73* (1), 189-191.

Alam, J., Sprinkle, M.A., Hermodson, M.A. & Krogmann, D.W. (1984). Characterization of cytochrome *c*-550 from cyanobacteria. *Biochimica et Biophysica Acta – Bioenergetics, 766,* 317-321.

Allen, J.F. (2002). Photosynthesis of ATP – electrons, proton pumps, rotors, and poise. *Cell, 110*, 273-276.

Allen, A.E., LaRoche, J., Maheswari, U., Lommer, M., Schauer, N., Lopez, P.J., Finazzi, G., Fernie, A.R. & Bowler, C. (2008). Whole-cell response of the pennate diatom P*haeodactylum tricornutum* to iron starvation. *Proceedings of the National Academy of Sciences USA, 105*(30), 10438-10443.

Altschul, S.F., Gish, W., Miller, W., Myers, E.W. & Lipman, D.J. (1990). Basic local alignment search tool. *Journal of Molecular Biology, 215*(3), 403-410.

Andersen, R.A., Berges, J.A. Harrison P.J. & Watanabe M.M. Recipes for freshwater and seawater media. In: *Algal Culturing Techniques* (Andersen, R.A. Ed.), Elsevier Academic Press: Burlington,MA, USA, 2005; pp. 429–538.

Antoshvili, M., Caspy, I., Hippler, M. & Nelson, N. (2019). Structure and function of photosystem I in *Cyanidioschyzon merolae. Photosynthesis Research, 139*, 499-508.

Apt, K.E., Grossman, A.R. & Kroth-Pancic, P.G. (1996). Stable nuclear transformation of the diatom *Phaeodactylum tricornutum*. *Molecular and General Genetics MGG, 252*, 572-579.

Armbrust, E.V. (2009). The life of diatoms in the world's oceans. *Nature, 459,* 185-192.

Arnon, D.I. (1949). Copper enzymes in isolated chloroplasts. Polyphenoloxidase in *Beta vulgaris*. *Plant Physiology, 24*(1), 1-15.

Aro, E-M., Virgin, I. & Andersson, B. (1993) Photoinhibition of photosystem II. Inactivation, protein damage and turnover. *Biochimica et Biophysica Acta, 1143*, 113-134.

Baers, L.L., Breckels, L.M., Mills, L.A., Gatto, L., Deery, M.J., Stevens, T.J., Howe, C. J., Lilley, K.S. & Lea-Smith, D.J. (2019). Proteome mapping of a cyanobacterium reveals distinct compartment organisation and cell-dispersed metabolism. *Plant Physiology, 181,* 1721-1738.

Bailey, S. & Grossman, A. (2008). Photoprotection in cyanobacteria: regulation of light harvesting. *Photochemistry and Photobiology, 84,* 1410-1420.

Bailleul, B., Berne, N., Murik, O., Petroutsos, D., Prihoda, J., Tanako, A., et al. (2015). Energetic coupling between plastids and mitochondria drives CO_2 assimilation in diatoms. *Nature, 524*, 366-369.

Baniulis, D., Yamashita, E., Zhang, H., Hasan, S.S. & Cramer, W.A. (2008). Structure-function of the cytochrome b_6f complex. *Photochemistry and Photobiology, 84,* 1349-1358.

Bendall, D.S. & Howe, C.J. The interaction between cytochrome *f* and plastocyanin or cytochrome c_6. In: *Cytochrome Complexes: Evolution, Structures, Energy Transduction, and Signaling* (Cramer, W.A. & Kallas, T., Eds.). Advances in Photosynthesis and Respiration *41*, Springer Science + Business Media, Dordrecht, The Netherlands, 2016; 631-655.

Benoiston, A.S., Ibarbalz, F.M., Bittner, L., Guidi, L., Jahn, O., Dutkiewicz, S. & Bowler, C. (2017). The evolution of diatoms and their biogeochemical functions. *Philosophical Transactions of the Royal Society B: Biological Sciences, 372*, 1-10.

Bernal-Bayard, P., Álvarez, C., Calvo, P., Castell, C., Roncel, M., Hervás, M. & Navarro, J.A. (2019). The singular properties of photosynthetic cytochrome c_{550} from the diatom *Phaeodactylum tricornutum* suggest new alternative functions. *Physiologia Plantarum, 166*, 199-210.

Bernal-Bayard, P., Puerto-Galán, L., Yruela, I., García-Rubio, I., Castell, C., Ortega, J.M., Alonso, P.J., Roncel, M., Martínez, J.I., Hervás, M. & Navarro, J.A. (2017). The photosynthetic cytochrome c_{550} from the diatom *Phaeodactylum tricornutum. Photosynthesis Research, 133*, 273-287.

Bernal-Bayard, P., Molina-Heredia, F.P., Hervás, M. & Navarro, J.A. (2013). Photosystem I reduction in diatoms: As complex as the green lineage systems but less efficient. *Biochemistry, 52*(48), 8687-8695.

Bernal-Bayard, P., Pallara, P., Castell, C., Molina-Heredia, F.P., Fernández-Recio, J., Hervás, M. & Navarro, J.A. (2015). Interaction of photosystem I from *Phaeodactylum tricornutum* with plastocyanins as compared with its native cytochrome c_6: Reunion with a lost donor. *Biochimica et Biophysica Acta – Bioenergetics, 1847*(12), 1549-1559.

Blaby-Haas, C.E. & Merchant, S.S. (2012). The ins and outs of algal metal transport. *Biochimica et Biophysica Acta – Molecular Cell Research, 1823,* 1531-1552.

Blanco, N.E., Ceccoli, R.D., Segretin, M.E., Poli, H.O., Voss, I., Melzer, M., et al. (2011). Cyanobacterial flavodoxin complements ferredoxin deficiency in knocked-down transgenic tobacco plants. *The Plant Journal, 65*, 922-935.

Blankenship, R.E. (2014). Molecular mechanisms of photosynthesis. Wiley-Blackwell, 2nd Edition.

Blaustein, R. (2016). The great oxidation event. *BioScience, 66*, 189-195.

Bottin, H. & Lagoutte, B. (1992). Ferredoxin and flavodoxin from the cyanobacterium *Synechocystis* sp. PCC 6803. *Biochimica et Biophysica Acta, 1101*(1), 48-56.

Bottin, H. & Mathis, P. (1985). Interaction of plastocyanin with the photosystem I reaction center: A kinetic study by flash absorption spectroscopy. *Biochemistry, 24*, 6453-6460.

Bowler, C., Allen, A.E., Badger, J.H., Grimwood, J., Jabbari, K., Kuo, A., et al. (2008). The *Phaeodactylum* genome reveals the evolutionary history of diatom genomes. *Nature, 456*, 239-244.

Bowler, C., Vardi, A. & Allen, A.E. (2010) Oceanographic and biogeochemical insights from diatom genomes. *Annual Review of Marine Science, 2*, 333–365.

Boyd, P. W. & Ellwood, M. J. (2010). The biogeochemical cycle of iron in the ocean. *Nature Geoscience, 3,* 675-682.

Boyd, P.W., Jickells, T., Law, C.S., Blain, S., Boyle, E.A., Buesseler, K.O., et al. (2007). Mesoscale iron enrichment experiments 1993-2005: Synthesis and future directions. *Science, 315*, 612-617.

Bozarth, A., Maier, U.G. & Zauner, S. (2009). Diatoms in biotechnology: modern tools and applications. *Applied Microbiology and Biotechnology, 82*(2), 195-201.

Bricker, T.M., Roose, J.L., Fagerlund, R.D., Frankel, L.K. & Eaton-Rye, J.J. (2012). The extrinsic proteins of Photosystem II. *Biochimica et Biophysica Acta – Bioenergetics, 1817*, 121-142.

Bruce, B.D. & Malkin, R. (1991). Biosynthesis of the chloroplast cytochrome b_6f complex: studies in a photosynthetic mutant of *Lemna*, *The Plant Cell, 3,* 203-212.

Buck, J.M., Bártulos, C.R., Gruber, A. & Kroth, P.G. (2018). Blasticidin-S deaminase, a new selection marker for genetic transformation of the diatom *Phaeodactylum tricornutum*. *PeerJ, 6,* 1-13.

Busch, A. & Hippler, M. (2011). The structure and function of eukaryotic photosystem I. *Biochimica et Biophysica Acta – Bioenergetics, 1807*, 864-877.

Butler, T., Kapoore, R.V. & Vaidyanathan, S. (2020). *Phaeodactylum tricornutum*: a diatom cell factory. *Trends in Biotechnology, 38*(6), 606-622.

Canutescu, A.A., Shelenkov, A.A. & Dunbrack, R.L. (2003) A graph-theory algorithm for rapid protein side-chain prediction. *Protein Science 12*, 2001–2014.

Case, D.A., Ben-Shalom, S.R., Brozell, D.S., Cerutti, T.E., Cheatham, T.E., et al. (2019) AMBER 2019, University of California, San Francisco.

Cassier-Chauvat, C. & Chauvat, F. (2014). Function and regulation of ferredoxins in the cyanobacterium, *Synechocystis* PCC 6803: Recent advances. *Life, 4,* 666-680.

Caspy, I., Borovikova-Sheinker, A., Klaiman, D., Shkolnisky, Y. & Nelson, N. (2020). The structure of a triple complex of plant photosystem I with ferredoxin and plastocyanin. *Nature Plants, 6*, 1300-1305.

Castell, C. (2016). Alternative redox proteins in photosynthesis. Master's thesis. University of Sevilla.

Castell, C., Bernal-Bayard, P., Ortega, J. M., Roncel, M., Hervás, M. & Navarro, J.A. (2021b). The heterologous expression of a plastocyanin in the diatom *Phaeodactylum tricornutum* improves cell growth under iron deficient conditions. *Physiologia Plantarum, 171,* 277-290.

Castell, C., Rodríguez-Lumbreras, L.A., Hervás, M., Fernández-Recio, J. & Navarro, J.A. (2021a). New insights into the evolution of the electron transfer from cytochrome *f* to photosystem I in the green and red branches of photosynthetic eukaryotes. *Plant and Cell Physiology*, doi:10.1093/pcp/pcab044.

Chan, L., Liu, X., Li, Y., Liu, C-C., Yang, F., Zhao, J. & Sui, S-F. (2015). Structural organization of an intact phycobilisome and its association with photosystem II. *Cell Research, 25,* 726-737.

Cheatham, T.E., Cieplak, P. & Kollman, P.A. (1999). A modified version of the Cornell *et al.* force field with improved sugar pucker phases and helical repeat. *Journal of Biomolecular Structure and Dynamics, 16*(4), 845-862.

Chen, T.M., Blundell, T.L. & Fernandez-Recio, J. (2007). pyDock: Electrostatics and desolvation for effective scoring of rigid-body protein-protein docking. *PROTEINS: Structure, Function and Bioinformatics, 68,* 503-515.

Chi, Y-I., Huang, L.S., Zhang, Z., Fernández-Velasco, J.G. & Berry, E.A. (2000). X-ray structure of a truncated form of cytochrome *f* from *Chlamydomonas reinhardtii*. *Biochemistry, 39,* 7689-7701.

Chida, H., Nakazawa, A., Akazaki, H., Hirano, T., Suruga, K., Ogawa, M., Satoh, T., Kadokura, K., Yamada, S., Hakamata, W., Isobe, K., Ito, T., Ishii, R., Nishio, T., Sonoike, K. & Oku, T. (2007). Expression of the algal cytochrome c_6 gene in *Arabidopsis* enhances photosynthesis and growth. *Plant and Cell Physiology, 48*(7), 948-957.

Chu, H-A. & Chiu, Y. (2016). Tue roles of cytochrome b_{559} in assembly and photoprotection of photosystem II revealed by site-directed mutagenesis studies. *Frontiers in Plant Science, 6*, 1-7. *Biochemistry, 33,* 6137-6149.

Chu, H-A., Nguyen, A.P. & Debus, R.J. (1994). Site-directed photosystem II mutants with perturbed oxygen-evolving properties. 1. Instability or inefficient assembly of the manganese cluster *in vivo*.

Cox, N., Pantazis, D.A. & Lubitz, W. (2020). Current understanding of the mechanism of water oxidation in photosystem II and its relation to XFEL data. *Annual Review of Biochemistry, 89*(1), 795-820.

Cramer, W.A. (2019). Structure-function of the cytochrome b_6f lipoprotein complex: a scientific odyssey and personal perspective. *Photosynthesis Research, 139*(1-3), 53-65.

Crepin, A. & Caffarri, S. (2018). Functions and evolution of Lhcb isoforms composing LHCII, the major light harvesting complex of photosystem II of green eukaryotic organisms. *Current Protein Peptide Science, 19*(7), 699-713.

Crichton, R.R. Iron Metabolism: From Molecular Mechanisms to Clinical Consequences, 4th ed.; John Wiley & Sons, Ltd.: Chichester, UK, 2016

Crimmins, D.L., Mische, S.M. & Denslow, N.D. (2005). Chemical cleavage of proteins in solution. *Current Protocols in Protein Science, 41*(1), 11.4.1-11.4.11.

Croce, R. & van Amerongen, H. (2013). Light-harvesting in photosystem I. *Photosynthesis Research, 116*(2-3)*,* 153-166.

Crowley, P.B., Otting, G., Schlarb-Ridley, B.G., Canters, G.W. & Ubbink, M. (2001). Hydrophobic interactions in a cyanobacterial plastocyanin−cytochrome *f* complex. *Journal of the American Chemical Society*, *123*(43), 10444-10453.

Crowley, P.B. & Ubbink, M. (2003). Close encounters of the transient kind: protein interactions in the photosynthetic redox chain investigated by NMR spectroscopy. *Accounts of Chemical Research, 36*(10), 723-730.

Cruz-Gallardo, I., Díaz-Moreno, I., Díaz-Quintana, A. & De la Rosa, M.A. (2012). The cytochrome *f*-plastocyanin complex as a model to study transient interactions between redox proteins. *FEBS Letters*, *586*, 646-652.

Daboussi, F., Leduc, S., Maréchal, A., Dubois, G., Guyot, V., Perez-Michaut, C., Amato, A., Falciatore, A., Juillerat, A., Beurdeley, M., Voytas, D.F., Cavarec, L. & Duchateau, P. (2014). Genome engineering empowers the diatom *Phaeodactylum tricornutum* for biotechnology. *Nature Communications, 5*, 1-7.

De Baar, H.J. W., Boyd, P.W., Coale, K.H, Landry, M.R., Tsuda, A., Assmy, P., et al., (2005). Synthesis of iron fertilization experiments: from the iron age in the age of enlightenment. *Journal of Geophysical Research, 110*, 1-24.

De la Rosa, M.A., Molina-Heredia, F.P., Hervás, M. & Navarro, J.A. Convergent evolution of cytochrome c_6 and plastocyanin. The evolutionary pathways of the two proteins are connected to the geochemical changes in iron and copper availabilities. In: *Photosystem I: the light driven plastocyanin:ferredoxin oxidoreductase* (Golbeck, J.H., Ed.). Advances in photosynthesis and respiration, *24.* Springer, Dordrecht, The Netherlands, 2006; 683-696.

De Martino, A., Meichenin, A., Shi, J., Pan, K. & Bowler, C. (2007). Genetic and phenotypic characterization of *Phaeodactylum tricornutum* (Bacillariophyceae) accessions. *Journal of Phycology, 43*, 992-1009.

Dhaouadi, F., Awwad, F., Diamond, A. & Desgagné-Phenix, I. (2020). Diatom's breakthroughs in biotechnology: Phaoedactylum tricornutum as a model for producing high-added value molecules. *American Journal of Plant Sciences, 11*(10).

Díaz-Moreno, I., Díaz-Quintana, A., Ubbink, M. & De la Rosa, M.A. (2005). An NMR-based docking model for the physiological transient complex between cytochrome *f* and cytochrome c_6. *FEBS Letter, 579,* 2891-2896.

Díaz-Moreno, I., Hulsker, R., Skubak, P., Foerster, M., Cavazzini, D., Finiguerra, M.G., et al. (2014). The dynamic complex of cytochrome c_6 and cytochrome *f* studied with paramagnetic NMR spectroscopy. *Biochimica et Biophysica Acta – Bioenergetics, 1837*, 1305-1315.

Díaz-Quintana, A., Hervás, M., Navarro, J.A. & De la Rosa, M.A. Plastocyanin and cytochrome c_6: the soluble electron carriers between the cytochrome b_6f complex and photosystem I. In: *Photosynthetic Protein Complexes: A Structural Approach* (Fromme, P., Ed.). Wiley-VCH Verlag GmbH & Co. KGaA, Weinheim, 2008; pp. 181-200.

Díaz-Quintana, A., Navarro, J.A., Hervás, M., Molina-Heredia, F.P., De la Cerda, B. & De la Rosa, M.A. (2003). A comparative structural and functional analysis of cyanobacterial plastocyanin and cytochrome c_6 as alternative electron donors to Photosystem I. Photosystem I reduction in cyanobacteria. *Photosynthesis Research, 75*, 97-110.

Drepper, F., Hippler, M., Nitschke, W. & Haehnel, W. (1996). Binding dynamics and electron transfer between plastocyanin and photosystem I. *Biochemistry, 35*(4), 1282-1295.

Ducruet, J.M. & Miranda, T. (1992). Graphical and numerical analysis of thermoluminescence and fluorescence F_0 emission in photosynthetic material. *Photosynthesis Research, 33*, 15-27.

Ducruet, J.M., Serrano, A., Roncel, M. & Ortega, J.M. (2011). Peculiar properties of chlorophyll thermoluminescence emission of autotrophically or mixotrophically grown *Chlamydomonas reinhardtii*. *Journal of Photochemistry and Photobiology B: Biology, 104*, 301-307.

Ducruet, J. & Vavilin, D. (1999). Chlorophyll high-temperature thermoluminescence emission as an indicator of oxidative stress: perturbating effects of oxygen and leaf water content. *Free Radical Research, 31*, S188-192.

Durán, R.V., Hervás, M., De la Rosa, M.A. & Navarro, J.A. (2005). In vivo photosystem I reduction in thermophilic and mesophilic cyanobacteria: the thermal resistance of the process is limited by factors other than the unfolding of the partners. *Biochemical and Biophysical Research Communications, 334,* 170-175.

Enami, I., Iwai, M., Akiyama, A., Suzuki, T., Okumura, A., Katoh, T., Tada, O., Ohta, H. & Shen, J-R. (2003). Comparison of binding and functional properties of two extrinsic components, cyt *c*550 and a 12 kDa protein, in cyanobacterial PSII with those in red algal PSII. *Plant and Cell Physiology, 44*(8), 820-827.

Enami, I., Kikuchi, S., Fukuda, T., Ohta, H. & Shen, J. (1998). Binding and functional properties of four extrinsic proteins of photosystem II from a red alga, *Cyanidium caldarium*, as studied by release – reconstitution experiments. *Biochemistry, 37*, 2787-2793.

Enami, I., Okumura, A., Nagao, R., Suzuki, T., Iwai, M. & Shen, J-R. (2008). Structures and functions of the extrinsic proteins of photosystem II from different species. *Photosynthesis Research, 98,* 349-363.

Enzing, C., Ploeg, M., Barbosa, M. & Sijtsma, L. Microalgae-based products for the food and feed sector: an outlook for Europe. In: *JRC Scientific and Policy Reports. European Comission.EUR-Scientific and Technical Research series* – ISSN 1831-9424; 2014.

Eswar, N., Webb, B., Marti-Renom, M.A., Madhusudhan, M.S., Eramian, D., Shen, M., Pieper, U. & Sali, A. (2007). Comparative protein structure modeling using MODELLER. *Current Protocols in Protein Science,* 2.9.1-2.9.23.

Evans, K.A. & Krogmann, D.W. (1983). The *c*-type cytochromes from the red alga *Porphyridium cruentum*. *Archives of Biochemistry and Biophysics, 227*(2), 494-510.

Falciatore, A., Casotti, R., Leblanc, C., Abrescia, C. & Bowler, C. (1999). Transformation of nonselectable reporter genes in marine diatoms. *Marine Biotechnology, 1*(3), 239–251.

Falciatore, A., Jaubert, M., Bouly, J.P., Bailleul, B. & Mock, T. (2020). Diatom molecular research comes of age: Model species for studying phytoplankton biology and diversity. *The Plant Cell*, *32*, 547-572.

Falkowski, P.G., Barber, R.T. & Smetacek, V. (1998). Biogeochemical controls and feedbacks on ocean primary production. *Chemistry and Biology of the oceans, 281*, 200-207.

Falkowski, P.G., Katz, M.E., Knoll, A.H., Quigg, A., Raven, J.A., Schofield, O. & Taylor, F.J. R. (2004). The evolution of modern eukaryotic phytoplankton. *Science, 305*, 354-360.

Farah, J., Rappaport, F., Choquet, Y., Joliot, P. & Rochaix, J.D. (1995). Isolation of a PsaF-deficient mutant of *Chlamydomonas reinhardtii*: efficient interaction of plastocyanin with the photosystem I reaction center is mediated by the PsaF-subunit. *The EMBO Journal, 14*(20), 4976-4984.

Fedorov, V.A., Kovalenko, I.B., Khruschev, S.S., Ustinin, D.M., Antal, T.K., Riznichenko, G. Y. & Rubin, A.B. (2019). Comparative analysis of plastocyanin-cytochrome *f* complex formation in higher plants, green algae and cyanobacteria. *Physiologia Plantarum, 166,* 320-335.

Field, C.B., Behrenfeld, M.J., Randerson, J.T. & Falkowski, P.G. (1998). Primary production of the biosphere: Integrating terrestrial and oceanic components. *Science, 281*(5374), 237-240.

Finazzi, G., Sommer, F. & Hippler, M. (2005). Release of oxidized plastocyanin from photosystem I limits electron transfer between photosystem I and cytochrome b_6f complex in vivo. *Proceedings of the National Academy of Sciences USA, 102*(19), 7031-7036.

Flori, S. (PhD Thesis). Light utilization in microalgae: The marine diatom *Phaeodactylum tricornutum* and the green algae *Chlamydomonas reinhardtii*. Agricultural sciences. Université Grenoble Alpes, 2016.

Flori, S., Jouneau, P.H., Bailleul, B., Gallet, B., Estrozi, L.F., Moricot, C., et al. (2017). Plastid thylakoid architecture optimizes photosynthesis in diatoms. *Nature Communications, 8*, 1-9.

Franklin, N.M., Stauber, J.L. & Lim, R.P. (2001) Development of flow cytometry-based algal bioassays for assessing toxicity of copper in natural waters. *Environmental Toxicology and Chemistry, 20*(1):160-170.

Frazão, C., Enguita, F.J., Coelho, R., Sheldrick, G.M., Navarro, J.A., Hervás, M., De la Rosa, M.A. & Carrondo, M.A. (2001). Crystal structure of low-potential cytochrome c_{549} from *Synechocystis* sp. PCC 6803 at 1.21 Å resolution. *Journal of Biological Inorganic Chemistry*, 6, 324-332.

Frazão, C., Soares, C.M., Carrondo, M.A., Pohl, E., Dauter, Z., Wilson, K.S., Hervás, M., Navarro, J.A., De la Rosa, M.A. & Sheldrick, G.M. (1995). *Ab initio* determination of the crystal structure of cytochrome c_6 and comparison with plastocyanin. *Structure, 3,* 1159-1169.

Fromme, P., Jordan, P. & Krauβ, N. (2001). Structure of photosystem I. *Biochimica et Biophysica Acta – Bioenergetics, 1507,* 5-31.

Gabb, H.A., Jackson, R.M. & Sternberg, M.J.E. (1997). Modelling protein docking using shape complementarity, electrostatics and biochemical information. *Journal of Molecular Biology, 272*(1), 106-120.

Gao, X., Bowler, C. & Kazamia, E. (2021). Iron metabolism strategies in diatoms, *Journal of Experimental Botany, 72*(6), 2165-2180.

García-Calderón, M., Betti, M., Márquez, A.J., Ortega, J.M. & Roncel, M. (2019). The afterglow thermoluminescence band as an indicator of changes in the photorespiratory metabolism of the model legume *Lotus japonicus*. *Physiologia Plantarum, 166*(1), 240-250.

García-Cañas, R., Giner-Lamia, J., Florencio, F.J. & López-Maury, L. (2021). A protease-mediated mechanism regulates the cytochrome c_6/plastocyanin switch in *Synechocystis* sp. PCC 6803. *Proceedings of the National Academy of Sciences USA,* 118: e2017898118.

Giammona, D.A. (PhD Thesis). An examination of conformational flexibility in porphyrins and bulky-ligand binding in myoglobin. University of California, Davis. 1984.

Goldman, J.C. & McCarthy, J.J. (1978) Steady state growth and ammonium uptake of a fast-growing marine diatom. *Limnology and Oceanography, 23*(4), 695-703.

Gong, X., Wen, J.Q., Fisher, N.E., Young, S., Howe, C.J., Bendall, D.S. & Gray, J.C. (2000). The role of individual lysine residues in the basic patch on turnip cytochrome *f* for electrostatic interactions with plastocyanin *in vitro*. *European Journal of Biochemistry, 267,* 3461-3468.

Greene, R.M., Geider, R.J., Kolber, Z. & Falkowski, P.G. (1992). Iron-induced changes in light harvesting and photochemical energy conversion processes in eukaryotic marine algae. *Plant Physiology. 100*(2), 565-575.

Grosdidier, S. & Fernández-Recio, J. (2008). Identification of hot-spot residues in protein-protein interactions by computational docking. *BMC Bioinformatics, 9,* 1-13.

Gross, E. L. & Pearson Jr., D.C. (2003). Brownian dynamics simulations of the interaction of *Chlamydomonas* cytochrome *f* with plastocyanin and cytochrome c_6. *Biophysical Journal, 85,* 2055-2068.

Grotjohann, I. & Fromme, P. (2005). Structure of cyanobacterial photosystem I. *Photosynthesis Research, 85,* 51-72.

Groussman, R.D., Parker, M.S. & Armbrust, E.V. (2015). Diversity and evolutionary history of iron metabolism genes in diatoms. *PLoS ONE, 10*(6), 1-25.

Grove, T.Z. & Kostic, N.M. (2003). Metalloprotein association, self-association, and dynamics governed by hydrophobic interactions: simultaneous occurrence of gated and true electron-transfer reactions between cytochrome *f* and cytochrome c_6 from *Chlamydomonas reinhardtii*. *Journal of the American Chemical Society, 125,* 10598-10607.

Guergova-Kuras, M., Bourdreaux, B., Joliot, A., Joliot, P. & Redding, K. (2001). Evidence for two active branches for electron transfer in photosystem I. *Proceedings of the National Academy of Sciences, 98*(8)*,* 4437-4442.

Guerrero, F., Sedoud, A., Kirilovsky, D., Rutherford, A.W., Ortega, J.M. & Roncel, M. (2011). A high redox potential form of cytochrome c_{550} in photosystem II from *Thermosynechococcus elongatus*. *Journal of Biological Chemistry, 286*(8), 5948-5994.

Guerrero, F., Zurita, J.L., Roncel, M., Kirilovsky, D. & Ortega, J.M. (2014). The role of the high potential form of the cytochrome *b*559: Study of *Thermosynechococcus elongatus* mutants. *Biochimica et Biophysica Acta – Bioenergetics, 1837,* 908-919.

Guo, J., Annet, A.L., Taylor, R.L., Lapi, S., Ruth, T.J. & Maldonado, M.T. (2010). Copper-uptake kinetics of coastal and oceanic diatoms. *Journal of Phycology, 46*, 1218-1228.

Guo, J., Green, B.R. & Maldonado, M.T. (2015). Sequence analysis and gene expression of potential components of copper transport and homeostasis in *Thalassiosira pseudonana*. *Protist, 166,* 58-77.

Guo, J., Lapi, S., Ruth, T.J. & Maldonado, M.T. (2012). The effects ofi ron and copper availability on the copper stoichiometry of marine phytoplankton. *Journal of Phycology, 48,* 312-325.

Guss, M.J. & Freeman, H.C. (1983). Structure of oxidized poplar plastocyanin at 1.6 Å resolution. *Journal of Molecular Biology, 169*(2), 521-563.

Haddadian, E.J. & Gross, E.L. (2005). A Brownian dynamics study of cytochrome *f* interactions with cytochrome c_6 and plastocyanin in *Chlamydomonas reinhardtii* plastocyanin, and cytochrome c_6 mutants. *Biophysical Journal, 88*(3), 2323-2339.

Haddadian, E.J. & Gross, E.L. (2006). A Brownian dynamics study of the effects of cytochrome *f* structure and deletion of its small domain in interactions with cytochrome c_6 and plastocyanin in *Chlamydomonas reinhardtii*. *Biophysical Journal, 90*(2), 566-577.

Haehnel, W., Jansen, T., Gause, K., Klösgen, R.B., Stahl, B., Michl, D., Huvermann, B., Karas, M. & Herrmann, R.G. (1994). Electron transfer from plastocyanin to photosystem I. *The EMBO Journal, 13*(5), 1028-1038.

Hall, D.O. (1976). Photobiological energy conversion. *FEBS Letters, 64*(1), 6-16.

Hanahan, D. (1983). Studies on transformation of *Escherichia coli* with plasmids. *Journal of Molecular Biology, 166*(4), 557-580.

Hasan, S.S., Yamashita, E. & Cramer, W.A. (2013). Transmembrane signaling and assembly of the cytochrome b_6f-lipidic charge transfer complex. *Biochimica et Biophysica Acta – Bioenergetics, 1827,* 1295-1308.

Heinz, S., Liauw, P., Nickelsen, J. & Nowaczyk, M. (2016). Analysis of photosystem II biogenesis in cyanobacteria. *Biochimica et Biophysica Acta – Bioenergetics, 1857*, 274-287.

Hervás, M., Navarro, J.A & De la Rosa, M.A. (2003). Electron transfer between membrane complexes and soluble proteins in photosynthesis. *Accounts of Chemical Research, 35,* 785-805.

Hervás, M., Navarro, J.A., Díaz, A., Bottin, H. & De la Rosa, M.A. (1995). Laser-flash kinetic analysis of the fast electron transfer from plastocyanin and cytochrome c_6 to photosystem I. Experimental evidence on the evolution of the reaction mechanism. *Biochemistry, 34*(36), 785-805.

Hippler, M. & Depprer, F. Electron transfer between photosystem I and plastocyanin or cytochrome c_6. In: *Photosystem I: the light driven plastocyanin:ferredoxin oxidoreductase* (Golbeck, J.H., Ed.). Advances in photosynthesis and respiration, *24.* Springer, Dordrecht, The Netherlands, 2006; pp. 499-513.

Hippler, M., Drepper, F., Haehnel, W. & Rochaix, J.D. (1998). The N-terminal domain of PsaF: Precise recognition site for binding and fast electron transfer from cytochrome c_6 and plastocyanin to photosystem I of *Chlamydomonas reinhardtii. Proceedings of the National Academy of Sciences USA, 95*(13), 7339-7344.

Hippler, M., Reichert, J., Sutter, M., Zak, E., Altschmied, L., Schröer, U., Herrmann, R.G. & Haehnel, W. (1996). The plastocyanin binding domain of photosystem I. *The EMBO Journal, 15*(23), 6374-6384.

Hippmann, A.A., Schuback, N., Moon, K.M., McCrow, J.P., Allen, A.E., Foster, L.J., Green, B.R. & Maldonado, M.T. (2017). Contrasting effects of copper limitation on the photosynthetic apparatus in two strains of the open ocean diatom *Thalassiosira oceanica. PLoS ONE, 12*(8), 1-34.

Ho, T.Y., Quigg, A., Finkel, Z.V., Milligan, A.J., Wyman, K., Falkowski, P.G., et al. (2003). The elemental composition of some marine phytoplankton. *Journal of Phycology, 39*, 1145-1159.

Huertas, M.J., López-Maury, L., Giner-Lamia, J., Sánchez-Riego, A.M. & Florencio, F.J. (2014). Metals in cyanobacteria: analysis of the copper, nickel, cobalt and arsenic homeostasis mechanisms. *Life, 4*, 865-886.

Hung, C-H., Huang, J-Y., Chiu, Y-F. & Chu, H-A. (2007). Site-directed mutagenesis on the heme axial-ligands of cytochrome b559 in photosystem II by using cyanobacteria *Synechocystis* PCC 6803. *1767*, 686-693.

Ifuku, K. & Noguchi, T. (2016). Structural coupling of extrinsic proteins with the oxygen-evolving center in photosystem II. *Frontiers in Plant Science, 7*, 1-11.

Inoue, T., Sugawara, H., Hamanaka, S., Tsukui, H., Suzuki, E., Kohzuma, T. & Kai, Y. (1999). Crystal structure determinations of oxidized and reduced plastocyanin from the cyanobacterium *Synechococcus sp.* PCC 7942. *Biochemistry, 38,* 6063-6069.

Ish-Horowicz, D. & Burke, J.F. (1981). Rapid and efficient cosmid cloning. *Nucleic Acids Research, 9*, 2989-2998.

Jeffrey, S.W. & Humphrey, G.F. (1975). New spectrophotometric equations for determining chlorophylls a, b, c1 and c2 in higher plants, algae and natural phytoplankton. *Biochemie und Physiologie der Pflanzen, 167*, 191-194.

Jiménez-García, B., Pons, C. & Fernández-Recio, J. (2013). pyDockWEB: A web server for rigid-body protein-protein docking using electrostatics and desolvation scoring. *Bioinformatics, 29*(13), 1698-1699.

Johnson, M.P. (2016). Photosynthesis. *Essays in Biochemistry, 60*, 255-273.

Joliot, P., Beal, D. & Rappaport, F. A new high-sensitivity 10-ns time-resolution spectrophotometric technique adapted to in vitro analysis of the photosynthetic apparatus. In: *Photosynthesis: Mechanisms and Effects* (Garab, G., Ed.). Springer, Dordrecht, The Netherlands, 1998; pp. 4247-4252.

Kang, C., Chitnis, P.R., Smith, S. & Krogmann, D.W. (1994). Cloning and sequence analysis of the gene encoding the low potential cytochrome *c* of *Synechocystis* PCC 6803. *FEBS Letters, 344*, 5-9.

Kannt, A., Young, S. & Bendall, D.S. (1996). The role of acidic residues of plastocyanin in its interaction with cytochrome *f*. *Biochimica et Biophysica Acta – Bioenergetics, 1277,* 115-126.

Kato, Y. & Sakamoto, W. (2010). New insights into the types and function of proteases in plastids. *International Review of Cell and Molecular Biology, 280,* 185-218.

Kayanja, G.E., Ibrahim, I.M. & Puthiyaveetil, S. (2021). Regulation of *Phaeodactylum* plastid gene transcription by redox, light, and circadian signals. *Photosynthesis Research*, *147*, 317-328.

Kazamia, E., Sutak, R., Paz-Yepes, J., Dorrel, R.G., Vieira, F.R.J., Mach, J., Morrissey, J., Leon, S., Lam, F., Pelletier, E., Camadro, J.M., Bowler, C. & Lesuisse, E. (2018). Endocytosis-mediated siderophore uptake as a strategy for Fe acquisition in diatoms. *Science Advances, 4*, 1-14.

Kerfeld, C.A. & Krogmann, D.W. (1998). Photosynthetic cytochromes *c* in cyanobacteria, algae, and plants. *Annual Review of Plant Biology, 49*, 397-425.

Kienzl, P.F. & Peschek, G.A. (1983). Cytochrome c-549 – an endogenous cofactor of cyclic photophosphorylation in the cyanobacterium *Anacystis nidulans. FEBS Letters, 162*(1), 76-80.

Kilian, O. & Kroth, P.G. (2004). Presequence acquisition during secondary endocytobiosis and possible role of introns. *Journal of Molecular Evolution, 58*(6), 712-721.

Kirilovsky, D., Roncel, M., Boussac, A., Wilson, A., Zurita, J. L., Ducruet, J.M., Bottin, H., Sugiura, M., Ortega, J.M. & Rutherford, A.W. (2004). Cytochrome c_{550} in the cyanobacterium *Thermosynechococcus elongatus*: Study of redox mutants. *Journal of Biological Chemistry, 279*(61), 52869-52880.

Klughammer, C. & Schreiber, U. (2016). Deconvolution of ferredoxin, plastocyanin, and P700 transmittance changes in intact leaves with a new type of kinetic LED array spectrophotometer. *Photosynthesis Research, 128,* 195-214.

Kohzuma, T., Inoue, T., Yoshizaki, F., Sasakawa, Y., Onodera, K., Nagatomo, S., Kitagawa, T., Uzawa, S., ISobe, Y., Sugimura, Y., Gotowda, M. & Kai, Y. (1999). The structure and unusual pH dependence of plastocyanin from the fern *Dryopteris crassirhizoma*: The protonation of an active site histidine is hindered by π-π interactions. *Journal of Biological Chemistry, 274*(17), 11817-11823.

Kong, L. & Price, N.M. (2019). Functional CTR-type Cu(I) transporters in an oceanic diatom. *Environmental Microbiology, 21*, 98-110.

Kong, L. & Price, N.M. (2020). Identification of copper-regulated proteins in an oceanic diatom, *Thalassiosira oceanica* 1005. *Metallomics*, *12*(7), 1106-1117.

Kooistra, W.H.C.F., Gersonde, R., Medlin, L.K. & Mann, D.G. The origin and evolution of the diatoms: Their adaptation to a planktonic existence. In: *Evolution of Primary Producers in the Sea* (Falkowski, P. G. & Knoll, A. H., Eds.). Academic Press, 2007; pp. 207-249.

Kramer, D.M., Johnson, G., Kiirats, O. & Edwards, G.E. (2004). New fluorescence parameters for the determination of Q_A redox state and excitation energy fluxes. *Photosynthesis Research, 79*, 209-2018.

Krieger-Liszkay, A. (2005). Singlet oxygen production in photosynthesis. *Journal of Experimental Botany, 56,* 337-346.

Kröger, N. & Poulsen, N. (2008). Diatoms – From cell wall biogenesis to nanotechnology. *Annual Review of Genetics, 42*(1), 83-107.

Krogmann, D.W. (1991). The low-potential cytochrome c of cyanobacteria and algae. *Biochimica et Biophysica Acta – Bioenergetics, 1058*, 35-37.

Kroh, G.E. & Pilon, M. (2020). Regulation of iron homeostasis and use in chloroplasts. *International Journal of Molecular Science, 21,* 3395.

Kropat, J., Tottey, S., Birkenblhl, R.P., Depège, N., Huljser, P. & Merchant, S. (2005). A regulator of nutritional copper signalling in *Chlamydomonas* is an SBP domain protein that recognizes the GRAC core of copper response element. *Proceedings of the National Academy of Sciences USA, 102*(51), 18730-18735.

Kroth, P. (2007). Molecular biology and the biotechnological potential of diatoms. *Advances in Experimental Medicine and Biology, 616,* 23-33.

Kuczynska, P., Jemiola-Rzeminska, M. & Strzalka, K. (2015). Photosynthetic pigments in diatoms. *Marine Drugs, 13,* 5847-5881.

Kroth, P. & Strotmann, H. (1999). Diatom plastids: Secondary endocytobiosis, plastid genome and protein import. *Physiologia Plantarum, 107*(1), 136-141.

Kuhlgert, S., Drepper, F., Fufezan, C., Sommer, F., Hippler, M. (2012). Residues PsaB Asp612 and PsaB Glu613 of photosystem I confer pH-dependent binding of plastocyanin and cytochrome c_6. *Biochemistry, 51*(37), 7297-7303.

Kurisu, G., Zhang, H., Smith, J.L. & Cramer, W.A. (2003). Structure of the cytochrome b_6f complex of oxygenic photosynthesis: tuning the cavity. *Science, 302*(5647), 1009-1014.

La Roche, J., Boyd, P.W., McKay, R.M.L. & Geider, R.J. (1996). Flavodoxin as an *in situ* marker for iron stress in phytoplankton. *Nature, 382,* 802-805.

Laemmli, U.K. (1970). Cleavage of structural proteins during the assembly of the head of bacteriophage T4. *Nature, 227*, 680-685.

Lange, C., Cornvik, T., Díaz-Moreno, I. & Ubbink, M. (2005). The transient complex of poplar plastocyanin with cytochrome *f*: effects of ionic strength and pH. *Biochimica et Biophysica Acta – Bioenergetics, 1707,* 179-188.

Lavaud, J., Six, C. & Campbell, D.A. (2016). Photosystem II repair in marine diatoms with contrasting photophysiologies. *Photosynthesis Research, 127*, 189-199.

Levering, J., Broddrick, J., Dupont, C.L., Peers, G., Beeri, K., Mayers, J., Gallina, A.A., Allen, A.E., Bernhard, O.P. & Zengler, K. (2016). Genome-scale model reveals metabolic basis of biomass partitioning in a model Diatom. *PLoS ONE, 11*(5), 1-22.

Levy, J.L., Angel, B. M., Stauber, J.L., Poon, W.L., Simpson, S.L., Cheng, S.H. & Jolley, D.F. (2008). Uptake and internalisation of copper by three marine microalgae: comparison of copper-sensitive and copper-tolerant species. *Aquatic Toxicology, 89*, 82-93.

Li, F., Beardall, J., Collins, S. & Gao, K. (2017). Decreased photosynthesis and growth with reduced respiration in the model diatom *Phaeodactylum tricornutum* grown under elevated CO_2 over 1800 generations. *Global Change Biology, 23*(1), 127-137.

Li, Z., Andrews, J.J., Eaton-Rye, R.L. & Burnap, R.L. (2004). *In situ* effects of mutations of the extrinsic cytochrome c_{550} of photosystem II in *Synechocystis* sp. PCC6803. *Biochemistry, 43,* 14161-14170.

Lodeyro, A.F., Ceccoli, R.D., Pierella Karlusich, J.J. & Carrillo, N. (2012). The importance of flavodoxin for environmental stress tolerance in photosynthetic microorganisms and transgenic plants. Mechanism, evolution and biotechnological potential. *FEBS Letters, 586,* 2917-2924.

Loll, B., Kern, J., Saenger, W., Zouni, A. & Biesiadka, J. (2005). Towards complete cofactor arrangement in the 3.0 Å resolution structure of photosystem II. *Nature, 438,* 1040-1044.

Lommer, M., Specht, M., Roy, A.S., Kraemer, L., Andreson, R., Gutowska, M.A., Wolf, J., Bergner, S.V., Schilhabel, M.B., Klostermeier, U.C., Beiko, R.G., Rosenstiel, P., Hippler, M. & La Roche, J. (2012). Genome and low-iron response of an oceanic diatom adapted to chronic iron limitation. *Genome Biology, 13*, 1-20.

Lowry, O.H., Rosebrough, N.J., Farr, A.L. & Randall, R.J. (1951). Protein measurement with the Folin phenol reagent. *Journal of Biological Chemistry, 193*, 265-275.

Lyons, T.W., Reinhard, C.T. & Planavsky, N.J. (2014). The rise of oxygen in Earth's early ocean and atmosphere. *Nature, 506,* 307-315.

Maldonado, M.T., Allen, A.E., Chong, J.S., Lin, K., Leus, D., Karpenko, N. & Harris, S.L. (2006). Copper-dependent iron transport in coastal and oceanic diatoms. *Limnology and Oceanography, 51*(4), 1729-1743.

Marchetti, A., Parker, M.S., Moccia, L.P., Lin, E.O., Arrieta, A.L., Ribalet, F., Murphy, M.E. P., Maldonado, M.T. & Armbrust, E.V. (2009). Ferritin is used for iron storage in bloom-forming marine pennate diatoms. *Nature, 457*, 467-470.

Marchetti, A., Schruth, D.M., Durkin, C.A., Parker, M.S., Kodner, R.B., Berthiaume, C.T., Morales, R., Allen, A.E. & Armbrust, E.V. (2012). Comparative metatranscriptomics identifies molecular bases for the physiological responses of phytoplankton to varying iron availability. *Proceedings of the National Academy of Sciences USA, 109*(6), E317-E325.

Markwell, M.A.K., Haas, S.M., Bieber, L.L. & Tolbert, N.E. (1978). A modification of the Lowry procedure to simplify protein determination in membrane and lipoprotein samples. *Analytical Biochemistry, 87*(1), 206-210.

Martin-Jézéquel, V. & Tesson, B. *Phaeodactylum tricornutum* polymorphism: an overview, In: *Advances in Algal Cell Biology* (Heimann, K. & Katsaros, C., Eds.). De Gruyter, Göttingen, 2012; Chapter 3, pp. 43-80.

Martínez-Fábregas, J., Díaz-Moreno, I., González-Arzola, K., Janocha, S., Navarro, J.A., Hervás, M., Bernhardt, R., Velázquez-Campoy, A., Díaz-Quintana, A. & De la Rosa, M.A. (2014). Structural and functional analysis of novel human cytochrome *c* targets in apoptosis. *Molecular and Cellular Proteomics, 13*(6), 1439-1456.

Martínez, S.E., Huang, D., Szczepaniak, A., Cramer, W.A. & Smith, J.L. (1994). Crystal structure of chloroplast cytochrome *f* reveals a novel cytochrome fold and unexpected heme ligation. *Structure, 2*(2), 95-105.

Mazor, Y., Borovikova, A. & Nelson, N. (2015). The structure of plant photosystem I super-complex at 2.8 Å resolution. *eLife* 2015; 4: e07433.

McKay, R.M.L., La Roche, J., Yakunin, A.F., Drunford, D.G. & Geider, R.J. (1999). Accumulation of ferredoxin and flavodoxin in a marine diatom in response to Fe. *Journal of Phycology*, *35,* 510-519.

McLachlan, J. (1964). Some considerations of the growth of marine algae in artificial media. *Canadian Journal of Microbiology, 10*(8104), 769-782.

Medina, M. (2009). Structural and mechanistic aspects of flavoproteins: photosynthetic electron transfer from photosystem I to $NADP^+$. *The FEBS Journal, 276*, 3942–3958.

Medina, M. & Gómez-Moreno, C. (2004). Interaction of ferredoxin-NADP(+) reductase with its substrates: optimal interaction for efficient electron transfer. *Photosynthesis Research, 79*, 113-131.

Merchant, S. & Bogorad, L. (1986). Rapid degradation of apoplastocyanin in Cu(II)-deficient cells of *Chlamydomonas reinhardtii*. *Journal of Biological Chemistry, 261*(34), 15850-15853.

Merchant, S.S., Schmollinger, S., Strenkert, D., Moseley, L. & Blably-Haas, C.E. (2020). From economy to luxury: copper homeostasis in *Chlamydomonas* and other algae. *Biochimica et Biophysica Acta – Molecular Cell Research, 1867,* 1-10.

Meyer, T.E., Zhao, Z.G., Cusanovich, M.A. & Tollin, G. (1993). Transient kinetics of electron transfer from a variety of c-type cytochromes to plastocyanin. *Biochemistry, 32,* 4552-4559.

Mitchell, P. (1961). Coupling of phosphorylation to electron and hydrogen transfer by a chemi-osmotic type of mechanism. *Nature, 191,* 144-148.

Molina-Heredia, F.P., Hervás, M., Navarro, J.A. & De la Rosa, M.A. (1998). Cloning and correct expression in *Escherichia coli* of the *pet*E and *pet*J genes respectively encoding plastocyanin and cytochrome c_6 from the cyanobacterium *Anabaena* sp. PCC 7119. *Biochemical and Biophysical Research Communications, 243*, 302-306.

Molina-Heredia, F.P., Wastl, J., Navarro, J.A., Bendall, D.S., Hervás, M., Howe, C.J. & De la Rosa, M.A. (2003). A new function for an old cytochrome? *Nature, 424,* 33-34.

Moore, J.K. & Braucher, O. (2008). Sedimentary and mineral dust sources of dissolved iron to the world ocean. *Biogeosciences, 5*, 631-656.

Morand, L.Z., Cheng, R.H., Krogmann, D.W. & Ho, K.K. Soluble electron transfer catalysts of cyanobacteria. In: *The Molecular Biology of Cyanobacteria* (Bryant, D.A., Ed.) Kluwer Academic Publishers, Dordrecht, 1994; pp. 381-407.

Morrisey, J. & Bowler, C. (2012). Iron utilization in marine cyanobacteria and eukaryotic algae. *Frontiers in Microbiology, 3,* 1-13.

Müh, F. & Zouni, A. (2013). The nonheme iron in photosystem II. *Photosynthesis Research, 116*, 295-314.

Murata, N., Takahashi, S., Nishiyama, Y. & Allakhverdiev, S.I. (2007). Photoinhibition of photosystem II under environmental stress. *Biochimica et Biophysica Acta, 1767*, 414-421.

Murray, M.G. & Thompson, W.F. (1980). Rapid isolation of high molecular weight plant DNA. *Nucleic Acids Research, 8*(19), 4321-4326.

Musiani, F., Dikiy, A., Semenov, A.Y. & Ciurli, S. (2005). Structure of the intermolecular complex between plastocyanin and cytochrome *f* from spinach. *The Journal of Biological Chemistry, 280*(19), 18833-18841.

Nagao, R., Ishii, A., Tada, O., Suzuki, T., Dohmae, N., Okumura, A., Iwai, M., Takahashi, T., Kashino, Y. & Enami, I. (2007). Isolation and characterization of oxygen-evolving thylakoid membranes and photosystem II particles from a marine diatom *Chaetoceros gracilis*. *Biochimica et Biophysica Acta, 1767,* 1353-1362.

Nagao, R., Kato, K., Suzuki, T., Ifuku, K., Uchiyama, I., Kashino, Y., Dohmae, N., Akimoto, S., Shen, J-R., Miyazaki, N. & Akita, F. (2019). Structural basis for energy harvesting and dissipation in a diatom PSII-FCPII supercomplex. *Nature Plants, 5,* 890-901.

Nagao, R., Moriguchi, A., Tomo, T., Niikura, A., Nakajima, S., Suzuki, T., Okumura, A., Iwai, M., Shen, J-R., Ikeuchi, M. & Enami, I. (2010a). Binding and functional properties of five extrinsic proteins in oxygen-evolving photosystem II from a marine centric diatom, *Chaetoceros gracilis. Journal of Biological chemistry, 285*(38), 29191-29199.

Nagao, R., Tomo, T., Noguchi, E., Nakajima, S., Suzuki, T., Okumura, A., Kashino, Y., Mimuro, M., Ikeuchi, M. & Enami, I. (2010b). Purification and characterization of a stable oxygen-evolving photosystem II complex from a marine centric diatom, *Chaetoceros gracilis*. *Biochimica et Biophysica Acta, 1797*, 160-166.

Nagao, R., Tomo, T., Noguchi, E., Suzuki, T., Okumura, A., Narikawa, R., Enami, I. & Ikeuchi, M. (2012). Proteases are associated with a minor fucoxanthin chlorophyll *a/c*-binding protein from the diatom, *Chaetoceros gracilis*. *Biochimica et Biophysica Acta, 1817,* 2110-2117.

Nagao, R., Tomo, T. & Noguchi, E. (2015). Effects of extrinsic proteins on the protein conformation of the oxygen-evolving center in cyanobacterial photosystem II as revealed by Fourier transform infrared spectroscopy. *Biochemistry*, *54*, 2022-2031.

Nakamura, Y., Gojobori, T. & Ikemura, T. (2000). Codon usage tabulated from international DNA sequence databases: status for the year 2000. *Nucleic Acids Research, 28*(1), 292.

Navarro, J.A., Hervás, M., de la Cerda, B. & de la Rosa, M.A. (1995). Purification and physiochemical properties of the low potential cytochrome c_{549} from the cyanobacterium *Synechocystis* sp. PCC 6803. *Archives of Biochemistry and Biophysics, 318*, 46-52.

Navarro, J.A., Hervás, M. & De la Rosa, M.A. (1997). Co-evolution of cytochrome c_6 and plastocyanin, mobile proteins transferring electrons from cytochrome b_6f to photosystem I. *Journal of Biological Inorganic Chemistry, 2,* 11–22.

Navarro, J.A., Hervás, M. & De la Rosa, M.A. Purification of plastocyanin and cytochrome c_6 from plants, green algae and cyanobacteria. In: *Photosynthesis Research Protocols, Methods in Molecular Biology, 684,* (Carpentier, R., Ed.). Springer Science+Business Media, 2011; 79-94.

Navarro, J.A., Lowe, C.E., Amons, R., Kohzuma, T., Canters, G.W., De la Rosa, M.A., Ubbink, M. & Hervás, M. (2004). Functional characterization of the evolutionary divergent fern plastocyanin. *European Journal of Biochemistry, 271*(16), 3449-3456.

Nawrocki, W.K., Bailleul, B., Picot, D., Cardol, P., Rappaport, F., Wollman, F. & Joliot, P. (2019). The mechanism of cyclic electron flow. *Biochimica et Biophysica Acta – Bioenergetics, 1860,* 433-438.

Neilson, J.A.D. & Durnford, D.G. (2010). Structural and functional diversification of the light-harvesting complexes in photosynthetic eukaryotes. *Photosynthesis Research, 106,* 57-71.

Nevo, R., Charuvi, D., Tsabari, O. & Reich, Z. (2012). Composition, architecture and dynamics of the photosynthetic apparatus in higher plants. *The Plant Journal, 70,* 157-176.

Nixon, P.J., Michoux, F., Yu, J., Boehm, M. & Komenda, J. (2010). Recent advances in understanding the assembly and repair of photosystem II. *Annals of Botany, 106*, 1-16.

Nosenko, T., Lidie, K.L, Van Dolah, F.M., Lindquist, E., Cheng, J.F & Bhattacharya, D. (2006). Chimeric plastid proteome in the Florida “red tide” dinoflagellate *Karenia brevis*. *Molecular Biology and Evolution, 23*(11), 2026-2038.

Not, F., Siano, R., Kooistra, W.H.C.F., Simon, N., Vaulot, D. & Probert, I. Diversity and ecology of eukaryotic marine phytoplankton. In: *Advances in Botanical Research* (Piganeau, G., Ed.). Academic Press, 2012; Vol. 64, pp. 1-53.

Nouet, C., Motte, P. & Hanikenne, M. (2011). Chloroplastic and mitochondrial metal homeostasis. *Trends in Plant Science, 16*(7), 395-404.

Nunn, B.L., Faux, J.F., Hippmann, A.A., Maldonado, M.T., Harvey, H.R., Goodlett, D.R., Boyd, P.W. & Strzepek, R.F. (2013). Diatom proteomics reveals unique acclimation strategies to mitigate Fe limitation. *PLoS ONE, 8*(10), e75653.

Okumura, A., Nagao, R., Suzuki, T., Yamagoe, S., Iwai, M., Nakazato, K. & Enami, I. (2008). A novel protein in photosystem II of a diatom Chaetoceros gracilis is one of the extrinsic proteins located on lumenal side and directly associates with PSII core components. *Biochimica et Biophysica Acta, 1777,* 1545-1551.

Ortega, J.M. & Roncel, M. (2021). The afterglow photosynthetic luminescence. *Physiologia Plantarum, 171*(2), 268-276.

Oudot-Le Secq, M.P., Grimwood, J., Shapiro, H., Armbbrust, E.V., Bowler, C. & Green, B.R. (2007). Chloroplast genomes of the diatoms *Phaeodactylum tricornutum* and *Thalassiosira pseudonana*: comparison with other plastid genomes of the red lineage. *Molecular Genetics and Genomics, 277*(4), 427-439.

Peers, G. & Price, N.M. (2006). Copper-containing plastocyanin used for electron transport by an oceanic diatom. *Nature, 441*, 341-344.

Pettersen, E.F., Goddard, T.D., Huang, C.C., Couch, G.S., Greenblatt, D.M., Meng, E.C. & Ferrin, T.E. (2004). UCSF Chimera – A visualization system for exploratory research and analysis. *Journal of Computational Chemistry, 13*, 1605-1612.

Pfaffl, M.W. (2001). A new mathematical model for relative quantification in real time RT-PCR. *Nucleic Acids Research, 29*, 2002-2007.

Pi, X., Zhao, S., Wang, W., Liu, D., Xu, C., Han, G., Kuang, T., Sui, S-F. & Shen, J-R. (2019). The pigment-protein network of a diatom photosystem II-light harvesting antenna supercomplex. *Science, 365*, 1-10.

Pierella Karlusich, J.J., Ceccoli, R.D., Graña, M., Romero, H. & Carrillo, N. (2015). Environmental selection pressures related to iron utilization are involved in the loss of the flavodoxin gene from the plant genome. *Genome Biology and Evolution, 7*(3), 750-767.

Pierella Karlusich, J.J., Lodeyro, A.F. & Carrillo, N. (2014). The long goodbye: The rise and fall of flavodoxin during plant evolution. *Journal of Experimental Botany, 65*(18), 5161-5178.

Pushnik, J.C. & Miller, G.W. (1989). Iron regulation of chloroplast photosynthetic function: mediation of PSI development. *Journal of Plant Nutrition, 12*(4), 407-421.

Qin, L. & Kostic, N.M. (1993). Importance of protein rearrangement in the electron-transfer reaction between the physiological partners cytochrome *f* and plastocyanin. *Biochemistry, 32,* 6073-6080.

Qin, X., Suga, M., Kuang, T. & Shen, J-R. (2015). Structural basis for energy transfer pathways in the plant PSI-LHCI supercomplex. *Science, 348,* 989-995.

Redinbo, M. R., Yeates, T.O. & Merchant, S. (1994). Plastocyanin: structural and functional analysis. *Journal of Bioenergetics and Biomembranes, 26*(1), 49-66.

Rizkallah, M.R., Frickenhaus, S., Trimborn, S., Harms, L., Moustafa, A., Benes, V., Gäbler-Schwarz, S. & Beszteri, S. (2020). Deciphering patterns of adaptation and acclimation in the transcriptome of *Phaeocystis antarctica* to changing iron conditions. *Journal of Phycology, 56*(3),747-760.

Roach, T. & Krieger-Liszkay, A. (2014). Regulation of photosynthetic electron transport and photoinhibition. *Current Protein and Peptide Science, 15*, 351-362.

Rogl, H., Kosemund, K., Kühlbrandt, W. & Collinson, I. (1998). Refolding of *Escherichia coli* produced membrane protein inclusion bodies immobilised by nickel chelating chromatography. *FEBS Letters*, *432,* 21-26.

Roncel, M., Boussac, A., Zurita, J.L., Bottin, H., Sugiura, M., Kirilovsky, D. & Ortega, J.M. (2003). Redox properties of the photosystem II cytochrome b_{559} and c_{550} in the cyanobacterium *Thermosynechococcus elongatus*. *Journal of Biological Inorganic Chemistry, 8*, 206-216.

Roncel, M., González-Rodríguez, A.A., Naranjo, B., Bernal-Bayard, P., Lindahl, M., Hervás, M., Navarro, J.A. & Ortega, J.M. (2016) Iron deficiency induces a partial inhibition of the photosynthetic electron transport and a high sensitivity to light in the diatom *Phaeodactylum tricornutum*. *Frontiers in Plant Science, 7*, 1-14.

Roncel, M., Kirilovsky, D., Guerrero, F., Serrano, A. & Ortega, J.M. (2012). Photosynthetic cytochrome c_{550}. *Biochimica et Biophysica Acta – Bioenergetics, 1817*(8), 1152-1163.

Roncel, M., Yruela, I., Kirilovsky, D., Guerrero, F., Alfonso, M., Roncel, R. & Ortega, J.M. (2007). Changes in photosynthetic electron transfer and state transitions in an herbicide-resistant D1 mutant from soybean cell cultures. *Biochimica et Biophysica Acta, 1767*(6), 694-702.

Runqing, Y. & Wei, D. (2020). Improving fucoxanthin production in mixotrophic culture of marine diatom *Phaeodactylum tricornutum* by LED light shift and nitrogen supplementation. *Frontiers in Bioengineering and Biotechnology, 8,* 820.

Rutherford, A.W., Renger, G., Koike, H. & Inoue, Y. (1984). Thermoluminiscence as a probe of photosystem II. The redox and protonation states of the secondary acceptor quinone and O_2-evolving enzyme. *Biochimica et Biophysica Acta – Bioenergetics, 767*, 548-556.

Saade, A. & Bowler, C. (2009). Molecular tools for discovering the secrets of diatoms. *BioScience, 59*(9), 757-765.

Sali, A. & Blundell, T.L. (1993). Comparative protein modelling by satisfaction of spatial restraints. *Journal of Molecular Biology, 234,* 779-815.

Sambrook, J. & Russell, D.W. *Molecular cloning: a laboratory manual*. Vol. 2, 3rd ed. Cold Spring Harbor Laboratory Press, New York, 2001.

Sancho, J. (2006). Flavodoxins: sequence, folding, binding, function and beyond. *Cellular and Molecular Life Sciences, 63*, 855-864.

Sandmann, G. (1986). Formation of plastocyanin and cytochrome c_{553} in different species of blue-green algae. *Archives of Microbiology, 145,* 76-79.

Sarewicz, M., Pintscher, S., Pietras, R., Borek, A., Bujnowicz, L., Hanke, G., Cramer, W.A., Finazzi, G. & Osyczka, A. (2021). Catalytic reactions and energy conservations in the cytochrome bc_1 and b_6f complexes of energy-transducing membranes. *Chemical Reviews, 121*(4), 2020-2108.

Sasse, J. & Gallagher, S.R. (2009). Staining proteins in gels. *Current Protocols in Molecular Biology,* 10.6.1-10.6.27.

Sawaya, M.R., Krogmann, D.W., Serag, A., Ho, K.K., Yeates, T.O. & Kerfeld, C.A. (2001) Structures of cytochrome *c*-549 and cytochrome c_6 from the cyanobacterium *Arthrospira maxima*. *Biochemistry, 40,* 9215-9225.

Scala, S., Carels, N., Falciatore, A., Chiusano, M.L. & Bowler, C. (2002). Genome properties of the diatom *Phaeodactylum tricornutum*. *Plant Physiology, 129,* 993-1002.

Schilder, J. & Ubbink, M. (2013). Formation of transient protein complexes. *Current Opinion in Structural Biology, 23*, 911-918.

Schindelin, J., Arganda-Carreras, I., Frise, E., Kaynig, V., Longair, M., Pietzsch, T., Preibisch, S., Rueden, C., Saalfeld, S., Schmid, B., Tinevez, J-Y., White, D.J., Hartenstein, V., Eliceiri, K., Tomancak, P. & Cardona, A. (2012). Fiji: An open-source platform for biological-image analysis. *Nature Methods, 9*(7), 676-682.

Schlarb-Ridley, B.G., Bendall, D.S. & Howe, C.J. (2003). Relation between interface properties and kinetics of electron transfer in the interaction of cytochrome *f* and plastocyanin from plants and the cyanobacterium *Phormidium laminosum*. *Biochemistry, 42,* 4057-4063.

Sechi, S. & Chait, B.T. (1998). Modification of cystein residues by alkylation. A tool in peptide mapping and protein identification. *Analytical Chemistry, 70*(24), 5150-5158.

Sétif, P. Electron transfer from the bound iron-sulfur clusters to ferredoxin/flavodoxin: Kinetic and structural properties of ferredoxin/flavodoxin reduction by photosystem I. In: *Photosystem I: the light driven plastocyanin:ferredoxin oxidoreductase* (Golbeck, J. H., Ed.). Advances in photosynthesis and respiration, *24.* Springer, Dordrecht, The Netherlands, 2006; pp. 439-454.

Sgherri, C., Pinzino, C. & Quartacci, Q.M. Reactive oxygen species and photosynthetic functioning: past and present. In: *Reactive oxygen species in plants: boon or bane – revisiting the role of ROS* (Singh, V.P., Singh, S., Tipathi, D.K., Prasad, S.M. & Chauhan, D.K., Eds.). John Wiley & Sons Ltd, Chichester, England, 2018; pp. 137-155.

Shahrokh, K., Orendt, A., Yost, G.S. & Cheatham, T.E. (2012), Quantum mechanically derived AMBER-compatible heme parameters for various states of the cytochrome p450 catalytic cycle. *Journal of Computational Chemistry, 33*(2), 119-133.

Shaked, Y. & Lis, H. (2012). Disassembling iron availability to phytoplankton. *Frontiers in Microbiology, 3,* 123.

Shen, J-R. (2015). The structure of photosystem II and the mechanism of water oxidation in photosynthesis. *Annual Review of Plant Biology, 66*, 23-48.

Shen, J-R., Qian, M., Inoue, Y. & Burnap, R.L. (1998). Functional characterization of *Synechocystis* sp. PCC 6803 Δ*psb*U and Δ*psb*V mutants reveals important roles of cytochrome *c*-550 in cyanobacterial oxygen evolution. *Biochemistry, 37*, 1551-1558.

Shen, J.R. & Inoue, Y. (1993). Binding and functional properties of two new extrinsic components, cytochrome c_{550} and a 12-kDa protein, in cyanobacterial photosystem II. *Biochemistry, 32,* 1825-1832.

Shen, M-Y. & Sali, A. (2006). Statistical potential for assessment and prediction of protein structures. *Protein Science, 15,* 2507-2524.

Shikanai, T. (2014). Central role of cyclic electron transport around photosystem I in the regulation of photosynthesis. *Current Opinion in Biotechnology, 26,* 25-30.

Shimazaki, K.I., Takamiya, K.I. & Nishimura, M. (1978). Studies on electron transfer systems in the marine diatom *Phaeodactylum tricornutum*. I. Isolation and characterization of cytochromes. *Journal of Biochemistry, 83*(6)*,* 1631-1638.

Siaut, M., Heijde, M., Mangogna, M., Montsant, A., Coesel, S., Allen, A., Manfredonia, A., Falciatore, A. & Bowler, C. (2007). Molecular toolbox for studying diatom biology in *Phaeodactylum tricornutum*. *Gene*, *406*(1-2), 23–35.

Sievers, F., Wilm, A., Dineen, D., Gibson, T.J., Karplus, K., Li, W., et al. (2011). Fast, scalable generation of high-quality protein multiple sequence alignments using Clustal Omega. *Molecular Systems Biology, 7,*(539).

Sigfridsson, K., He, S., Modi, S., Bendall, D.S., Gray, J. & Hansson, Ö. (1996). A comparative flash-photolysis study of electron transfer from pea and spinach plastocyanins to spinach Photosystem I. A reaction involving a rate-limiting conformational change. *Photosynthesis Research, 50*(1), 11-21.

Sommer, F., Drepper, F., Haehnel, W. & Hippler, M. (2004). The hydrophobic recognition site formed by residues PsaA-Trp651 and PsaB-Trp627 of photosystem I in *Chlamydomonas reinhardtii* confers distinct selectivity for binding of plastocyanin and cytochrome c_6. *Journal of Biological Chemistry, 279*(19), 20009-20017.

Sommer, F., Drepper, F., Haehnel, W. & Hippler, M. (2006). Identification of precise electrostatic recognition sites between cytochrome c_6 and the photosystem I subunit PsaF using mass spectrometry. *Journal of Biological Chemistry, 281*(46), 35097-35103.

Soriano, G.M., Cramer, W.A. & Krishtalik, L. (1997). Electrostatic effects on electron-transfer kinetics in the cytochrome *f*-plastocyanin complex. *Biophysical Journal, 73*, 3265-3276.

Stothard, P. (2000). The sequence manipulation suite: JavaScript programs for analyzing and formatting protein and DNA sequences. *BioTechniques, 28*(6).

Straus, N.A. Iron deprivation: Physiology and gene regulation. In: *The Molecular Biology of Cyanobacteria* (Bryant DA, Ed.). Kluwer Academic Publishers, Dordrecht, 1994; pp. 731-750.

Strickland, J.D.H. & Parsons, T.R. (1972). A practical handbook of seawater analysis. *Bulletin Fisheries Research Board of Canada, 167,* 1-311.

Stroebel, D., Choquet, Y., Popot, J.L. & Picot, D. (2003). An atypical haem in the cytochrome b_6f complex. *Nature, 426*, 413-418.

Strzepek, R.F. & Harrison, P.J. (2004). Photosynthetic architecture differs in coastal and oceanic diatoms. *Nature, 431,* 689-692.

Studier, F.W. & Moffatt, B.A. (1986). Use of the bacteriophage T7 RNA polymerase to direct selective high-level expression of cloned genes. *Journal of Molecular Biology, 189*(1), 113-130.

Su, X., Ma, J., Pan, X., Zhao, X., Chang, W., Liu, Z., Zhang, X. & Li, M. (2019). Antenna arrangement and energy transfer pathways of a green algal photosystem-I-LHCI supercomplex. *Nature Plants, 5,* 273-281.

Szabo, E. & Colman, B. (2007). Isolation and characterization of carbonic anhydrases from the marine diatom *Phaeodactylum tricornutum*. *Physiologia Plantarum, 129*(3), 484-492.

The law of the sea (2019). *Nature Geoscience, 2,* 153.

Tikhonov, A.N. The Cytochrome b_6f complex: biophysical aspects of its functioning in chloroplasts. In: *Membrane protein complexes: structure and function*. *Subcelullar Biochemistry* (Harris, J. & Boekema, E., Eds.). Springer, Singapore, 2018; Vol. 87.

Tottey, S., Patterson, C.J., Banci, L., Bertini, I., Felli, I.C., Pavelkova, A., Dainty, S., Pernil, R., Waldron, K.J., Foster, A.W. & Robinson, N.J. (2012). Cyanobacterial metallochaperone inhibits deleterious side reactions of copper. *Proceedings of the National Academy of Sciences USA, 109*(1), 95-100.

Twining, B.S. & Baines, S.B. (2013). The trace metal composition of marine phytoplankton. *Annual Review of Marine Science, 5*, 191-215.

Ubbink, M., Ejdebäck, M., Karlsson, B.G. & Bendall, D.S. (1998). The structure of the complex of plastocyanin and cytochrome *f*, determined by paramagnetic NMR and restrained rigid-body molecular dynamics. *Structure, 6*(3), 323-335.

Umena, Y., Kawakami, K., Shen, J-R. & Kamiya, N. (2011). Crystal structure of oxygen-evolving photosystem II at a resolution of 1.9 Å. *Nature, 473*, 55-60.

Vavilin, D.V. & Ducruet, J.M. (1998). The origin of 115-130°C thermoluminescence bands in chlorophyll-containing material. *Photochemistry and Photobiology, 68*(2), 191-198.

Vavilin, D.V., Matorin, D.N. & Rubin, A.B. (2002). High-temperature thermoluminescence of chlorophyll as a method to study lipid peroxidation in planktonic algae. *Archid Für Hydrobiologie, 153*(4), 685-701.

Veith, T. & Büchel, C. (2007). The monomeric photosystem I-complex of the diatom *Phaeodactylum tricornutum* binds specific fucoxanthin chlorophyll proteins (FCPs) as light-harvesting complexes. *Biochimica et Biophysica Acta – Bioenergetics, 1767*, 1428-1435.

Viola, S., Bailleul, B., Yu, J., Nixon, P., Sellés, J. & Joliot, P. (2019). Probing the electric field across thylakoid membranes in cyanobacteria. *Proceedings of the National Academy of Sciences USA*, *116*(43), 21900-21906.

Vogt, L., Vinyard, D.J., Khan, S. & Brudvig, G.W. (2015). Oxygen-evolving complex of Photosystem II: an analysis of second-shell residues and hydrogen-bonding networks. *Current Opinion in Chemical Biology, 25,* 152-158.

Wang, W., Zhao, S., Pi, X., Kuang, T., Sui, S-F. & Shen, J-R. (2020). Structural features of the diatom photosystem II-light-harvesting antenna complex. *FEBS Journal*, 287, 2191-2200.

Wijffels, R.H., Kruse, O. & Hellingwerf, K.J. (2013). Potential of industrial biotechnology with cyanobacteria and eukaryotic microalgae. *Current Opinion in Biotechnology, 24*(3), 405-413.

Woodward, F.I. (2007). Global primary production. *Current Biology, 17*(8), 269-273.

Xiao, Y., Zhu, Q., Yang, Y., Wang, W., Kuang, T., Shen, J-R. & Han, G. (2020). Role of PsbV-Tyr137 in photosystem II studied by site-directed mutagenesis in the thermophilic cyanobacterium *Thermosynechococcus vulcanus*. *Photosynthesis Research, 146,* 41-54.

Xu, C., Pi, X., Huang, Y., Han, G., Chen, X., Qin, X., Huang, G., Zhao, S., Yang, Y., Kuang, T., Wang, W., Sui, S-F. & Shen, J-R. (2020). Structural basis for energy transfer in a huge diatom PSI-FCPI supercomplex. *Nature Communications, 11,* 5081.

Yadav, S.K., Khatri, K., Rathore, M.S. & Jha, B. (2018). Introgression of *UfCyt* c_6, a thylakoid lumen protein from a green seaweed *Ulva fasciata* Delile enhanced photosynthesis and growth in tobacco. *Molecular Biology Reports, 45,* 1745-1758.

Yamada, S., Park, S.Y., Shimizu, H., Koshizuka, Y., Kadokura, K., Satoh, T., Suruga, K., Ogawa, M., Isogai, Y., Nishio, T., Shiro, Y. & Oku, T. (2000). Structure of cytochrome c_6 from the red alga *Porphyra yezoensis* at 1.57 Å resolution. *Acta Crystallographica Section D, Biological Cyrstallography, 56,* 1577-1582.

Zouni, A., Witt, H.T., Kern, J., Fromme, P., Kaub, N., Saenger, W. & Orth, P. (2001). Crystal structure of photosystem II from *Synechococcus elongatus* at 3.8 Å resolution. *Letters to Nature, 409,* 739-743.

Zurita, J.L., Roncel, M., Aguilar, M. & Ortega, J.M. (2005). A thermoluminescence study of Photosystem II back electron transfer reactions in rice leaves. Effects of salt stress. *Photosynthesis Research 84*(1-3), 131-137.


UNIVERSIDAD DE SEVILLA


CSIC
Consejo Superior de Investigaciones Científicas


GOBIERNO
DE ESPAÑA
MINISTERIO
DE EDUCACIÓN, CULTURA
Y DEPORTE


Junta de Andalucía